Rajan Jaiswal

Waste as feed to a biomass gasification reactor

Dissertation for the degree of Ph.D
Process, Energy and
Automation Engineering

**Faculty of Technology, Natural
Sciences and Maritime Studies**

University of
South-Eastern Norway

Rajan Jaiswal

Waste as feed to a biomass gasification reactor

A PhD dissertation in
Process, Energy and Automation Engineering

Dedication

To my parents, wife, supervisors, and friends, without whom this work would not have been possible.

Preface

This thesis is submitted as a partial fulfilment of the criteria for the Doctor of Philosophy (Ph.D.) degree within the Process, Energy, and Environmental Technology program at the University of South-Eastern Norway. The thesis is structured into two sections. Part 1 provides an overview of the research project, and Part 2 presents the scientific papers and conference contributions. The research was conducted at campus Porsgrunn from March 2020 to February 2024. Completing this dissertation would not have been possible without the generous assistance and encouragement from several remarkable individuals.

First and foremost, I express my sincere gratitude to my main supervisor, Associate Professor Rajan Kumar Thapa, whose expertise and invaluable insights have been instrumental in shaping this research. His guidance, patience, and trust in my skills have allowed me to carry this work with confidence at my own pace, make mistakes, learn from them, and grow. Apart from academic supervision, he has been a guardian to me, and with his mentorship, my life in Norway has been joyful.

I want to express my deepest gratitude to my co-supervisor, Professor Britt M.E. Moldestad, for her motherly encouragement, advice, and guidance during these seven years of my studies in Norway. She has supervised me since 2016, when I started my master's program at USN. During these periods, she gave me the opportunity to learn and conduct research, provided me with the necessary resources to develop my skills, and gave me this life-changing opportunity to pursue a doctoral degree. She has extraordinary qualities to motivate the students with her positive feedback when their motivation is low. I consider myself fortunate to have Prof. Britt as my mentor.

My sincere appreciation goes to my co-supervisor, Prof. Marianne S. Eikeland, for her constructive feedback and support. I am grateful to my co-supervisor, Prof. Henrik K. Nielsen, for his guidance and insights and allowing me to use the UiA laboratory. My special thanks go to Associate Prof. Nora C. I. Furuvik for always encouraging and supporting me with a good heart whenever needed. I sincerely thank Dr Cornelius. E. Agu for his guidance and for sharing his in-depth expertise on the topic. Sincere appreciation to Dr. Janitha Bandara for his generous suggestions and collaborative work. I want to thank Om Prakash Chapagain, Dr. Ramesh Timilsina and Nastaran Samani for sharing their ideas. Special thanks to Alexander (IT), Øyvind (Workshop), Franz (Powder and Material Lab), and Fredrik (Process Lab) for helping me and making my work easier during this period.

In all, I express my gratitude to my family members for their unwavering love, support, and motivation throughout my lifetime, though words cannot completely capture the depth of my sincere appreciation. I am forever indebted to them, particularly my older brother Pramendra, who has been a constant pillar of support in different phases of my journey. I am heartily thankful to my wife, Chandani, for her love, care, and sacrifice during this period.

Porsgrunn, February 2024
Rajan Jaiswal

Acknowledgements

Abstract

Solid waste management has been a global challenge. With the growing population, an increase in solid waste from households, agriculture, and industries is inevitable. At the same time, rapid industrialization and technological advancements due to increasing population have increased the energy demand significantly. The predominant reliance on fossil fuels has led to severe environmental consequences, including greenhouse gas emissions, global warming, rising sea levels, extreme weather conditions, and depletion of fossil fuel reserves. Consequently, the need for alternative energy sources has become crucial. This study explores the utilization of waste for energy production, aiming to address two global problems: waste management issues and supply for the clean energy demand. Thermochemical conversion technology, such as gasification, has gained attention when it comes to converting wastes into energy. The main combustible gas components from the gasification process are methane, hydrogen, and carbon monoxide, which can be useful for producing biofuels and chemicals or for power generation. The major challenge in utilizing wastes in a gasification reactor is to convert solid wastes and their mixture as fuel and operate the reactor economically to produce high-quality synthesis gas. The choice of a gasification reactor is critical for economical operation as it should allow to handle a wide variety of feedstock. In this regard, a bubbling fluidized bed reactor (BFB) is a better option among various thermal reactors available since BFB provides the flexibility to use a wide variety of feedstocks and provides uniform heat and mass transfer for thermal degradation.

This project investigates various challenges when converting waste to high calorific value feedstock (fuel) and utilizing such feedstock for energy recovery in a BFB gasification reactor. The task has been accomplished using a combination of experimental work and CPFD simulations. For the experimental work, three different BFB reactors were employed to gain better understanding of the fluid dynamic behaviour coupled with thermochemical conversion phenomena in a BFB gasifier. The fluidized bed setups used in this work include: (i) a cold flow BFB reactor equipped with pressure sensors, (ii) a cold flow BFB reactor equipped with electrical capacitance tomography (ECT) sensors, and (iii) a 20 kW BFB gasifier. The cold models were used to investigate the fluid dynamics behaviour of the bed, such as mixing and segregation, bubble dynamics and fluidization regime. The results from the cold model test were used to select operating parameters for the gasification experiments. For the gasification experiments, the 20 kW BFB gasifier was operated in autothermal and allothermal modes with several waste feedstocks and air as the gasifying medium. The feedstocks from various sources, such as municipal solid wastes (MSW), agricultural wastes, garden residue, and industrial wastes, were used as fuel for the gasifier. All the waste feedstocks, paper, fish, garden residue, sawdust, coffee grounds, barley straw, bark, and grass were used in the pellet form except for wood chips. Among these feedstocks, barley straw, saw dust, bark and coffee grounds were pelletized using a lab-scale pellet mill. The syngas production potential of the feedstocks and the reactor performance at different reactor operating conditions were

assessed based on the carbon conversion efficiency, chemical conversion efficiency, thermal conversion efficiency, and gas yield strengths.

Similarly, computational particle fluid dynamic (CPFD) models were developed to investigate the thermal and hydrodynamic behaviour of the reactor and determine the operational parameters suitable for running the gasifier at optimal conditions. The CPFD simulation were developed in the commercial software Barracuda VR 21.1.1 and the results were validated with experimental data obtained from the 20 kW gasifier and cold bed rigs. The CPFD models were used to address challenges such as slug in the bed, excess steam in the product gas, unconverted carbon, reduced gas residence time, and inadequate distribution of gas and biomass in the bed. The simulations also explore the influence of bubble properties, biomass feeding position, and air supply patterns on the reactor performance.

The air-gasification tests with the feedstocks, wood chips, grass pellets and wood pellets revealed that at equivalence ratio (ER) <0.16, the syngas quality was enhanced with lower nitrogen yield at reactor temperature above 800 ℃ . About 70-75% of the carbon conversion efficiency was achievable at allothermal reactor conditions. However, grass pellets showed agglomerations in the bed at reactor temperature 800 ℃ and wood chips caused blockage in the feeding system. Similarly, the low-grade feedstocks, fish pellets (animal waste origin), garden waste pellets (plant origin) and paper pellets (MSW) were gasified in an autothermal mode with air as gasifying medium and at reactor initial temperature of 650 ℃. The reactor initial temperature was selected by considering the pyrolysis temperature and ash melting temperature of the feedstock. The result depicted that overall conversion efficiency of the paper pellets reached approximately 80-90%, garden waste pellets exhibited a conversion efficiency of 50-60% and the fish pellets demonstrated a lower conversion efficiency of 22-40%. The reduced conversion efficiency of the fish pellets was ascribed to the animal-based origin of the feedstock, containing fats and proteins, necessitating higher temperatures for degradation. Notably, despite the high moisture content of paper pellets (26 wt.%), the results indicated a higher conversion efficiency. This suggested that the moisture content had little to no influence on the conversion process when the feedstock was injected on the top of the bed. Pelletization experiments with coffee grounds, sawdust, bark and barley straw revealed that optimal conditions for the pelletization of the feedstocks were at the die temperature of 50℃-60℃, a moisture content of 9-14 wt.%, and a roller-to-die distance of 4 mm. Mechanically durable pellets with enhanced compression strength improved the conversion efficiency of the feedstock during gasification tests. Over the ER of 0.15-0.32, the carbon conversion efficiency of the feedstock coffee grounds pellets and straw pellets reached about 75%, demonstrating that both wastes are potential feedstock for energy recovery.

CPFD simulations with two different feeding positions of the biomass (on the top of the bed and in the bed near to the bottom of the reactor) in the gasifier showed that in-bed feeding of the biomass was better compared to top bed feeding. The result demonstrated that higher

carbon conversion, uniform reactor temperatures and better gas quality yield were achieved with in-bed biomass feeding. Similar, different modes of air supply such as: (i) uniform air distribution (with air distributor), (ii) with side nozzles, and (iii) multiple injection points were investigated in a BFB reactor. The result demonstrated that air can be injected in the fluidized bed with the side nozzles while maintaining similar fluid dynamics properties of the bed compared to air distributor as flow boundary conditions. Thus, side nozzles as flow boundary conditions can be employed to minimize the cost and avoid operational challenges related to the presence of air distributor in the gasifier. Also, the CPFD model results illustrated that for an auto-thermal operation of the reactor with maximum hydrogen yield in the product gas, the steam-to-air ratio was 0.05. Based on the experimental measurements and CPFD model simulations, a simple correlation ($gD_b/u_0 = 3.0$), based on superficial gas velocity (u_0) and average bubble diameter over the bed (D_b) for efficient biomass gasification in a bubbling fluidized bed was developed. The result revealed that at the optimum gas residence time, the concentration of hydrogen is maximum while the concentrations of carbon dioxide and water vapor are minimum in the product gas. This proposed model can, therefore, be used to size the reactor or set the operating gas velocity to achieve optimum gasification.

Keywords: Waste feedstocks; Pelletization; Bubbling fluidized bed; Gasification; Bubble properties; Equivalence ratio; Allothermal; Auto-thermal; Air-steam gasification.

List of papers

Paper 1

R. Jaiswal, R. K. Thapa, and B. M. E. Moldestad, "Study of agricultural waste gasification in an air-blown bubbling fluidized bed using a CPFD model," in ***Proceedings of The 61st SIMS Conference on Simulation and Modelling SIMS 2020***, *September 22-24, Virtual Conference, Finland*, 2021.

DOI: 10.3384/ecp20176393.

Paper 2

J. C. Bandara, R. Jaiswal, H. K. Nielsen, B. M. E. Moldestad, and M. S. Eikeland, "Air gasification of wood chips, wood pellets and grass pellets in a bubbling fluidized bed reactor," ***Energy***, vol. 233, p. 121149, Oct. 2021,

DOI: 10.1016/J.ENERGY.2021.121149.

Paper 3

R. Jaiswal, N. C. I. S. Furuvik, R. K. Thapa, and B. M. E. Moldestad, "A CPFD model to investigate the influence of feeding positions in a gasification reactor," ***International Journal of Energy Production and Management***, vol. 5, no. 3, 2020,

DOI: 10.2495/EQ-V5-N3-223-233.

Paper 4

R. Jaiswal, M. S. Eikeland, B. M. E. Moldestad, and R. K. Thapa, "Influence on the fluidization pattern of a freely bubbling fluidized bed with different modes of air supply," in ***Proceedings of the 63rd International Conference of Scandinavian Simulation Society, SIMS 2022***, *Trondheim, Norway, September 20-21, 2022*, 2022.

DOI: 10.3384/ecp192041.

Paper 5

R. Jaiswal, B. M. E. Moldestad, M. S. Eikeland, H. K. Nielsen, and R. K. Thapa, "~~Image Processing and Measurement of the Bubble Properties in a Bubbling Fluidized Bed Reactor~~," ***Energies***, vol. 15, no. 21, 2022,

DOI: 10.3390/en15217828.

Paper 6

R. Jaiswal, C. E. Agu, H. Nielsen, M. Eikeland, B. Moldestad, and R. Thapa, "Investigation of Bubble Properties in a Bubbling Fluidized-Bed Gasification Reactor Using a Computational Particle Fluid Dynamic Model," *Industrial & Engineering Chemistry Research*, vol. 62, no. 21, pp. 8500–8514,

Paper 7

R. Jaiswal, C. E. Agu, H. Nielsen, M. Eikeland, B. Moldestad, and R. Thapa, "Alternative Energy - Evaluation of Waste Feedstocks for Heat Generation and Syngas Production," Submitted for publication to the Journal*, Fuel*.

Paper 8

R. Jaiswal, C. E. Agu, H. Nielsen, M. Eikeland, B. Moldestad, and R. Thapa, "Enhanced hydrogen production from gasification of wood pellets in a fluidized bed reactor with air-steam as oxidizing medium," Accepted for publication in the Journal*, Springer - *Communications in Computer and Information Science*.

Table of contents

Part 1
Overview

1 Introduction

Gasification is an old method for extracting energy from coal which has gained renewed interest in waste-to-energy conversion process. However, achieving commercial breakthrough in waste-to-energy technologies necessitates the utilization of a broad range of wastes and their mixture. Therefore, in depth understanding of waste-to-fuel and the efficient utilization of wastes to energy technologies is required. The conversion of waste materials to a usable form of fuel and utilization of such waste driven fuel in a thermochemical waste-to-energy conversion technology (typically gasification) remains an active area of research currently. This study investigates the gasification of waste feedstocks to produce high-calorific-value gases in a fluidized bed gasifier, employing experimental methods, mathematical modelling, and computational fluid dynamic simulations.

1.1 Background and motivation

With the growing population, an increase in solid waste from households, agriculture, and industries is inevitable. The world is expected to generate about 46 billion tons of wastes annually by 2050 [1] . Despite strict measures and regulations adopted by countries to reuse, recycle and handle wastes, more than three-quarters of the solid wastes are still incinerated or landfilled. The world bank report mentioned that 37 % of solid wastes were landfilled globally, 33% were openly dumped and 11 % of the total wastes were incinerated in the year 2016 [2]. It is reported that in the year 2020, about 9% of greenhouse gas emissions were from waste [3]. In addition to the greenhouse gas emission, the wastes if remained unmanaged, will pollute the water resources, contaminate the fertile soil, and degrade public health with wide variety of respiratory diseases [4]. Therefore, it is of utmost importance to handle the wastes in a way that environmental components are preserved with low carbon footprints.

At the same time, rapid industrialization, and technological advancements due to the increasing population have surged the energy demand significantly. However, more than 83 % of the energy need globally is fulfilled by the fossil fuel consumptions [5]. The continuous exploitation of the fossil fuel resources has led to dramatic increase in greenhouse gases, global warming, rise in the sea levels, extreme weather conditions and depletion of fossil fuel reserves. Consequently, these impacts have serious social, economic, and environmental ramifications [6], [7], [8], [9]. Therefore, switching to an alternative energy source is evident. In this regard, utilizing wastes for energy production is a wise alternative to address two major issues: waste management problems and supply clean energy demand. Waste can be converted into energy via thermal decomposition methods such as incineration, pyrolysis, combustion, and gasification. Among the thermochemical conversion processes, the gasification of solid wastes gives higher gaseous output [10] . The main combustible gas

components from the gasification process are methane, hydrogen, carbon monoxide which can be useful for producing biofuels and chemicals or for power generation [11]. This work investigates the use of gasification technology to produce syngas from various wastes as feedstocks.

The major challenge at present is handling various types of solid wastes and their mixture as a fuel to the gasification reactor and operate the reactor economically to produce high-quality synthesis gas. The wastes are available in different forms and cannot be fed to the reactor directly. Therefore, it has to be converted into the right shape and size to transport or fed into the reactor. Drying and pelletization of wastes are viable options that increases the calorific value of fuel and makes it easier to transport and feed to the reactor [12]. Additionally, when it comes to handling a wide variety of solid wastes, the choice of a gasification reactor is critical for economical operation. In this regard, a bubbling fluidized bed reactor is a better option among various thermal reactors available since it provides flexibility to use a wide variety of feedstocks and provides uniform heat and mass transfer for thermal degradation [13]. The multi-phase and multi-particle flow with a series of homogenous and heterogeneous reactions in a bubbling fluidized bed (BFB) gasification reactor is a complex phenomenon. Therefore, a proper understanding of the reactor operating conditions like equivalence ratio, temperature, bed material to biomass ratio, segregation and mixing is essential for efficient operation, proper design, and scale up of such reactors. On the contrary, the lack of proper understanding of thermochemical conversion in a BFB gasification reactor leads to several challenges such as entrainment of the particles in product gases, agglomeration, non-uniform product gases due to segregation, large bubbles bypassing the bed and slug formation [14], [15], [16], [17].

This project investigates various challenges which occur when converting waste to fuel as feedstock and utilizing such feedstock for energy recovery in a BFB gasification reactor. Feedstocks are prepared in the form of pellets by pelletizing the solid wastes. The syngas production potential for different feedstocks is tested in a 20 kW BFB gasification reactor at USN. The reactor performance based on carbon conversion efficiency and product gas yield at different operating conditions with various feedstocks are evaluated. In addition, Computational Particle Fluid Dynamic (CPFD) models are developed to study waste gasification. The CPFD models are used to investigate the thermal and hydrodynamics behaviour of the reactor and obtain the operational parameter suitable to run the gasifier in an optimal condition.

1.2 Research objectives

While using waste as feed to the biomass gasification reactor, the major challenge is utilizing various types of solid wastes and their mixture as a fuel to the reactor and operate the reactor efficiently to produce a high-quality product gas. The major objectives of this work are outlined as follows:

   A. Feedstock preparation and characterization of waste feedstocks and bed material for utilization in a bubbling fluidized bed gasifier.
   B. Gasification of wastes feedstock in a bubbling fluidized bed gasification reactor.
   C. To provide optimal parameters for efficient operation of the bubbling fluidized bed gasifier based on computational studies and experiments.
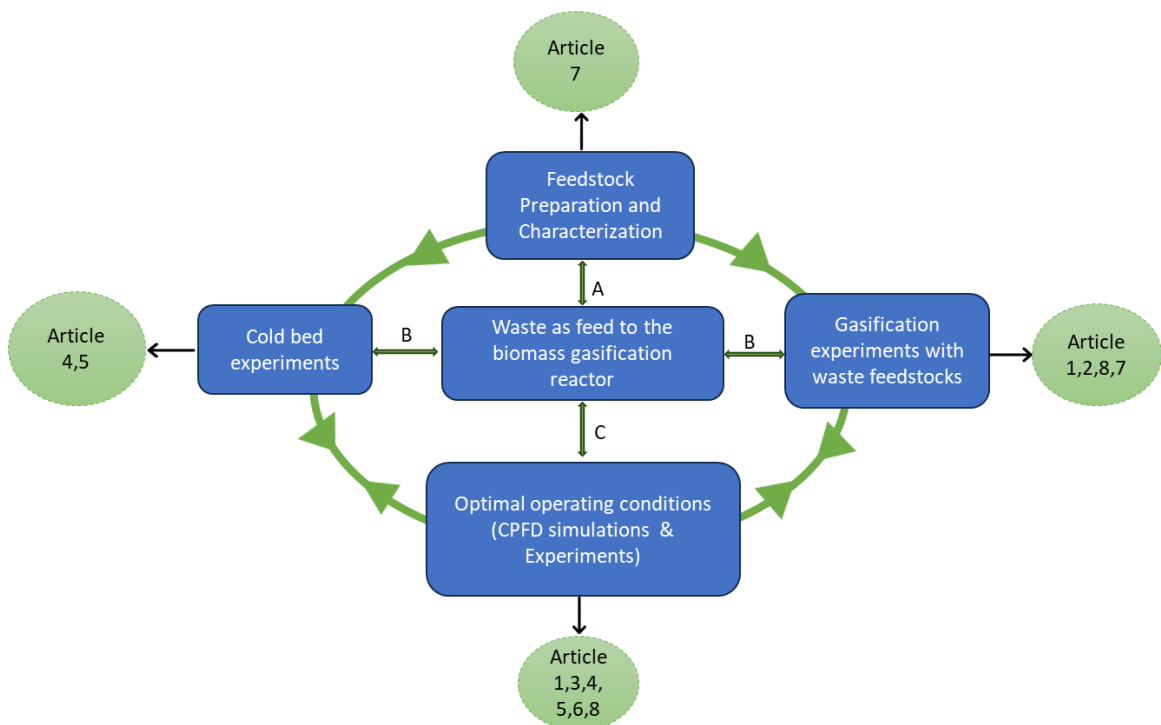

Figure 1: Summary of the thesis task.

1.3 Research scope

This project investigates various challenges associated with the gasification of solid wastes and thus, directly contribute to increase the knowledge within the field of solid waste management using gasification. Utilization of solid waste from different sources via gasification, will not only contribute to preserve the environmental components but will also contribute to meet the increasing energy needs in the world. Thus, this project will be highly relevant for policy makers, industries and researchers interested in developing innovative technology that helps to solve environmental problems and at the same time generate revenue.

To obtain the main objective, the project has focused on the following broad areas.

- Preparation and pelletization of the solid waste feedstocks.
- Characterization of the feed properties through analytical methods.
- Bed material preparation and characterization.
- Experiments on the cold bed rig to evaluate optimal operating conditions and fluid dynamic behaviour of the reactor.
- Gasification experiments on a 20 kW bubbling fluidized bed reactors with various waste feedstocks at different operating conditions.
- Analysis of product gas produced from the gasification of several types of solid waste.
- Develop a 3D computational particle fluid dynamic model in Barracuda VR based on the experimental data obtained from the cold bed and gasification experiments.
- Investigate different parameters that influence the product gas quality and reactor efficiency using the CPFD model and experimental tests.
- Find optimal operating parameters for efficient operation of the gasifier with high quality product gas yield.

1.4 Research limitation

While trying to achieve the overall goals, this research remains constrained to a specific number of investigations. The subsequent list underscores the limitation of this thesis due to the time constraints and challenges associated with the experimental setup.

- Only sand particles have been used as the bed material in the gasification reactor.
- The experimental measurements are based on air as the fluidizing and gasifying agent.
- A relatively small bed diameter, 10 cm is used in this work, thus necessitating further investigation into the scaling up of the results obtained.
- Tar measurement and entrainments of the particles, which also give indication about the gasification quality, are not obtained.

1.5 Overall Thesis Layout

The thesis consists of 7 chapters and an annexure containing eight papers, either published or submitted. Chapter 1 provides an overview of the research background, research objectives, scope, and limitations. Chapter 2 contains literature review of global waste scenario, waste-to-energy conversion via different waste-to-energy technologies particularly thermal treatment methods. In addition, Chapter 2 provides literature review of densification of the solid wastes and the bubbling fluidized bed reactor for conversion of the solid wastes into valuable product. Chapter 3 presents the description of the experimental set up of the cold fluidized bed reactors, a 20 kW gasifier, the pellet machine, analytical methods for the characterization of the particles and different mathematical model implemented in this study. Chapter 4 discuss the CPFD model development including the information on grid configuration, boundary conditions, particle modelling parameters, drag model, governing equations, and chemical kinetics. The results and summary of the articles are briefly discussed in Chapter 5. Chapter 6 discuss the main finding of the results and highlight the contribution of the thesis. Chapter 7 summarizes the research project with conclusions and outlines future work. The Annexure compiles published, accepted, and submitted scientific articles.

2 Literature Review

2.1 Global waste scenario and waste to energy potential

The world rapid industrial revolution and economic growth have been built upon the premises: take, make, and dispose. Therefore, global waste management faces challenges with unprecedented waste generation which is estimated to increase by approximately 70 % (3.4 billion tonnes) by 2050 compared to 2.01 billion tonnes produced in the year 2016 [2]. Of the waste produced in 2016, 40 % is not managed in an environmentally safe manner [2]. On a daily basis, the average person produces approximately 0.74 kilograms of waste, ranging from as little as 0.11 kilograms to as much as 4.54 kilograms, depending on the socio-economic factor and population density [2]. For instance, China comprises approximately 18 % of the world's population and is the largest contributor to global municipal solid wastes (MSW), making up more than 15% of the total waste generated [18]. Nevertheless, when evaluating waste generation per capita, the rankings undergo a significant shift, with a different country emerging as the top producer. When considering the amount of waste per capita, USA, Canada, and Australia are on the top list. Although representing only 16 percent of the world population, high-income countries are responsible for generating a significant portion of the world waste, accounting for approximately 34 percent, which equates to 683 million tonnes [2]. Projections indicate that daily per capita will significantly influence waste generation. The regional waste generation and per-person waste generation globally in 2016 and the forecast for up to 2050 are depicted in Figure 2.
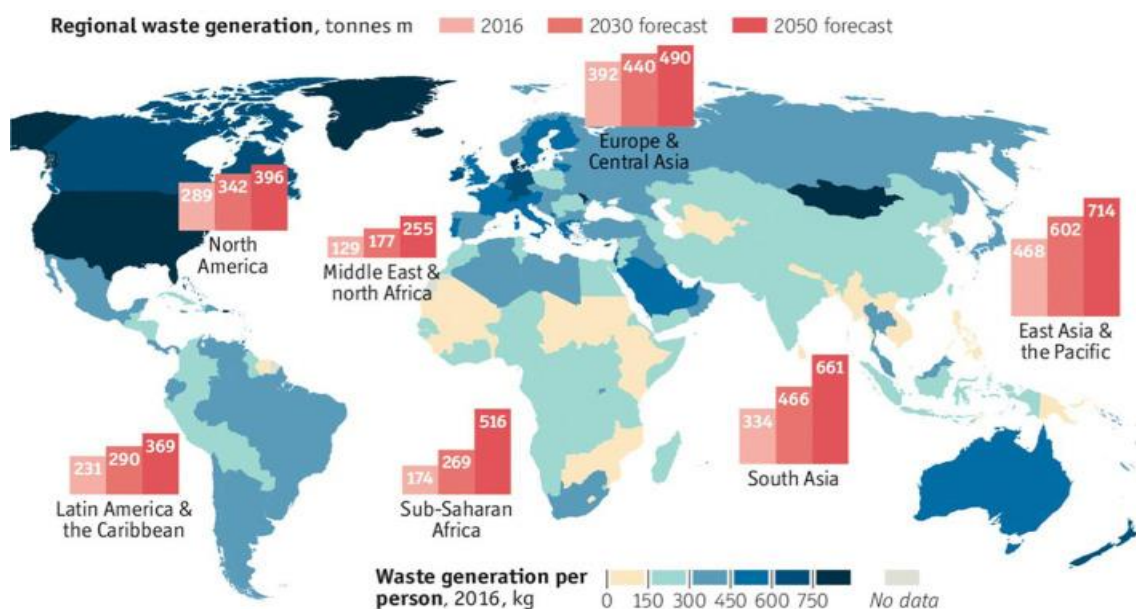

Figure 2:Waste generation trend globally and projection [19] .

The waste generation forecast illustrates that high-income countries are expected to increase waste production by 19 percent by 2050 [2]. In contrast, low- and middle-income countries are anticipated to experience a significant increase, approximately exceeding 40 percent, as their living standard and income grow [2]. These trends highlight the urgent need for adopting global waste management methods that are environmentally friendly and sustainable. However, the World Bank estimated that 33 percent of wastes are openly disposed, and 25 percent are deposited in landfills (shown in Figure 3 b) [2]. Such large amounts of unmanaged waste dumping caused serious environmental, social, and human health problems [9]. It was estimated that 18 % of global methane emissions was from unmanaged wastes [20]. In addition, the world is facing surge in energy demand at an unprecedented rate. However, the primary energy source is still fossil fuel, accounting for about 83 % of the energy used globally [5]. The depletion of fossil fuel reserves and rate of release of greenhouse gas by using fossil fuel consumption has proven that we need to shift to alternative sustainable energy sources urgently. In this regard, utilizing unprecedented amounts of waste to extract energy can solve two significant global challenges: waste management problems and supply of clean energy demand. The municipal solid wastes consist of 44% food wastes, 17 % paper and carboard wastes, 19 % garden and wood residue and others as shown in Figure 3 (a). Each waste type has significant energy potential depending on the types of technology employed for the energy recovery.

(a)   (b)
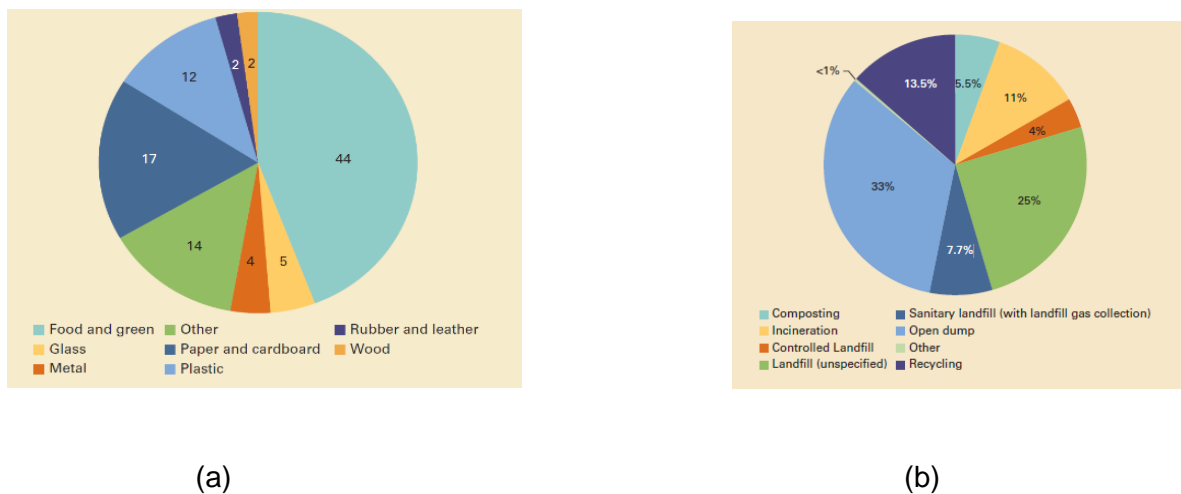
Figure 3: (a) Global waste generation source, (b) different waste treatment methods [2].

Several studies have demonstrated the potential of extracting energy from the waste. The International Renewable Energy Agency has provided an estimate indicating that the global potential for energy generation from the Waste-to-Energy (WTE) sector alone is approximately 13 gigawatts. USA produced 14.5 MWh of electricity from 84 WTE plants in 2012 [21]. Similarly, China developed 28 circulating fluidized bed plants to produce electricity, which process 800 tonnes/d of food waste with high moisture and low calorific value [22]. Likewise, Xiaoxuan et al. conducted an economic feasibility analysis regarding the conversion of municipal, agricultural, and industrial waste. Their findings indicated that

utilizing agricultural solid waste and food waste through anaerobic digestion systems could substitute for 61.46% of natural gas and 38.54% of coal consumption in the UK. Moreover, the study highlighted that harnessing methane from landfill sites containing municipal solid waste in Delhi could provide electricity to 8-18 million households and generate 7140 gigawatt-hours of power with a projected potential to produce 31,346 and 77,748 gigawatt-hours by the years 2030 and 2060, respectively [23]. Atul and colleagues conducted a comprehensive review of 100 published articles from 2010 to 2017, focusing on Waste-to-Energy (WTE) technology employed for waste management across various countries. Their findings strongly endorse WTE as a promising technological solution for energy recovery with minimal environmental repercussions. The study also includes a summarized cost analysis of various WTE technologies, presented in Table 1. The author underscores that WTE technologies exhibit efficiency and cost-effectiveness, establishing them as a viable method for efficiently managing waste [24].

Table 1: Comparison of the cost for WTE technologies [24].

WTE technologies	Capital cost (US$/tonne of MSW/year)	Capital cost (US$/tonne of MSW/year)
Incineration	400-700	40-70
Pyrolysis	400-700	50-80
Gasification	250-850	45-85
Anaerobic digestion	50-350	5-35
Landfilling with gas recovery	10-30	1-3

It is important to note that the choice between different WTE technologies depends on the specific goals of waste treatment, resource recovery, and energy generation, which depends on the characteristics of the waste feedstock, the available resources, and the cost of plant as well as the social acceptability. Each WTE technology has advantages and limitations, and the selection should be based on a thorough assessment of the given waste scenario.

2.2 Waste to energy conversion technologies

The waste to energy conversion technologies offers sustainable and environmental friendly approach to handle solid waste while generating valuable resources. Waste can be converted to energy through thermochemical conversion routes or biological conversion routes. Alternatively, the waste can be landfill by following sanitary disposal methods. The thermochemical conversion routes include pyrolysis, gasification and combustion and the biological conversion routes consists of composting and anaerobic digestion. Figure 4 depicts a graphical overview of waste to energy recovery processes, along with different types of fuel and energy sources that can be derived from the municipal wastes.
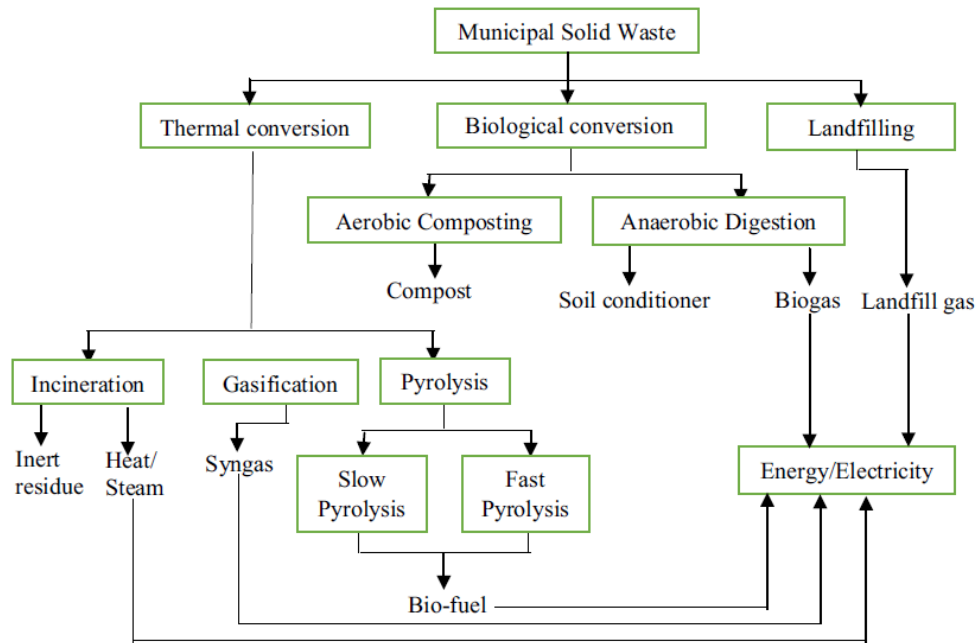
Figure 4:Different WTE technologies applied for the treatment of MSW [24].

2.2.1 Landfills

Sanitary landfilling is defined as the controlled disposal of wastes on land to reduce the negative impact on the environment through biogas recovery and leachate management (as shown in Figure 5). However, unsanitary landfilling offers a simpler and affordable solution for disposal of the increasing waste quantity and is the most common practice in developing countries, that poses a serious threat to the environment [25]. Previous studies showed that landfilling causes the highest environmental impact compared to other waste management options[26], [27]. It has been reported that in most of the cities of developing countries, the waste is disposed on low lying areas located at the outskirts of the city [28], [29]. When the factors such as environmental impact, health impact, land degradation, and groundwater contamination are considered, landfilling becomes the worst option. Developed countries have started to discourage landfilling of wastes through strict regulations, waste reduction and recycling. The landfill leachate (a dark effluent of unusually variable composition with recalcitrant compounds) is a major polluting substance released from landfills or dumpsites that pollutes the nearby surface water courses and groundwater aquifers [30]. According to European commission, only 10–15% of the total waste generated should go for landfilling and it should be the last option [31].
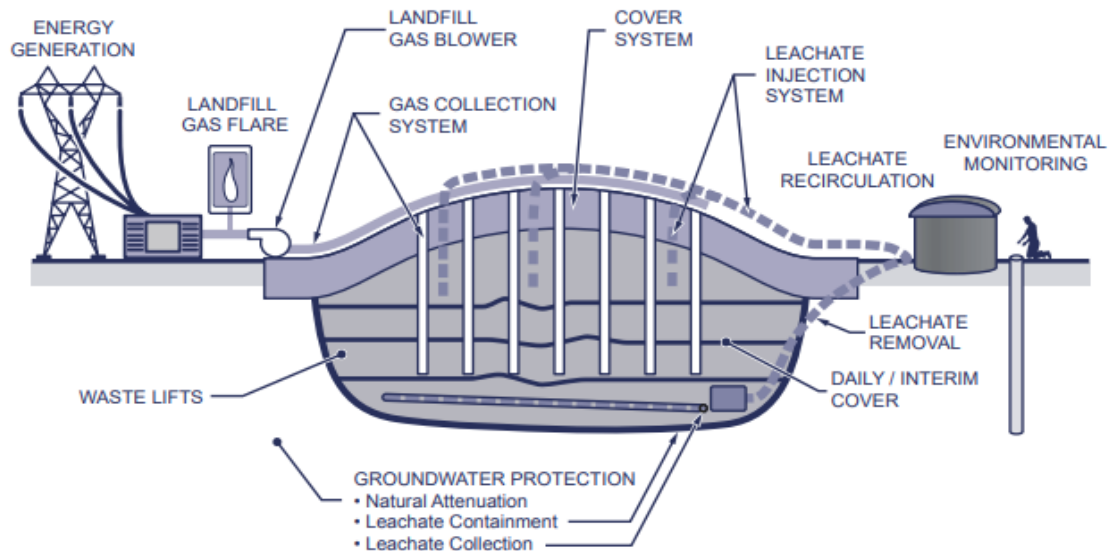
Figure 5: Landfill method for waste treatment [32].

2.2.2 Biological treatment

Another waste to energy conversion route is anaerobic digestion, which includes biological treatment of the wastes. Anaerobic digestion, also known as biomethanation, is a microbial process that degrades organic biodegradable matter without oxygen, leading to the production of biogas. The quality of the generated biogas depends on various process parameters and substrate composition, typically comprising of 50–75% methane (CH_4), 25–50% carbon dioxide (CO_2), and 1–15% of other gases, such as water vapor, ammonia (NH_3), and hydrogen sulphide (H_2S) [33]. This biogas can serve as an energy source. Anaerobic digestion has the additional benefit of converting organic waste into valuable resources. The resulting slurry or sludge can be utilized as a soil conditioner or organic amendment in agriculture. The quality of solid products obtained from anaerobic digestion depends on the feedstock quality, including proteins, minerals, and vitamin content [34], [35]. The anaerobic digestion process involves multiple stages, including hydrolysis, fermentation, and methanogenesis, where complex organic compounds are broken down into methane. The process can be categorized as "wet" or "dry," depending on the moisture content of the input materials. Anaerobic digestion has the potential to produce significantly more methane from municipal solid waste (MSW) in a short period compared to landfilling. It can also generate electricity but requires a relatively long duration for microbial reactions. Co-digestion with low-nitrogen waste materials is suggested to address issues like high ammonia concentrations.

Furthermore, the quality of biogas can be enhanced by removing carbon dioxide and other trace gases, making it suitable as a transportation fuel called biomethane. Anaerobic digestion is increasingly used for energy recovery from MSW, particularly in regions with high-moisture waste, demonstrating its economic and environmental sustainability. However,

unlike thermal treatment methods, anaerobic digestion has limitations when handling a wide variety of hazardous wastes. In addition, the biological conversion methods are slow and thus have reduced energy output yield (in the form of electricity and heat) and waste volume reduction as compared to the thermal waste treatment method [36], [37].

2.2.3 Thermal treatment

Thermal treatment in WTE technologies refers to the process by which solid waste is decomposed thermochemically into product gas (called as syngas), char, and heat energy. Thermal degradation methods have been used for a long time for extraction of energy from commercial feedstock such as wood pellets [38], [39]. Similarly, applying thermal methods to convert solid wastes into energy not only preserves the landfill space but also facilitates to manage the wastes by producing valuable products [40], [41]. Thermal conversion of solid waste typically follows three conversion routes: combustion/incineration, pyrolysis, and gasification. Depending on the temperature and the oxidizing medium employed, the thermal treatment of solid wastes can be combustion, pyrolysis, or gasification. When excess air is supplied during the conversion of solid wastes at high temperatures, the process is called combustion. The combustion is an exothermic process that releases a significant amount of heat energy that can be utilized for power generation or heat sources. Therefore, the main product of combustion is heating energy, and the byproducts are CO_2, steam, and ash. Initially, combustion was used to reduce waste, leading to environmental pollution. However, with improvement in combustion technology, several modern incineration plants with gas cleaning systems are developed. These plants give a more efficient conversion of waste into heat energy and cause less environmental harm [42]. Similarly, another thermal conversion method that can be utilized for the waste management is pyrolysis. Unlike combustion, the pyrolysis process converts solid waste into non-condensable gases, liquid, and solid carbon at a relatively lower temperature and in the absence of oxidizing medium. Owing to the endothermic nature of the pyrolysis process, a constant supply of thermal energy is required to break the large hydrocarbon molecules of solid wastes into smaller hydrocarbon molecules. Depending on the feed rate of solid wastes, the heating rate and the types of reactors, the pyrolysis process can be slow pyrolysis or fast pyrolysis. Fast pyrolysis produces mainly liquid bio-oil while solid pyrolysis produces solid char and gaseous products. Considering the diversity of the waste feedstocks, the pyrolysis process can be useful for waste management which has been demonstrated in several studies [43], [44]. Due to the low calorific value of product gas with large amount of CO_2 release during combustion of waste feedstock, the combustion process is less attractive economically and environmentally as a waste to energy technology choice. Similarly, the pyrolysis process demands significant amount input energy which again increases the operational cost. Alternatively, the gasification technology can be employed for effective handling of waste feedstocks which is economically beneficial and environmentally friendly compared to the other two conversion routes combustion and pyrolysis [45], [46]. In the gasification process, the solid wastes are partially oxidized with limited supply of oxidizing gas (air, steam, oxygen,

or their mixture) thereby preventing combustion. Therefore, during the gasification process the complex carbonaceous solid molecular structure breaks down and packs energy into chemical bonds in the gaseous molecules. The product gas from the gasification contains mainly a mixture of CO, H_2, CH_4, CO_2, H_2O, and some higher hydrocarbons. Gasification of solid wastes has several potential benefits over combustion and pyrolysis specifically in terms of operating conditions and various reactor types suited for specific purposes. Gasification reactors are basically fixed bed, fluidized bed and entrained flow reactors as shown in Figure 6.

Fixed bed gasifiers are described as reactors where biomass is introduced from the upper section, enabling clear distinction of gasification stages. These reactors function as single columns and typically employ air for gasification, with partial combustion of char particles generating the necessary heat. They are classified into downdraft and updraft gasifiers based on the direction of airflow in relation to biomass flow. Updraft gasifiers exhibit higher tar content (10-20 wt.%) and operate within a temperature range of 750-1000°C, while downdraft gasifiers, running at higher temperatures (1200-1400°C), experience reduced tar content due to enhanced heavy hydrocarbon cracking [47], [48]. However, downdraft gasifiers tend to have higher ash content and require low-moisture feedstock, limiting the range of usable biomass types. In contrast, fluidized bed gasifiers employ inert bed material in a fluidized state to facilitate heat transfer and fuel-particle distribution (mixing). Various designs, such as bubbling fluidized bed (BFB), circulating fluidized bed (CFB), and dual fluidized bed (DFB), offer versatility in terms of biomass introduction and gas velocity [49]. BFB gasifiers, for instance, allow biomass to be fed from the top or the side of the bed, with a higher gas velocity to minimize particle elutriation effects and accommodate different particle sizes. On the other hand, the CFB gasifiers demand higher gas velocity, and smaller particle size. The dual fluidized bed configuration, comprising interconnected BFB and CFB columns, enhances gas quality and is suitable for highly endothermic steam gasification. Alternatively, entrained flow gasifiers are highly efficient and operate at high temperatures exceeding 1200°C, yielding minimal tar compared to other gasification technologies. They are often used in coal gasification but face challenges when processing biomass due to the need for feedstock pulverization. Gasification processes are categorized based on multiple factors, including the internal flow of biomass, the choice of gasifying agents (air, oxygen, steam, or a combination), and whether the process is auto-thermal or allothermal. Initial stages involve drying and pyrolysis, followed by combustion and gasification reactions, with the degree of gasification significantly impacting the gas quality. The reactor type, gasifying agent, biomass properties, temperature, residence time, and catalysts all influence on the gas composition [47], [50], [51], [52], [53]. The choice of gasification reactor depends on the intended use of the product gas. For example, updraft fixed bed designs are suitable for small-scale applications, while downdraft systems are preferred for medium-scale internal combustion engines and boilers. Fluidized bed reactors offer uniform conditions and scalability, with options like bubbling and circulating fluidized beds. The dual reactor circulating fluidized bed configuration enhances gas quality, allows for carbon-to-hydrogen ratio adjustment, and is

suitable for endothermic steam gasification. Entrained flow reactors are highly efficient but require fine particle sizes, making them traditionally suitable for coal gasification. This compilation provides a comprehensive understanding of gasification technologies, emphasizing their suitability for different biomass types and end-use applications.
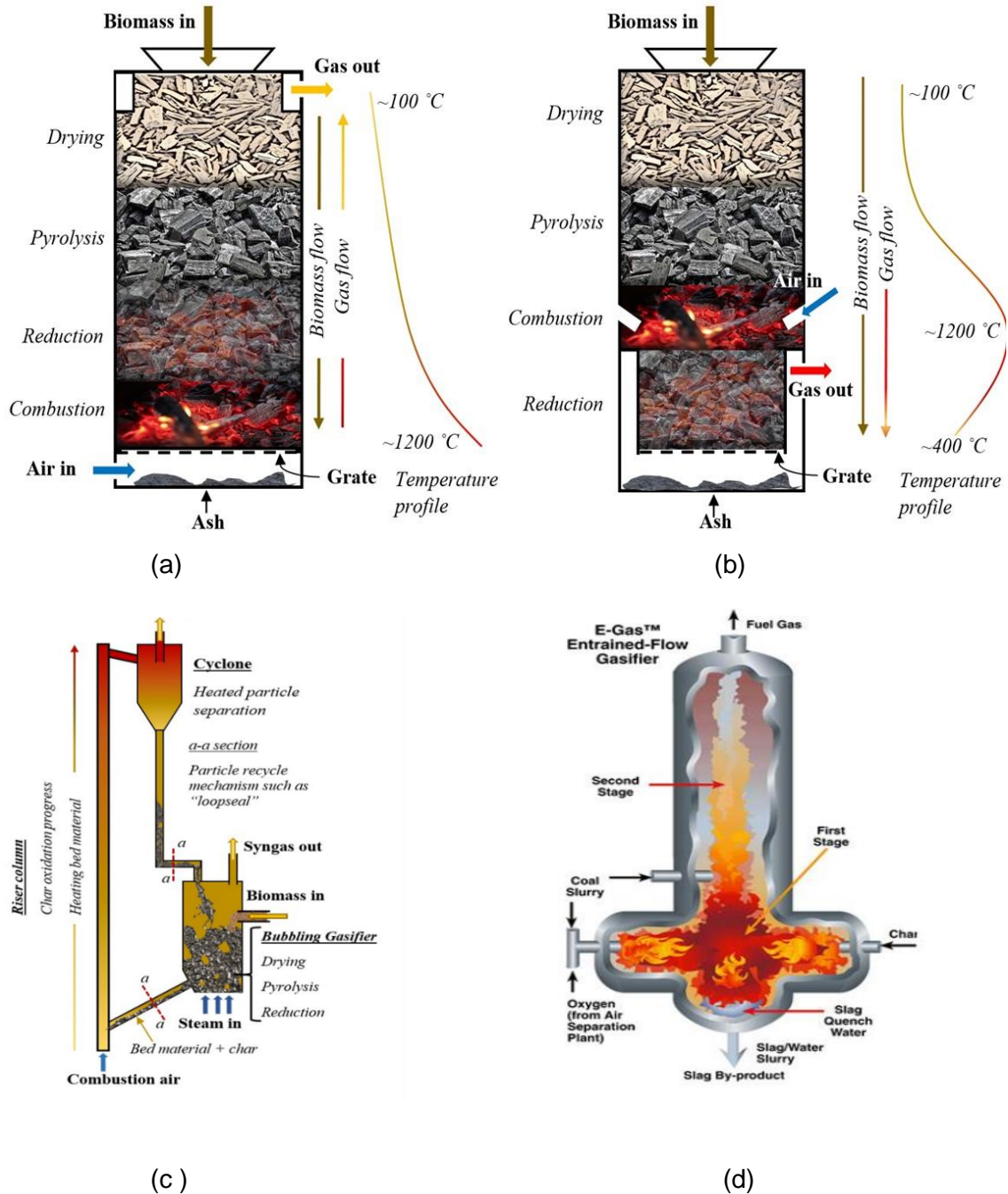

(a)

(b)

(c)

(d)

Figure 6: (a) updraft gasifier, (b) downdraft gasifier, (c) dual-fluidized bed reactor, (d) entrained flow gasifier [49], [54].

2.3 Densification of wastes to fuel for higher combustion efficiency

The carbon containing waste provides immense potential for energy extraction via different WTE technologies. However, the raw waste feedstock typically exhibits characteristics such as low density, high moisture content, large physical dimensions, and relatively low energy density [55].The wastes in original form are difficult to handle, transport, store and utilize. Therefore, the pre-treatment of wastes is necessary for efficient management and utilization in a WTE technology. The pre-processing or pre-treatment of the waste includes converting the waste into correct shape, size, moisture content and density via different processes. Mainly, the pre-processing methods includes size reduction, torrefaction, steam explosion, hydrothermal carbonization, and biological treatment. Several studies have demonstrated improvement in the properties such as total surface area, grindability, reactivity, and the binding characteristics of the raw wastes after pretreatment [12], [55], [56], [57]. Densification of the wastes becomes easier after pre-processing thus can be converted as needed feedstock for their utilization in different WTE technology. Common techniques for densifying waste into fuel include briquetting, bailing, pelletization, and extrusion [58]. The choice of technique depends on the waste composition, moisture content, and intended end use. In this work, the pelletization method is used for the densification of various waste feedstocks therefore only the pelletization method is discussed here.

Pelletization is the most common method for densification of solid fuels and has been widely used by the wood pellet industry. In recent years, several studies have shown increasing interest in densification as a technique to convert residues into an energy source [59], [60], [61], [62]. Pelletization of biomass/waste involves mass and energy densification for materials with low bulk densities, raising the initial bulk density from 40–200 kg/m^3 to a final range of 600–800 kg/m^3 [63]. The waste in the form of pellets enhances the transportation and storage of the feedstock and facilitates better handling and flowability of waste during feeding in the reactor, while reducing dust formation [64], [65].The pellets are produced in a pelletizer which consists of the main parts, roller and die with cylindrical press channels as illustrated in Figure 7 (b). The die is either ring shaped or a flat plate. During the pelletization process the roller which is in the close proximity to the die (with minimum gap between roller and die) moves continuously. The raw biomass/waste particles are thus squeezed into the die press channel each time the roller rotates over the channel forming a layered structure of the pellet as shown in Figure 7b (figure in the left). The raw biomass on the die can be categorized into different components. As the raw feed is squeezed into the steel die channel, friction force is produced due to the fixed inner steel surface of the die channel resulting in the pressure build up. Therefore, the pressure exerted by the roller must overcome the backward pressure exerted by the raw particles for stable pellet production during pelletization.
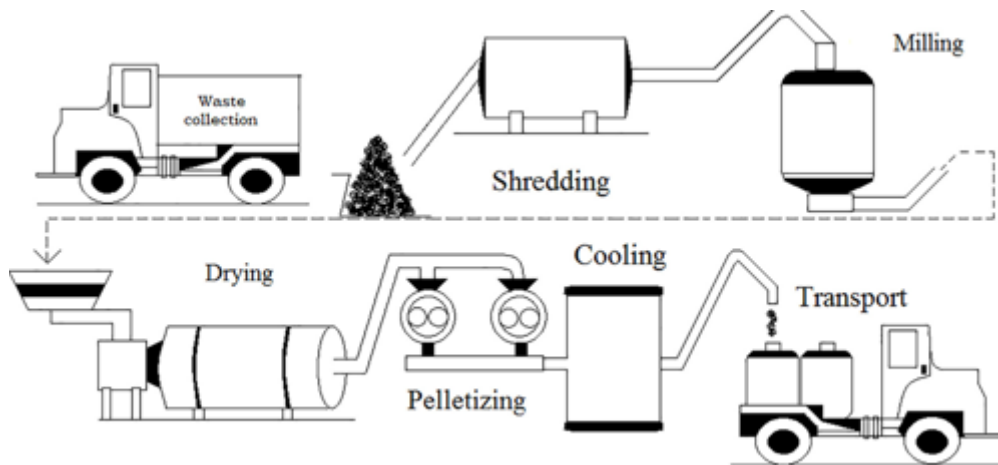
(a)
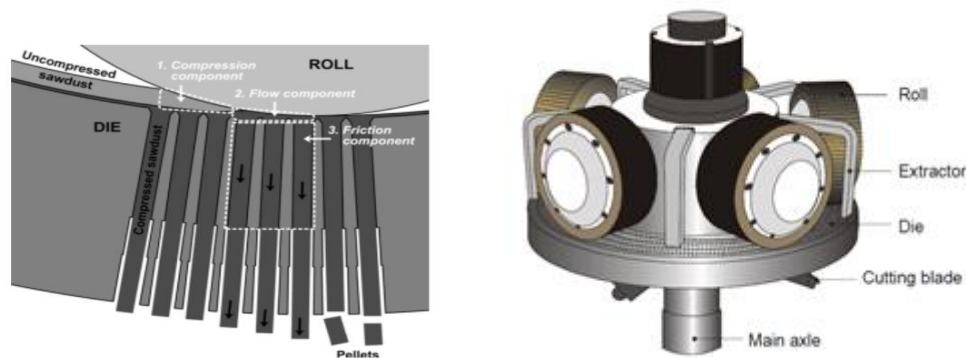
(b)

Figure 7. (a) Processes during the pelletization of the raw waste feedstock, (b) different components involved in the pelletization process [66], [67].

Studies have indicated that length to diameter ratio of the press channel, plays a significant role in determining the level of pressure produced within the press channel [68], [69]. The pellets produced must be of a certain standard for commercial purposes or must meet the requirements for waste-to-energy technology feed quality. The quality of pellets depends on the properties of the feedstock, including biomass type, moisture content, and size of the particles [70]. For a given feedstock, the quality of the pellets also depends on the pelletization process which includes operational conditions, pelletizer type, and binding agents [59], [69], [71]. The pelletization process is accompanied by the pre-processing of the raw wastes prior to the pelletization which includes shredding, drying, and milling. Schematic representation of the processes involved in pelletization of the raw waste feedstock is illustrated in Figure 7 (a). The pellet market has experienced growth in recent years for

various raw materials [72], [73], [74], [75].The quality of pellets is determined by the specific requirements of the end-users, considering the heating system and handling characteristics. As a result, comprehending the physical and chemical properties of the wastes is crucial for efficient utilization of in a WTE technology that follows thermal conversion routes. For instance, physical properties like density impact the heating rate and thermal efficiency of the particles. On the other hand, chemical properties, such as the ultimate analysis, proximate analysis, and calorific value govern the combustion process.

2.4 Gasification of wastes in a bubbling fluidized bed gasifier

Gasification in a bubbling fluidized bed takes place in the temperature range of 600°C -1000 °C where the particle bed acts as a thermal flywheel and provides the required heat for conversion. Gas is forced at a sufficient velocity through the particle bed The particle bed (typically sand, limestone, olivine etc.) to transform the static bed into a fluid like state where the particles move and circulate continuously. Therefore, the quality of fluidization significantly depends on the superficial gas velocity, reactor geometry and bed particles. As the gas flows through the particle bed, it exerts frictional forces or drag on the particles. The superficial gas velocity at which the drag force counterbalances the weight of the particles, and the static bed starts to fluidize is called the minimum fluidization velocity (U_{mf}). The minimum fluidization velocity is an important parameter in the process optimization of any fluidized bed systems and has been subject to several studies [76], [77]. The minimum fluidized velocity can be estimated from the following simplified Ergun equation (2. 1) [78], [79]. With further increase in gas velocity beyond minimum fluidization velocity, the bed transit into the bubbling regime with appearance of bubbles in the bed. The bubbling fluidized bed can be characterized as the formation of distinct gas bubbles, frequent movement and interchange of particles and good mixing of gas-solid particles within the bed. The bubbles formed in the bed facilitates excellent mixing and heat transfer, making BFB suitable for various applications such as combustion, gasification, drying and chemical reactions. Particularly, in the gasification process where solid-gas interactions are the primary driving factor, the bubbles formed in the bed offer good contact between the solid-gas particles, ensuring efficient heat and mass transfer. Therefore, the study of bubble proprieties and its influence on the hydrodynamic behaviour in the fluidized bed has been subject of wide research [17], [80], [81]. The bubble properties including bubble diameter, rise velocity and frequency can be predicted from different correlation as listed in equations 2.2-2.7 [79], [82], [83], [84]:

$$U_{mf} = \frac{d_p^2 (\rho_p - \rho_g) g}{150 \mu_g} * \frac{\varepsilon_{mf}^3 \varphi_p^2}{1 - \varepsilon_{mf}} \qquad (2.1)$$

Where, ρ_p, ρ_g, μ_g, ε_{mf}, φ_p are the particle density, gas density, gas viscosity, void, particle sphericity respectively.

$$U_b = U_{mf} + U_g \tag{2.2}$$

$$d_b = 0.652[A(U_0 - U_{mf})]^{0.4} - \left(0.652[A(U_0 - U_{mf})]^{0.4} - d_{b0m}\right) \exp\left(-0.3\frac{h}{D}\right) \tag{2.3}$$

$$d_{b0m} = 0.00376(U_0 - U_{mf})^2 \tag{2.4}$$

$$u_b = 12.51\varphi_D(U_0 - U_{mf})^{0.362}d_b^{0.52} \tag{2.5}$$

$$u_b = (U_0 - U_{mf}) + 0.711\sqrt{(gd_b)} \tag{2.6}$$

$$f_b = \left(0.52\left(\frac{d_b}{D}\right)^{1.48} + mu_b^n d_b\right)^{-1} \tag{2.7}$$

Here, U_{mf}, U_0, d_b, g are minimum fluidization velocity, superficial gas velocity, bubble diameter and acceleration due to gravity, respectively. $\varphi_D = 0.337$ is the model coefficient for the test particles, $m = 0.05$ and $n = -4.379$ within the bubble regime are dimensionless model coefficient and model parameter.

d_b, h, D are in [cm] and U_0, U_{mf} are in [cm/s]. A is cross sectional area of the bed and d_{b0m} is the initial bubble size near to the distributor, u_b is the bubble rise velocity, and f_b is the bubble frequency.
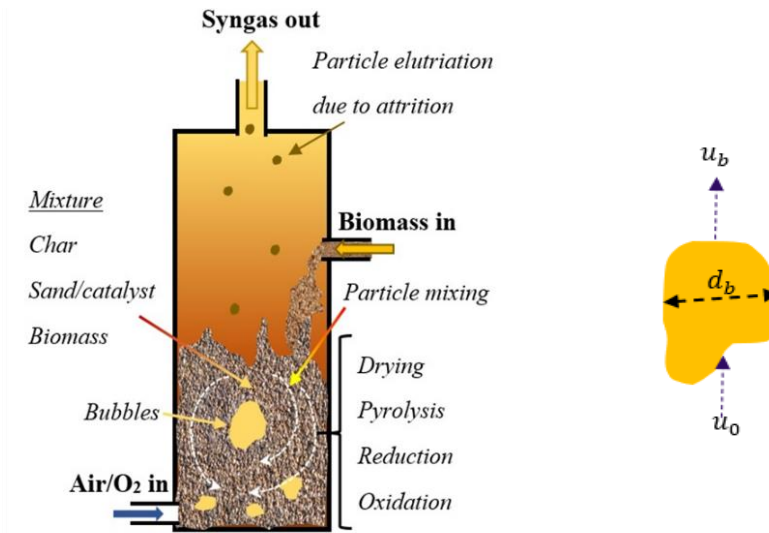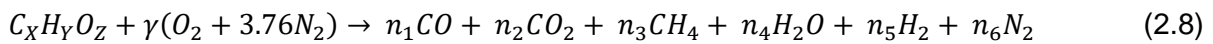

Figure 8: Illustration of process involve in bubbling fluidized bed gasifier [49].

In the gasification process, the solid wastes are partially oxidized with limited amount of oxygen or steam that prevents combustion. The conversion of solid waste to product gases in a gasification process occurs in complex thermochemical routes. The first step is drying and devolatilization. The solid fuels are converted into volatile gases, char, and tar after pyrolysis. The char then is gasified with gasifying agent (air and steam) through reduction and partial oxidation reaction routes. The process can be autothermal or allothermal, depending on the gasifying agent and the type of reactors. When using air as a gasifying medium, the gasification process can be driven auto-thermally which again depends on the fuel to air ratio. The heat required for the chemical conversion of the fuel is supplied by the partial oxidation reactions. Contrary, the exothermic reactions are absent when steam is used as the gasifying agent, and thus an external heat source is needed. The advantages of using steam as a gasifying medium is that it produces a synthesis gas with a higher heating value (8-18MJ/m³ N). With air as gasifying, the caloric value of synthesis gas is comparatively lower and are in the range of 4-7MJ/m³ N [49], [85]. The advantage of using air as fluidizing gas is that it is cheaper, and some gas turbines available in the market enable to use lower calorific value syngas gas to produce electricity.

The composition of product gas post gasification depends on the biomass constituent element and the gasifying agent. Biomass molecules may contain traces of nitrogen and sulfur in addition to large percentage of carbon, hydrogen, and oxygen. Neglecting the nitrogen and sulfur constituents, a unit of biomass can be represented as $C_X H_Y O_Z$, where X, Y and Z are the mole fractions of carbon, hydrogen, and oxygen, respectively in the molecule. Assuming a one-step process, biomass conversion into gaseous product under a limited supply of air $(O_2 + 3.76N_2)$ can be globally expressed as:

$$C_X H_Y O_Z + \gamma(O_2 + 3.76N_2) \rightarrow n_1 CO + n_2 CO_2 + n_3 CH_4 + n_4 H_2O + n_5 H_2 + n_6 N_2 \qquad (2.8)$$

where $\gamma = \left(\frac{\breve{M}_{bio}}{\breve{M}_{air}}\right) AFR$ and n_i; $i = \{1,2,..,6\}$, is the number of moles of each gas species contained in the product gas. $\breve{M}_{bio}$ and $\breve{M}_{air}$ are molecular weights of biomass and air, respectively.

The expression above implies that for a constant value of AFR (air-fuel ratio) defined as the ratio of mass flowrate of air to mass flowrate of biomass, the composition and distribution of gases in the product is the same, suggesting maximum conversion and stable product. However, in practice, this might not be the case owing to the competitive side reactions among the reacting species. Other factors that may also influence on the product composition include contact/residence time between the fuel particles and gasifying gas, temperature as well as mass distribution within the reactor. The degree at which these factors influence the gasification varies with different reactor design and operating conditions.

Biomass conversion is kinetic limited; therefore, to enhance gas diffusion, promote higher heat transfer and increase contact area, the size of biomass fed into the reactor should be rather low (< 50 mm). Below a certain temperature (< 200 °C), only the drying process is possible where the moisture content evaporates, leaving behind dry solid fuel. At a higher temperature up to 500°C, the dry particles undergo devolatilization or pyrolysis where it is decomposed into char, tar and light gases as illustrated in Figure 9. The light gases consist of mainly CO, CO_2, CH_4, H_2 and H_2O. Composition of the pyrolysis product including the drying process also depends on the residence time and temperature where the rate constants, k [1/s] can be modelled in the Arrhenius form, equation 2.9:

$$k = A exp\left(-\frac{E}{RT}\right) \qquad (2.9)$$

Values of the frequency factor, A [1/s] and the activation energy, E [J/mol] for each step can be obtained as described in Chan et al. [86]. In the presence of a gasifying agent, e.g., limited amount of air, the combustible gases (CO, CH_4, H_2) and char (rich in carbon) undergo partial oxidation, releasing heat energy while reducing the chemical energy content of the pyrolyzed biomass. Moreover, with the limited supply of oxygen, some amount of tar will remain unconverted in the product gas. Possible reactions during the biomass gasification with air, which are also implemented in the computational model are as listed in the Table 2.
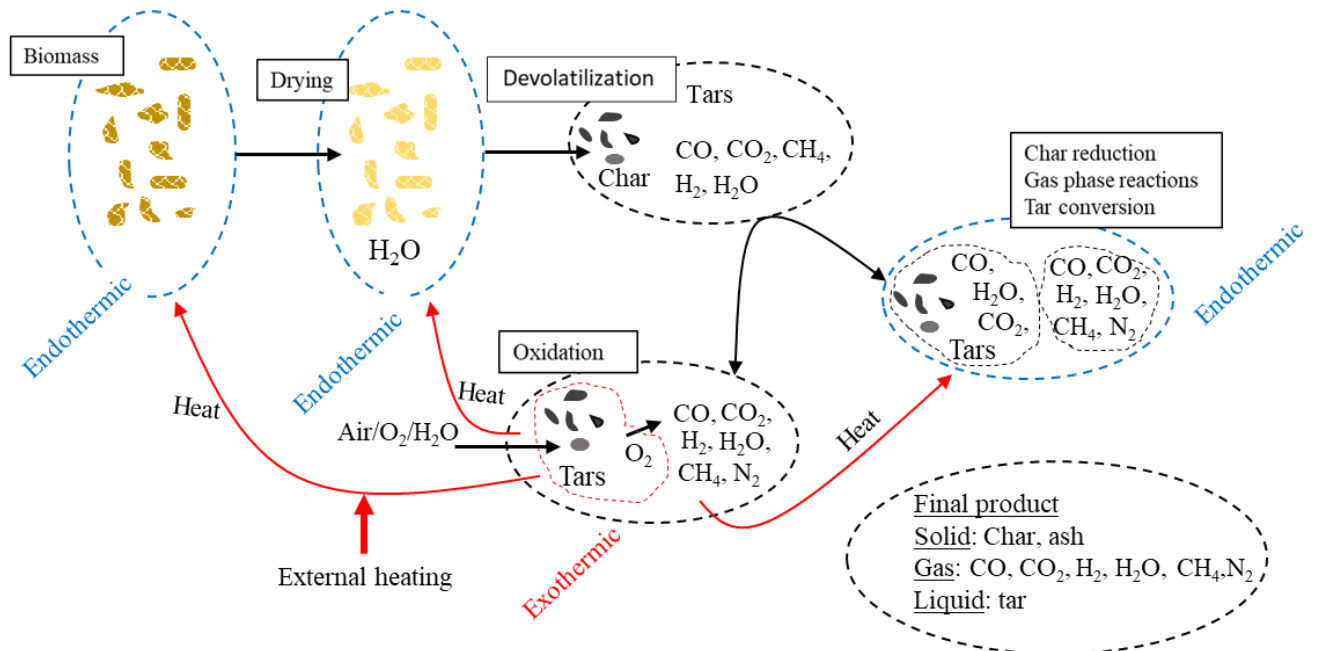

Figure 9. Illustration of steps involved in biomass gasification [87].

Table 2: Basic reactions involved in gasification [88].

Heterogenous reactions	Enthalpy
Char partial combustion $2C + O_2 \leftrightarrow 2CO$	$-111 kJ/mol$
CO2 gasification $C + CO2 \leftrightarrow 2CO$	$+172 kJ/mol$
Char partial combustion $C + H_2O \leftrightarrow H_2+CO$	$+131 kJ/mol$
Homogeneous reactions	**Enthalpy**
CO oxidation $CO + 0.5O_2 \leftrightarrow CO_2$	$-2844 kJ/mol$
H_2 oxidation $H_2 + 0.5O_2 \leftrightarrow H_2O$	$-242 kJ/mol$
CH_4 oxidation $CH_4 + 2O_2 \leftrightarrow CO_2 + 2H_2O$	$-242 kJ/mol$
Water gas shift reaction $CO + H_2O \leftrightarrow CO_2 + H_2$	$-41.2 kJ/mol$
Methane reforming $CH_4 + H_2O \leftrightarrow CO + 3H_2$	$+206 kJ/mol$

2.5 CFD simulations

Experimental studies are often time consuming and expensive. Owing to the opaque nature of the gasifier and high temperature operating environment, measurement of the certain parameters experimentally can be challenging. In this regard, computational fluid dynamic models can be employed to predict the gasifier thermochemical behaviour at different operating conditions provided that the CPFD model is validated properly.

There are mainly two types of CPFD approaches used to study fluid dynamics of the fluidized bed: the Eulerian-Eulerian method and the Eulerian-Lagrangian method [89], [90]. In the Eulerian-Eulerian approach, one particle phase is considered, where only two interacting phases exist, the particle phase and the gas phase. The Eulerian-Eulerian approach is also called as Two-Fluid Model (TFM). The major drawback of the TFM method is that it accounts for the particles with the same density, diameter and coefficient of restitution which often results in inaccurate prediction of the bed properties [91], [92]. The Eulerian- Lagrangian approach, also known as a discrete element model (DEM), is more reliable and predicts fluid dynamics better than TFM [93]. Individual particles are tracked with the DEM method, and particle-particle collision is considered, unlike in the TFM model. Therefore, DEM requires enormous computing power to simulate fluidized bed reactors [92]. Another Eulerian-Lagrangian approach, which is known as Computational Particle Fluid Dynamics (CPFD), uses Multiphase-particle in cell (MP-PIC). This approach has gained popularity in recent days due to its capacity to simulate industrial fluidized bed reactors [94], [95]. In the MP-PIC

approach, particles with similar attributes, such as density, volume, etc., are grouped to form a parcel accounted as a computational particle. In this way, the number of computational particles is reduced in the simulations, which reduces the computational time. In this work, the MP-PIC simulations using a commercial software Barracuda Virtual Reactor is used to investigate the optimal operating conditions of the BFB gasifier.

3 Material and methods

This section provides descriptions of three cold bed experimental set up, a 20-kW gasifier, pellet machine, materials used, feedstock characterization, and the mathematical model implemented in this study.

3.1 Feedstock preparation, pelletization and characterization of the feedstock

In this section, the experimental methodology employed for pellet production using a laboratory-scale pellet machine is discussed, along with an examination of the pellets properties.

3.1.1 Feedstock preparation and pelletization

The materials employed in this study consist of wastes from diverse sources, including agricultural, industrial, and municipal sources. Nine different feedstocks were utilized, including grass, wood, garden residue, fish wastes, barley straw, paper/cardboard, coffee grounds, sawdust, and bark. These feedstocks were utilized in the pellet form for the gasification experiments except wood chips and are categorized into three groups as listed below:

1. Commercial pellets.
2. Pellets from homogenous raw materials prepared at the industrial lab facilities.
3. Pellets from a mixture of wastes (co-pelletization) prepared at the university laboratory.

The first group of feedstocks for the gasification experiments were commercial pellets such as wood and grass pellets. Initially, commercial pellets were utilized to assess the feasibility of waste gasification in a bubbling fluidized bed gasifier and to determine optimal operating parameters for enhanced gasification efficiency. The second group involved lower-grade feedstock such as wood chips, garden waste, paper/cardboard, and fish waste. These

feedstocks were pelletized at industrial (SCANSHIP and SINTEF) pelletization facilities. The quality of the produced gas under various gasifier operating conditions was measured and analyzed. Characterization of the pellets were carried out at the USN, laboratory and also the samples were sent to the certified Norwegian-based laboratory EUROFINS for analysis.

In the third group, food and agricultural waste feedstocks were pelletized and co-pelletized under varied operating conditions to achieve pellets with improved physical properties and combustion characteristics. Coffee wastes were collected from the university canteen (USN, Porsgrunn), barley straw from the farm, and sawdust from the wood processing industry. Pre-processing of the raw feedstock was conducted to achieve smaller sizes and suitable moisture content for pelletization. Due to the limited binding properties of coffee grounds, co-pelletization with a mixture of sawdust, straw, and barley was performed. The co-pelletization of the mixture wastes strengthened the pellet mechanical strength and enhanced the combustion properties.

A lab-scale pellet mill, KAHL pelleting press 14-175, was used for the pelletization which resembles the industrial pelletization. The pellet press consists of a pan grinder roller, die with effective bores of diameter 6 mm, silo for the feed inlet, breaking off device (cutter), frequency converter and temperature sensor. The schematic representation of the pelletizer and various components are illustrated in Figure 10. During the pelletization, the raw biomass/wastes were added vertically from the above inlet funnel into the interior which formed a product layer on the die that was rolled over continuously by the pan grinder rollers. Consequently, the product was pre-compacted and pressed into the effective bores of the die which further compacted resulting in a cylindrical strand (pellets) below the die. A breaking-off device below the die broke the solidified strand into the desired length and the pellets were transported to the discharge device. For a given feedstock, the quality of the pellet was determined by adjusting the operating parameters such as the aspect ratio, the rotation speed of the main shaft (roller speed), the distance between the roller and die, the die temperature and the cutter distance below the die. The influence of these parameters on the physical characteristics of the pellets are discussed in the result and discussion section. The properties of pelletized feedstocks were characterized and are available in the corresponding articles.
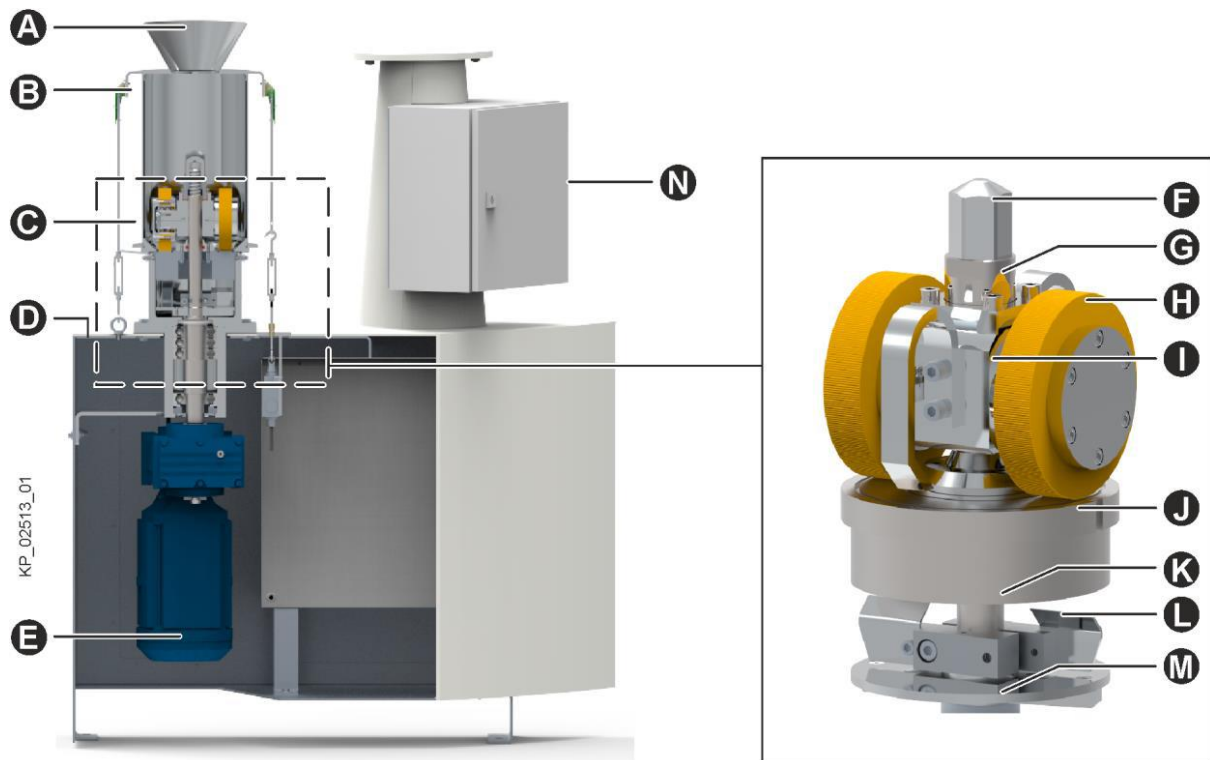
Diagram legend

A   Inlet funnel   B   Dust hood
C   Upper part   D   Machine frame
E   Geared motor   F   Cap nut
G   Adjusting nut   H   Pan grinder roller
I   Pan grinder head   J   Die
K   Main shaft   L   Breaking-off device
M   Discharge device   N   Control system of the machine

Figure 10: Schematic representation of the pellet machine and different components.

3.1.2 Characterization of the feedstock

In this section, the techniques used to assess the properties of pellets derived from coffee grounds, barley straw, sawdust, and bark residue are outlined. The evaluation methods encompass measurements of mechanical and durability strength, moisture and ash content, calorific value, density, ash melting temperature, and fiber structure.

3.1.2.1 Mechanical strength and durability test

Prior to the gasification tests, the properties of the pellets were assessed, and only those with suitable characteristics were chosen for the experiments. Pellet strength is an important parameter influencing the residence time of the fuel, fines release during transportation, and the gasification process in a fluidized bed gasifier. The physical properties of pellets are characterized by their mechanical and durability strength when exposed to harsh conditions. In this study, the mechanical strength of pellets (straw pellets, coffee pellets, and a mixture of coffee, sawdust, and bark pellets) was determined by measuring the maximum radial compressive strength the pellets could endure. A hardness tester (Amandus Kahl, available at UiA laboratory) was employed for the tensile strength measurement. During the test, the pellet underwent compression by a tip connected to a spring (as shown in Figure 11). The spring moved through a piston connected to a motor, and the pellet broke when it reached the maximum compression strength. The corresponding breaking mass was observed from the spring gauge value, and the compression strength (T_s) of the pellets was then calculated using Equation 3.1.

$$T_s = \frac{m_s g}{\pi r l} \tag{3.1}$$

where, m_s is the mass of the sample pellets, g is acceleration due to gravity, r is the radius of the pellets, and l is the length of the pellets.
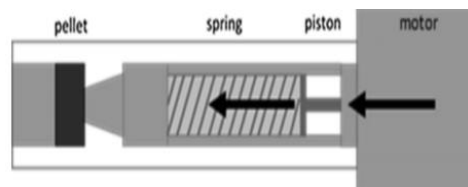
Figure 11: Schematic representation of the pellet hardness tester [96].

Mechanical strength of the pellets directly influences their durability. The weaker pellets are more likely to produces fines when subject to collision and frictions. The durability in this work for each feedstock were measured using an ISO tumbler 1000+ (designed according to the ISO 17831-1). For the durability test, a known load (approximately 1 kg) of the pellets was placed in a steel box which rotated 500 times per 10 min. After the test, the pellets were sieved with a 3.15 mm sieve to extract the fines and the mechanical durability (M_d) of the pellets was computed from equation 3.2.

$$M_d = \frac{M_f}{M_i} * 100 \tag{3.2}$$

Where, M_i is the initial mass of the pellets and M_f is the mass of the pellets after test.

Similarly, the density of the pellets was computed as:

$$\rho_p = \frac{m}{\pi r^2 l}$$ (3.3)

Where, m is the mass of the pellet. The mass of the pellet was measured on a weighing scale with readability of 0.01 mg, and the radius and length by a vernier caliper with a precision of 0.01 mm.

3.1.2.2 Moisture content, calorific value, and ash fraction

The moisture and ash content of the pellets were carried out according to EN standard procedures using the muffle furnaces (available at UiA, Grimstad). The known mass of the samples was placed in porcelain crucible and dried for 24 h at 105 °C in the muffle furnace. The moisture fraction was calculated by the difference in the sample weight. Similarly the ash fraction of the samples was obtained using a programable muffle furnace. The known mass of the samples with crucible was placed inside the furnace and the temperature of the furnace was programmed to 450 °C-500 °C for the first hour and again increased to 700 °C-750 °C for the next hours. After, six hours from the start of the furnace, the crucible were removed from the furnace and cooled to the room temperature in a glass desiccator. The ash percent was measured from the retained mass in the crucibles. An oxygen bomb calorimeter (Model C6000 Adiabatic calorimeter, IKA ®) was used to determine the calorific value of the sample pellets. All the measurement were carried out in triplets.

3.1.2.3 Ash sintering and melting
The fluidized bed gasifier faces a challenge in maintaining reactor operation free of agglomerates. Agglomeration in the bed poses a risk of bed defluidization, compromising the benefits of fluidized bed heat transfer. To prevent the formation of clinker (agglomerates), understanding the ash melting properties of the fuel before gasification experiments is crucial. Prior knowledge of these properties allows the selection of optimal reactor operating conditions, mitigating ash-related challenges during the gasification of waste feedstock in a fluidized bed reactor. The sample of ash were prepared in the pellet form for analysis of ash melting behaviour using a heating microscope (available at UiA, Grimstad). The instrument allowed to observe the physical transformations of the samples under controlled (pre-programmed) heating conditions. The detailed explanation is mentioned in the result section. Typically, ash melting occurs over a temperature range where the solid phase coexists with its liquid phase, providing valuable insights into the agglomeration tendency of the fuel at

specific temperatures. The characteristic temperatures at which the ash particles (as sample of the feedstock) were transformed into different stages were automatically captured during the measurement period. Information extracted from the images defining four characteristic temperatures with coffee pellets ash samples are illustrated in Table 3.

Table 3: Change in the shadow profile of the ash sample (of the coffee pellet) at different characteristic temperatures.

Description	Initial Deformation. First sign of shrinkage (ST)	Spherical appearance. First sign of rounding (DT)	Hemispherical form. Half the original height. (HT)	The cylindrical test piece has effectively melted. (FT)
Shadow profile	- 994 -	- 2718 -	- 2785 -	- 2961 -

3.1.2.4 SEM analysis

The quality of the pellets was assessed by visualizing the surface morphology at the nanoscale through Scanning Electron Microscopy (SEM). SEM employs a concentrated electron beam to meticulously scan the sample surface, generating images of high resolution. Interaction between the electron beam and the sample, coupled with detectors capturing signals, including secondary electrons, facilitates the creation of detailed images. Prior to the test, the samples of pellets and raw feedstock were prepared by coating with a thin layer of conductive material to enhance conductivity and imaging quality. SEM was then utilized to examine the samples, capturing their topography, fiber texture, and bonding characteristics at varying resolutions. The outcomes of the SEM analysis are elaborated in the result section.

3.2 Cold fluidized bed set up with pressure sensors

Efficient thermochemical conversion in a fluidized bed gasifier requires well establish flow and fluid dynamic behaviour in the bed. The fluid dynamic behaviour of the bubbling fluidized bed can be characterized by the properties such as minimum fluidization velocity, bubble dynamics, segregation, and mixing pattern in the bed. These properties are significantly influenced by the superficial gas velocity, reactor dimensions and bed height. Therefore, it is necessary to select operational parameter that gives maximum reactor conversion efficiency

and product yield. However, it is difficult to study the influence of such parameters in the gasifier owing to their opaque nature and high cost associated with its operation and modification. The cold flow models are widely used to study the influence of operational parameters. In this work, three different cold flow models of the fluidized bed reactors were employed. The three cold fluidized bed models include reactor with distributor plate and pressure sensors, reactor with ECT sensors and distributor plate, and reactor with pressure sensors and without distributor plate.

The cold bed set ups equipped with pressure sensors consist of a 3D transparent cold bed column of height 1.4 m and diameter 0.084 m as depicted in Figure 12 (b-c). A set of pressure transducers are connected to the pressure tapping points installed along the wall of the column. The distance between two consecutive pressure points along the column height is 10 cm. Compressed air at ambient conditions is supplied through an air supply hose fitted at the plenum below a porous plate distributor or orifice. The flow of air into the column is controlled by the air control valves attached to the rig. LabVIEW, a data acquisition software, is used to record the pressure drop along the column height. Initially the reactor is filled with bed material and fluidized and compressed air is passed through the static bed. As the gas velocity is increased the static bed transforms into fluid-like state and start to fluidize (called as minimum fluidization velocity). With the further increase in gas velocity the bed transits into bubble regime, slugging regime, turbulent or pneumatic conveying, depending on the gas velocity. The fluid dynamic behaviour of the bed and transition regime of the bed at different gas velocity can be predicted from the pressure data measured at different heights [97]. In a bubbling fluidized bed, operating the reactor above the minimum fluidization velocity typically in a bubbling regime is important. The cold bed model with pressure sensors consists of two configurations one with distributor plate for the air supply and another with orifice or side nozzles for air injection. Although a distributor provides uniform air distribution inside the reactor, it faces operational challenges and additional costs. Therefore, the gasifier used in this work consists of two side orifices for air injection. To correctly quantify the fluidization characteristic of the particles, similar configuration was necessary in addition to the cold model with distribution plate. A new set-up of 10 cm diameter (similar to the gasifier reactor) with side nozzles as air injection boundary (depicted in Figure 12 d) was designed and build during this thesis period. The plot of minimum fluidization velocities based on the pressure data from the two cold model set ups are illustrated in Figure 12 a. For the same particle and gas velocities, the result shows variation in the minimum fluidization velocity of the bed varied for each configuration.
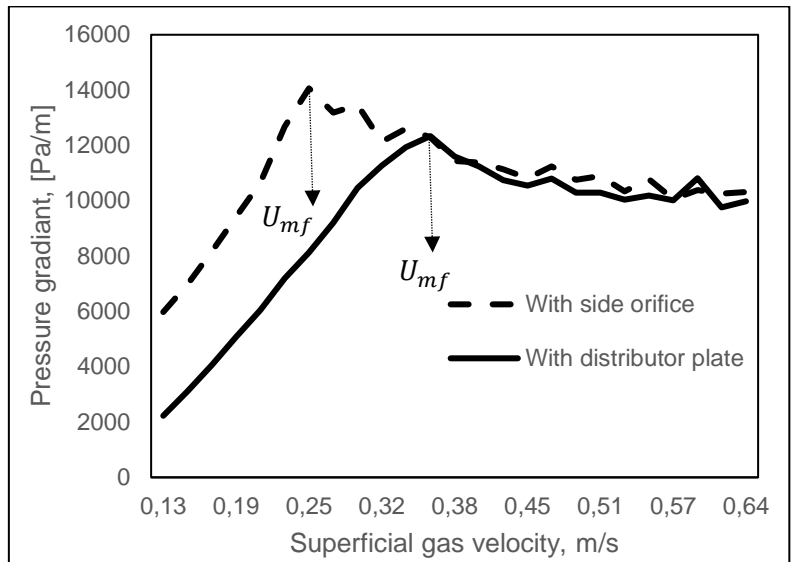
(a)
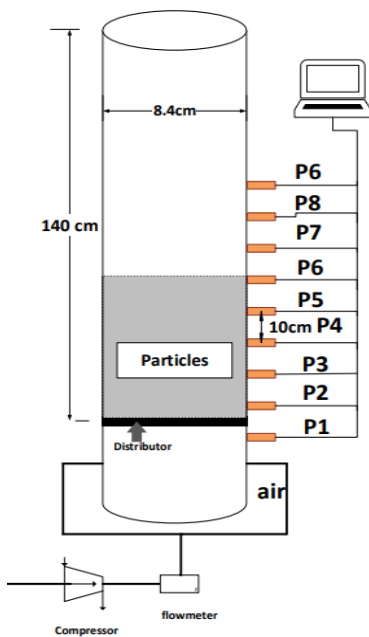
(b)   (c)   (d)

Figure 12: (a) Pressure gradient vs superficial gas velocity plot obtained from the pressure sensor data for two cold models equipped with pressure sensors, (b) schematic representation of the cold model bed rig, (c)cold bed set up, (d) cold bed set up with orifice as inlet flow boundary conditions.

3.3 Cold fluidized bed set up with ECT sensors

Cold BFB reactor equipped with ECT sensors is a cylindrical transparent column of 140 cm in height and 10.4 cm in internal diameter. The column is fitted with an air distributor at the bottom and is open to the atmosphere. The air distributor is 3 mm thick and 40% porous with a flow area of 34 cm^2 which allows the fluidizing gas to pass through the bed uniformly. The ECT32 software is used to measure solid volume fraction fluctuation and can display the bed images in real time. The online images were extracted from the capacitance measurements using the Linear Back Projection algorithm. The twin-plane ECT sensors applied are located 15.7 and 28.7 cm above the air distributor where each sensor comprises equally spaced 12 electrodes mounted on the outer wall of the column (as shown in Figure 14). The raw data produced from the ECT sensors were either in the form of a numerical matrix or an image that covered the entire sensor-measuring area. For proper measurement of solid distribution, the cross-section of each sensor is divided into 32 × 32 square pixels of which 812 effectively lie within the bed. Each pixel holds a normalized relative permittivity value between 0 and 1, which represents the solid volume fraction. The sensor calibration was performed before the experiment at both extreme cases, i.e., when the sensor area is filled with the lower-permittivity material (air) and then with the higher-permittivity material (bed particles). For each flow velocity, the data were logged for 60 s at a sampling frequency of 100 Hz, resulting a total of 6000 frames over the sampling period. The bed fluidization characteristics were assessed through the particle volume fraction measurement, typically, the bubble properties and transition of bubbling to slugging regime as illustrated in Figure 13.

(a) (b)
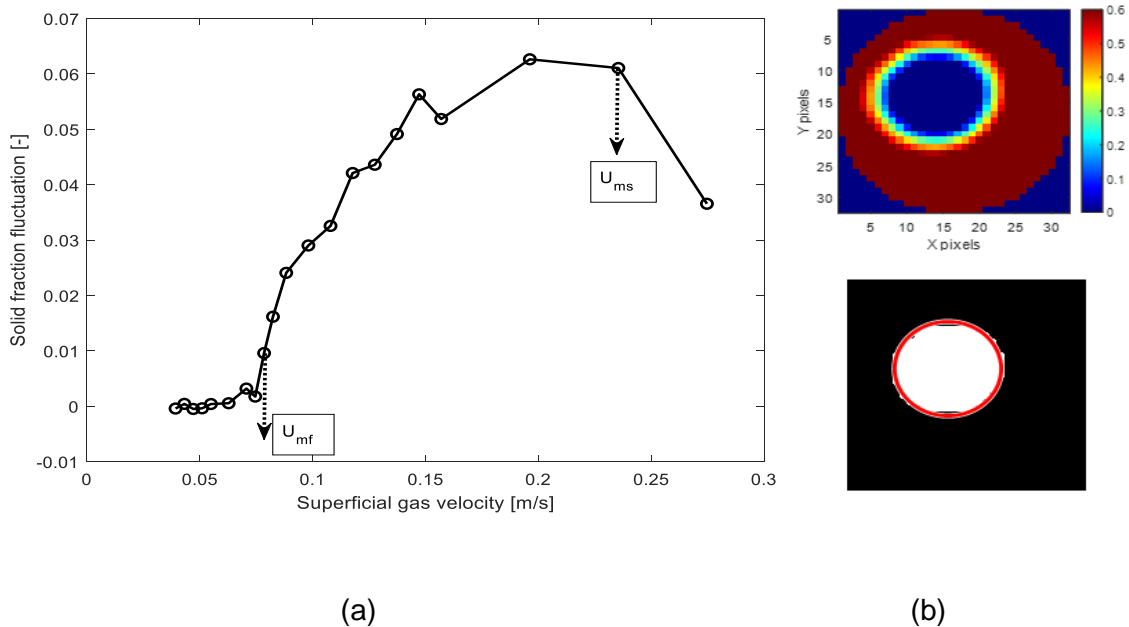
Figure 13:(a) Illustration of minimum fluidization velocity (U_{mf}) and slugging velocity (U_{ms}) of a bed obtained from fluctuation of solid volume fraction at different gas velocities, (b) Illustration of the emulsion bubble regions (top) and equivalent bubble region (bottom).
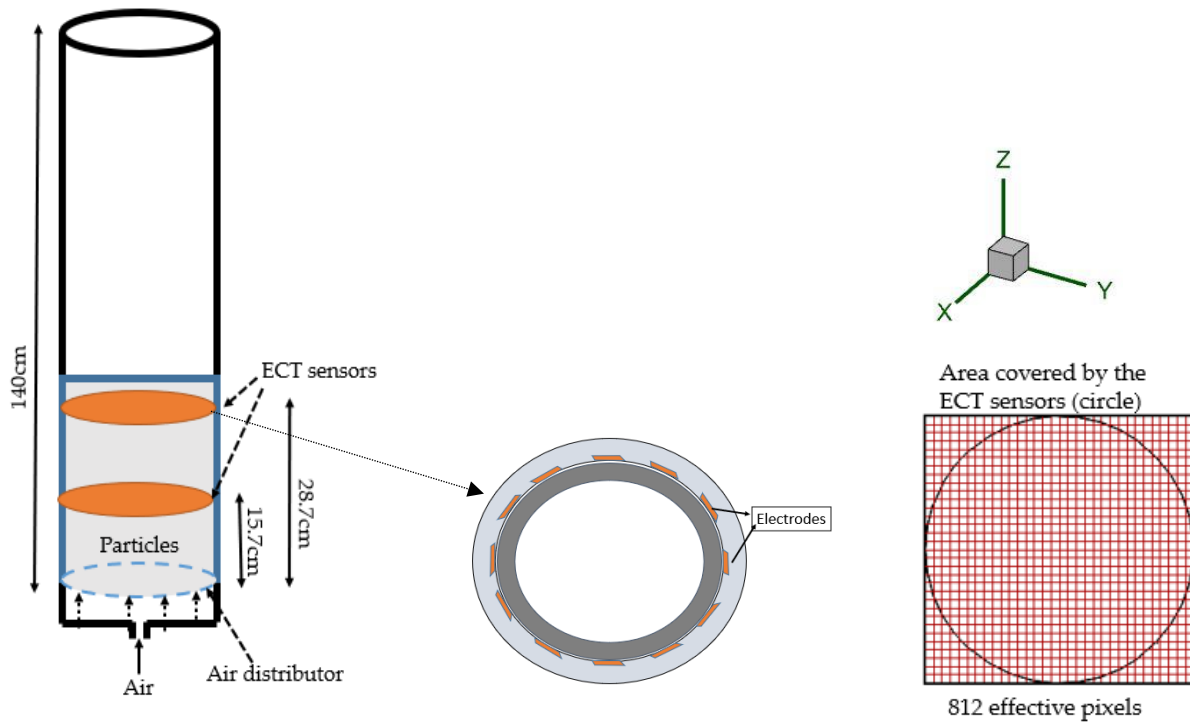
Figure 14:Schematic representation of the ECT set up, electrodes and effective area covered by the sensors.
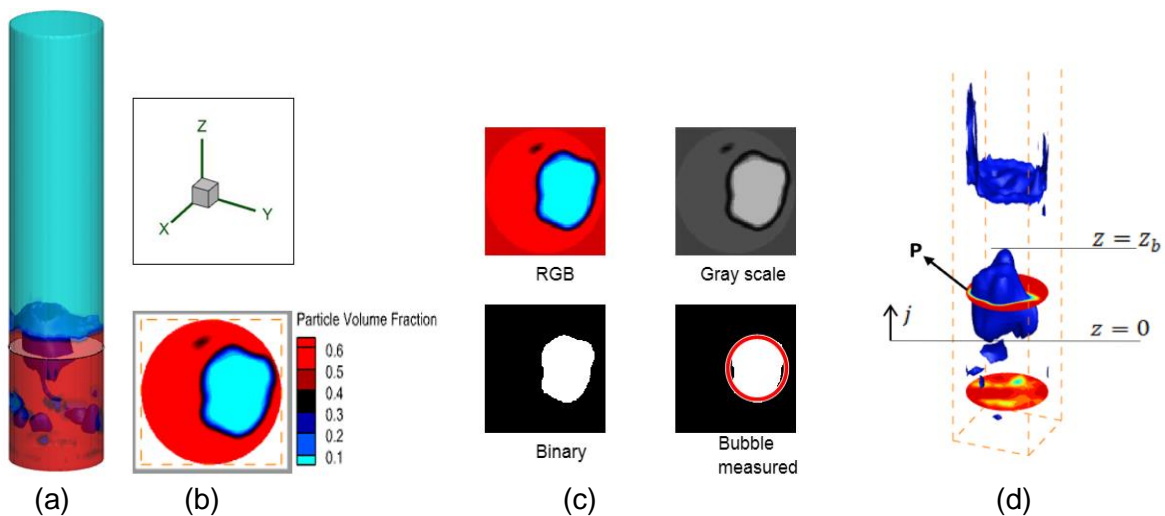
Figure 15. (a-c) Bubble measured from XY-Plane (horizontal plane) at height 25.8 cm and at superficial gas velocity 0.25 m/s, (d) three-dimensional view of bubbles in the CFPD simulation domain.

To determine the bubble properties, the initial step was to identify the bubbles at various positions. The Bubble positions were determined within regions where the solid volume fraction reached zero. Employing a threshold value for the solid-gas fraction ranging from 0 to 0.2 allowed to differentiate the bubbles in the bed from the emulsion phase. This study utilized a threshold value of ≤ 0.2 (solid volume fraction) to characterize the bubble region.

To validate the applicability of this gas-solid threshold, a meticulous examination of the boundary region was conducted, assessing the solid volume fraction of cells at the boundary between the bubble and the emulsion phases (as depicted in Figure 15b-c). The MATLAB scripts were used to calculate the bubble properties from the measured solid volume fraction across the planes and images extracted after post-processing the data. Detailed explanation of the method employed to identify the bubble properties from the extracted image and data along the planes are available in Article 5 and Article 6 respectively.

The maximum projected area is considered the same as the cross-sectional area of the bubble through the center. The bubble diameter based on the ECT data was therefore obtained as described below.

$$D_b = \frac{1}{n} \Sigma_k \left(\sqrt{\frac{4}{\pi} A_{max,k}} \right) \tag{3.4}$$

Here, n is the number of frames over which flow of bubbles are identified and $A_{max,k} = (N_{max,k}/N_{eff})A_B)$ is the maximum projected area across the measurement plane at frame k, where $N_{max,k}$ is the number of pixels occupied by the projected bubble, $N_{eff} = 812$ is the effective number of pixels across the bed and A_B is the bed cross sectional area.

Contrary to Eq. (3.4), the true bubble diameter can be obtained from measurement of the bubble volume after being identified. In the CPFD model simulation, bubble dimension can be described in three-dimensional space, thereby providing value for the bubble volume. Using the solid fraction of 0.2 for the bubble-emulsion phase boundary, Figure 15 (d) presents a typical three-dimensional view of a bubble formed in the bed. If V_b is the volume of the bubble, the volume-equivalent spherical bubble diameter, D_b was be obtained from

$$D_b = \sqrt[3]{\frac{6V_b}{\pi}} \tag{3.5}$$

Supposing S_b is the projected area at the plane **P**, the bubble volume is thus.

$$V_b = \int_0^{z_b} S_b dz \tag{3.6}$$

Where z_b is the height of the bubble. Since an analytical expression of S_b is cumbersome, the volume of bubble was computed as

$$V_b \approx \frac{A}{2N_{eff}} \Delta z \sum_j^{n_z} \left(N_{b,j} + N_{b,j-1} \right) ;$$

$$n_z = z_b/\Delta z \tag{3.7}$$

Here, Δz is the size of the computational grid along the vertical axis and $N_{b,j}$ is the number of grids on the horizontal plane occupied by the bubble at the position j. With bubble volume estimated from Eq. (3.6), the true bubble diameter can then be established from Eq. (3.7).

3.4 Gasification experimental set up

The gasification experimental set up consists of a 20kW bubbling fluidized bed reactor developed in collaboration with University of South-Eastern Norway and University of Natural and Life Sciences BOKU, Austria. The reactor is a cylindrical column made of stainless-steel with 1.5 m in height, 10 cm in diameter and thickness of 4mm. The reactor is operated at an atmospheric pressure and equipped with a number of thermocouples and pressure sensors mounted along the reactor heights as shown in Figure 16 (b). Pressure and temperature are measured along the reactor column, air pre-heater, air inlet, product gas outlet, silo, screw conveyer and heating coil. Three heating coils are surrounding the reactor wall externally to supply heat to reactor during the start-up. To prevent heat loss, the outer side of the reactor is insulated with fiberglass of thickness 200mm. For the fluidizing gas supply, the reactor consists of two inlets (diameter ~0.83 cm) at the lower section as shown in Figure 16 (b). The fluidizing gas is heated 300- 400℃ before passing into the reactor with an air-preheater. The cut off temperature of the air-preheater and reactor were set to 600 ℃ and 1000 ℃ respectively. The inlet mass flow rate of fluidizing air was controlled by a BROOK air flowmeter (3809 series). For the feedstock storage, the reactor is integrated with a silo and the pellets from the silo are conveyed to the reactor via two screw conveyers one mounted to the silo (a cold screw conveyer) and another (hot screw conveyer) attached to the reactor as shown in Figure 16 a. The details of the feeding system design and calibration are discussed in the Article 2 and Article 8. As shown in Figure 16 a, the two screws are connected with non-conductive flanges to avoid heat flow to the silo. In addition, nitrogen is continuously flushed through the silo at a volume flow of 0.6 Liter/minute to prevent heat and product gas flow to the silo.
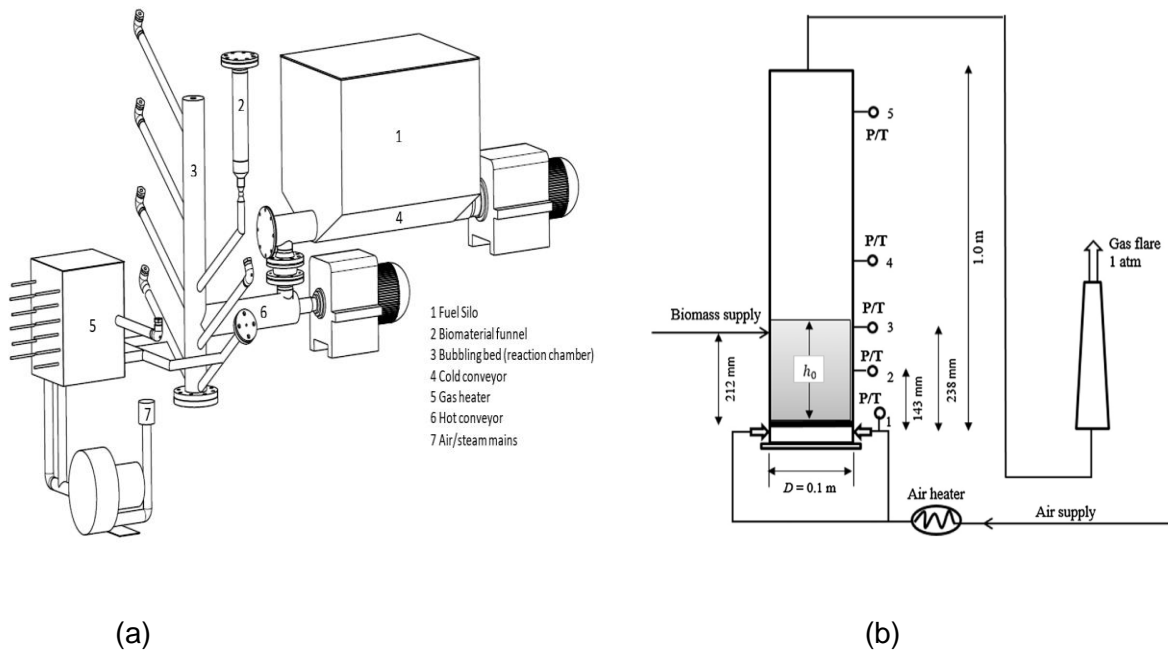
Figure 16:(a) 20 kW gasification reactor set up with different components, (b) schematic representation of the reactor showing thermocouples and pressure sensors positions.

Initially the reactor was filled with 2-2.5 kg bed material (sand particles) via the bed material funnel as shown in Figure 16(a). The density of the sand particles was 2650 kg/m^3 and the size of the particles varied in the experiments and details about bed particle size can be found in the articles. The static bed was fluidizing by the passing the air through the particle bed and the bed was heated up to 400 ℃ with the electric heater and the air pre-heater on. At 400 ℃ , a small amount of biomass was fed to the reactor to initiate the combustion process in the excess air environment until the bed temperature reached 650 ℃ . Once the reactor temperature reached 650 ℃ the biomass flow rate was kept constant and the air supply to the bed was adjusted to start the gasification of feedstock. Depending on the reactor temperature, the heater was turned on/off to maintain the desired temperature.

The bed pressure and temperature were constantly monitored which was useful in identifying changes in the hydrodynamic behaviour of the bed, accumulation of char, and clinker formation. The gas samples were extracted at 10 min intervals and kept for cooling down in order to let the tar to condense. Precautionary measures were always taken to remove the gas volume collected inside the sampling pipe during the previous sampling by flushing out the gas with 200 ml syringe three/ four times before taking the sample. The samples were analysed in an offline SRI gas chromatography (GC) where CO2 was detected by a silica gel packed column and N_2, O_2, CH_4, and CO by molecular sieve 13X packed column. Helium was the carrier gas. Therefore, the gas chromatography could not detect hydrogen. The fraction of H_2 and H_2O was estimated from the developed mathematical model. The accuracy of calculating the H_2 composition was validated with several samples using N2 as the carrier gas. With the known feedstock feed rate, air supply and measured syngas compositions, the

lower heating value of synthesis gas (LHV), the gas yield (GY), carbon conversion efficiency (CCE %), cold gas efficiency (CGE %), thermal energy and chemical energy were chosen to quantify the reactor performance.

Further, calculation of energy value of the product gas requires complete composition of the gas stream. Hydrogen and water vapor are among the vital species for this evaluation. Since the gas chromatography used in the analysis provides no information for these two gas species, an elemental and a mole balance were used in the estimations. Assuming a molecule of biomass is represented by $C_X H_Y O_Z N_W$ where the constituent elements are carbon (C), hydrogen (H), oxygen (O) and nitrogen (N), neglecting the Sulphur content. Disregarding the entrainment of char and assuming a complete conversion of the biomass particles supplied during the measurement period, equation (3.8) expresses the stoichiometry of the reactions.

$$C_X H_Y O_Z N_W + r(O_2 + 3.76N_2) = n_1 CO + n_2 CO_2 + n_3 CH_4 + n_4 H_2 + n_5 H_2O + n_6 N_2 + n_7 O_2 \quad (3.8)$$
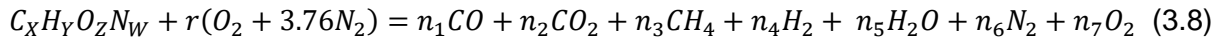
$$\begin{cases} \beta = \left(\frac{AFR}{\emptyset\varphi}\right)\left(\frac{\widehat{M}_{bio}}{\widehat{M}_{air}}\right) \\ \emptyset = 1 - w_{ash} \\ \varphi = 1 - w_{mois} \end{cases} \quad (3.9)$$

Where AFR is the mass flow rate of air to biomass supplied, w_{ash} and w_{mois} are the mass fractions of ash and moisture, respectively in the biomass and $\widehat{M}$ is the molecular mass of the indicated substance. With n denoting the total number of moles of the gaseous species in the product and y_j the mole fraction of the different species $j = \{CO, CO_2, CH_4, H_2, H_2O, N_2, O_2\}$, the elemental balance of equation (3.8) yields:

$$n_4 = \left(3y_{CO} + 4y_{CO_2} + y_{O_2}\right) - \frac{1}{n}\left(2X + Z + 2\beta - \frac{Y}{2}\right) \quad (3.10)$$

$$n = \frac{W + 7.52\beta}{2y_{N_2}} \quad (3.11)$$

$$y_{H_2} = \frac{n_4}{n} \quad (3.12)$$

By mole balance, the water vapor y_{H_2O} can be estimated from,

$$y_{H_2O} = 1 - \left(y_{CO} + y_{CO_2} + y_{CH_4} + y_{H_2} + y_{N_2} + y_{O_2}\right) \quad (3.13)$$

Considering that some amount of hydrogen and carbon are left in the tar and char, the mass fraction of unconverted hydrogen, $x_{hydrogen}$ and carbon, x_{carbon} relative to a unit of biomass are obtained from equations (3.14) and (3.15), respectively, which are also derived from the elemental balance of the reaction stoichiometry.

$$x_{hydrogen} = \frac{\beta}{n}\left(\frac{Y}{n} - y_{H_2}\right) \tag{3.14}$$

$$x_{carbon} = \frac{\beta}{n}\left\{X - \left(y_{CO} + y_{CO_2} + y_{CH_4}\right)\right\} \tag{3.15}$$

The number of atoms, X, Y, Z and W of the biomass constituents in an ash-free condition as well as the biomass molecular weight are given by equation (3.16), where $\%w_i$ is the weight fraction of each constituent element.

$$\begin{cases} \widehat{M}_{bio} = \frac{1}{1-w_{ash}} \Sigma \left\{\frac{1}{100}\widehat{M}_i(\%w_i)\right\} \\ k = \frac{1}{1-w_{ash}}\left(\frac{\widehat{M}_{bio}}{\widehat{M}_i}\right)\left(\frac{1}{100}(\%w_i)\right) \\ k : \{X, Y, Z, W\}; \quad i = \{C, H, O, N\} \end{cases} \tag{3.16}$$

4 Computational particles fluid dynamic simulations (CPFD)

The CPFD model developed in this work employed Barracuda VR (Version 21.1.1). Barracuda allows to simulate the dynamic and reactive gas-solid flow of the gasification process within a bubbling fluidized bed reactor. Barracuda VR is a commercial numerical tool designed explicitly for multiphase flow systems, such as fluidized bed reactors. This tool enables the simulation of computational particles in order of 10^{15}. Barracuda adopts a three-dimensional multiphase particle-in-cell approach to model gas-particle flow, incorporating detailed considerations of fluid-particle coupling, thermal physics, and reaction chemistry. Barracuda virtual reactor employs a combined Eulerian and Lagrangian approach to simulate fluid-particle interactions. Solid particles are modelled using discrete Lagrangian methods, while Eulerian grid of cells represents the fluid.

4.1 Governing equations for gas phase and particle motion

The governing equations used for the MP-PIC approach where the gas phase is solved as the continuum and particle phase as discrete as briefly described in equations 4.1-4.4. Details of the computational model in Barracuda can be found in [98], [99], [100], [101].

Equations (4.1) and (4.2) outline the mass and momentum of the gas phase, and Equation (4.3) describes the probability density function $f(x, u_p, \rho_p, V_P, t)$ for tracking the particle positions in the flow system.

$$\frac{\partial(\varepsilon_g \rho_g)}{\partial t} + \nabla.\left(\varepsilon_g \rho_g u_g\right) = \delta \dot{m}_p \qquad (4.1)$$

$$\frac{\partial(\varepsilon_g \rho_g u_g)}{\partial t} + \nabla\left(\varepsilon_g \rho_g u_g u_g\right) = -\nabla p + F + \varepsilon_g \rho_g g + \nabla\left(\varepsilon_g \tau_g\right) \qquad (4.2)$$

where, $\rho_g, u_g, \varepsilon_g$ and τ_g are the density, velocity, voidage and stress tensor of the gas phase respectively. The particle tracking function f are conserved as :

$$\frac{\partial f}{\partial t} + \nabla\left(f u_p\right) + \nabla u_p\left(f A_p\right) = 0. \qquad (4.3)$$

The probability density function, $f(x, u_p, \rho_p, V_P, t)$, describes the particle phase, where x is the location in space, u_p is the particle velocity, ρ_p is the particle density, V_P is the particle volume and t is the time. The mass source term in Equation 4.1 can be written as:

$$\delta \dot{m}_p = -\iiint f \frac{dm_p}{dt} dm_p du_p dT_P. \qquad (4.4)$$

where, m_p is the mass of the particles. The particle acceleration A_p is described as:

$$A_p = D_P\left(u_g - u_p\right) - \frac{1}{\varepsilon_p \rho_p}\nabla \tau_p + \frac{\bar{u}_p - u_p}{\tau D}. \qquad (4.5)$$

Based on the close pack volume fraction, ε_{cp}, the local particle volume fraction, $\varepsilon_p = 1 - \varepsilon_g$, and the solid compression pressure, P_s, the inter-particle stress, τ_p is obtained from

$$\tau_p\left(\varepsilon_p\right) = \frac{P_s \varepsilon_p^\beta}{\max\left[\varepsilon_{cp} - \varepsilon_p, \alpha(1 - \varepsilon_p)\right]} \qquad (4.6)$$

Equations (4.7) and (4.8) describe the particle volume fraction and the momentum transfer rate between the gas and the solid phase. Similarly, equations (4.9) and (4.10) is applied for gas and solid phases, respectively.

$$\varepsilon_p = \iiint f \frac{m_p}{\rho_p} dm_p du_p dT_P. \tag{4.7}$$

$$F = -\iiint f \left\{ m_p \left[D_P (u_g - u_p) - \frac{1}{\rho_p} \nabla p \right] + u_p \frac{dm_p}{dt} \right\} dm_p du_p dT_P. \tag{4.8}$$

$$\frac{\partial(\varepsilon_g \rho_g H_g)}{\partial t} + \nabla(\varepsilon_g \rho_g u_g H_g) = \varepsilon_g \left(\frac{\partial p}{\partial t} + u_g \nabla p \right) - \nabla(\varepsilon_g k_g \nabla T_g) + f Q_{pg} + Q_w \tag{4.9}$$

$$C_v \frac{dT_p}{dt} = \frac{A_P}{m_P} h_{pg} (T_g - T_p) \tag{4.10}$$

p is the fluid pressure and F is the total force exerted on the fluid by the particles, where DP is the gas-particle momentum transfer coefficient. The gas temperature, T_g, is related to the specific enthalpy, H_g, and its magnitude is determined by the quantity of heat-exchanged with the particles, Q_{pg}, and with the environment, Q_w, through the reactor wall. The particle temperature, T_p, depends on the single particle surface area, A_P, mass, m_P, and the specific heat capacity, Cv. Since the reactor in this study is properly insulated to minimize interactions with the environment, $Q_w= 0$ can be applied.

4.2 Drag Model

The momentum transfer F between gas and particles depends on the drag model, which greatly influences the accuracy of the model simulation. The Wen-Yu equation is applied when $\varepsilon_g > 0.8$ while the Ergun equation is used if $\varepsilon_g < 0.8$.

$$D_{P,W} = \frac{3}{4} C_d \frac{\rho_g}{\rho_p} \frac{|u_g - u_p|}{d_p} \tag{4.11}$$

where the particle drag coefficient, C_d is obtained from:

$$C_d = \begin{cases} \frac{24}{Re_p} \varepsilon_g^{-2.65}, Re_p < 0.5 \\ \frac{24}{Re_p} \varepsilon_g^{-2.65} (1 + 0.15 Re_p^{0.687}), 0.5 \le Re_p \le 1000. \\ 0.44 \varepsilon_g^{-2.65}, Re_p > 1000 \end{cases} \tag{4.12}$$

$$D_{P,E} = \left(\frac{180 \varepsilon_P}{Re_p \varepsilon_g} + 2 \right) \left(\frac{\rho_g |u_g - u_p|}{d_p \rho_p} \right). \tag{4.13}$$

As used in Barracuda, the following combination is obtained for the gas-particle drag function. With a linear coefficient of 2 and a non-linear coefficient of 180 for the Ergun model, several studies have shown good prediction of the fluid dynamic behaviour of a BFB reactor using the blended Wen-Yu and Ergun drag model [97], [102].

$$D_P = \begin{cases} D_W, \varepsilon_P < 0.75\varepsilon_{cp} \\ (D_E - D_W)(\frac{\varepsilon_P - 0.75\varepsilon_{cp}}{0.85\varepsilon_{cp} - 0.75\varepsilon_{cp}}) + D_W, 0.75\varepsilon_{cp} \geq \varepsilon_p \geq 0.85\varepsilon_{cp} \\ D_E, \varepsilon_P > 0.85\varepsilon_{cp} \end{cases} \tag{4.14}$$

4.3 Reaction, reaction Kinetics and heat transfer

The thermochemical conversion in a fluidized bed typically occurs in the form of homogeneous, deposition, consumption, and catalytic reactions. The continuous reactions in the fluidized bed reactors are accompanied by rapid consumption or release of the gaseous or solid components, thereby altering the gas-solid fraction and the fluidization pattern. Conversely, the reaction rates and the reactant availability will be a strong function of the gas and solid mixing. Therefore, it is vital to model the reactions together with the particle fluid dynamic and heat transfer in the fluidized bed gasifier. Different sets of homogeneous and heterogenous reactions and their kinetic rate employed for the CPFD model development are listed in Table 4. The rate of release of volatiles, the fluid-to-particle heat transfer [103], [104] as implemented in the model development are included in the equations (4.15-4.17).

Rate of release of volatile components

$$dm/dt = -k\,m\,[kg/s] \tag{4.15}$$

rate coefficient: k=0.05Te$^{(-5500/T)}$ [1/s]

Fluid-to-particle heat transfer coefficient

$$h = \frac{(c_0 Re^{n1} Pr^{0.33} + c_1)k_f}{D_p} + c_2\,[J/m^2 sK] \tag{4.16}$$

$Re = |U_f - U_p|D_p/v_f, Pr = c_p\mu_f/k_f$, where, $c_0 = 0.37, c_1 = 0.1, c_2 = 0, n1 = 0.6$

c_0, c_1, c_2 and $n1$are adjustable model parameters, k_f is the thermal conductivity of the fluid, and d_p is the particle diameter, ρ_f is density of fluid, U_f is fluid velocity, μ_f is fluid viscosity. The fluid to particle heat transfer coefficient based on the correlation proposed by McAdams et al.[103] has been used in the virtual reactor to capture fluid-to-particle heat transfer in the fluidized bed.

Dense phase heat transfer coefficient

$$h_d = \frac{c_0 Re_p^{n1} k_f}{D_p} \left[\frac{J}{m^2 sK}\right]$$

(4.17)

$Re_p = \rho_f U_f d_p / \mu_f$, where, $c_0 = 0.525$, , $n1 = 0.75$

c_0 and $n1$ are adjustable model parameter, k_f is the thermal conductivity of the fluid, d_p is the particle diameter, ρ_f is density of fluid, U_f is fluid velocity, μ_f is fluid viscosity. The default dense phase heat transfer coefficient values are taken from Yang et al.[104]. m_s in Table 4 is the mass of carbon.

Table 4: Reactions and rate kinetics used in the CPFD model.

Heterogenous reactions	Corresponding kinetics
Char partial combustion $2C + O_2 \leftrightarrow 2CO$	$r = 4.34 \times 10^{10}\, m_s \exp\left(\frac{-13590}{T}\right)[O_2]$
CO2 gasification $C + CO2 \leftrightarrow 2CO$	$r = 1.12 \times 10^6\, m_s f \exp\left(\frac{-13590}{T}\right)[O2]$
Char partial combustion $C + H_2O \leftrightarrow H_2 + CO$	$r = 1.272 T^1\, m_s \exp\left(\frac{-22645}{T}\right)[H_2O]$
Homogeneous reactions	**Corresponding kinetics**
CO oxidation $CO + 0.5O_2 \leftrightarrow CO_2$	$r = 5.62 \times 10^{12} \exp\left(\frac{-16000}{T}\right)[CO][\,O_2]^{0.5}$
H_2 oxidation $H_2 + 0.5O_2 \leftrightarrow H_2O$	$r = 5.69 \times 10^{11} \exp\left(\frac{-17610}{T}\right)[H2][\,O_2]^{0.5}$
CH_4 oxidation $CH_4 + 2O_2 \leftrightarrow CO_2 + 2H_2O$	$r = 5.0118 \times 10^{11}\, T^{-1} \exp\left(\frac{-24357}{T}\right)[CH4][\,O_2]$
Water gas shift reaction $CO + H_2O \leftrightarrow CO_2 + H_2$	$r = 7.68 \times 10^{10}\, T^1 \exp\left(\frac{-36640}{T}\right)[CO]^{0.5}[H_2O]$
Methane reforming $CH_4 + H_2O \leftrightarrow CO + 3H_2$	$r = 3.00 \times 10^5 \exp\left(\frac{-15042}{T}\right)[CH4][H_2O]$

4.4 CPFD set up and operational parameters

The 20 kW pilot scale bubbling fluidized bed gasifier and cold flow model were simulated to assess the reactor performance and identify the best operating conditions. To create a virtual reactor for numerical calculations, a CAD geometry of the reactor column was produced in STL format using SolidWorks and imported in Barracuda VR. The reactor was divided into a total of number 15984-102,400 of cells with uniform grid generation setting available in Barracuda. The grid size is a critical parameter influencing the simulation results, and therefore, the cell size was selected depending on the requirements. For instance, fine grids were employed for capturing the fluctuation of solid volume fraction within the bed and coarse grids were selected to measure the product gas compositions in the free board region. The grid allowed to define

boundary conditions and control volumes for all fluid field calculations. The reactor was operated at atmospheric pressure with pressure boundary conditions at the reactor outlet. Different data points were defined along the reactor height to capture the transient properties (fluid and particle temperature, pressure, gas fraction, gas and particle velocity, particle volume fraction etc.) of the reactor. Similarly, the air/steam inlet flow boundary condition was defined at the bottom of the column and the biomass inlet flow boundary condition was defined at the height of 22 cm from the bottom. Figure 17 illustrates the boundary conditions, transient data points, and grids as implemented in the CPFD model. Likewise, different parameter employed in the CPFD model development are listed in the Table 5. The detailed configuration of the simulation set up, feedstock and bed material properties are available in the corresponding articles. Techplot and MATLAB scripts were used to analyse and process the simulation data.

Table 5: Simulation parameters employed for the CPFD model.

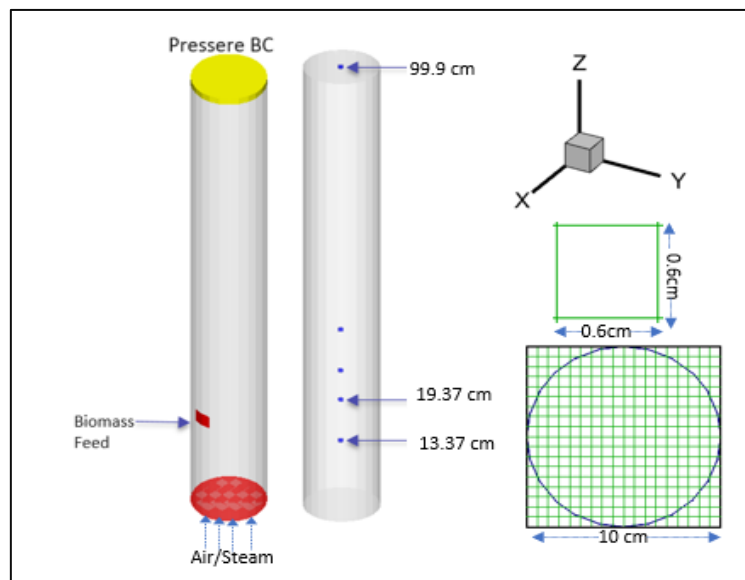| Parameters	Value
Close pack fraction	0.64
Solid Volume fraction	0.534
Total computational cells	60000- 102400
Time step	0.001 s
Simulation time	200 s- 700 s
Reactor temperature	(600-900)°C
Equivalence ratio	0.08-0.35
Steam-to-air ratio (SA)	0.01-0.2
Bed material density (Sand)	2650 kg/m^3

Figure 17: CPFD model set up showing Boundary Conditions, data points and computational grids.

5 Results and Summary of the papers

The thesis is structured as a combination of research articles. The results are summarised and discussed briefly in this section. The findings and discussion related to additional analysis of the results described in this section can be found in the published or submitted articles. This section primarily focuses on aligning with the results predicted from the CPFD model at different operating conditions, findings from the gasification experiments using various feedstocks, and results from the pelletization and co-pelletization of the wastes materials.

5.1 CPFD model for prediction of grass pellet gasification (Article 1)

As stated in the objective, this study employed CPFD simulations to investigate and find the optimal operating conditions for the gasification of wastes in a bubbling fluidized bed reactor. For the CPFD model development, a three-dimensional model of the fluidized bed gasifier was developed by considering the hydrodynamics of the gas-solid phase, particle size distribution of the bed material and biomass, and reaction kinetics involved in the conversion of wastes during gasification. The CPFD model for the prediction of grass pellets gasification was developed. The CPFD model was subsequently validated by comparing the syngas compositions obtained from the gasification experiments on the 20 kW gasifier, as illustrated in Figure 18 a. The CPFD model was then used to investigate the syngas production potential from grass pellets at different reactor temperatures, bed heights, and air-to-fuel ratios. The result showed increment in the product gas yield with increase in average reactor temperature when the initial bed height was changed from 20 cm to 30 cm. Comparison of syngas at air to fuel ratios, 0.4, 0.6, 0.8, 1, 1.2, showed decrease in the product gas quality with increase in the air to fuel ratio from 0.4 to 1.2. More carbon dioxide and nitrogen were released in the product gas at the higher value the of air-to-fuel ratio. Also, decrease in the $CH_4, CO, and H_2$ fractions in the product gas reduced the heating value of the gas. On the other hand, when the reactor temperature was increased from 600°C to 900°C, the product gas quality was enhanced. The fraction of hydrogen and carbon monoxide in the product gas increased to 21% and 19% respectively. Similarly, the CGE of the product gas increased from 58% to 66.6% with increase in reactor temperature. The grass pellet showed promising properties as feedstock for energy recovery.
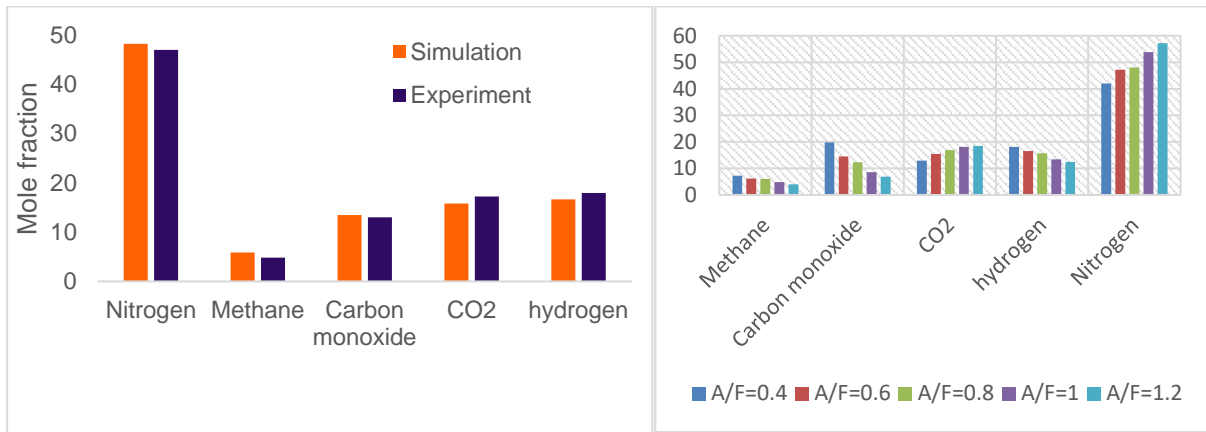
(a)

(b)
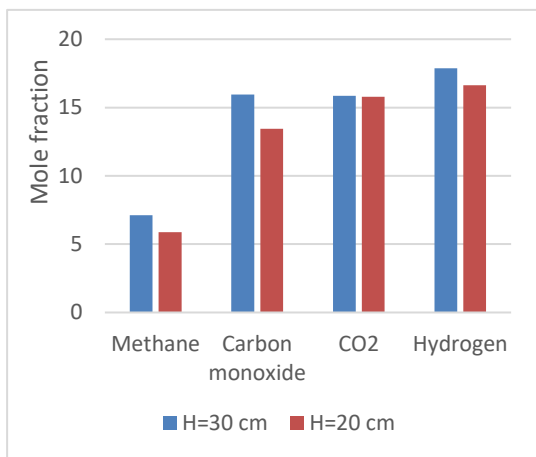
(c)
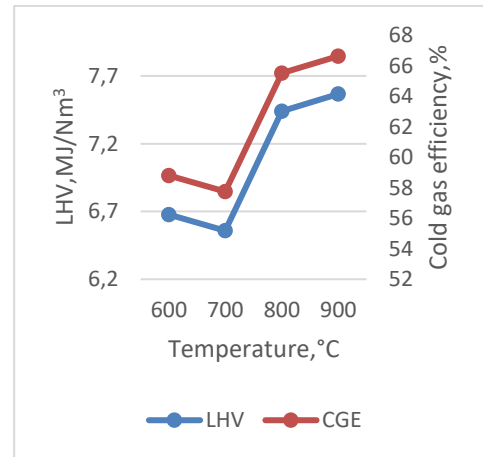
(d)

Figure 18: (a) Comparison of the product gas compositions from the experiment and CPFD simulations, (b), (c),(d) influence of air-to-fuel ratios, bed height and reactor temperature on the product gas predicted by the CPFD model.

5.2 Influence of biomass feed position (Article 3)

The efficiency of the gasification process relies on several factors, including the interaction between fuel, bed material, and gasifying agent. These factors are influenced by the feedstock feed positions along the reactor height. Thus, the fuel feed location is an important parameter that significantly impacts the gasification efficiency. When fuel particles have a longer contact time with the bed material, it promotes efficient carbon conversion and

reduces the tar formation. To evaluate the influence of the feedstock feed positions on the product gas compositions and char conversion rate, two different feeding positions were selected. The two feed positions include feeding biomass above the surface of the bed (on-bed feed) and at the lower part of the reactor near the bottom of the bed (in-bed-feed) as shown in Figure 19 (d). To explore the impact of different feed positions, the CPFD model developed for the gasification of wood pellets was used. The method employed for the model development and validation details can be found in the Article 3. The wood pellets feed rate and mass of the bed material was kept constant both in the in-bed and on-bed feed positions. Thus, change in the total mass of the bed was only dependent on the wood pellets conversion rate or presence of unreacted carbon in the bed. The total particle mass of the bed for the on-bed and in-bed feed positions during the conversion period of 700s are illustrated in Figure 19. As depicted in the Figure 19 c, for both scenarios, the total mass of the particles initially increases rapidly, followed by a subsequent decrease after a certain period. This initial rapid increase was attributed to the slower conversion rate of char, during which the system utilized maximum heat for biomass volatilization and the dominant endothermic reactions. After a specific time, exothermic reactions compensated for heat loss, leading to an increased char conversion rate, resulting in a gradual increase in the total mass of the bed. During the first 100 seconds, both the on-bed and in-bed feeding cases exhibited a similar rate of total mass increase. However, after 100 seconds, the total mass increment is higher in the on-bed feeding case. This is because wood pellets dropped on the surface of the bed did not interact uniformly with the bed material, causing more char particles to remain unreacted and accumulated on the bed surface, ultimately increasing the total mass of the bed. With the in-bed feed, the fuel particles were well mixed within the bed accompanied by enhanced reactor performance in terms of enriched product gas quality and uniform reactor temperature as depicted in Figure 19 and Figure 20 respectively.

Figure 20 compares the temperature profiles of the reactor under the on-bed and in-bed feed conditions. The results reveal variations in temperature along the reactor height. Notably, temperatures are lower near the feed positions in both scenarios. In the case of the on-bed feed, there is a significant temperature increase above the bed surface, away from the feed position. Conversely, in the in-bed feed scenario, the reactor temperature is lower in the freeboard zone near the outlet. These distinct temperature zones, as depicted in Figure 20, indicate multiple thermal conversion phenomena within the reactor. The lower temperatures observed at the feed positions are a result of endothermic reactions during rapid devolatilization.
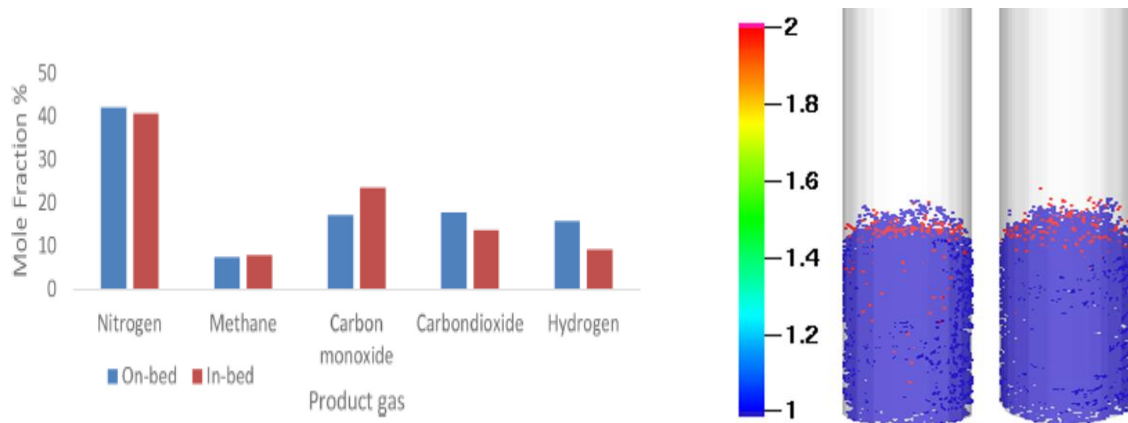
(a)

(b)
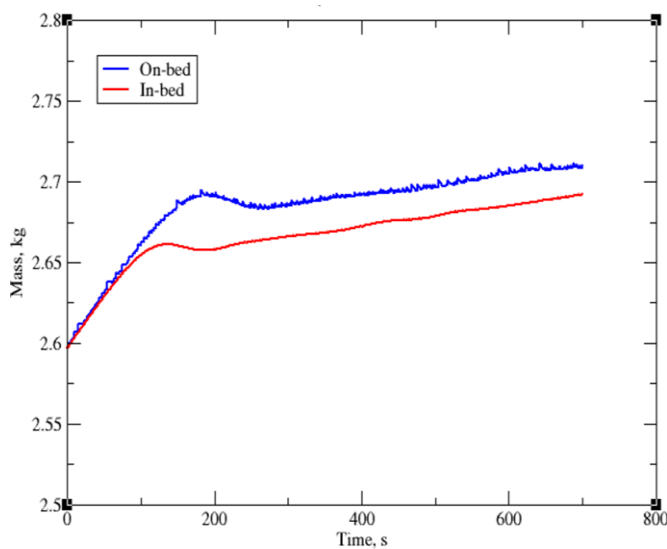
(c)
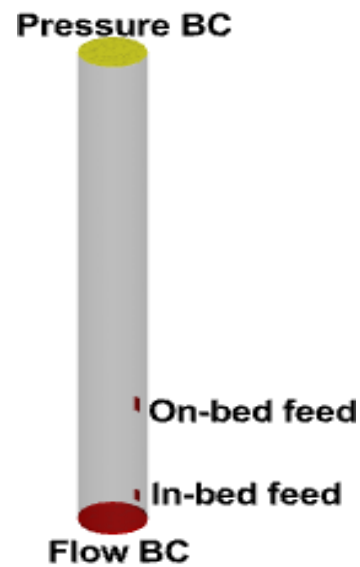
(d)

Figure 19: (a) Average product gas compositions for the on-bed and in-bed feed, (b) Particle species of the bed (in-bed feed to the left and on-bed feed to the right), (c) Change in total mass of the bed with time, (d) Boundary Conditions.

In the on-bed feed conditions, volatilization primarily occurred above the bed surface or in the freeboard zone, supported by the consistent average temperature of the bed beneath the feed positions over the measurement period. Despite the expectation that rapid biomass volatilization above the bed surface would decrease the freeboard zone temperature, an opposing trend was observed. One side of the reactor near the feed position exhibited lower temperatures, while on the opposite side the temperature was significantly higher (Figure 20 a). This uneven temperature distribution is attributed to dominant char partial oxidation reactions due to the presence of char particles above the bed surface. In the case of in-bed

feed, the reactor temperature remains uniform within the bed. Despite the anticipated decrease in the bed temperature due to continuous release of volatile components due to endothermic reactions in the in-bed feed, the observed uniformity suggests otherwise (Figure 20 b).
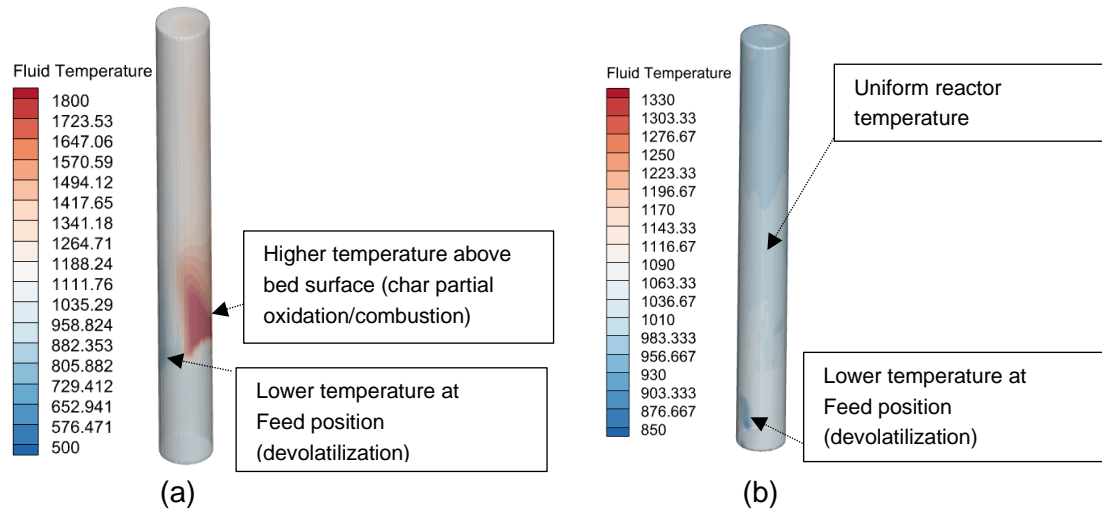
Figure 20: (a) Average fluid temperature (K) of the reactor for the on-bed feed, (b) Average reactor temperature (K) for the in-bed feed.

Further investigation involved measuring gas species and dilute phase (bubble) temperatures at various positions within the bed. The average temperature of the bubbles in the bed was directly influenced by thermochemical conversion within the reactor, and vice versa. The bubble average temperature varied with the bubble size and position as it ascends through the bed, as illustrated in Figure 21(c). Monitoring the bubble average temperature throughout the bed provided insights into both the bubble and the bed thermal behaviour. Figure 21 (a-b) compares histogram plots of the bubble average temperature for the on-bed and in-bed feed conditions. The findings reveal that, for on-bed feed, the average temperature of bubbles falls within the range of 1000 K to 1060 K, with the peak frequency occurring at 1010 K, aligning with the bed particle temperature. This observation ascertained the thermochemical conversion of the biomass during the on-bed feed primarily occurring above the bed surface or in the freeboard zone. In contrast, under in-bed feed conditions, the average temperature of bubbles exhibits fluctuations ranging from 850 K to 1300 K, as depicted in Figure 21 (b). These fluctuations occurred from simultaneous endothermic and exothermic reactions within the bed. Specifically, endothermic reactions, such as devolatilization, contribute to a reduction in the average temperature of bubbles, while partial char oxidation reactions elevated the temperature. Further validation of this argument was achieved by analyzing the average temperature of bubbles at various locations within the bed as depicted in Figure 21 (c).
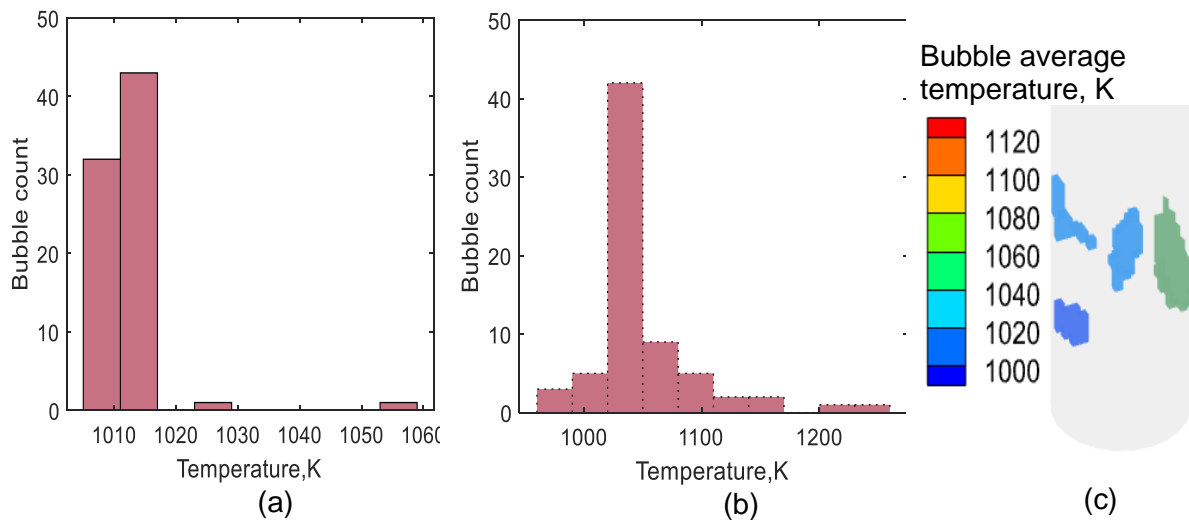
Figure 21: (a) bubble frequency vs bubble average temperature for on-bed feed, (b) bubble frequency vs bubble average temperature for in-bed feed, and (c) Instantaneous bubble temperature within the bed.
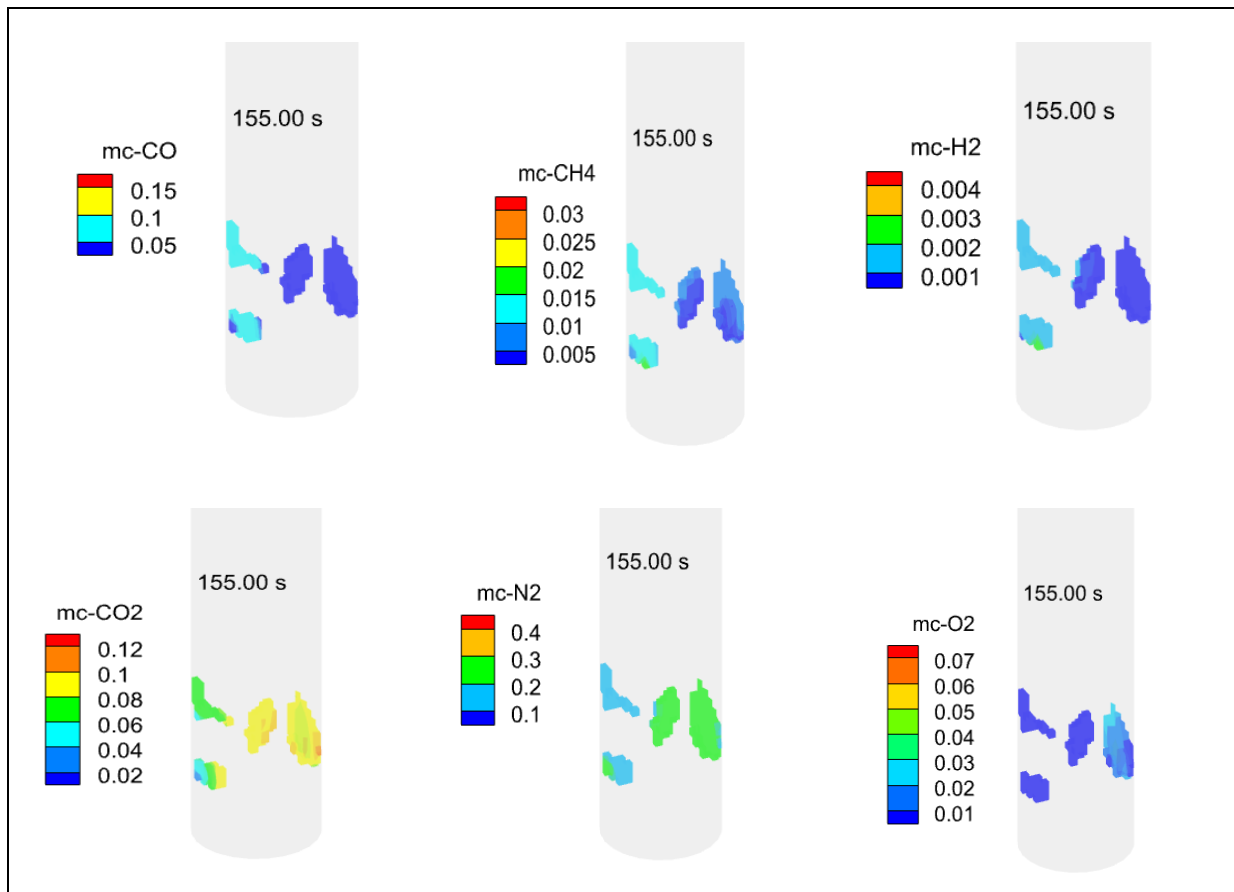
Figure 22:Instantaneous mass fraction (mc) of gas species in the bubbles distributed throughout the bed during on bed feed.

Additionally, the gas species measurement within the bubbles suggested diverse conversion phenomena at different regions of the reactor. The entire bed was categorized into either the emulsion phase or the bubble phase, where the dilute phase (or bubbles) comprised gas

species evolved during the gasification of wood pellets and the oxidizing agent. Consequently, examining the species distribution in the bubble phase offered insights into the gas distribution within the bubbles. Figure 22 illustrates the instantaneous mass fraction of gas species in the bubbles at different bed positions after 155 seconds. The results indicate that the mass fraction of CO, CH_4, and H_2 is predominant in the bubbles near the feed position, as depicted in the upper part of Figure 22. While, on the other side of the bed, CO_2 and N_2 dominate. This confirms rapid devolatilization and gas-phase reactions near the feed region, while the other side of the bed is dominated by the char partial oxidation.

5.3 Influence of air supply/injection method (Article 4)

The distribution of gas within a reactor profoundly impacts the conversion process and the specific fluidization regime in which the reactor operates. The efficiency of the oxidizing medium for feedstock conversion is intricately dependent on the uniformity of gas distribution across the cross-section of the reactor, including the bubble dynamics. Consequently, gas distribution significantly influences critical factors such as mixing, fluid dynamics, and heat and mass transfer within the reactor. In fluidized bed reactors, the fluidizing gas can be supplied to the particle bed through a distributor plate or nozzles. The distributor plate is a common method that ensures even gas distribution, supports the bed material, promotes effective gas-solid mixing, prevents channelling, and minimizes dead zones. Alternatively, gas can be supplied through orifices or nozzles at the reactor side or bottom. Each gas supply method has its limitations and advantages. While a distributor plate improves distribution, it increases auxiliary power consumption and requires maintenance due to potential clogging. Operating without a distributor plate can save costs and maintenance efforts. This work investigates the fluid dynamics behaviour of the bed without a distributor and compare it with uniform air supply methods, providing insights into optimizing fluidization quality without a distributor. For this, a cold flow model of the fluidized bed reactor with different air injection methods were simulated using the CPFD model. For the case without air distributor, the bed is fluidized with air supply from two nozzles (holes) located at the opposite side of the reactor wall. The pressure and flow boundary conditions are illustrated in Figure 23. The fluid dynamics behaviour of the bed in terms of solid fraction fluctuations and bubble properties are reported briefly and a method to improve the fluidization quality of the bed without an air distributor is proposed. The results from the CPFD simulations are compared with experimental data obtained from a cold fluidized bed equipped with ECT sensors and an air distributor for the model validation. The detailed procedure for the model development and validation is available in Article 4. To characterize the fluidization pattern of the bed, the average solid fraction fluctuation for the flow boundary conditions, including injections BC, nozzle BC, and uniform BC, are compared as shown in Figure 23.

The results indicate that in experimental measurements with an air distributor, the solid fraction was lower toward the center of the bed but increased near the reactor wall. The

CPFD model predicted a similar trend of solid fraction fluctuation for injection flow BC and uniform flow BC. However, the fluctuations in solid fraction for both cases were less smooth than the experimental measurements due to the presence of smaller bubbles when using uniform and injection flow BCs. The increased flow boundary area led to the formation of multiple smaller-sized bubbles compared to the experimental measurement. The reduction in solid fraction in the lower region of the bed near the center signifies a higher gas fraction in that area. Gas in a fluidized bed typically rises from the lower region to the upper region in the form of bubbles. Consequently, the depression of the solid fraction near the center and its increase near the wall illustrate that bubbles rise upwards, primarily following a path near the center of the reactor. In cases with two nozzles near the reactor wall for flow BCs, the solid fraction fluctuation was lower near the wall, where the nozzles were located, and also near the center of the bed. The fluidizing gas takes the form of bubbles, with some passing near the wall and others following a path closer to the center of the bed.
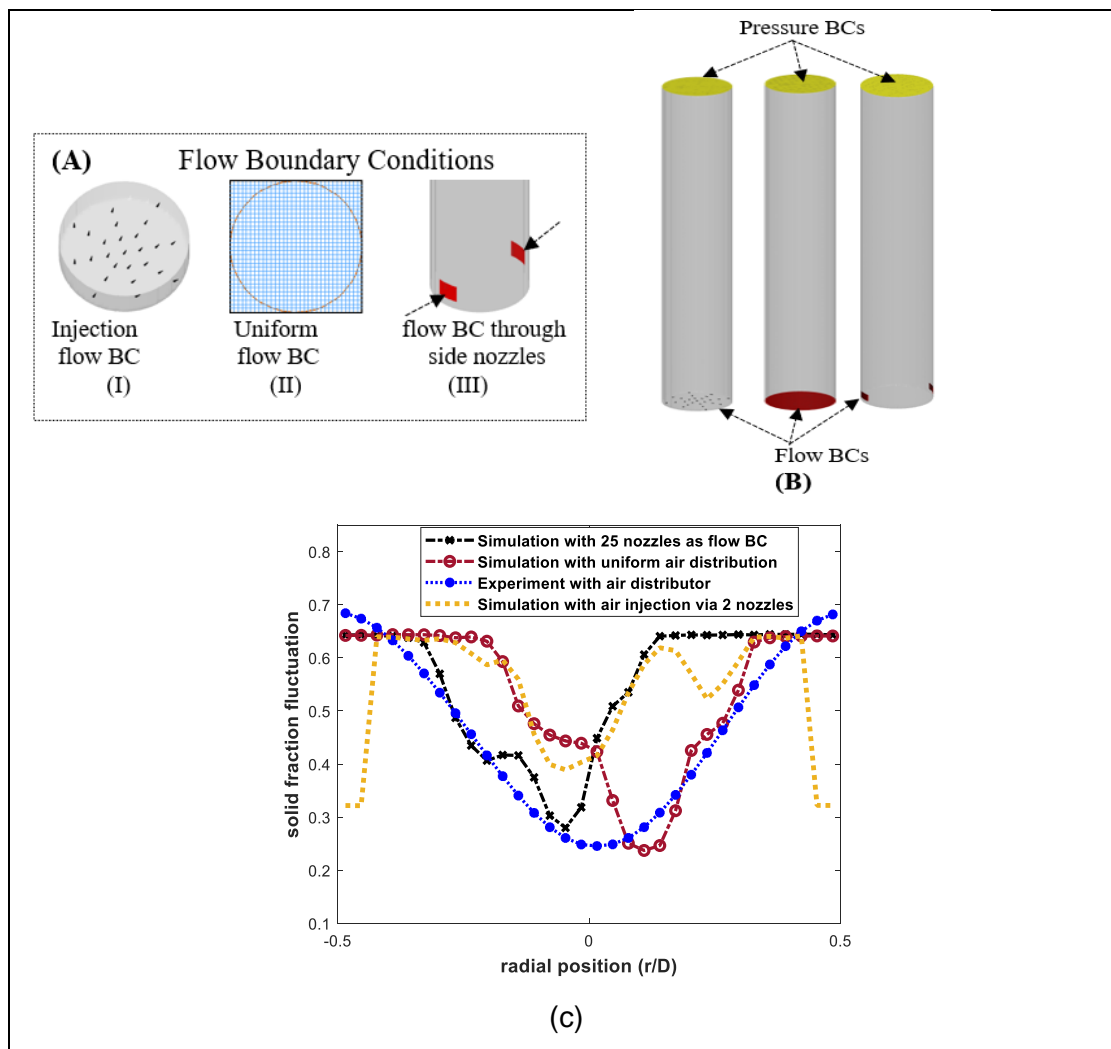
Figure 23: (A-B) flow and pressure boundary conditions, (c) Radial distribution of the solid volume fraction for different flow boundary conditions at superficial gas velocity 0.15 m/s.

Comparing different flow boundary conditions, it was observed that with uniform flow, bubbles of varying sizes between 2.5 cm and 5 cm were present, with a dominant frequency of 3 cm bubble diameter (shown in Figure 24). However, when using two nozzles for airflow, larger bubble diameters were observed at the same air flow rate compared to uniform and injection flow BCs. On the other hand, injection flow with 25 nozzles resulted in smaller and uniformly sized bubbles, indicating better fluidization quality which could improve the heat transfer and mixing. Conversely, the presence of large bubbles in flow BC via two nozzles could bypass the bed, potentially leading to slugging and turbulent regime. To address this, optimizing fluidizing gas flow by increasing the number of side nozzles along the reactor wall was proposed. Increasing the number of side nozzles helped to prevent particle entrainment, reduced bubble size, and increased bubble frequency, ultimately improving the fluidization quality of the bed. CPFD simulations were used to model a scenario with four different nozzles along the reactor wall, demonstrating enhanced fluidization quality of the bed as illustrated in Figure 25.
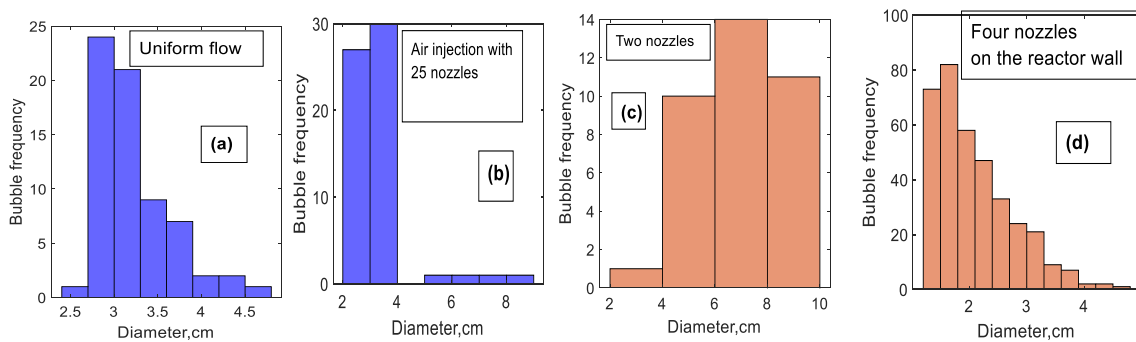
Figure 24: Bubble frequency vs bubble diameter for different air supply Boundary conditions.
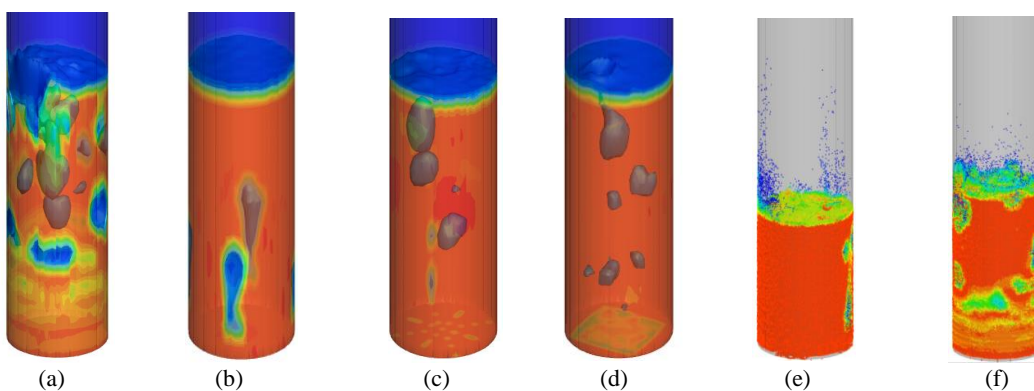
Figure 25:Iso-surface of the bubbles in the bed during, air injection via four nozzles, two side nozzles,25 nozzles at the bottom of the reactor, and uniform flow BC respectively, (e) Particle volume fraction of the bed with two side nozzles flow BC and (f) Particle volume fraction of the bed with four side nozzles flow BC.

5.4 Influence of the bubble properties in a BFB gasification reactor (Article 5 & 6)

The efficiency, operation, and design of bubbling fluidized bed (BFB) reactors are intricately related to the bed dynamics behaviour, which is greatly impacted by bubble properties. In a bubbling fluidized bed, an appropriate regime is one where the bed exhibits excellent fluidization quality without any slug. The key characteristics of smooth fluidized bed include a high number of bubbles, evenly distribution throughout the bed, and smaller bubble sizes. Bubbles play a vital role in ensuring effective solid circulation and promoting gas-solid contact, which are essential for heat and mass transfer within the reactor. To establish the effective operating conditions for efficient conversion processes, this study investigate the dynamic and thermal behavior of a BFB reactor. This investigation incorporates a combination of experimental measurements and computational particle-fluid dynamics simulations and are divided into two parts. The first part includes the measurement of the bubble properties in a cold bubbling fluidized bed reactor with sand particle as bed material (Article 5). The second part includes investigation of bubble properties with a bed of char and sand particle mixture in cold flow conditions. Further, the study investigates thermal and dynamical flow conditions in a 20 kW gasifier with wood pellets as feed (Article 6). A model has been proposed based on the bubble diameter and gas velocity which can be employed for sizing BFB reactors and determining the optimal operating gas velocity to achieve efficient gasification.

5.4.1 Bubble properties in a cold flow model

For the experimental measurement of the bubble properties, ECT sensors was employed. Similarly, to simulate the virtual reactor utilizing a CPFD tool (Barracuda VR), it was necessary to establish a grid that defines the control volume, cells, and boundary conditions for the fluid field calculations. A total of 102,400 cells were assigned through uniform grid generation, dividing the reactor into uniform cells. Such large computational cell count was chosen to align with the ECT experimental setup, ensuring the virtual reactor cross-section could also be divided into 32x32 pixels. It is important to note that reducing the grid size could decrease computational time but might introduce a certain level of bias when comparing simulated results with experimental data. The bubble properties including bubble rise velocity, and bubble frequency and bubble dimeter with the bed containing sand particle at ambient conditions are discussed in the Article 5. The influence of the bubble diameter on the bed thermal and dynamical properties are discussed in this section. As depicted in Figure 24 (a-b), the CPFD model accurately predict the bubble diameter in a bed containing sand and a binary mixture of the sand and char particles. The result illustrates that below 0.25 m/s, the various beds exhibit a bubbling regime. Evaluating the effects at various char loads, the bubble diameter is smaller in the bed with 5% wt. char compared to the bed of pure sand

particles. This phenomenon is associated to an increased solid packing density resulting from a small fraction of char particles mixed well with the fluidized sand particles. Additionally, the limited amount of char particles dragged into the bubble wakes, leading to bubble breakup. This continuous breakup enhanced the fluidization quality, delaying the onset of slug flow, as depicted in the Figure 26 b. As the char fraction increased, the bed voidage was enhanced, facilitating rapid bubble growth due to reduced bed resistance. Consequently, the bubble diameters in the 10% wt. char bed were larger than the bed with pure sand at given gas velocities.

(a)   (b)
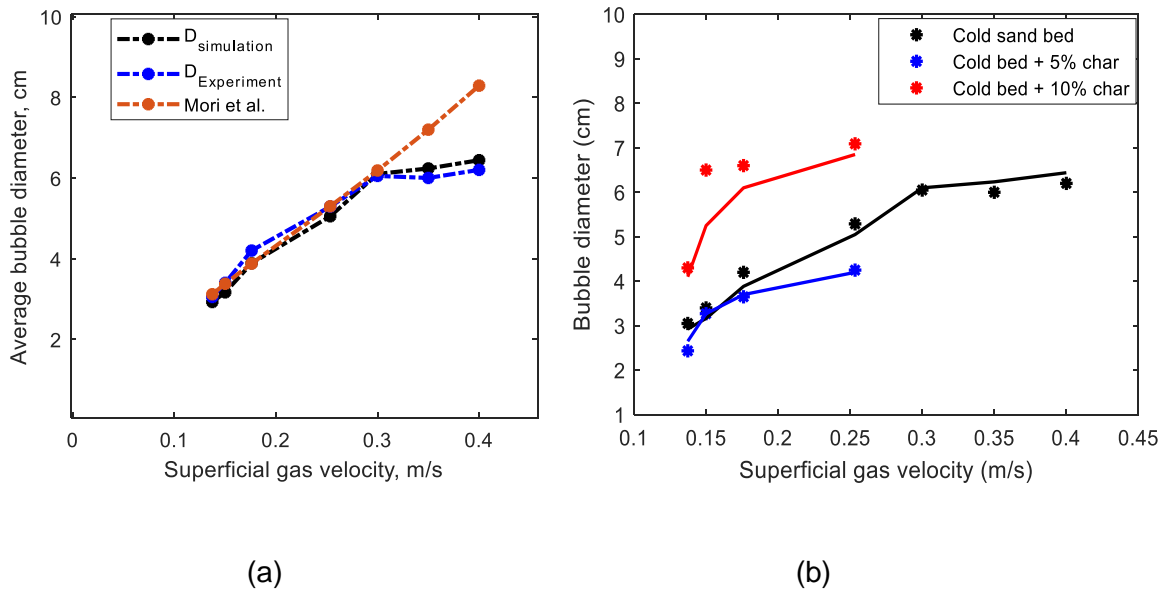
Figure 26. (a) Comparison of the bubble properties in the bed with sand particles measured from the ECT set up, simulation data and correlation proposed by Mori et al., (b)Variation of bubble diameter in cold beds, comparing the behaviour at different biomass loads across a range of superficial gas velocities, where doted points are experimental values and solid lines are the simulated values.

5.4.2 Influence of the bubbles on a conversion of the biomass in a BFB reactor

Further the CPFD model was used to predict the influence of the bubble dynamics on the thermal and dynamical behaviour including char load in the bed, temperature and gas distribution, and gas residence time.

Effect of the bubble on biomass load and performance

At the same air-fuel ratio, the gas composition should remain consistent regardless of the air flowrate. However, result illustrates variations in gas species distribution at different air flowrates, indicating that fluidized bed flow behaviour (bubble dynamics) influences biomass conversion (Article 6). Increasing air flowrate at a constant air-fuel ratio led to a higher biomass feed rate, potentially causing increased sensible heat loss, lower conversion rates, and a corresponding rise in unconverted char particles in the bed. Figure 27 (a) depicts bubble evolution in gasification at a 2 kg/h air flowrate, comparing beds with 5% and 10% wt. char particles against cold beds. While superficial gas velocity u_0 differs, the excess velocity $(u_0 - u_{mf})$ is similar at approximately 0.17 m/s. Despite the expected similar behavior at the same $u_0 - u_{mf}$, the flow dynamics in the Figure reveals differing bubble behaviour across the beds due to varying char particle amounts. In cold beds, mainly single bubbles rise through the central axis, whereas the hot bed exhibits multiple bubbles spread across. The higher bubble frequency in the hot bed is due to increased solid packing density from a lower volume fraction of accumulated char particles. During gasification, fluidizing gas consumption and volatile gas release contributed to a higher gas fraction in the hot bed compared to the equivalent cold bed. Unlike cold bed conditions, devolatilization and char conversion caused significant changes in bed void fraction in the hot bed. This variation in gas-solid fractions altered the bubble properties. Figure 27 (b) compares average bubble diameter in the hot bed at different air flowrates, revealing increase in bubble diameter with excess gas velocity and biomass load. Smaller bubbles formed at lower feed rates, growing with increased biomass feed rate due to higher char accumulation. In the reacting hot bed, bubbles are distributed throughout the cross-section, influenced by chaotic movement during formation and rise. Gas released in the bed impacts bubble movement, contributing to their random distribution. The increase in bubble diameter and the reduction in bubble frequency as air flowrate increased could negatively impact conversion efficiency. The associated rise in the bubble velocity with increase in the bubble diameter could hinder gasification due to a decrease in the gas residence time.
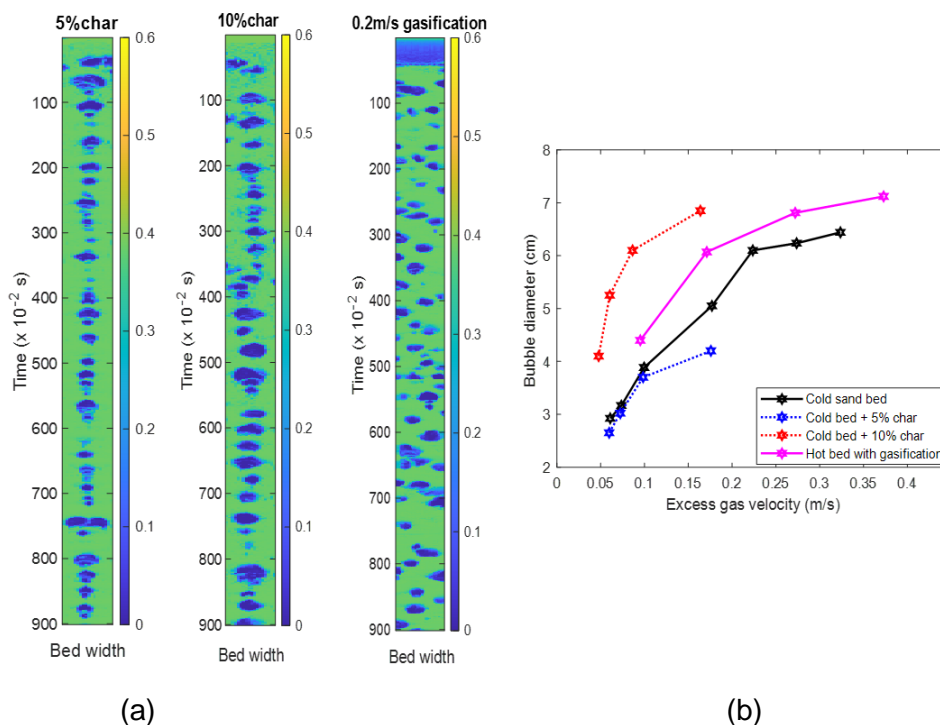
Figure 27. (a) Stacks of measurement plane over time, showing evolution of bubbles in cold beds with different char loads (5 & 10 %wt.) and gas velocity of 0.25 m/s compared with behavior in the bed with wood pellets gasifying at 2 kg/h air flow (b) variation of bubble diameter with excess velocity and biomass load, comparing hot and cold beds.

Effect of the bubble on temperature and gas species distribution

Figures 28 and 29 illustrate temperature and gas species distributions at 2 and 3 kg/h air flowrates. At the biomass feeding plane (at the height 5 cm), particle temperature is nearly uniform. The decrease in gas and particle temperatures, especially along the central axis, suggests endothermic activities like biomass devolatilization. The bed temperature near the wall, closer to the target value of 1020 K, implies a larger fraction of biomass particles along the central axis, particularly near the bed bottom, leading to a temperature distribution similar to the solid fraction. Toward the bed surface, endothermic conversion of char particles with gasifying agents dominates particle oxidation, causing a further decrease in particle temperature. Competitive gas phase reactions (Water-gas and Boudouard reactions) occur along the bed height, resulting in an equilibrium temperature slightly lower than the target across the bed. Bed temperature decreases with increasing air flowrate, associated with higher endothermic activities due to increased char accumulation.
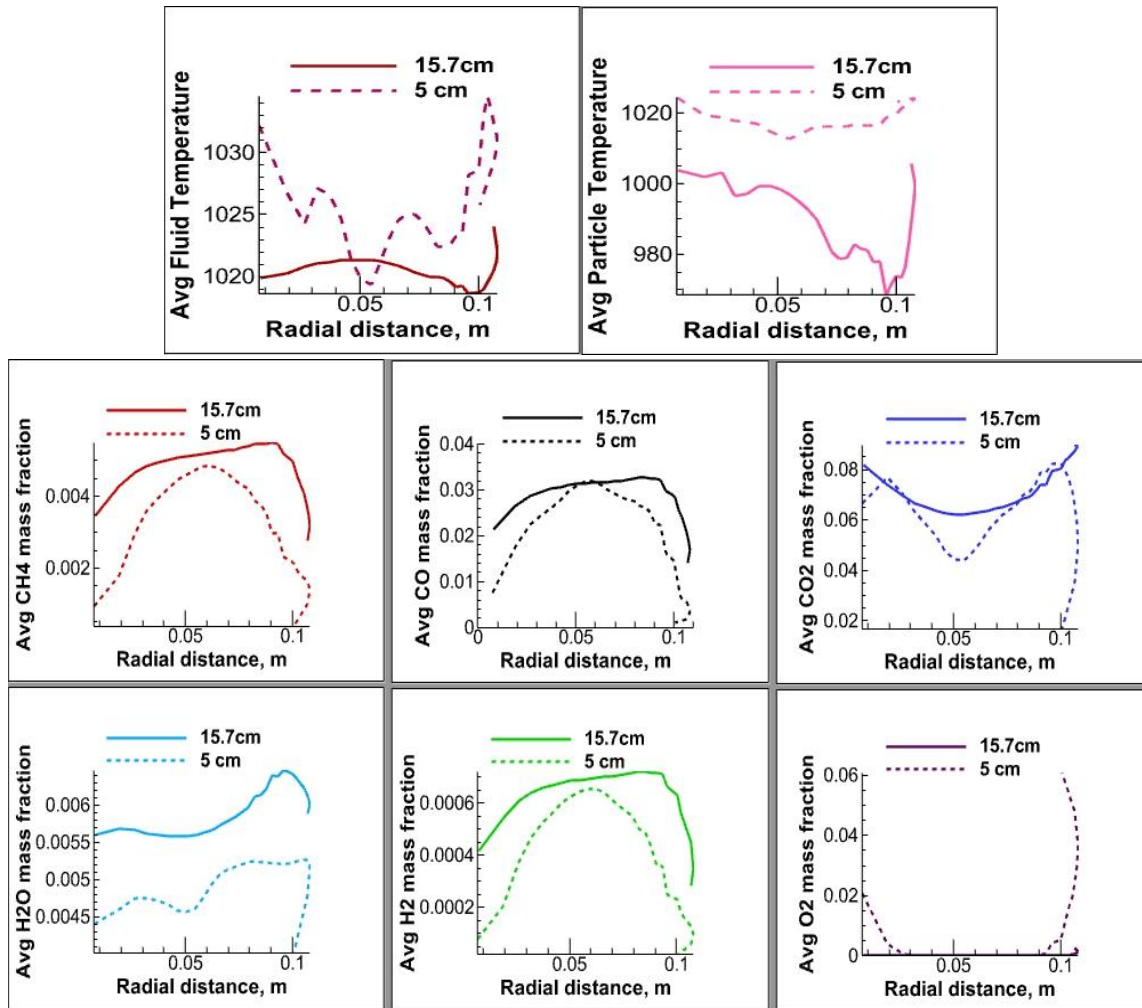
Figure 28. Radial distributions of temperature and gas species concentration within the gasifier bed, comparing behavior over the bed height at air flowrate of 2 kg/h.

The gas species distribution profile differs from gas temperature across different air flowrates. At lower air flowrates, the gas fraction increases toward the central axis, while the fraction decreases toward the center as superficial gas velocity increases. Considering oxygen concentration at different air flowrates, the gas fraction distribution variation is explained. Oxygen is present near the walls, indicating low concentrations of char particles and combustible gas species. At 2 kg/h air flowrate, O_2 is completely consumed along the bubble path, with the convex distribution of the evolved gas species (shown in Figure 28). Oxygen presence along the central axis at 3 kg/h indicates low oxidation activities at higher gas flowrate, although some improvement is noted towards the upper part of the bed. Larger bubbles with higher rise velocity at 3 kg/h may result in lower contact time between char particles and active gas species. Gasification being kinetic limited, the decrease in particle temperature along the bubble path significantly impacts char-oxygen reactions (shown in Figure 29).
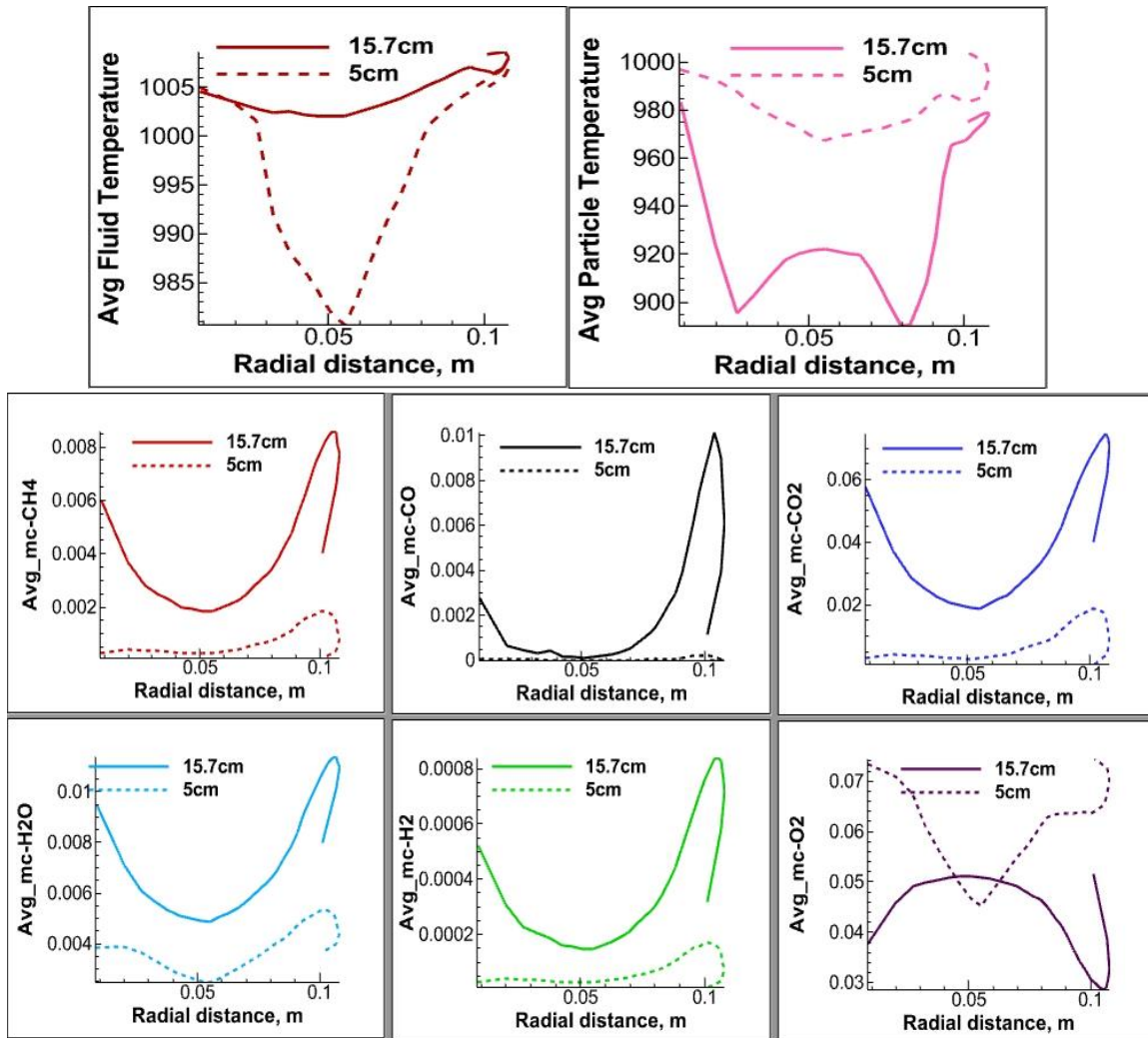
Figure 29. Radial distributions of temperature and gas species concentration within the gasifier bed, comparing behavior over the bed height at air flowrate of 3 kg/h.

Effect of the bubble on gas residence time and product gas distribution

Assuming constant flow velocities, a relation between the bubble diameter (D_b) and the relative gas residence times τ_r was established as:

$$\tau_r = \frac{gD_b}{u_0(u_0 - u_{mf})}$$

(5.1)

The derivation of the Eq. (5.1) is outlined in Article 6. According to Equation (5.1), τ_r increases with a larger bubble diameter. In a bubbling bed, the relative gas residence time is a characteristic value that reduces with excess gas velocity due to the growing bubble diameter. Figure 30 (a) illustrates the trajectory of τ_r, primarily influenced by the solid packing density. In cold beds with a relatively small biomass fraction, the bed behavior resembles that of pure sand particles. As biomass content increases, leading to larger bed

voidage than pure sand particles, τ_r aligns with the hot bed at the same excess velocity. However, at higher velocities where bubbles are fully developed or slugs start flowing in the bed, the residence time decreases towards values independent of the flow condition.

(a)   (b)
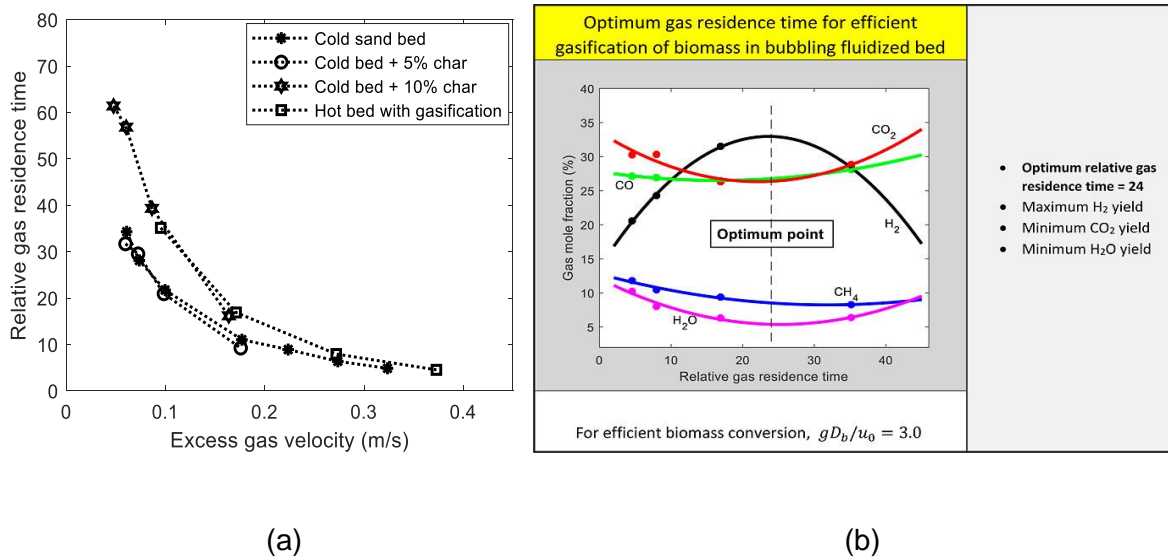
Figure 30. (a) Variation of relative gas residence time with excess gas velocity, showing (b) the effect on product gas composition in bubbling bed gasifier.

The gas species composition in the product gas against the relative gas residence time is shown in Figure 30 (b). The findings highlight that the time the gas spends in the bed plays a significant role for the conversion steps within the reactor. The optimal relative residence time is approximately 24, characterized by the highest hydrogen yield and minimal yields of carbon dioxide and water vapor. This suggests that gasification processes, targeting the conversion of CO_2 and H_2O to CO and H_2, perform optimally when $\tau_r \approx 24$. Below the optimum residence time, the H_2 concentration decreases, while that of CO_2 exceeds CO due to poor oxygen utilization in the bed and active oxidation of combustible gases in the freeboard. When $\tau_r > 24$, inadequate particle distribution in the bed leads to the escape of O_2 into the freeboard through the wall region of the bed, resulting in the oxidation of combustible gases and a reduction in their concentrations in the product gas. Since $\tau_r \approx 24$ with $u_0 - u_{mf} \approx 0.13$ m/s (estimated from Figure 30 (a)) as the corresponding excess gas velocity at the best gasification performance, Eq. (5.2) can be derived from Eq. (5.1). Equation (5.2) establishes the conditions for operating a bubbling fluidized bed biomass gasifier with optimal efficiency.

$$\frac{gD_b}{u_0} = 3.0; \quad [m/s] \tag{5.2}$$

5.5 Air gasification of wood chips, wood pellets and grass pellets in a bubbling fluidized bed reactor (Article 2)

In general, the equivalence ratios of 0.15-0.4 are used for the gasification with air as gasifying medium. However, higher equivalence ratio is associated with increase in nitrogen concentration, diluting the product gas quality. This observation was reported in earlier studies with wood pellets and grass pellets in the section 5.1. With an aim to minimize the addition of nitrogen in the product when using air as gasifying medium, equivalence ratios of 0.08-0.16 were selected in this work. While gasification is generally an endothermic process, the use of air as a gasifying medium introduces partial oxidation reactions that may compensate for the heat demand of the endothermic conversion steps, depending on the amount of air used. The result demonstrated, decreasing bed temperature at an equivalence ratio of 0.15. Therefore, in this work external electrical heating source is employed for the gasification experiments. A 20 kW bubbling fluidized bed reactor was utilized to gasify three different types of feedstocks: wood chips, wood pellets, and grass pellets. The details of the experimental setup and comprehensive findings can be found in Article 2. The investigation encompassed diverse operating conditions, examining four equivalence ratios (ERs) ranging from 0.08 to 0.16 and temperatures set at 650℃, 750℃, and 800℃.

The temperature profile along the reactor height at an initial bed temperature of 650℃ and for different Equivalence Ratios (ERs) is depicted in Figure 31. Temperature sensors T8, T3, and T4 are positioned at the air inlet, inside the bed, and just above the bed, respectively. Electrical heaters were active for lower ERs of 0.08 and 0.1, maintaining an average reactor wall temperature of 750℃. Consequently, the product gas experienced continuous heating from the bed surface to the exit. For the same amount of external heat supply, the temperature gained in the 0.08 ER scenario exceeded the temperature in the 0.1 ER conditions due to the lower gas flow. Conversely, gas outlet temperatures at ERs of 0.13 and 0.16 remained relatively constant from above the bed to the exit, and electrical heaters were inactive, aligning the reactor wall temperature with bed temperature. The observed temperature drop just above the bed (T4) is attributed to the endothermic characteristics of the progressing pyrolysis reaction. While the bed temperature remained nearly constant at around 650℃, comparing different ERs introduces slight uncertainty due to temperature variations at the gas exit.
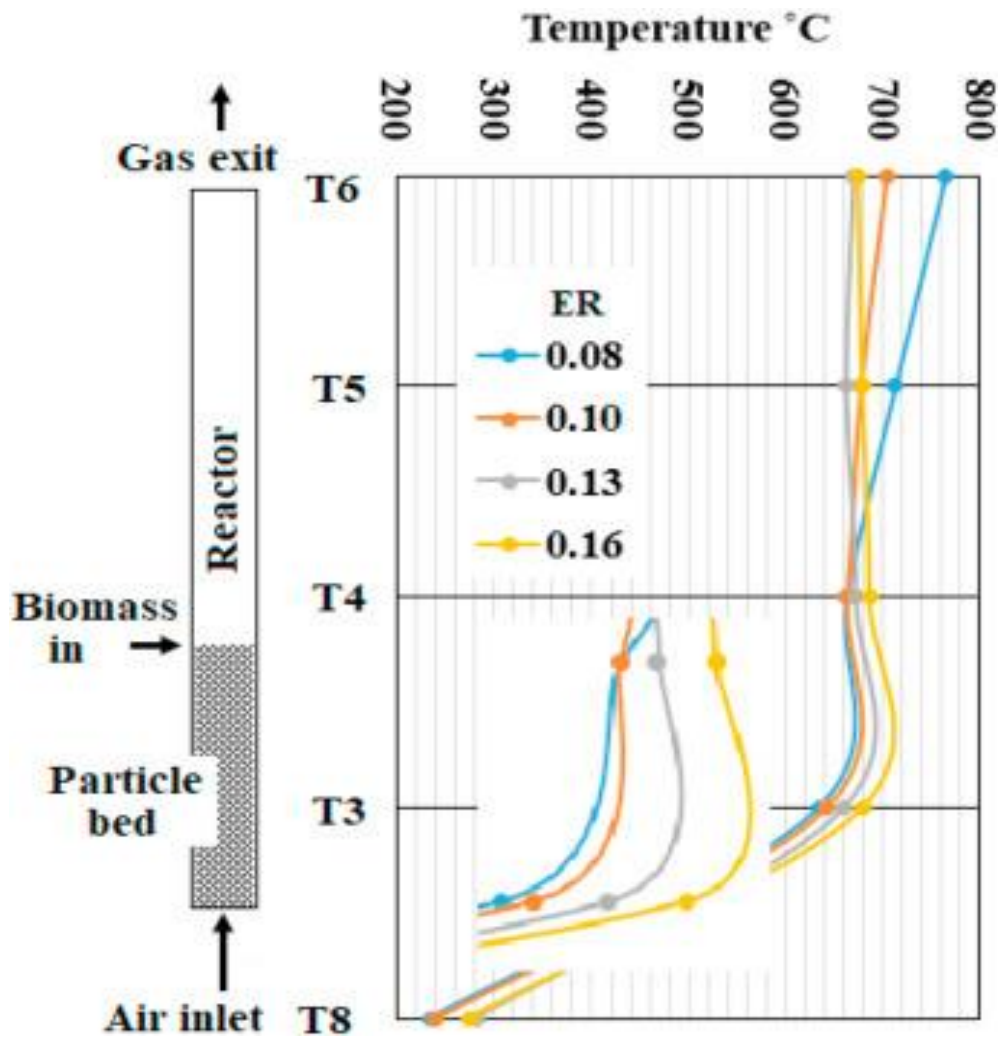
Figure 31: Temperature profile along the reactor height at 650 ºC operation (initial bed temperature) for different ERs during gasification of the woodchips.

(a)

ER	Product Gas	Gas Yield	LHV	CCE	CGE	Energy Rate
	(Nm³/h)	(Nm³/kg biomass	(MJ/Nm³)	%	%	MJ/h
650°C						
0.08	2.11	0.92	5.52	38.80	28.15	11.65
0.1	2.44	1.06	4.53	38.90	26.70	11.05
0.13	3.07	1.33	4.31	50.13	31.98	13.24
0.16	3.27	1.42	3.41	46.62	26.97	11.16
750°C						
0.08	2.71	1.18	6.86	54.10	44.85	18.57
0.1	2.78	1.21	5.35	46.92	35.89	14.86
0.13	2.92	1.27	3.91	41.78	27.59	11.42
0.16	3.31	1.44	3.68	46.66	29.47	12.20
800°C						
0.08	2.90	1.26	7.25	57.83	50.89	21.07
0.1	2.77	1.21	5.48	45.36	36.67	15.18
0.13	3.22	1.40	4.94	51.79	38.42	15.90
0.16	4.32	1.88	5.68	75.83	59.27	24.54

(b)

Figure 32: (a) Product gas composition of wood chips at different equivalence ratios and reactor temperatures, (b) gasification performance indicators for wood chips.

The transportation of feedstock to the reactor was facilitated by a screw conveyor at flow rates specific to each feedstock: 2.3 kg/h for wood chips, 2.42 kg/h for wood pellets, and 2.7 kg/h for grass pellets. The gasifier performance was evaluated across various reactor temperatures and equivalence ratios (ERs). The analysis focused on key parameters, including the lower heating value of synthesis gas (LHV), gas yield (GY), carbon conversion efficiency (CCE%), and cold gas efficiency (CGE%). Figure 32-34 (a) illustrates the percentage gas compositions for wood chips, while Figure 32-34 (b) illustrates an overview of the gasification performances of the corresponding feedstocks. The findings provide valuable insights into the complexities associated with variations in biomass feedstocks at different operating conditions during gasification experiments. The gasification of grass pellets proved unsuccessful due to agglomerations and low carbon conversion. However, wood chips and wood pellets demonstrated successful outcomes, producing product gas with favourable CO and H_2 compositions. Lower temperatures, coupled with increased ER, resulted in reduced gas quality due to N_2 dilution. Conversely, at 800℃, the minor reduction in H_2 and CO content with increased ER was outweighed by improved carbon conversion and gas yield. Specially, at 800℃ and 0.16 ER, wood chips exhibited H_2 and CO contents of 16.9% and 20%, respectively, while wood pellets showed 17.2% and 18.8%. A reactor temperature of 650℃ was insufficient for acceptable gas composition and carbon conversion. Gas quality progressively improved at 750℃, achieving approximately 50% carbon conversion. The optimal performance for wood chips occurred at 800℃ and 0.16 ER, achieving a 75% carbon conversion efficiency. For wood pellets, ER values of 0.125 and 0.15 at 800℃ delivered the best overall performance with a 70% carbon conversion. Using lower ER values than those reported in the literature aimed to identify the minimum ER sufficient to maintain a steady char content without accumulation in the bed. An ER around 0.15 was identified as the minimum value, requiring additional electrical heating to sustain the reactor temperature around 800℃.

(a)

ER	Product Gas	Gas Yield	LHV	CCE	CGE	Energy Rate
	(Nm³/h)	(Nm³/kg biomass)	(MJ/Nm³)	%	%	(MJ/h)
650°C						
0.075	2.02	0.84	5.38	33.64	25.00	10.89
0.1	2.14	0.88	3.36	28.19	16.54	7.20
0.125	2.57	1.06	2.91	31.25	17.14	7.47
0.15	3.01	1.25	2.71	36.69	18.76	8.17
750°C						
0.075	2.29	0.94	6.05	38.28	31.72	13.82
0.1	3.03	1.25	6.00	50.60	41.77	18.19
0.125	3.37	1.39	5.19	52.36	40.12	17.48
0.15	3.86	1.60	4.89	58.28	43.42	18.91
800°C						
0.075	2.41	1.00	6.40	41.23	35.42	15.43
0.1	2.61	1.08	5.13	39.42	30.73	13.39
0.125	4.11	1.70	6.45	69.93	60.85	26.51
0.15	4.30	1.78	5.66	70.62	55.91	24.35

(b)

Figure 33: (a) Product gas composition for wood pellets at different equivalence ratios and reactor temperatures, (b) gasification performance indicators for wood pellets.

(a)

ER	Product Gas	Gas Yield	LHV	CCE	CGE	Energy Rate
	(Nm^3/h)	$(Nm^3/kg$ biomass	(MJ/Nm^3)	%	%	(MJ/h)
650°C						
0.07	1.77	0.65	3.96	22.43	14.33	7.01
0.1	2.11	0.78	3.02	23.71	13.03	6.38
0.12	2.51	0.92	2.41	26.06	12.36	6.05
0.14	3.03	1.11	2.43	30.95	15.04	7.36
750°C						
0.07	2.08	0.76	5.26	28.50	22.33	10.93
0.1	2.35	0.86	3.85	27.81	18.48	9.05
0.12	2.42	0.89	2.60	24.38	12.89	6.31
0.14	3.18	1.17	3.14	34.94	20.34	9.96
800°C						
0.07	2.08	0.76	5.26	28.50	22.33	10.93
0.1	2.35	0.86	3.85	27.81	18.48	9.05

(b)

Figure 34: (a) Product gas composition for grass pellets at different equivalence ratios and reactor temperatures, (b) gasification performance indicators for grass pellets.

5.6 Alternative Energy - Evaluation of Waste Feedstocks for Heat Generation and Syngas Production (Article 7)

This study evaluates conversion of different low grade waste feedstocks in a bubbling fluidized bed for energy and syngas productions. To ensure a high energy content, the different feedstocks, wood, paper, garden, and fish wastes are densified and used in pellet form in an air gasifier over the equivalence ratio 0.16 – 0.35. For a fair comparison, the tests are carried out at about the same starting bed temperature, 650 ℃. To ascertain the impact of the bed behavior on the conversion process, the analysis of the bed temperature, pressure and accumulated char over the duration of the test at a given air-fuel ratio is presented in Table 6 and discussed subsequently. The assessment of gasifier performance and feedstock energy production potential involved a thorough evaluation of parameters, including unconverted carbon, chemical and thermal energy fractions, gas yield, and overall conversion efficiency. The detailed methodology for estimating these parameters is provided in Article 7, and the summarized results are presented here.

Table 6:Parameters derived from gasification of the different feedstocks at different air flow rates.

Feedstock	$\dot{m}_{air}$ [kg/h]	$\dot{m}_{bio}$ [kg/h]	T_{bed} [℃]	T_{out} [℃]	$x_{hydrogen}$ [%]	x_{carbon} [%]	Unconverted char, Ref [--]	FI (-)
Wood pellet	3	2.95	710	636	0.04	1.50	9.23	1.16
	4	2.95	742	694	0.03	1.98	8.03	1.55
	5	2.95	752	712	0.01	2.13	7.25	1.91
	6	2.95	743	725	0.40	3.41	6.75	2.21
Fish Pellet	3	3.14	705	671	3.90	5.19	9.30	1.03
	4	3.14	621	638	2.98	5.37	9.27	1.06
	5	3.14	743	711	2.03	5.15	7.34	1.67
	6	3.14	744	736	1.90	5.54	6.75	1.98
Paper pellet	3	3.21	768	636	0.32	2.54	8.67	0.88
	4	3.21	790	624	0.25	2.10	7.63	1.14
	5	3.21	762	728	0.49	3.71	7.17	1.31
	6	3.21	763	703	0.32	3.53	6.60	1.55
Garden Waste pellets	3	3.15	744	697	0.60	3.07	9.09	1.38

4	3.15	737	598	0.36	3.26	8.23	1.69
5	3.15	815	653	0.31	3.41	6.90	2.40
6	3.15	791	710	0.32	3.76	6.50	2.71

For each feedstock, Figure 35 depicts the total pressure drop across the bed over time at two distinct air flow rates, 3 and 6 kg/h. When the bed achieves full fluidization, the pressure drop remains relatively stable for different gas rates. The magnitude of the pressure drop is influenced by the bed voidage. At lower air flow rates, higher fuel particle accumulation occurs due to a lower conversion rate. The increased biomass load raises the bed voidage, subsequently reducing the pressure drop. This trend is observed consistently across various feedstocks. Over time, the pressure drop tends to increase at different air flow rates, indicating a reduction in bed voidage due to the increasing fluidizing gas from pyrolysis and char gasification. Notably, paper pellets exhibit significantly higher bed fluctuation across different air flow rates, suggesting inadequate fluidization compared to other feedstocks, as ascertained by the fluidization index (Table 6). Among the four biomasses, wood pellets exhibit the most stable bed behavior, followed by garden waste pellets, attributed to their relatively high fluidization index. Fish pellets, despite having a comparable particle equivalent diameter to wood pellets, demonstrate higher bed instability due to their lower char density.

Figure 35 Change in total pressure of the bed during gasification of (a) paper pellets, (b) fish pellets, (c) garden waste pellets and (d) wood pellets.

Compared to the pressure drop, Figure 36 illustrates a similar trend in bed temperature for the different feedstocks. The rising temperature over time signifies progressive oxidations dominating the endothermic pyrolysis of the feed biomass. At a 3 kg/h air flow rate, the increased accumulation of the char particles contributes to higher sensible heat loss. The bed temperature behavior also suggests partial fluidization at lower air flow rates (FI < 1.6). As biomass is fed from the top and gas from the bottom, the increasing bed temperature implies char particles sinking into the bed with rising gas flow, potentially due to an increase in solid circulation. The paper pellets having higher particle size and lower density, could likely have undergone initial downward segregation at lower gas rates and subsequent upward segregation at higher air flow rates. Consequently, a higher amount of char particles is present in the bed, resulting in a higher bed temperature at lower air flow rates compared to higher rates. On average, the bed temperature is higher than the exit temperature across the different air flow rates (as shown in Table 6). Since the raw biomass is fed on top, this suggests that devolatilization of the fuel particles is rapid and may have been completed before the particles moves into the bed. Neglecting heat loss, the lower exit temperature also indicates that a significant amount of heat is absorbed from the gas during the drying and pyrolysis processes. In the freeboard, it is expected that some exothermic activities occur, which should include the water-gas-shift reaction between H_2O and CO , and others involving oxidation of the fuel gases: CO, H_2 and CH_4 by the residual oxygen. However, the relative difference between the exit and bed temperatures indicates that the possible exothermic reactions rarely occurred, therefore there is little or no O_2 in the freeboard. This was confirmed from the O_2 yield in the product gas.
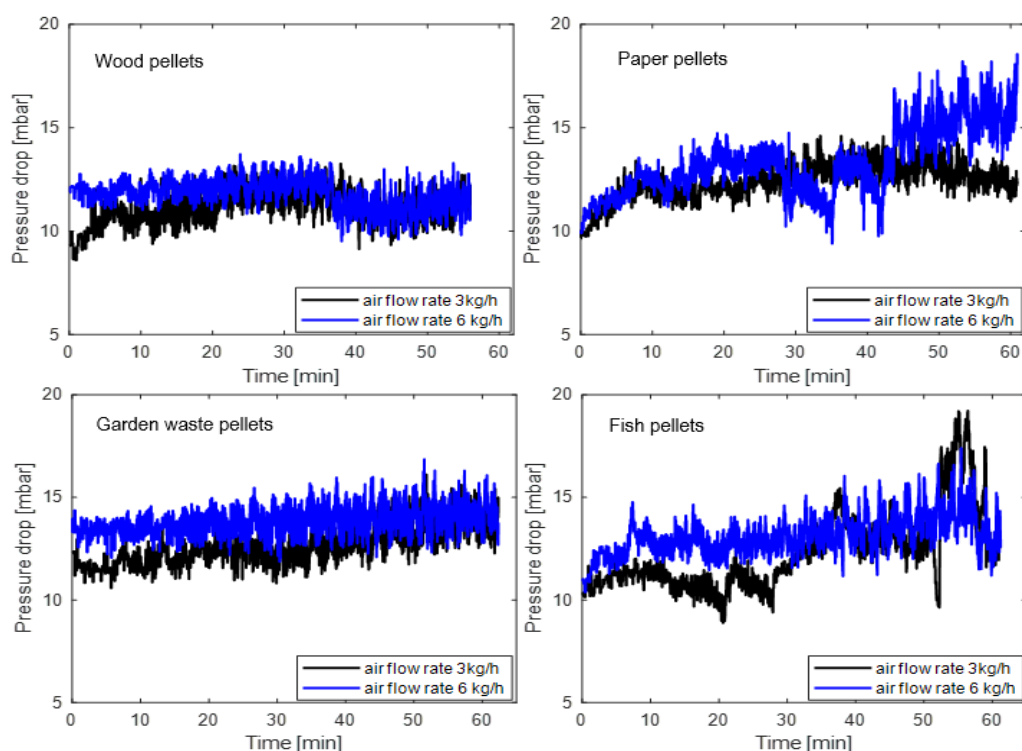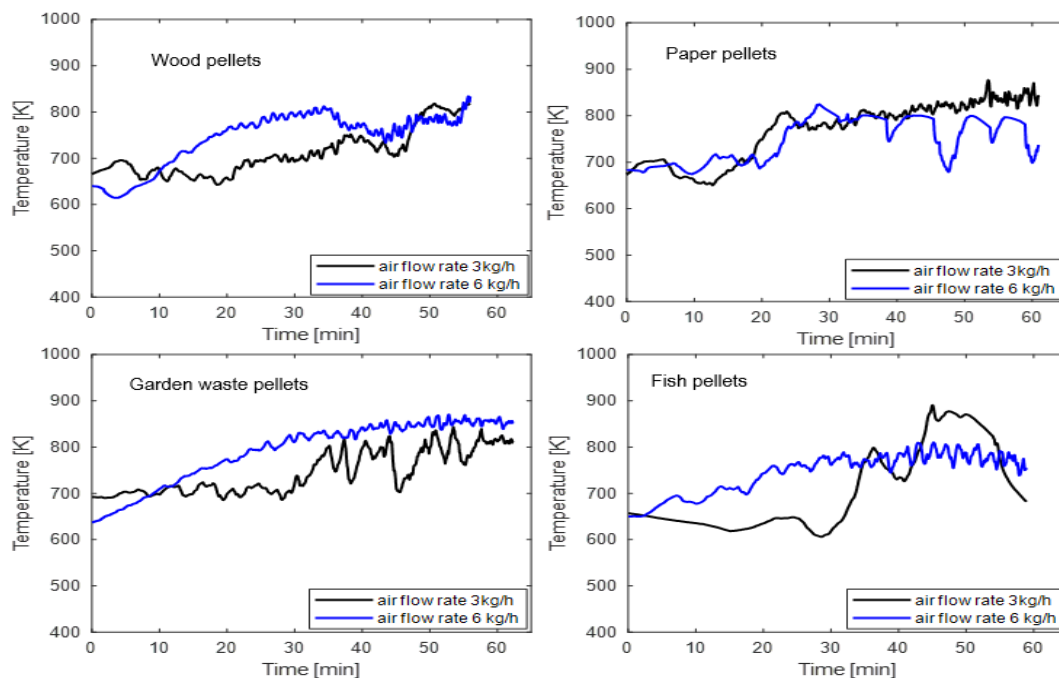

Figure 36 Change in temperature in the bed during gasification of (a) paper pellets, (b) fish pellets, (c) garden waste pellets and (d) wood pellets.

Figure 37 compares the product gas species for the different feedstocks at different air flow rates. While the mole fraction of N_2 increases with increasing air rate, the indicated O_2 concentrations are stable low across the different the different flow rates. As expected, the nitrogen fraction is highest, and it is ranging from 41% to 56%. Variation in the fractions of other gases in the product gas contribute to changes in the nitrogen fraction. In addition to a greater amount of nitrogen elements in the Fish pellets, the relatively lower values of CO, CO_2 and H_2 in the product gas contribute significantly to the higher nitrogen fraction from the Fish biomass. For each of the air flow rates, the bed temperature with the fish pellets is lower compared to other feedstocks. This can therefore be considered as the major factor contributing to the lower gas composition of the fuel gases. Overall, the wood pellets show a higher composition of the fuel gases compared to other feedstocks. The garden waste on the other hand shows a better composition than the paper pellets, indicating a higher conversion probably due to a better mixing of the bed particles. For each of the feedstocks, the concentration of the fuel gases decrease as the air flow rate increases.
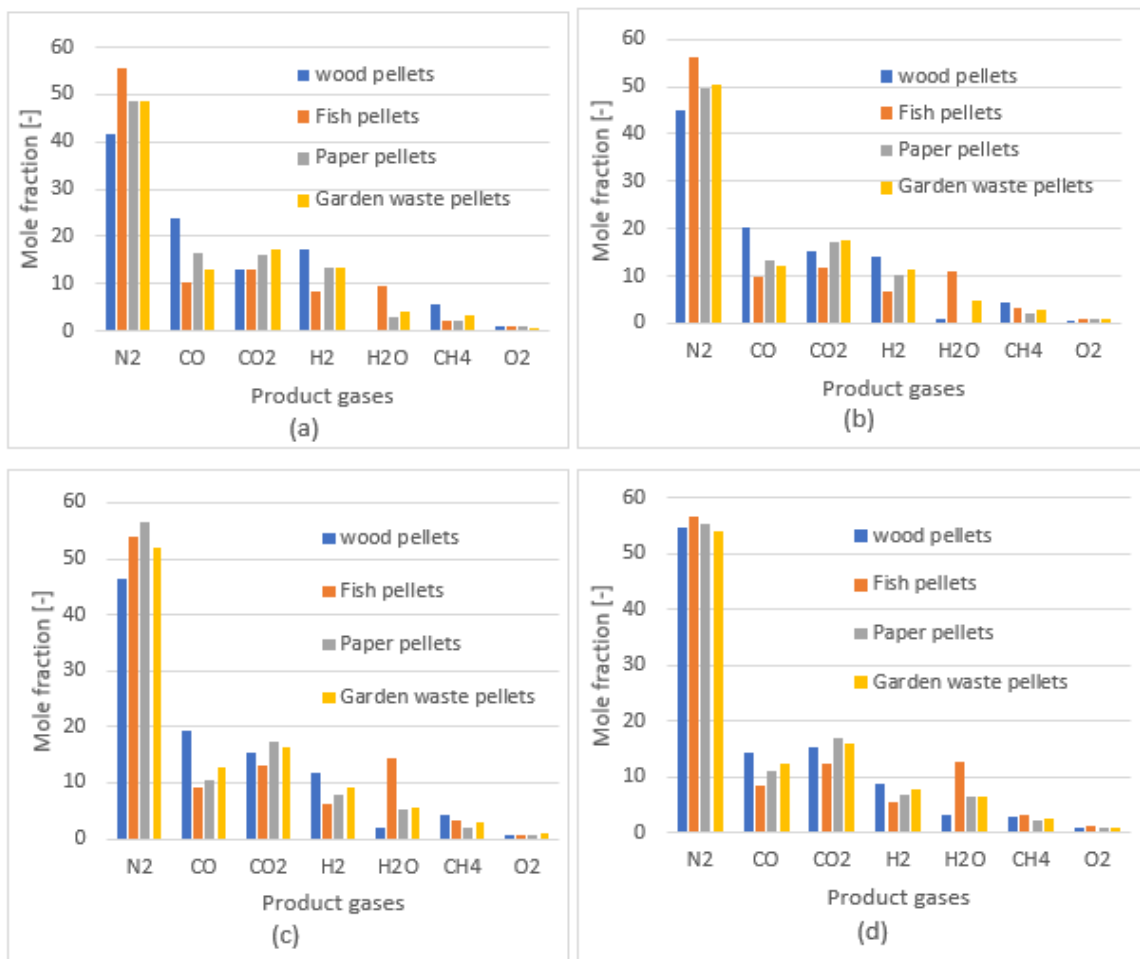
Figure 37 Product gas compositions obtained from gasification of the feedstocks at air flow rate (a) 3kg/h, (b) 4kg/h, (c) 5kg/h and (d) 6kg/h.

The chemical energy decreases with an increasing equivalence ratio due to the oxidation of the fuel gas species as shown in Figure 38. The oxidation process, accompanied by heat evolution, leads to an increase in thermal energy with the supplied oxygen amount. While the relative amount of chemical energy is similar for the different feedstocks, the overall energy efficiency varies significantly. Paper pellets exhibit the highest efficiency, exceeding 80%, while fish pellets are below for 40% across the tested equivalence ratio range. Wood pellets, with the highest relative chemical energy value differing from other feedstocks, contribute to the overall efficiency decreasing with increasing equivalence ratio. Despite wood pellets having the lowest gas yield among plant-based biomasses, the higher energy efficiency compared to garden waste can be attributed to its superior carbon conversion efficiency, resulting in a gas with a high CO content.

(a)   (b)
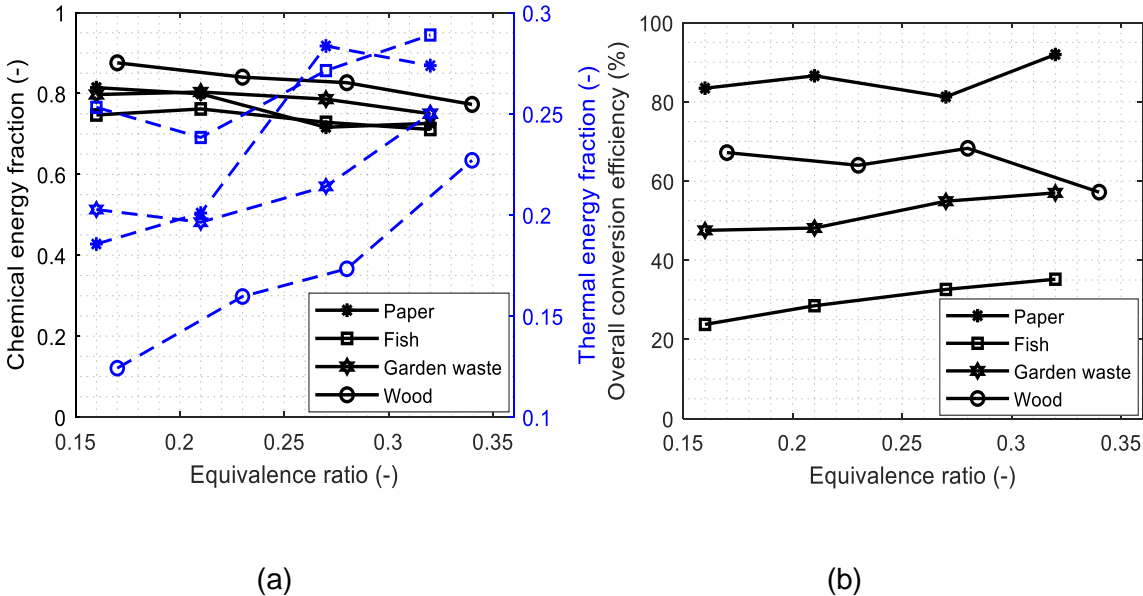
Figure 38: (a) Chemical and thermal energy fraction measured for the feedstocks at different ERs, (b) Overall conversion efficiency of the feedstocks at different ERs.

5.7 Pelletization and Co-pelletization of waste feedstock (coffee wastes, saw dust, and barley straw) for syngas recovery (Unpublished work)

As discussed in the literature section, the food wastes, and agricultural wastes account for about 60 % of the total wastes. Therefore, to test the energy recovery potential of such low-grade feedstocks, coffee grounds and barley straw, were selected. It was necessary to undergo a significant pre-treatment and densification process followed by analytical analysis prior to their utilization. For instance, the initial moisture content of coffee waste was approximately 50-60 wt.%, and the large size barley straw wastes had a moisture content of around 20-25 wt.%. A hammer mill was used to reduce the size of the barley straw to 1-5 mm prior to the pelletization. Similarly, each feedstock was dried, and the moisture content was adjusted to 9-15 wt.%. The pelletization of the pretreated raw wastes was performed as discussed in the Chapter 3. The results illustrated that the pellets produced form the coffee grounds waste were weak and fragile. The pellets lack sufficient strength to be conveyed via screw conveyer to the reactor (as depicted in Figure 39 A). Therefore, to enhance the pellets mechanical strength, 3-5 wt.% of saw dust were added to the coffee grounds. Depending on the initial moisture content, die temperature, and the gap between the roller, the pellets quality was significantly influenced as shown in the Figure 39 (B-D) and Table 7.

With a higher die temperature (>60 ℃), the pellets were formed in the shape similar to smaller tablets (shown in Figure 39 B). Whereas lower die temperature (< 45 ℃), resulted in non-uniform and weak pellets (Figure 39 C). It was found that the die temperature of 50-60 ℃, initial moisture content of 9 wt.% and the gap between the roller and die of 4 mm were optimal operating conditions for the production of uniform shape and enhanced mechanical strength pellets from coffee grounds (illustrated in Figure 39 D). The mechanical durability of the pellets was increased from about 25 % to 75 % due to strong bonding between the molecules of the mixture particles (saw dust and coffee grounds) at mentioned operating conditions. Also, the compression strength of the particles was increased from 0.2 MPa to 0.4 MPa as shown in Figure 40.

Similarly, for the barley straw, the die temperature influenced the quality of the pellets significantly. At lower die temperatures (< 40 ℃), the moisture was trapped in the pores of the pellets forming bulge and swollen structure as depicted in Figure 39 E. For the same initial moisture content and gap between die and roller, the change in die temperature by 10 ℃ resulted in improved pellets properties. As the die temperature was increased, the binding properties of the particles were improved resulting in good quality pellets (with uniform shape and enhanced strength as depicted in Figure 39 F). The mechanical durability and compression strength of the straw pellets at different operating conditions are compared in Figure 40.

Figure 39:Pellets formed at different operating conditions: (A) only coffee grounds pellets, (B) coffee grounds with coffee grounds (94 wt.%), saw dust (3 wt.%), and bark (3 wt.%) at die temperature greater than 60°C, (C) coffee grounds with coffee grounds (94 wt.%), saw dust (3 wt.%), and bark (3 wt.%) at die temperature 30°C-45°C, (D) coffee grounds with coffee grounds (92 wt.%), saw dust (5 wt.%), and bark (3 wt.%) at die temperature 50°C-60°C, (E) straw at die temperature 30°C-45°C, and (F) straw at die temperature 50°C-60°C,
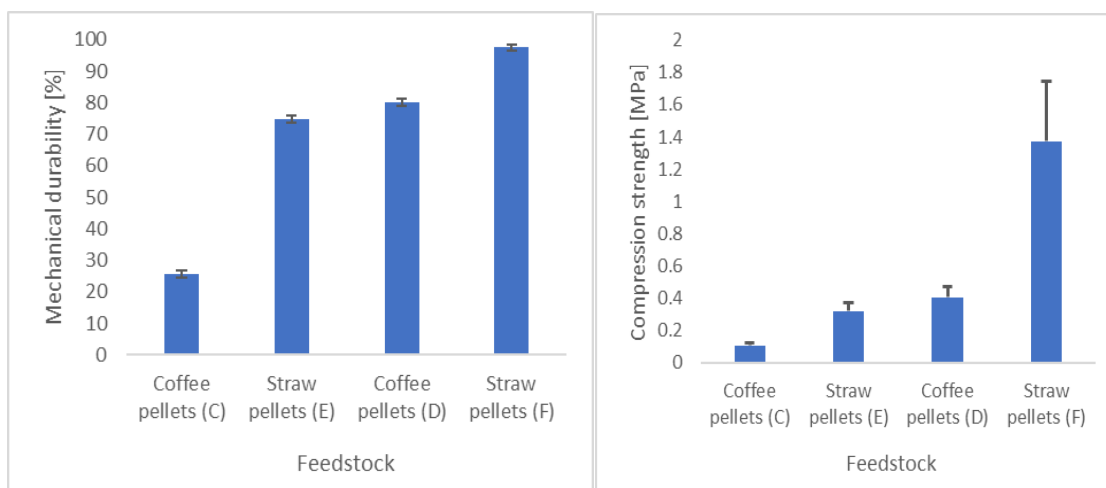
(a)   (b)

Figure 40: (a) Comparison of the mechanical durability and (b) compression strength of the pellets obtained at different operating conditions.

To examine the binding phenomena during pelletization, the samples of the pellets at different operating conditions were analysed using scanning electron microscope (SEM). The results depicted that the mixture of coffee grounds, saw dust and bark pellets produced at the die temperature 50-60 ℃, has strong interparticle bonds. At this die temperature range, the fiber structure of the saw dust melted forming strong bonding forces between the particles (depicted in Figure 41 f) which resulted in the pellets with strong mechanical strength. Die temperature above > 60 ℃ resulted in the fractured structure due to weak bonding between the particles (Shown in Figure 41 e). Similar trend was observed for the straw pellets at die temperature 50-60 ℃ where the fiber structure of the straw melted forming solid bridges. This resulted in greater mechanical durability of the pellets due to strong adhesion, and mechanical interlocking between the particles (illustrated in Figure 41 c).

(a)   (b)   (c)

(d)   (e)   (f)
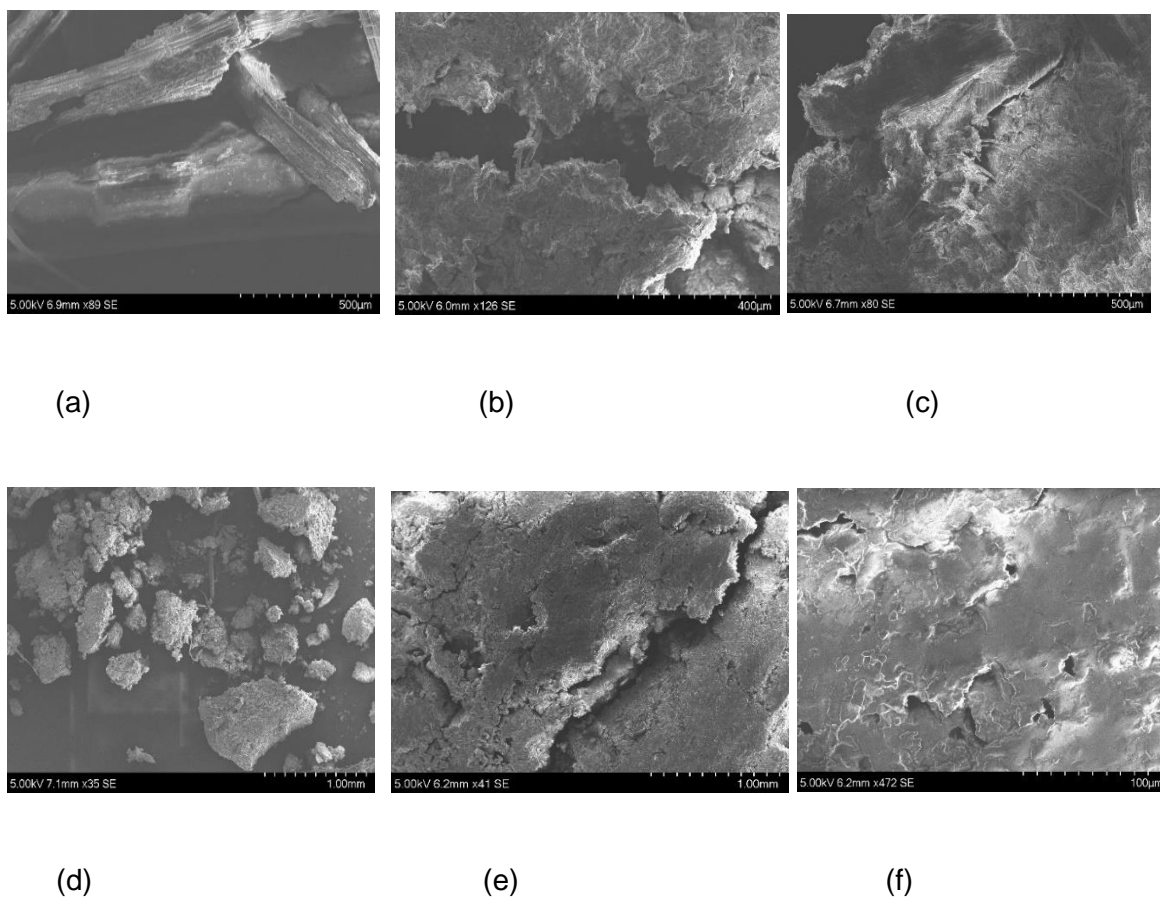
Figure 41: SEM micrographs at different magnification of samples obtained from the (a) raw barley straw, (b) pellets produced from barley straw (E) at die temperature in the range of 30℃-40 ℃, (c) pellets produced from barley straw (F) at die temperature in the range of 50℃-60 ℃, (d) raw coffee grounds, (e) pellets produced from the mixture saw dust, bark and coffee grounds (B) at die temperature > 60 ℃, (f) pellets produced from the mixture saw dust, bark and coffee grounds (D) at die temperature in the range of 50℃-60 ℃.

Table 7:Operating conditions during pelletization of different feedstocks.

	Moisture content,(wt.%)	Die temperature, (℃)	Gap between roller and die, (mm)
Coffee **(A)**	15	30-40	5
Coffee (94 wt.%) + saw dust (3 wt.%) + bark (3 wt. %) **(B)**	12	60>	5
Coffee (94 wt.%) + saw dust (3 wt.%)+ bark (3 wt. %) **(C)**	9	30-45	4
Coffee (92 wt.%) + saw dust (5 wt.%) + bark (3 wt. %) **(D)**	9	50-60	4
Barley straw **(E)**	14	30-40	4
Barley straw **(F)**	14	50-60	4

For the gasification experiments, the reactor temperature was selected by considering the ash melting temperature of the coffee and straw pellets, which helped to avoid ash related challenges in the gasifier. The different stages of the melting phenomenon of the ash obtained from coffee grounds pellets and barley straw pellets were examined using heating microscope. The results illustrated in Figure 44 shows the characteristic temperature profile of the ash melting phenomena measured at different stages by the SEM. The SEM measurements for the feedstocks are summarized in Table 8. The deformation temperature was selected as the upper limit of the bed operating temperature for the gasification experiments.

Table 8: Different characteristics temperature of the coffee grounds and barley straw wastes ash pellets measured by using heating microscope.

Description	ST,[℃]	DT[℃]	HT[℃]	FT[℃]
Coffee pellets	831	927	1350	1400
Straw pellets	835	1040	1150	1180
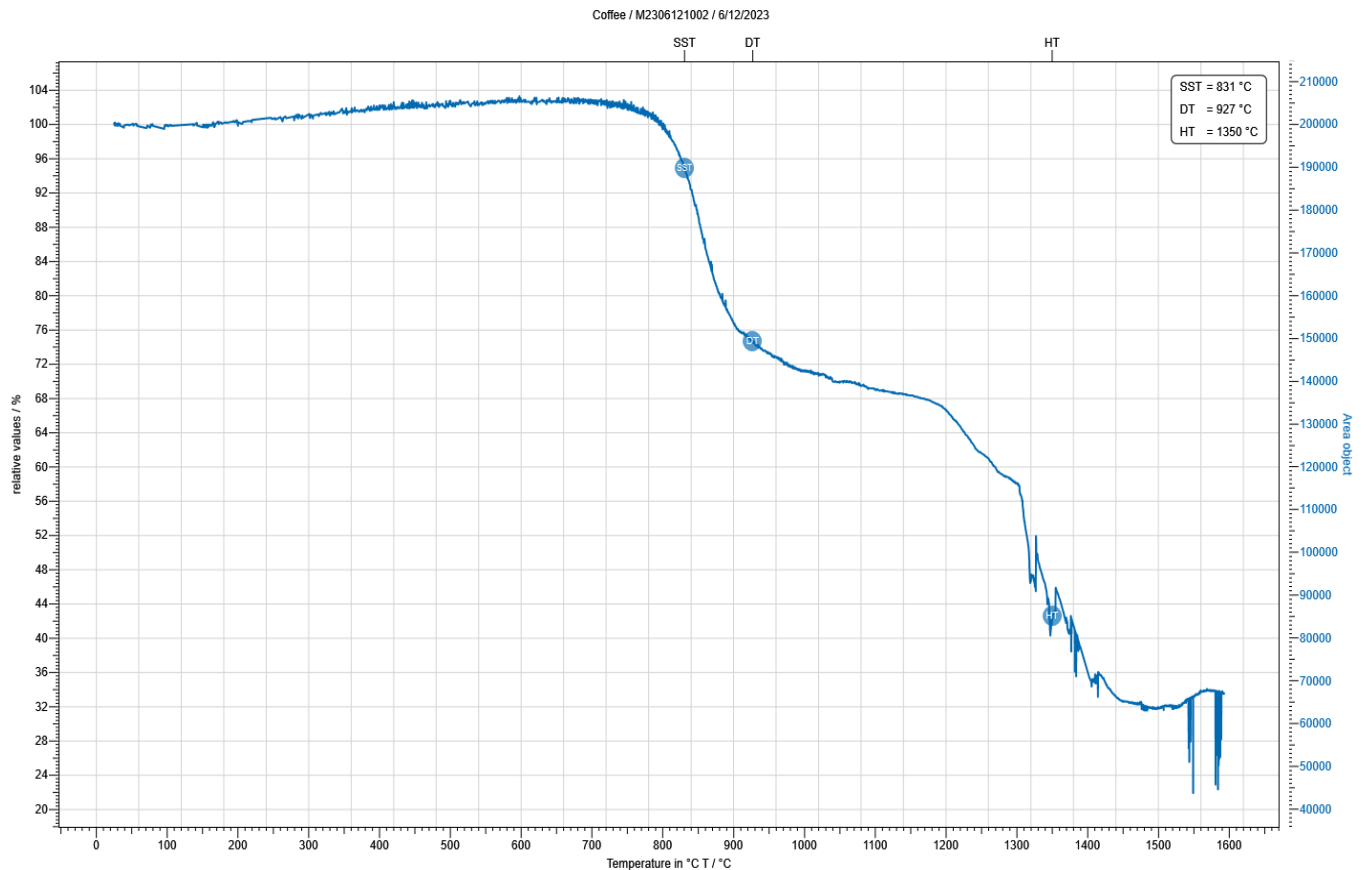
Figure 42: Change in characteristic temperature of the coffee grounds ash pellets measured with time by using heating microscope.

The gasification of the feedstocks, barley straw pellets, mixture of coffee grounds and saw dust and bark pellets were carried with air as the gasifying medium. The reactor performance and syngas production potential are assessed based on the product gas composition, gas yield strength, thermal conversion efficiency, chemical conversion efficiency, and bed fluidizing index at different operating conditions. The results summarized here is the overall conversion efficiency of the reactor measured at different operating conditions (reactor temperature and equivalence ratios). The overall conversion efficiency is assessed as the sum of thermal conversion efficiency and chemical conversion efficiency. The result illustrates that for all the three feedstocks, the overall conversion efficiency was greater than 50 % at all operating conditions. At the reactor operating temperature within the range of 600-700℃ and at lower equivalence ratio of 0.16, the overall efficiency was about 75%, 65 % and 60 % for the feedstock F, C and D respectively. At the reactor operating temperature of 800 ℃ for the same equivalence ratio the overall efficiency decreases by approximately 10 % as depicted in the Figure 43. The decrease in efficiency was due to lower fluidizing index of the bed. At lower equivalence ratio lower density biomass/char particles segregated on the top. With further increase in the reactor temperature at same air flow rates the gases

expanded with the bed vicinity which further decreases the fluidizing index at higher segregation rates. Therefore, most of the conversion took place in the freeboard region resulting in higher H_2O fraction in the syngas thus decreases the overall conversion efficiency. However, when the equivalence ratio was increased above 0.2, the overall conversion efficiency was higher at the reactor operating temperature above 800℃ compared to that of 700℃. The overall conversion efficiency was about 76% and highest with the mixture of coffee and 5 wt.% saw dust compared to the other feedstocks at equivalence ratio of 0.32 and a reactor operating temperature of 800℃.
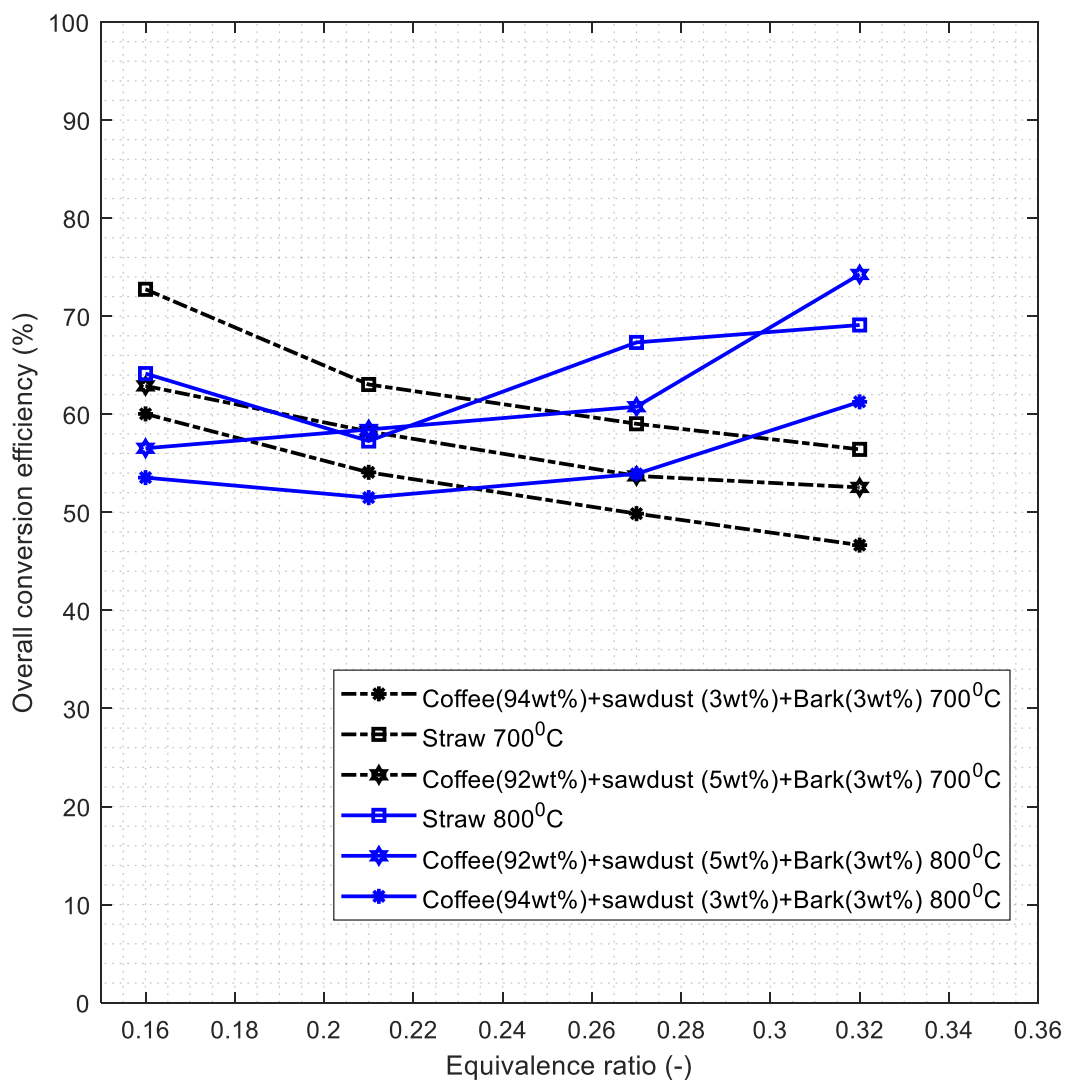
Figure 43:Overall conversion efficiency of the waste feedstocks, coffee grounds, saw dust and bark pellets and barley straw pellets at different operating conditions.

5.8 CPFD model for the prediction air-steam gasification (Article 8)

The product gas yield and quality are not only determined by the feedstock types but are also significantly affected by the type of oxidizing gas used. Air, as a gasifying medium, produces syngas with lower calorific value. In contrast, steam gasification enhances the hydrogen content, increasing calorific value significantly. However, steam gasification is an energy-intensive process that demand significant amount of input energy which increases the operational cost. Alternatively, combining steam and air gasification can be a cost-effective approach to generate hydrogen-rich syngas with lower operational cost. For this, the CPFD model developed was used to simulate gasification of the commercial pellets (wood pellets) under air-steam oxidizing medium. The aim was to obtain the optimal parameters at which the hydrogen-rich syngas can be produced from an auto-thermal gasification of wood pellets using air-steam as the gasifying medium in a bubbling fluidized bed gasifier (Article 9). For an auto-thermal gasification, the reactor must self-sustain the energy demand for the conversion which is again dependent on the equivalence ratio and initial bed temperature. Typically, an equivalence ratio ranging from 0.15 to 0.3 is well-suited for achieving the highest gas yield when air is used as the oxidizing agent in the gasification process. However, this specific equivalence ratio may not be efficient for effective conversion when employing a steam-air mixture as the fluidizing gas. This is because the selected equivalence ratio could lead to decrease in reaction rates due to a drop in bed temperature. Therefore, to find an optimal equivalence ratio, the CPFD model was used to simulate thermal air flow gasification. The optimal equivalence ratio was quantified based on the higher heating value gases, a lower amount of unreacted carbon in the bed, and higher bed temperature suitable for the addition of steam. The change in bed temperature and unconverted carbon fraction with time at equivalence ratio in the range 0.15-0.3 is depicted in Figure 44. The initial bed temperature of 1073 K was selected by accounting the bed sintering temperature and pyrolysis temperature. The result illustrates that at equivalence ratio 0.13, the bed temperature decreased initially due to dominant endothermic reactions followed by the pyrolysis reactions. However, the average bed temperature stabilized later and fluctuated around 1050 K, indicating that the partial char oxidation reaction provided the thermal energy required for the endothermic reactions.

Conversely, elevated average bed temperature was observed at equivalence ratios 0.2, 0.25, and 0.3. The rise in the bed temperature was due to the availability of sufficient oxidizing medium in the reactor that promoted the oxidation reactions releasing heat to the system. Similarly, the fluctuation in the total mass of particles for different equivalence ratios are shown in Figure 44 (b). The bed material mass was constant. Therefore, the change in particle mass is due to variation in conversion rate of supplied biomass at different equivalence ratios. As illustrated in the Figure 44 (b), the total particle mass initially increased during the first 200s and then decreased. The initial increment in the particle mass

was due to char accumulation in the bed with lower conversion rate of the biomass compared to total inlet flow rate of supplied biomass. The maximum accumulation rate of the char particles in the bed was higher at an equivalence ratio of 0.15 and lower at an equivalence ratio of 0.3. Due to higher oxygen availability in bed, the char conversion rate occurred faster at an equivalence ratio of 0.3, resulting in a higher bed temperature. Comparing the product gas composition, the results depict that at the equivalence ratio 0.15, the product gas compositions were enriched with CH4, CO and H_2. This trend was analogous to the result predicted for the grass pellets mentioned in the section 5.1. As the air supply was increased, the product gas was diluted with nitrogen, resulting in lower CH4, CO and H2 fractions and higher CO2 concentration in the product gas. Consequently, for the attainment of superior gas quality using air as the oxidizing medium, a lower equivalence ratio is favoured. However, when utilizing steam-air as the fluidizing gas, it becomes apparent that at the lower equivalence ratio of 0.15, as illustrated in Figure 44 (a), the reactor may not self-sustain the necessary thermal energy required for the conversion. Therefore, when selecting an equivalence ratio for employing air-steam as the fluidizing gas, it is imperative to consider a combination of parameters, including product gas quality, reactor temperature, and the presence of unconverted carbon in the bed.

An equivalence ratio of 0.25 was chosen for steam addition because, under this condition, the reactor operates at a higher temperature, with less char accumulation in the bed, resulting in improved gas quality. At a specified equivalence ratio of 0.25 and an initial bed temperature of 1073K, the introduction of steam was implemented together with air, serving as both the gasifying and fluidizing medium. Air-to-steam ratio ranging from 0.01 to 0.2 was employed, and the effects of this steam addition on the resulting outlet product gas, bed temperature, and char conversion were evaluated. In Figure 45, the optimal steam-to-air ratio (SA) is illustrated, depicting the conditions under which the highest hydrogen yield and the proportion of CO and H2 in the product gas were achieved. When air served as the gasifying medium at an equivalence ratio of 0.25, the hydrogen concentration in the product gas was 11 vol.%. Upon introducing 1 wt.% steam into the air inlet, the H2 fraction in the product gas nearly doubled to 21.5 vol.% as depicted in Figure 45 (a). As the steam-to-air ratio increased, the hydrogen fraction in the product gas also increased, reaching a peak at the steam-to-air ratio of 0.05 wt.%, after which it declined with a further increase in the steam fraction in the gas supply. The initial increase in the hydrogen fraction up to the steam-to-air ratio of 0.05 was attributed to the enhanced water gas shift reaction, steam gasification reaction, and methane reforming reaction (as presented in Table 4). These reactions involved the conversion of CO, CH_4, and carbon, in the presence of added steam, to produce a hydrogen-rich syngas. However, the hydrogen concentration in the product gas subsequently decreased due to the presence of excess unreacted steam in the reactor, as illustrated in Figure 45 a. The excess steam in the reactor led to a reduction in the reactor temperature, resulting in restriction of the water gas shift reaction and thus, lower hydrogen fraction beyond the SA of 0.05.
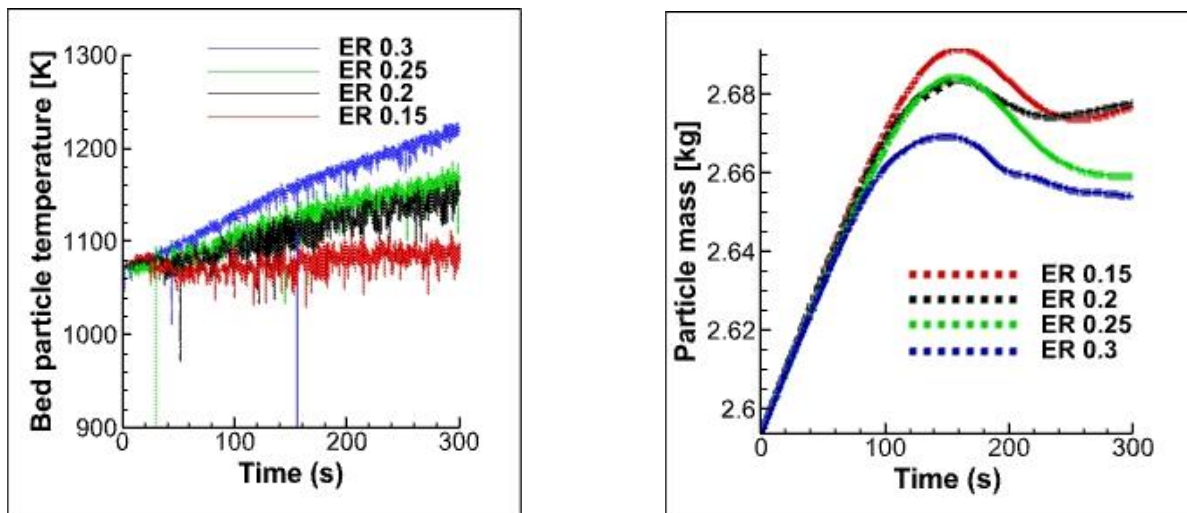
Figure 44: (a) Fluctuation in bed temperature with time at different equivalence ratios, (b) fluctuation of bed mass vs time at different equivalence ratios.

Furthermore, the ratio (γ') between fuel gases (CO and H_2) and (CO_2 and H_2O) are compared in the Figure 45(b). The findings indicate that when utilizing up to 5 wt.% steam in the inlet gas, the CO fraction in the product gas increased together with the H_2 yield, owing to the enhancement of steam and CO2 gasification reactions with char. This resulted in a peak value of $\gamma' \cong 4$. However, γ' decreased with a further increase in the steam concentration in the inlet flow, primarily due to the rise in the unreacted H2O concentration in the product gas. Therefore, for a given equivalence ratio, the amount of steam that can facilitate efficient conversion depends on both the bed temperature and the quantity of unreacted carbon particles in the bed. The bed temperature must be maintained at a level sufficient to support both homogeneous and heterogeneous reactions, while the amount of unconverted carbon in the bed should be in proportion (below 10 wt. %) to ensure that the fluid dynamics remain unimpeded. A high char load on the bed can lead to a transition from the bubbling regime to slugging or defluidization, thus impeding the conversion process. As illustrated in Figure 45 (d), the bed temperature began to decline significantly at an SA ratio of 0.2 with an increase in the mass of unconverted carbon in the bed. Simultaneously, the CO2 fraction slightly decreased at an SA ratio of 0.2, and the H2O fraction increased tenfold as the SA ratio was raised from 0.05 to 0.2. The decreased bed temperature, reduced CO2 fraction, and increased carbon content in the bed indicate slower oxidation reactions at an SA ratio of 0.2. In contrast, at a steam-air ratio of 0.05, the bed temperature was self-sustained at the required thermal input (as depicted in Figure 45 d), resulting in an improved gas yield, with lower char accumulation in the bed (refer to Figure 45c).
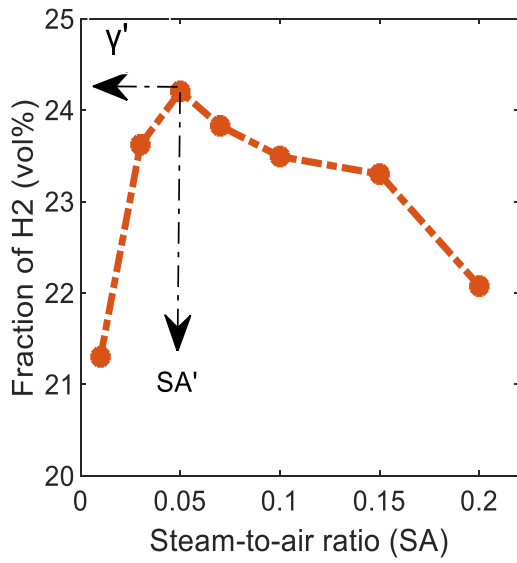
(a)
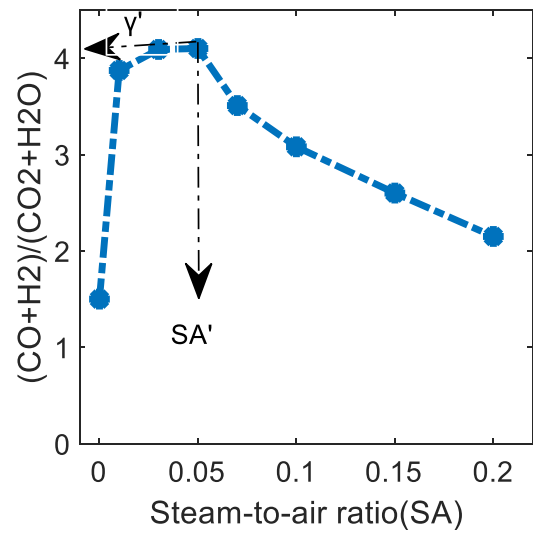
(b)
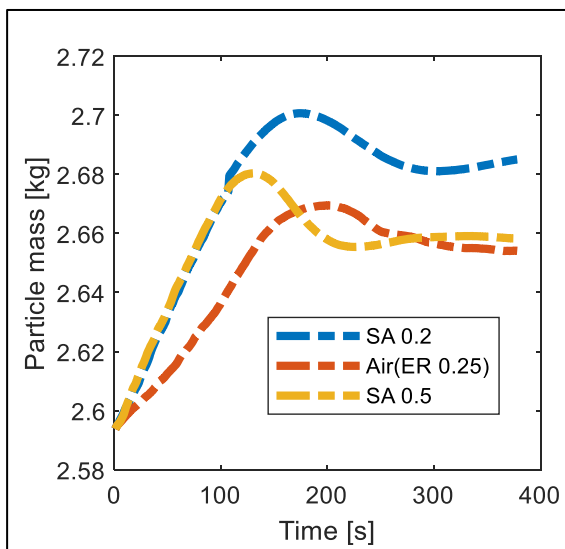
(c)
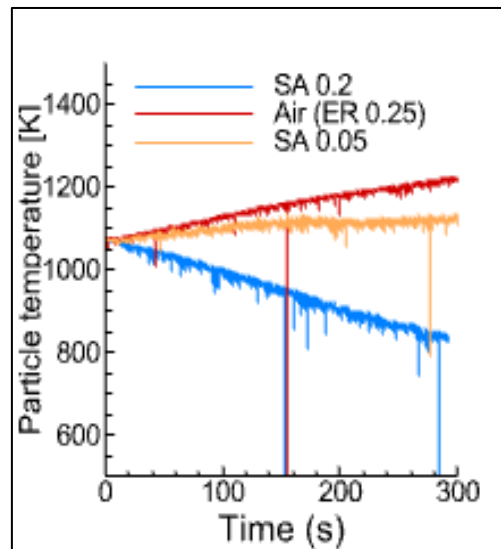
(d)

Figure 45: (a) Change in hydrogen fraction in the product gas outlet at different steam-to-air ratios, (b) optimal steam-to-air ratio for higher quality gas yield, (c)change in particle mass vs time at different steam to air ratios and (d) fluctuation in the particle temperature at different steam to air ratios.

6 Discussion of the results and contributions

As discussed in chapter 1, the main objective of this work is to investigate the gasification of waste feedstocks in a BFB reactor. The contribution of this work is to operate a BFB gasifier at optimal conditions with a wide category of waste feedstock to obtain higher quality syngas. Therefore, the result of this work is inclined towards addressing the problems encountered during utilizations of waste in a BFB reactor and can be categorized under experimental findings and CPFD simulation results. The experimental works include densification of waste feedstocks into mechanically durable pellets and gasification of waste feedstocks for syngas recovery at optimal reactor operating conditions. Similarly, simulation work contributes to identify optimal operating parameters and overcome challenges associated with the experimental measurements.

Air gasification at an equivalence ratio above 0.2 is a common practice. However, utilizing higher ERs, particularly in air gasification, possesses disadvantages as it dilutes the product gas with nitrogen. With the goal to minimize excess air supply beyond what is necessary for pure gasification, different ERs below 0.2 was tested in an allothermal operation mode. The minimum ER was defined as the airflow required to convert all the char without any accumulation in the reactor bed. Two commercial feedstocks, wood pellets and grass pellets, were gasified at temperatures from 650℃ to 800℃ and compared with a low-grade feedstock wood chips. From this study the minimum equivalence ratio and the reactor temperature required to get about 75 % carbon conversion efficiency was obtained. Similarly, the study identified challenges such as agglomeration conditions in the bed, lower carbon conversion, non-uniformity in the reactor temperature, discontinuous feeding of the biomass due to blockage in the screw. The investigation also identified challenges, including agglomeration conditions in the bed, lower carbon conversion, and non-uniformity in reactor temperature. While this study was valuable for selecting parameters for running the gasifier in an allothermal mode, allothermal gasification processes are mostly suitable for lab scale. To implement allothermal gasification on an industrial scale is costly. Therefore, the next approach was to run the gasifier in an autothermal mode by utilizing a wide variety of feedstocks. For this, different low-grade feedstocks such as fish pellets (animal waste origin), garden wastes (plant wastes) and paper pellets (MSW) were selected, and the syngas and heat generation potential were assessed in an autothermal gasification mode. The feedstock varied in size, density, moisture, and ash content. The influence of these properties in the fluidizing index of the bed were accessed together with the gas yield strength, chemical conversion efficiency and thermal conversion efficiency. To address the issue related to discontinuous feeding of the feedstock, an appropriate screw feeding system with proper screw thread and diameter suitable for each feedstock type was used.

Other contributions of this work include densification of low grade waste feedstocks such as coffee grounds, barley straw, saw dust and bark in the pellets form without any binders or chemicals. The lab scale pelletizer was used to identify optimal parameters such as die temperature, moisture content of the raw feed and distance between die and roller for producing mechanical durable pellets with higher compression strength. Similarly, the mixture of these feedstocks were utilized for co-pelletization, and the influence on the properties of the pellets were assessed by analytic methods. Also, the influence of the co-pelletization of the wastes on the syngas quality were identified.

During the series of gasification tests, some uncertainties such as lower gas residence time, slug in the bed, improper air/gas distribution, unconverted carbon, sudden fluctuation in the reactor temperature, segregation etc. were identified. To overcome such challenges, which were difficult to encounter experimentally, CPFD simulations were used which were used. For instance, the CPFD model was developed to investigate the air supply methods which include supply of air through uniform air distribution, and side nozzles. The influence of the air supply methods on the bed dynamics and the air distribution in the bed were investigated. Similarly, two different modes of biomass injection methods i.e., on the top of the bed or in the bed were studied. The influence of biomass injection on the temperature distribution, biomass segregation, unconverted carbon and product gas yield was investigated. The bubble dynamics in the BFB plays critical role in the heat transfer, mixing and segregation, contact between gas and solid phase thus, govern the temperature distribution of the reactor and affect the overall conversion efficiency. This study focuses on bubbling fluidized bed gasifier. Therefore, special attain has been given to investigate the influence of the bubble properties on the fluid dynamics and thermal behaviour of the gasifier. A simple mathematical model has been proposed based on the superficial gas velocity and bubble diameter to set operational parameters for high-quality gas yield and higher gas residence time during biomass gasification.

Using steam as a gasifying medium is a promising method to enhance hydrogen yield in the product gas. However, steam gasification is an endothermic process that demand high energy input. Therefore, a method has been proposed based on the CPFD simulations to use mixtures of air and steam as the gasifying medium and run the reactor in an autothermal mode for higher hydrogen yield in the product gas. The overview of the major findings and problems or challenges encountered for energy recovery from wastes in a BFB reactor are depicted in Figure 46.
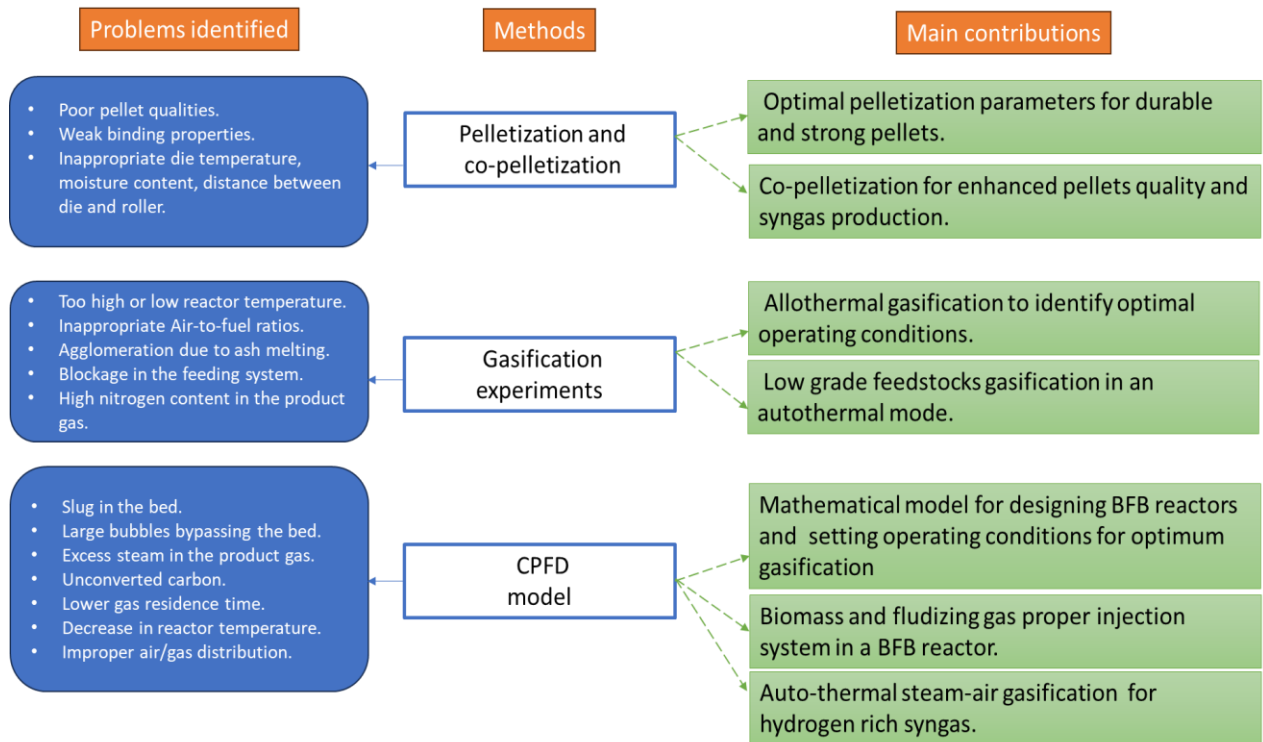
Figure 46:Schematic representation of the main findings of this work, and experimental and simulation work employed to identify the problems/challenges encountered during gasification of the waste feedstocks in a BFB gasifier and pelletization of raw feedstocks and their mixture using a lab scale pelletizer.

7 Conclusion and recommendations

The aim of this work was to use waste feedstocks and their mixtures as fuel in a bubbling fluidized bed gasifier and operate the reactor at optimal conditions for a high-quality product gas. The task has been accomplished using a combination of experimental work and CPFD simulations. For the experimental work, three different BFB reactors were employed to gain better understanding of the fluid dynamic behaviour coupled with thermochemical conversion phenomena in a BFB. The fluidized bed setup used in this work includes: (i) a cold flow BFB reactor equipped with pressure sensors, (ii) a cold flow BFB reactor equipped with ECT sensors and (iii) a 20 kW BFB gasifier. The cold flow model of the fluidized bed reactor was employed to investigate the fluid dynamic behaviour of the bed containing bed material, char and biomass, bubble dynamics, mixing and segregation, and fluidization regime. The results from the cold flow model were used to select the operating parameters, such as gas velocity, particle diameter, and static bed height for the gasification experiments. Air was used as the gasifying medium for the gasification experiments on a 20 kW BFB gasifier operated in both autothermal and allothermal modes with waste feedstocks.

Different waste feedstocks from various sources, such as MSW, agricultural, garden, and industrial waste, were used as fuel for the gasifier. All the waste feedstocks, paper, fish, garden residue, sawdust, coffee grounds, barley straw, bark, and grass were used in the pellet form except for wood chips. Among these feedstocks, barley straw, sawdust, bark and coffee grounds were pelletized using a lab-scale pellet mill, KAHL pelleting press 14-175. The results illustrated that the pellet quality was significantly influenced by the die temperature, initial moisture content of the feedstock, and the distance between roller and die. Optimal conditions for the pelletization of coffee grounds and barley straw were observed at the die temperature ranging from 50℃ to 60℃, a moisture content between 9% and 14% by weight, and a roller-to-die distance of 4 mm. These conditions resulted in the production of mechanically durable pellets with enhanced compression strength.

Allothermal air-gasification of the feedstocks, wood chips, grass pellets, and wood pellets was carried out at ERs < 0.16 to reduce nitrogen concentration in the product gas. The results demonstrated that wood chips could obtain about 75% carbon conversion efficiency at ER 0.16 and at reactor temperature 800℃. On the other hand, the grass pellets formed agglomerates at a reactor temperature of 800℃. ER, of 0.15 at temperature 800ºC for wood pellets, delivered the best overall performance with a 70% carbon conversion. These tests with commercial feedstocks, wood and grass pellets, and a low-grade feedstock (wood chips) allowed to identify challenges, including agglomeration conditions in the bed, lower carbon conversion, non-uniformity in the reactor temperature and blockage in the feeding system. Subsequently, adjustments were made in selecting operational parameters to minimize the mentioned challenges and run the reactor in an auto-thermal mode.

For the auto-thermal gasification tests, an initial bed temperature of 650℃ was selected by considering the ash sintering and pyrolysis temperatures of the feedstocks. The low-grade feedstocks, fish pellets (animal waste origin), garden wastes (plant wastes), and paper pellets (MSW) were gasified over an equivalence ratio of 0.15-0.35, and the syngas and heat generation potential were assessed. The result showed that the overall conversion efficiency (chemical and thermal conversion efficiency) of paper pellets reached approximately 80-90%, garden waste exhibited a conversion efficiency of 50-60%, and fish pellets demonstrated a lower range of 22-40%. The diminished conversion efficiency of fish pellets was ascribed to

the animal-based origin of the feedstock, containing fats and proteins, necessitating higher temperatures for degradation. Notably, despite the high moisture content of paper pellets (26 wt.%), the results indicated a higher conversion efficiency. This suggested that the moisture content had little to no influence on the conversion process when the feedstock was injected on the top of the bed.

Similarly, the waste feedstocks, coffee, and barley straw were gasified over the equivalence ratio of 0.15-0.32 at two different reactor temperatures, 700 ℃ $\pm$ 25 ℃. and 800℃ ± 25 ℃ in an allothermal mode. The result illustrated that at 800℃ ± 25℃ reactor temperature, the conversion efficiency increased by approximately 10% when the equivalence ratio was increased from 0.15 to 0.32. On the other hand, at reactor temperature 700℃ ± 25 ℃ the opposite trend was observed. The maximum conversion efficiency of the coffee grounds and straw reached up to 76%, which showed both the wastes as potential feedstock for energy recovery when compared to the commercial wood pellets over the same gasification conditions. In addition, the result demonstrated that the conversion efficiency of the pellets improved with the enhancement in mechanical durability and compression strength. Through a comprehensive series of experimental tests, challenges within a BFB gasifier, including issues such as slugs or large bubbles bypassing the bed, excess steam in the product gas, unconverted carbon, reduced gas residence time, and inadequate distribution of gas and biomass in the bed, were identified. Computational Particle Fluid Dynamics (CPFD) simulations were utilized to address these complexities, providing a valuable tool for investigating challenges that would have been challenging to address through experimental means.

The CPFD simulations were carried out using the commercial software Barracuda VR 21.1.1. In a BFB gasifier, the challenges above are significantly influenced by the bubble properties in the bed. Therefore, the dynamical and thermal properties of the bubbles were investigated using the CPFD simulations and experimental measurements. The CPFD model was validated with the experimental data obtained from the ECT measurements and gasification experiments. The result revealed that smaller bubble sizes with high bubble frequency appeared in the hot gasifying bed compared to cold bed conditions. Increasing the gas flow rate at a constant air-fuel ratio increased the bubble diameter and amount of unconverted char particles with different degrees of reactions across the bed, reducing the gas residence time and lowering the biomass conversion efficiency. A simple correlation was proposed based on bubble diameter and superficial gas velocity, which can be used to design a BFB gasifier and set operational parameters to achieve optimum gasification.

The CPFD model was also used to simulate air-steam gasification to enhance the syngas quality and assess the possibility of running the reactor in an autothermal mode with air-steam. First, the equivalence ratio at which the reactor temperature could self-sustain the required heat for steam addition was obtained. The results illustrated at ER 0.25 and initial bed temperature of 1073 K, the reactor maintained a higher temperature with less char accumulation; thus, ER 0.25 was selected for steam addition with a steam-to-air ratio ranging from 0.1 to 0.2. The result revealed that the hydrogen fraction in the product gas was approximately double when 1 wt.% steam was added to the inlet gas. However, with a steam-to-air ratio exceeding 0.05 wt.%, the product gas quality declined with unreacted water vapour. This study was performed at one initial bed temperature. However, for an autothermal operation, the initial bed temperature significantly influences the reactor temperature during conversion for a continuous process. Therefore, other initial bed temperatures should be investigated to find the optimal steam-to-air ratio, and the result should be validated experimentally.

Similarly, the CPFD simulations were used to assess the influence of biomass feeding position in a BFB gasifier. Two feeding positions were selected: on the top of the bed and in the bed near to the bottom of the reactor. The result revealed that in-bed feeding of the biomass was more effective with respect to the product gas quality, reactor temperature uniformity, and amount of unreacted carbon in the bed. This study needs to be further investigated with a wide distribution of bed material and biomass with varied density, size, and moisture content.

Further, simulations were carried out to investigate the influence on the fluidization patterns of the bubbling bed with different modes of air supply: (i) uniform air distribution (with air distributor), (ii) with side nozzles, and (iii) multiple injection points. The result demonstrated that air can be injected in the fluidized bed with the side nozzles while maintaining similar fluid dynamics properties of the bed compared to air distributor as flow boundary conditions. Thus, side nozzles as flow boundary conditions can be employed to minimize the cost and avoid operational challenges related to the presence of air distributor in the gasifier. However, additional attempts should be made to investigate the flow dynamics behaviour with side nozzles as airflow boundary conditions in the bed containing the biomass and bed materials mixture at hotbed conditions as this study was conducted at ambient conditions.

Finally, the following extended experimental works are suggested for further research to utilize waste in a BFB reactor and run the reactor in an auto-thermal mode:

- Experiments with catalyst or olivine particles as the bed material could help to run the reactor in an auto-thermal mode at lower bed temperatures.
- Experiments to find optimal steam-to-air ratios for autothermal gasification of several waste feedstocks.

8 References

[1]   A. Maalouf and A. Mavropoulos, "Re-assessing global municipal solid waste generation," *Waste Management and Research*, vol. 41, no. 4, 2023, doi: 10.1177/0734242X221074116.

[2]   S. Kaza, L. C. Yao, P. Bhada-Tata, and F. Van Woerden, *What a Waste 2.0: A Global Snapshot of Solid Waste Management to 2050*. 2018. doi: 10.1596/978-1-4648-1329-0.

[3]   EPA (GHGRP Sector Profile), "2011-2020 Greenhouse Gas Reporting Program Sector Profile: Waste Sector."

[4]   S. Mor and K. Ravindra, "Municipal solid waste landfills in lower- and middle-income countries: Environmental impacts, challenges and sustainable management practices," *Process Safety and Environmental Protection*, vol. 174. 2023. doi: 10.1016/j.psep.2023.04.014.

[5]   X. Wang, Y. Lu, C. Chen, X. Yi, and H. Cui, "Total-factor energy efficiency of ten major global energy-consuming countries," *J Environ Sci (China)*, vol. 137, 2024, doi: 10.1016/j.jes.2023.02.031.

[6]   T. Rasheed *et al.*, "Valorisation and emerging perspective of biomass based waste-to-energy technologies and their socio-environmental impact: A review," *J Environ Manage*, vol. 287, 2021, doi: 10.1016/j.jenvman.2021.112257.

[7]   N. Ferronato and V. Torretta, "Waste mismanagement in developing countries: A review of global issues," *International Journal of Environmental Research and Public Health*, vol. 16, no. 6. 2019. doi: 10.3390/ijerph16061060.

[8]   J. T. Powell, M. R. Chertow, and D. C. Esty, "Where is global waste management heading? An analysis of solid waste sector commitments from nationally-determined contributions," *Waste Management*, vol. 80, 2018, doi: 10.1016/j.wasman.2018.09.008.

[9]   Z. Zhang, M. Z. Malik, A. Khan, N. Ali, S. Malik, and M. Bilal, "Environmental impacts of hazardous waste, and management strategies to reconcile circular economy and eco-sustainability," *Science of the Total Environment*, vol. 807. 2022. doi: 10.1016/j.scitotenv.2021.150856.

[10]   L. Lombardi, E. Carnevale, and A. Corti, "A review of technologies and performances of thermal treatment systems for energy recovery from waste," *Waste Management*, vol. 37, 2015, doi: 10.1016/j.wasman.2014.11.010.

[11]   S. Heidenreich and P. U. Foscolo, "New concepts in biomass gasification," *Prog Energy Combust Sci*, vol. 46, pp. 72–95, Feb. 2015, doi: 10.1016/J.PECS.2014.06.002.

[12]   T. Wongsiriamnuay and N. Tippayawong, "Effect of densification parameters on the properties of maize residue pellets," *Biosyst Eng*, vol. 139, 2015, doi: 10.1016/j.biosystemseng.2015.08.009.

[13]   A. Gómez-Barea and B. Leckner, "Modeling of biomass gasification in fluidized bed," *Prog Energy Combust Sci*, vol. 36, no. 4, pp. 444–509, Aug. 2010, doi: 10.1016/J.PECS.2009.12.002.

[14]   X. Wu, J. Peng, Y. Zhang, and Z. Wang, "Elutriation characteristics of multi-component mixtures in a fluidized bed pyrolysis process," *Particuology*, vol. 58, 2021, doi: 10.1016/j.partic.2021.01.018.

[15]   K. J. Timmer, "Carbon conversion during bubbling fluidized bed gasification of biomass," 2008.

[16]   N. C. I. S. Furuvik, L. Wang, R. Jaiswal, R. Thapa, M. S. Eikeland, and B. M. E. Moldestad, "Experimental study and SEM-EDS analysis of agglomerates from gasification of biomass in fluidized beds," *Energy*, vol. 252, p. 124034, Aug. 2022, doi: 10.1016/J.ENERGY.2022.124034.

[17]   C. E. Agu, L. A. Tokheim, M. Eikeland, and B. M. E. Moldestad, "Determination of onset of bubbling and slugging in a fluidized bed using a dual-plane electrical capacitance tomography system," *Chemical Engineering Journal*, vol. 328, 2017, doi: 10.1016/j.cej.2017.07.098.

[18]   S. K. Awasthi *et al.*, "Processing of municipal solid waste resources for a circular economy in China: An overview," *Fuel*, vol. 317, 2022, doi: 10.1016/j.fuel.2022.123478.

[19]   The Economist, "Global waste generation will nearly double by 2050," 2018. doi: https://www.economist.com/graphic-detail/2018/10/02/global-waste-generation-will-nearly-double-by-2050.

[20]   J. Aleluia and P. Ferrão, "Characterization of urban waste management practices in developing Asian countries: A new analytical framework based on waste characteristics and urban dimension," *Waste Management*, vol. 58, 2016, doi: 10.1016/j.wasman.2016.05.008.

[21]   A. Kumar, E. Singh, R. Mishra, and S. Kumar, "Solid Waste to Energy: Existing Scenario in Developing and Developed Countries," in *Handbook of Solid Waste Management: Sustainability through Circular Economy*, 2022. doi: 10.1007/978-981-16-4230-2_84.

[22]   X. gang Zhao, G. wu Jiang, A. Li, and L. Wang, "Economic analysis of waste-to-energy industry in China," *Waste Management*, vol. 48, 2016, doi: 10.1016/j.wasman.2015.10.014.

[23]   X. Peng *et al.*, "Recycling municipal, agricultural and industrial waste into energy, fertilizers, food and construction materials, and economic feasibility: a review," *Environmental Chemistry Letters*, vol. 21, no. 2. 2023. doi: 10.1007/s10311-022-01551-5.

[24]   A. Kumar and S. R. Samadder, "A review on technological options of waste to energy for effective management of municipal solid waste," *Waste Management*, vol. 69. 2017. doi: 10.1016/j.wasman.2017.08.046.

[25]   Z. Wang and L. Geng, "Carbon emissions calculation from municipal solid waste and the influencing factors analysis in China," *J Clean Prod*, vol. 104, 2015, doi: 10.1016/j.jclepro.2015.05.062.

[26]   A. Emery, A. Davies, A. Griffiths, and K. Williams, "Environmental and economic modelling: A case study of municipal solid waste management scenarios in Wales," *Resour Conserv Recycl*, vol. 49, no. 3, 2007, doi: 10.1016/j.resconrec.2006.03.016.

[27]   F. Cherubini, N. D. Bird, A. Cowie, G. Jungmeier, B. Schlamadinger, and S. Woess-Gallasch, "Energy- and greenhouse gas-based LCA of biofuel and bioenergy systems: Key issues, ranges and recommendations," *Resour Conserv Recycl*, vol. 53, no. 8, 2009, doi: 10.1016/j.resconrec.2009.03.013.

[28]   P. R. PRASHANTHI, "Environmental and Health Risk Assessment for Municipal Solid Waste Dump-Yard in Chidambaram," *Int J Adv Sci Eng Technol*, vol. 6, no. 1, 2018.

[29]   A. K. Biswas, S. Kumar, S. S. Babu, J. K. Bhattacharyya, and T. Chakrabarti, "Studies on environmental quality in and around municipal solid waste dumpsite," *Resour Conserv Recycl*, vol. 55, no. 2, 2010, doi: 10.1016/j.resconrec.2010.08.003.

[30]   G. T. Müller, A. Giacobbo, E. A. dos Santos Chiaramonte, M. A. S. Rodrigues, A. Meneguzzi, and A. M. Bernardes, "The effect of sanitary landfill leachate aging on the biological treatment and assessment of photoelectrooxidation as a pre-treatment process," *Waste Management*, vol. 36, 2015, doi: 10.1016/j.wasman.2014.10.024.

[31]   N. Scarlat, F. Fahl, and J. F. Dallemand, "Status and Opportunities for Energy Recovery from Municipal Solid Waste in Europe," *Waste Biomass Valorization*, vol. 10, no. 9, 2019, doi: 10.1007/s12649-018-0297-7.

[32]   FCM, "Solid Waste as a Resource ." doi: https://data.fcm.ca/documents/tools/GMF/Solid_Waste_as_a_Resource_Review_of_Waste_Technologies_EN.pdf.

[33]   K. C. Surendra, D. Takara, A. G. Hashimoto, and S. K. Khanal, "Biogas as a sustainable energy source for developing countries: Opportunities and challenges," *Renewable and Sustainable Energy Reviews*, vol. 31. 2014. doi: 10.1016/j.rser.2013.12.015.

[34]   B. Bharathiraja, T. Sudharsana, J. Jayamuthunagai, R. Praveenkumar, S. Chozhavendhan, and J. Iyyappan, "Retraction notice to 'Biogas production -A review on composition, fuel properties, feed stock and principles of anaerobic digestion' (Renewable and Sustainable Energy Reviews (2018) 90 (570–582), (S1364032118301904) (10.1016/j.rser.2018.03.093))," *Renewable and Sustainable Energy Reviews*, vol. 94. 2018. doi: 10.1016/j.rser.2018.08.010.

[35]   B. Bharathiraja, T. Sudharsana, J. Jayamuthunagai, R. Praveenkumar, S. Chozhavendhan, and J. Iyyappan, "Biogas production – A review on composition, fuel

properties, feed stock and principles of anaerobic digestion," *Renewable and Sustainable Energy Reviews*, vol. 90. 2018. doi: 10.1016/j.rser.2018.03.093.

[36] H. D. Beyene, A. A. Werkneh, and T. G. Ambaye, "Current updates on waste to energy (WtE) technologies: a review," *Renewable Energy Focus*, vol. 24. 2018. doi: 10.1016/j.ref.2017.11.001.

[37] R. Kothari, V. V. Tyagi, and A. Pathak, "Waste-to-energy: A way from renewable energy sources to sustainable development," *Renewable and Sustainable Energy Reviews*, vol. 14, no. 9. 2010. doi: 10.1016/j.rser.2010.05.005.

[38] C. S. Goh *et al.*, "Wood pellet market and trade: A global perspective," *Biofuels, Bioproducts and Biorefining*, vol. 7, no. 1, 2013, doi: 10.1002/bbb.1366.

[39] R. Sikkema, M. Steiner, M. Junginger, W. Hiegl, M. T. Hansen, and A. Faaij, "The European wood pellet markets: Current status and prospects for 2020," *Biofuels, Bioproducts and Biorefining*, vol. 5, no. 3, 2011, doi: 10.1002/bbb.277.

[40] Z. Afailal, N. Gil-Lalaguna, I. Fonts, A. Gonzalo, J. Arauzo, and J. Luis Sánchez, "Thermochemical valorization of argan nutshells: Torrefaction and air–steam gasification," *Fuel*, vol. 332, 2023, doi: 10.1016/j.fuel.2022.125970.

[41] F. J. C. Pirotta, E. C. Ferreira, and C. A. Bernardo, "Energy recovery and impact on land use of Maltese municipal solid waste incineration," *Energy*, vol. 49, no. 1. 2013. doi: 10.1016/j.energy.2012.10.049.

[42] M. Karim and B. Corazzini, "The current status of MSW disposal and energy production: a brief review of waste incineration ," *MOJ Ecology & Environmental Sciences*, vol. 4, no. 1, 2019, doi: 10.15406/mojes.2019.04.00129.

[43] M. Novotný *et al.*, "The use of biochar made from biomass and biosolids as a substrate for green infrastructure: A review," *Sustain Chem Pharm*, vol. 32, 2023, doi: 10.1016/j.scp.2023.100999.

[44] J. A. Ippolito *et al.*, "Feedstock choice, pyrolysis temperature and type influence biochar characteristics: a comprehensive meta-data analysis review," *Biochar*, vol. 2, no. 4. 2020. doi: 10.1007/s42773-020-00067-x.

[45] V. Belgiorno, G. De Feo, C. Della Rocca, and R. M. A. Napoli, "Energy from gasification of solid wastes," *Waste Management*, vol. 23, no. 1, 2003, doi: 10.1016/S0956-053X(02)00149-6.

[46] J. Lee, K. Y. A. Lin, S. Jung, and E. E. Kwon, "Hybrid renewable energy systems involving thermochemical conversion process for waste-to-energy strategy," *Chemical Engineering Journal*, vol. 452. 2023. doi: 10.1016/j.cej.2022.139218.

[47] P. Sharma, B. Gupta, M. Pandey, K. Singh Bisen, and P. Baredar, "Downdraft biomass gasification: A review on concepts, designs analysis, modelling and recent advances," *Mater Today Proc*, vol. 46, pp. 5333–5341, Jan. 2021, doi: 10.1016/J.MATPR.2020.08.789.

[48] T. M. Ismail and M. A. El-Salam, "Parametric studies on biomass gasification process on updraft gasifier high temperature air gasification," *Appl Therm Eng*, vol. 112, 2017, doi: 10.1016/j.applthermaleng.2016.10.026.

[49] J. C. Bandara, R. Jaiswal, H. K. Nielsen, B. M. E. Moldestad, and M. S. Eikeland, "Air gasification of wood chips, wood pellets and grass pellets in a bubbling fluidized bed reactor," *Energy*, vol. 233, p. 121149, Oct. 2021, doi: 10.1016/J.ENERGY.2021.121149.

[50] E. Shayan, V. Zare, and I. Mirzaee, "Hydrogen production from biomass gasification; a theoretical comparison of using different gasification agents," *Energy Convers Manag*, vol. 159, 2018, doi: 10.1016/j.enconman.2017.12.096.

[51] S. J. Suryawanshi, V. C. Shewale, R. S. Thakare, and R. B. Yarasu, "Parametric study of different biomass feedstocks used for gasification process of gasifier—a literature review," *Biomass Conversion and Biorefinery*, vol. 13, no. 9. 2023. doi: 10.1007/s13399-021-01805-2.

[52] J. Corella, J. M. Toledo, and G. Molina, "A Review on Dual Fluidized-Bed Biomass Gasifiers," *Industrial & Engineering Chemistry Research*, vol. 46, no. 21, pp. 6831–6839, Sep. 2007, doi: 10.1021/ie0705507.

[53] J. Ren, J. P. Cao, X. Y. Zhao, F. L. Yang, and X. Y. Wei, "Recent advances in syngas production from biomass catalytic gasification: A critical review on reactors, catalysts, catalytic mechanisms and mathematical models," *Renewable and Sustainable Energy Reviews*, vol. 116. 2019. doi: 10.1016/j.rser.2019.109426.

[54]   NATIONAL ENERGY TECHNOLOGY LABORATORY, "Commercial Gasifiers."

[55]   N. Said, M. M. Abdel Daiem, A. García-Maraver, and M. Zamorano, "Influence of densification parameters on quality properties of rice straw pellets," *Fuel Processing Technology*, vol. 138, 2015, doi: 10.1016/j.fuproc.2015.05.011.

[56]   E. T. Kostas, D. Beneroso, and J. P. Robinson, "The application of microwave heating in bioenergy: A review on the microwave pre-treatment and upgrading technologies for biomass," *Renewable and Sustainable Energy Reviews*, vol. 77. 2017. doi: 10.1016/j.rser.2017.03.135.

[57]   T. O. Olugbade and O. T. Ojo, "Biomass Torrefaction for the Production of High-Grade Solid Biofuels: a Review," *Bioenergy Research*, vol. 13, no. 4. 2020. doi: 10.1007/s12155-020-10138-3.

[58]   J. S. Tumuluru, C. T. Wright, K. L. Kenney, and J. R. Hess, "A technical review on biomass processing: Densification, preprocessing, modeling and optimization," in *American Society of Agricultural and Biological Engineers Annual International Meeting 2010, ASABE 2010*, 2010. doi: 10.13031/2013.29874.

[59]   T. Wang *et al.*, "Effect of molasses binder on the pelletization of food waste hydrochar for enhanced biofuel pellets production," *Sustain Chem Pharm*, vol. 14, 2019, doi: 10.1016/j.scp.2019.100183.

[60]   J. S. Song, S. H. Lim, M. Y. Jung, and K. H. Kim, "A study on the pelletization of powdered radioactive waste by roll compaction," *Journal of Nuclear Fuel Cycle and Waste Technology*, vol. 17, no. 2, 2019, doi: 10.7733/jnfcwt.2019.17.2.203.

[61]   H. Li *et al.*, "Co-pelletization of sewage sludge and biomass: The energy input and properties of pellets," *Fuel Processing Technology*, vol. 132, 2015, doi: 10.1016/j.fuproc.2014.12.020.

[62]   M. Iqbal, A. Nadeem, and M. Butt, "Refused derived fuel pellets from municipal solid waste and rice husk," *Bangladesh Journal of Scientific and Industrial Research*, vol. 54, no. 4, 2019, doi: 10.3329/bjsir.v54i4.44567.

[63]   I. Obernberger and G. Thek, "Physical characterisation and chemical composition of densified biomass fuels with regard to their combustion behaviour," *Biomass Bioenergy*, vol. 27, no. 6, 2004, doi: 10.1016/j.biombioe.2003.07.006.

[64]   P. Pradhan, S. M. Mahajani, and A. Arora, "Pilot scale production of fuel pellets from waste biomass leaves: Effect of milling size on pelletization process and pellet quality," *Fuel*, vol. 285, 2021, doi: 10.1016/j.fuel.2020.119145.

[65]   S. V. Kanageswari, L. G. Tabil, and S. Sokhansanj, "Dust and Particulate Matter Generated during Handling and Pelletization of Herbaceous Biomass: A Review," *Energies*, vol. 15, no. 7. 2022. doi: 10.3390/en15072634.

[66]   M. Rivera-Tenorio and R. Moya, "Potential for pellet manufacturing with wood waste from construction in Costa Rica," *Waste Management and Research*, vol. 38, no. 8, 2020, doi: 10.1177/0734242X19893022.

[67]   W. Stelte, A. R. Sanadi, L. Shang, J. K. Holm, J. Ahrenfeldt, and U. B. Henriksen, "Recent developments in biomass pelletization - a review," *Bioresources*, vol. 7, no. 3, 2012, doi: 10.15376/biores.7.3.stelte.

[68]   J. K. Holm, U. B. Henriksen, J. E. Hustad, and L. H. Sørensen, "Toward an understanding of controlling parameters in softwood and hardwood pellets production," *Energy and Fuels*, vol. 20, no. 6, 2006, doi: 10.1021/ef0503360.

[69]   W. Stelte, J. K. Holm, A. R. Sanadi, S. Barsberg, J. Ahrenfeldt, and U. B. Henriksen, "Fuel pellets from biomass: The importance of the pelletizing pressure and its dependency on the processing conditions," *Fuel*, vol. 90, no. 11, 2011, doi: 10.1016/j.fuel.2011.05.011.

[70]   M. Arshadi, R. Gref, P. Geladi, S. A. Dahlqvist, and T. Lestander, "The influence of raw material characteristics on the industrial pelletizing process and pellet quality," *Fuel Processing Technology*, vol. 89, no. 12, 2008, doi: 10.1016/j.fuproc.2008.07.001.

[71]   C. Rhén, R. Gref, M. Sjöström, and I. Wästerlund, "Effects of raw material moisture content, densification pressure and temperature on some properties of Norway spruce pellets," *Fuel Processing Technology*, vol. 87, no. 1, 2005, doi: 10.1016/j.fuproc.2005.03.003.

[72]   A. E. Atabani *et al.*, "Emerging potential of spent coffee ground valorization for fuel pellet production in a biorefinery," *Environ Dev Sustain*, vol. 25, no. 8, 2023, doi: 10.1007/s10668-022-02361-z.

[73]   A. Palma *et al.*, "Experimental Study of the Combustion of and Emissions from Olive and Citrus Pellets in a Small Boiler," *Fire*, vol. 6, no. 8, 2023, doi: 10.3390/fire6080288.

[74]   S. Nasiri, A. Hajinezhad, M. H. Kianmehr, and S. Tajik, "Enhancing municipal solid waste efficiency through Refuse Derived Fuel pellets: Additive analysis, die retention time, and temperature impact," *Energy Reports*, vol. 10, 2023, doi: 10.1016/j.egyr.2023.07.039.

[75]   T. Miranda, I. Montero, F. J. Sepúlveda, J. I. Arranz, C. V. Rojas, and S. Nogales, "A review of pellets from different sources," *Materials*, vol. 8, no. 4, 2015, doi: 10.3390/ma8041413.

[76]   M. Ge, H. Zhou, A. Vaidheeswaran, W. Rogers, D. Fan, and C. Li, "Multi-scale experimental investigation on the fluidization of Geldart B 13X zeolite particles: A comprehensive dataset for CFD validation," *Chemical Engineering Journal*, vol. 471, 2023, doi: 10.1016/j.cej.2023.144724.

[77]   Y. Zhou, T. Wang, and J. Zhu, "Investigation on minimum fluidization velocity in a modified Geldart's diagram," *Chemical Engineering Journal*, vol. 453. 2023. doi: 10.1016/j.cej.2022.139984.

[78]   D. Kunii and O. Levenspiel, *Fluidization Engineering*, Second. 1991.

[79]   D. Gidaspow, *Gidaspow D. Multiphase Flow and Fluidization: Continuum and Kinetics Theory Descriptions*. Academic Press Inc.,San Diego, California, USA, 1994.

[80]   C. Emeka Agu, B. M. E. Moldestad, and C. Pfeifer, "Assessment of Combustion and Gasification Behavior in a Bubbling Fluidized Bed Reactor: A Comparison between Biomass with and without Chemical Additives," *Energy & Fuels*, vol. 34, no. 8, pp. 9654–9663, Jul. 2020, doi: 10.1021/acs.energyfuels.0c01408.

[81]   C. E. Agu, L. A. Tokheim, C. Pfeifer, and B. M. E. Moldestad, "Behaviour of biomass particles in a bubbling fluidized bed: A comparison between wood pellets and wood chips," *Chemical Engineering Journal*, vol. 363, pp. 84–98, May 2019, doi: 10.1016/J.CEJ.2019.01.120.

[82]   S. Mori and C. Y. Wen, "Estimation of bubble diameter in gaseous fluidized beds," *AIChE Journal*, vol. 21, no. 1, 1975, doi: 10.1002/aic.690210114.

[83] C. E. Agu, L. A. Tokheim, M. Eikeland, and B. M. E. Moldestad, "Improved models for predicting bubble velocity, bubble frequency and bed expansion in a bubbling fluidized bed," *Chemical Engineering Research and Design*, vol. 141, pp. 361–371, Jan. 2019, doi: 10.1016/J.CHERD.2018.11.002.

[84] J. Davidson, *Fluidized particles, in Mobile Particulate Systems.* Springer, 1995.

[85] P. M. Lv, Z. H. Xiong, J. Chang, C. Z. Wu, Y. Chen, and J. X. Zhu, "An experimental study on biomass air-steam gasification in a fluidized bed," *Bioresour Technol*, vol. 95, no. 1, 2004, doi: 10.1016/j.biortech.2004.02.003.

[86] W. C. R. Chan, M. Kelbon, and B. B. Krieger, "Modelling and experimental verification of physical and chemical processes during pyrolysis of a large biomass particle," *Fuel*, vol. 64, no. 11, 1985, doi: 10.1016/0016-2361(85)90364-3.

[87] R. Timsina *et al.*, "Experimental evaluation of wood and grass pellets in a bubbling fluidized bed gasifier," *Energy Reports*, vol. 9, 2023, doi: 10.1016/j.egyr.2023.03.041.

[88] P. Basu, "Gasification Theory and Modeling of Gasifiers," *Biomass Gasification Design Handbook*, pp. 117–165, Jan. 2010, doi: 10.1016/B978-0-12-374988-8.00005-2.

[89] P. Lettieri and L. Mazzei, "Challenges and issues on the CFD modeling of fluidized beds: A review," *Journal of Computational Multiphase Flows*, vol. 1, no. 2, 2009, doi: 10.1260/175748209789563937.

[90] D. Gidaspow, *Multiphase Flow and Fluidization: Continuum and Kinetic Theory Descriptions*. 2012. doi: 10.1016/C2009-0-21244-X.

[91] A. Acosta-Iborra, C. Sobrino, F. Hernández-Jiménez, and M. de Vega, "Experimental and computational study on the bubble behavior in a 3-D fluidized bed," *Chem Eng Sci*, vol. 66, no. 15, pp. 3499–3512, Aug. 2011, doi: 10.1016/J.CES.2011.04.009.

[92] N. G. Deen, M. Van Sint Annaland, M. A. Van der Hoef, and J. A. M. Kuipers, "Review of discrete particle modeling of fluidized beds," *Chem Eng Sci*, vol. 62, no. 1–2, pp. 28–44, Jan. 2007, doi: 10.1016/J.CES.2006.08.014.

[93]   J. Wang, M. A. Van Der Hoef, and J. A. M. Kuipers, "Comparison of two-fluid and discrete particle modeling of dense gas-particle flows in gas-fluidized beds," *Chem Ing Tech*, vol. 85, no. 3, 2013, doi: 10.1002/cite.201200101.

[94]   D. M. Snider, S. M. Clark, and P. J. O'Rourke, "Eulerian-Lagrangian method for three-dimensional thermal reacting flow with application to coal gasifiers," *Chem Eng Sci*, vol. 66, no. 6, 2011, doi: 10.1016/j.ces.2010.12.042.

[95]   S. Kraft, F. Kirnbauer, and H. Hofbauer, "CPFD simulations of an industrial-sized dual fluidized bed steam gasification system of biomass with 8 MW fuel input," *Appl Energy*, vol. 190, 2017, doi: 10.1016/j.apenergy.2016.12.113.

[96]   L. Riva *et al.*, "Analysis of optimal temperature, pressure and binder quantity for the production of biocarbon pellet to be used as a substitute for coke," *Appl Energy*, vol. 256, 2019, doi: 10.1016/j.apenergy.2019.113933.

[97]   R. Jaiswal, C. E. Agu, R. K. Thapa, and B. M. E. Moldestad, "Study of fluidized bed regimes using Computational Particle Fluid Dynamics," in *Proceedings of The 59th Conference on imulation and Modelling (SIMS 59), 26-28 September 2018, Oslo Metropolitan University, Norway*, 2018. doi: 10.3384/ecp18153271.

[98]   P. J. O'Rourke and D. M. Snider, "Inclusion of collisional return-to-isotropy in the MP-PIC method," *Chem Eng Sci*, vol. 80, 2012, doi: 10.1016/j.ces.2012.05.047.

[99]   M. J. Andrews and P. J. O'Rourke, "The multiphase particle-in-cell (MP-PIC) method for dense particulate flows," *International Journal of Multiphase Flow*, vol. 22, no. 2, pp. 379–402, Apr. 1996, doi: 10.1016/0301-9322(95)00072-0.

[100]   D. M. Snider, "An Incompressible Three-Dimensional Multiphase Particle-in-Cell Model for Dense Particle Flows," *J Comput Phys*, vol. 170, no. 2, 2001, doi: 10.1006/jcph.2001.6747.

[101]   D. M. Snider, "Three fundamental granular flow experiments and CPFD predictions," *Powder Technol*, vol. 176, no. 1, 2007, doi: 10.1016/j.powtec.2007.01.032.

[102]   J. M. Weber, K. J. Layfield, D. T. Van Essendelft, and J. S. Mei, "Fluid bed characterization using electrical capacitance volume tomography (ECVT), compared to CPFD software's barracuda," *Powder Technol*, vol. 250, 2013, doi: 10.1016/j.powtec.2013.10.005.

[103] L.-S. Fan and C. Zhu, *Principles of Gas-Solid Flows*. 1998. doi: 10.1017/cbo9780511530142.

[104] W.-C. Yang, "Handbook of fluidization and fluid-particle systems," *China Particuology*, vol. 1, no. 3, 2003, doi: 10.1016/s1672-2515(07)60126-2.

Part 2
Scientific papers

Paper 1

Study of agricultural waste gasification in an air-blown bubbling fluidized bed using a CPFD model

Study of agricultural waste gasification in an air-blown bubbling fluidized bed using a CPFD model

Rajan Jaiswal   Rajan K. Thapa   Britt M. E. Moldestad

Department of Process, Energy and Environmental Technology, University of South-Eastern Norway, Norway,
{rajan.jaiswal rajan.k.thapa, britt.moldestad}@usn.no

Abstract

Gasification using a fluidized bed is a promising technology to convert agricultural residues into product gases. In this work, the syngas production potential from agricultural waste (grass pellets) is studied using a Computational Fluid Dynamic (CPFD) model. The CPFD model is developed in a simulation software Barracuda virtual reactor and validated against the experimental data. Experiments are carried out in a 20 kW bubbling fluidized bed gasification reactor that operates with air as fluidizing gas. Grass pellets of size 5mm-30 mm in length and diameter of 5mm are used as the feed.

The CPFD model considers the hydrodynamics of the gas-solid phase and reaction kinetics involved. Influence of the static bed height, bed temperature, and air to fuel ratio on the product gas composition ($CH_4, CO, CO_2, and\ H_2$) and char conversion efficiency are investigated. Initial bed heights of 200 mm and 300 mm are used for the analysis. Biomass is fed at 2.46 kg/hr while the air supplied is varied to obtain the air to fuel ratio at 0.4, 0.6, 0.8, 1, and 1.2. The result shows that the increase in bed height has a significant effect on the reactor temperature but very small effect on the product gas composition and char conversion rate. An increase in bed temperature from 600℃ to 800℃ improves the gasifier performance in terms of maximum product gases yield and enhanced char conversion rate. Increase in the air to fuel ratio from 0.4-1.2 reduces the $CH_4, CO,\ and\ H_2$ fractions in the product gas and increases the CO_2 concentration. The results obtained from the CPFD model are in good agreement with the experimental results and literature data. Thus, the CPFD model developed in this work can be utilized to optimize the gasification reactor used in a lab and industrial scale.

Keywords: grass pellets, gasification, bubbling-fluidized bed, CPFD

1   Introduction

With the world's growing population, increase in solid wastes from households, agriculture and industries are inevitable. Strict laws and regulations are set up in the EU regions and other countries like USA and Japan to reuse and recycle the municipal solid waste (MSW). Despite such strict measures three quarters of the MSW are still incinerated or landfilled. Converting such wastes into energy not only preserves the landfill space, but also facilitates the increasing energy demand. Thermochemical conversion technologies such as pyrolysis, combustion, and gasification enable efficient conversion of solid wastes to different energy forms such as heat and electricity. Gasification of solid wastes has several potential benefits over combustion specifically in terms of operating conditions and various reactor types suited for specific purposes. In the gasification process, the solid wastes are partially oxidized with limited amount of oxygen or steam that prevents combustion. The conversion of solid waste to product gases in a gasification process occurs in complex thermochemical routes. The first step is drying and devolatilization. The solid fuels are converted into volatile gases, char, and tar after pyrolysis and then the char is gasified with a gasifying agent (air or steam) at temperatures in the range of 600-900℃. The process can be autothermal or allothermal, depending on the gasifying agent and the type of reactors. When using air as a gasifying medium, the process is driven auto-thermally. The heat required for the chemical conversion of the fuel is supplied by partial oxidation reactions. The exothermic reactions are absent when steam is used as the gasifying agent, and thus an external heat source is needed. The advantages of using steam as gasifying medium is that a synthesis gas with a higher heating value ($15 - 20\ MJ/Nm^3$) is produced. When using air, the caloric value of the synthesis gas is in the range of $4 - 8\ MJ/Nm^3$. The advantage of using air as fluidizing gas is that it is cheaper, and some gas turbines available in the market enable to use lower calorific value syngas to produce electricity.

The main gas components obtained from the gasification process are methane, hydrogen, carbon monoxide and carbon dioxide. The product gases can be useful for producing biofuels and chemicals or can be used to operate gas turbines and reciprocating engines. Gasification using fluidized bed has been considered as an flexible technology that can use a wide range of fuels. Fluidized beds provide major advantages such as uniform mixing and heat transfer (Jaiswal, 2018; Jaiswal, 2019), which enables efficient conversion of carbonaceous solid into product gases. The feedstock to the gasifier has to be cheaper and more flexible in order to make the process economically sustainable. Thus,

utilizing wastes from forest, agriculture and household as feed reduces the overall costs. Over the past few years, industrial companies and researchers around the world have assessed the benefits of converting solid waste into energy and valuable chemical products. Many researches have focused on investigating different parameters that influence the product gas composition and the gasifier efficiency.

Arena *et al.* performed gasification tests with different types of waste-derived fuel in a pilot scale bubbling fluidized bed using air as the gasifying agent and olivine and quartz sand as the bed material. The authors reported that gasification of polyolefin plastic wastes increases the hydrogen concentration by (20-30%) in the syngas. In a similar study with solid recovered fuel (SRF), the authors concluded that the SRF could be gasified to obtain a syngas of valuable quality for energy applications (Arena *et al., 2010).*

Xiao *et al.* studied gasification of polypropylene plastic waste in a fluidized bed gasifier of diameter 100 mm and a height of 4.2 m. The authors studied the effect of equivalence ratio, bed height and fluidization velocity on the product yield distribution, gas compositions, and gas-heating value. They found that polypropylene with air as the gasifying agent, can produce a fuel gas with a calorific value in the range of 5.2-11.4 MJ/Nm³. (Xiao *et al.*, 2007)

Alvarez *et al.* studied hydrogen production from gasification of a mixture of plastic and wood sawdust using steam. Adding 20% of polyethylene to the biomass (sawdust), they found that the gas yield and the hydrogen concentration increased due to the synergetic effects between increased gas components. (Alvarez *et al.*, 2014)

Predicting performance of the fluidized bed gasifier with a simulation model is of great importance for optimum design of the reactor to achieve maximum efficiency. The CFD model can provide detail knowledge about the operational parameters to be selected. Several researches have been conducted in the fluidized bed gasification using simulation tools (Niu, 2013; Erkiaga, 2014; Shen, 2008; Chen, 2016). However, most of the studies available in literature, either lack experimental validation of the simulation model or the model does not account for the particle size distribution of the bed material and fuel particles. Particle size distribution is an important parameter that largely influences the heat and mass transfer within the bed (Grace, 1991; Beetstra, 2009) thus affect reactor performance.

In this work, a Computational Particle Fluid Dynamic (CPFD) software Barracuda VR is used. It is a commercial simulation software specially designed for the particle-fluid system. Unlike other CFD software, it is possible to define computational particles similar to the experiments with a size distribution in Barracuda. Many studies have been devoted to gain more insight into the gasification of biomass in the past using Barracuda VR (Jaiswal, 2020; Bandara, 2020; Thapa, 2016). However, limited researches are available in the field of gasification of solid wastes using a CPFD tool. In this work, the syngas production potential from agricultural waste (grass pellets) is studied using a CPFD model. The CPFD model is validated against experimental data. The CPFD model considers the hydrodynamics of the gas-solid phase and reaction kinetics involved. The influence of the static bed height, the bed temperature and the air to fuel ratio on the product gases $(CH_4, CO, CO_2, and\ H_2)$ and char conversion efficiency are investigated.

2 Experiment

The experimental set up used in this work consists of a 20kW reactor made up of stainless steel. The reactor is 1 m in height and the internal diameter is 0.1 m. Three electrical heaters are mounted on the reactor wall and heat up the reactor during operation. An air preheater is used to heat the compressed air (fluidizing gas) before it is passed into the reactor. Thermocouples and pressure sensors are placed at different heights to measure the temperature and pressure variation during the operation of the reactor. The schematic diagram of the reactor is shown in Figure 1. The biomass feedstock is supplied into the reactor by the means of two screw conveyors. A cold screw conveyer transports the biomass from the silo to the hot screw conveyer at a specified rate. The hot screw conveyor runs continuously and injects biomass into the reactor. The bed material is added to the reactor with a funnel type opening (2) attached to the wall of the reactor. A sampling line is attached at the outlet of the reactor. The gas samples are collected at certain intervals, and are analyzed in an offline gas chromatography (GC). The GC uses helium and nitrogen as the carrier gas. The hydrogen concentration is measured using nitrogen as the carrier gas, while methane, carbon monoxide, and carbon dioxide and nitrogen concentration are measured using helium as the carrier gas.

Experiments were carried out using grass pellets of 5 mm diameter and 5-30 mm in length. Sand is used as the bed material and air as the fluidizing gas.
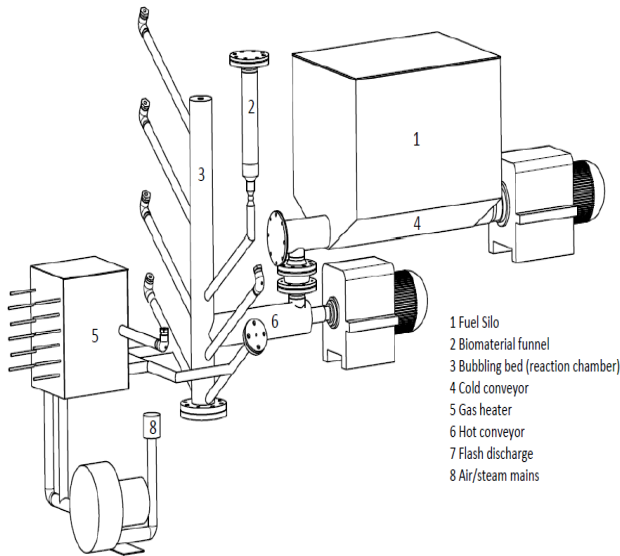
Figure 1. Experimental setup.

3 Result and Discussion

3.1 CPFD model

The developed CPFD model uses three-dimensional multiphase particle-in-cell approach for the CFD simulation of gas-particle flows. The chemistry module available in Barracuda enables to define the reactions and reaction rates involved in the gasification process. Therefore, the CPFD model simulates the thermal and chemical kinetics at the particle level providing more realistic modeling compared to other simulation software. The chemical reactions and corresponding rate kinetics used in the CPFD model are listed in Table 1.
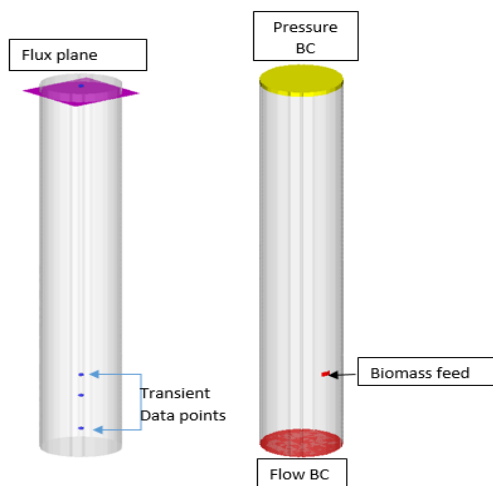

Figure 2. Transient data points, flux plane, flow and pressure boundary conditions and feed position (From left)

A CAD geometry in STL format, drawn in SolidWorks was imported, and total cells of 7128 were created using the default grid setting available in Barracuda. The properties of fuel particles (grass pellets), bed material (sand), and fluidizing gas (air) are

defined as that of the experimental data. The pressure and flow boundary conditions (of air and fuel particles), transient data points, and the flux plan defined in the CPFD model are shown in Figure 2. Grass pellets (the fuel particles) of sizes 5-30cm in length and 5mm in diameter are used. It has a bulk density of 743 $kg/m3$ and a lower heating value of 16.7 MJ/kg. Sand particles of density 2600 $kg/m3$ and mean diameter $345\mu m$ are used as the bed material. For the simulations, the drag model proposed by Wen Yu is used. The drag model of the particle calculates the force acting on the particle by the flow of fluid around it. The simulated product gas compositions are compared with the experimental data for validation of the model. The comparison is shown in Figure 3. The result shows that the model can predict the product gas compositions close to the experimental data.

Table 1. Chemical reactions and reaction rate (Xie, 2016; Bates, 2017; Soli, 2016).

| *Chemical reactions*	*Kinetics*
Char partial combustion R1:$2C + O_2 \leftrightarrow 2CO$	r = 4.34×10^{10} m$_s\theta_f$ exp$\left(\frac{-13590}{T}\right)$[O$_2$]
CO oxidation R2:$CO + 0.5O_2 \leftrightarrow CO_2$	r = 5.62×10^{12} exp$\left(\frac{-16000}{T}\right)$[CO][O$_2$]$^{0.5}$
H$_2$ oxidation R3:$H_2 + 0.5O_2 \leftrightarrow H_2O$	r = 5.69×10^{11} exp$\left(\frac{-17610}{T}\right)$[H$_2$][O$_2$]$^{0.5}$
CH$_4$ oxidation R4:$CH_4 + 2O_2 \leftrightarrow CO_2 + 2H_2O$	r = 5.0118×10^{11} T^{-1} exp$\left(\frac{-24357}{T}\right)$[CH$_4$][O$_2$]
Water gas shift reaction R5:$CO + H_2O \leftrightarrow CO_2 + H_2$	r = 7.68×10^{10} T exp$\left(\frac{-36640}{T}\right)$[CO]$^{0.5}$[H$_2$O]
Methane reforming R6:$CH_4 + H_2O \leftrightarrow CO + 3H_2$	r=3.00×105exp$\left(\frac{-15042}{T}\right)$[CH$_4$][H$_2$O]
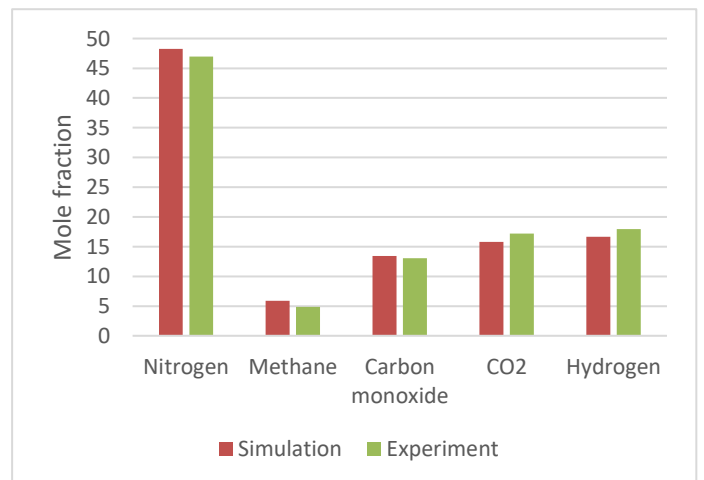
Figure 3. Product gas compositions obtained from the CPFD model and experiments (model validation).

3.2 Effect of static bed height

Change in static bed height in a bubbling fluidized bed gasifier effects the bed hydrodynamic behavior (Jaiswal, 2018), the residence time of the fuel particles and the temperature of the bed. In this section, influence of the static bed height on the product gas composition and the reactor performance are discussed.

Figure 4 shows the product gas composition at static bed height of 300 mm and 200 mm. For both the cases, the air to fuel (A/F) is 0.6 and the reactor is operated at 700°C. The result shows that with increase in bed height from 200 mm to 300 mm at the same operating conditions the methane, carbon monoxide and hydrogen concentration in the product gas increases while the carbon dioxide concentration remains the same. The total heat content of the system increased with increased bed height. When the grass pellets are injected into the reactor at fluidizing conditions, the fuel particles first sink downwards in the bed and then tends to move upward due to densities differences (Jaiswal, 2019; Agu, 2019). The increase in bed height allows the fuel particles to interact with the heated bed material and the fluidizing gas for a longer time when the contact area is increased. Thus, the residence time of the fuel particles is increased, which favored the breakdown of heavy hydrocarbons, tar and char when exposed to high temperature. A similar trend is found in the experimental work performed by (Xiao *et al.*, 2007). They tested three initial bed heights and confirmed that for an equivalence ratio maximum gas yield is obtained at a specific bed height.
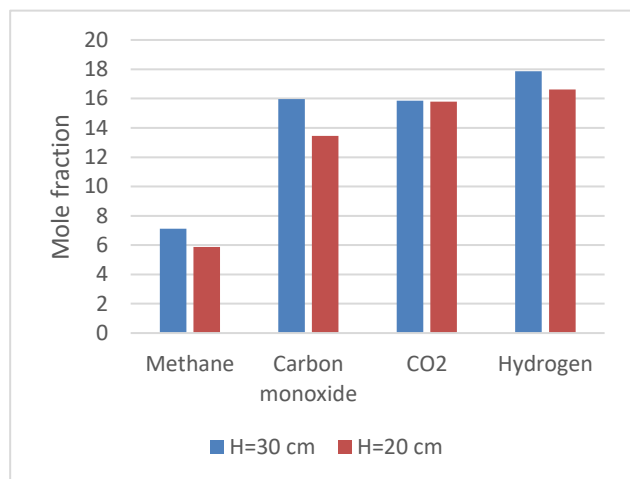
Figure 4. Change in the product gas composition with initial bed height.

3.3 Effect of equivalence ratio

Equivalence ratio is defined as the ratio of air to fuel supplied divided by the air to fuel ratio required for stoichiometric combustion, and is one of the important parameters in gasification of biomass with air. The equivalence ratio influences the product gas quality and

quantity. Increase in equivalence ratio increases the amount of oxidant in the gasifier, and thus it influences the conversion of char and tar into the product gases depending on the temperature of the reactor.

In this work, the fuel supply (grass pellets) to the reactor is kept constant, while increasing the air flowrate and thereby increasing the equivalence ratio. Figure 5 shows the change in product gas composition at increased air to fuel ratio from 0.4 to 1.2. The concentration of methane, carbon monoxide and hydrogen is decreased and carbon dioxide concentration is increased with increase in the A/F ratio. This is because more oxygen is added to the system that accelerates the carbon monoxide, hydrogen and methane oxidation reaction routes (R2-R4). In addition, the elevated nitrogen into the reactor with increased air to fuel ratios dilutes the product gas composition and reduces its heating value.
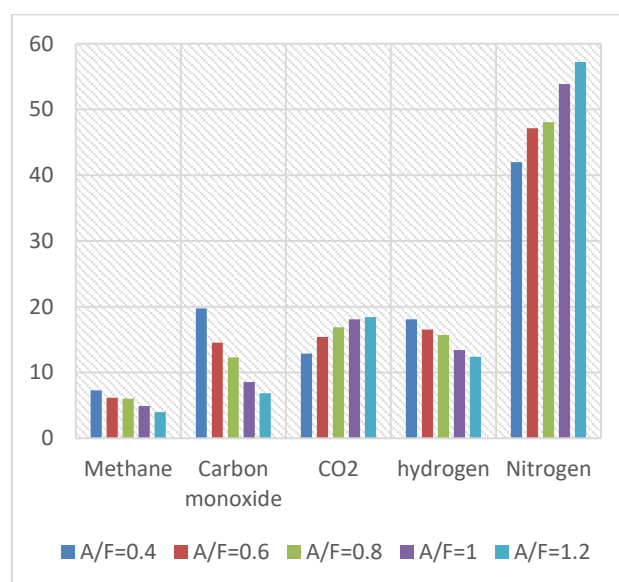
Figure 5. Product gas compositions at different air to fuel ratio.

3.4 Effect of temperature

Temperature in the gasifier determines the rate of chemical reactions involved in the gasification of biomass. The rate at which biomass is converted into volatile components, char, tar and finally into the product gases is influenced by the temperature in the bed and freeboard zone of the reactor. Lower temperature can end up with too much tar in the product gas and slow conversion rate of the char. While too high temperature may allow the ash to melt and stick together the bed materials, forming agglomerates and defluidization of the bubbling fluidized bed. Thus, the reactor must be operated at an optimum temperature so that the fuel particles are converted into better quality product gases with maximum gasifier efficiency.
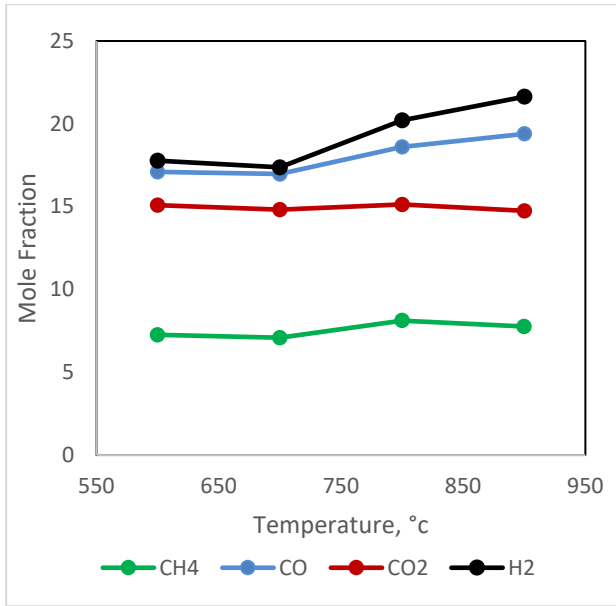
Figure 6. Product gas compositions at different reactor temperatures.

Four cases with temperatures 600°C, 700°C, 800°C, and 900°C are tested at air flowrate of 2 kg/hr and grass pellets feed rate at 2.46kg/hr. The initial bed height is 200mm for all the cases. Figure 6 depicts the product gas composition obtained at different reactor temperatures. With change in temperature from 600°C to 900°C, the concentration of hydrogen and carbon monoxide increased significantly and the methane fraction increased slightly. The reason is that the reaction routes (shown in Table 1), char partial oxidation (R1), water-gas-shift reaction (R5) and methane reforming (R6), are enhanced with the increase in temperature. The fraction of hydrogen and carbon monoxide increased from 17% to 21% and 19% respectively. Increase in quantity of higher calorific value gases enhance the lower heating value (LHV) of the product gas. The LHV and cold gas efficiency (CGE) of the product gas with change in temperature is shown in Figure 7. LHV of the product gas increases from 6.8 MJ/Nm^3 to 7.5 MJ/Nm^3. Since the CGE of the product gas is directly related to LHV of the gas (shown in equation 1), the CGE of product gas increases with increase in LHV of the gas. The CGE of the product gas increased from 58% to 66.6%.

$$CGE(\%) = \frac{LHV \ of \ the \ syngas*syngas \ flow \ rate*100}{LHV \ of \ the \ fed \ grass \ pellets*grass \ pellets \ feed \ rate} \qquad (1)$$

$$LHV \left(\frac{MJ}{Nm^3}\right) = \frac{CO*126.36+H_2*107.98+CH_4*358.18}{1000} \qquad (2)$$
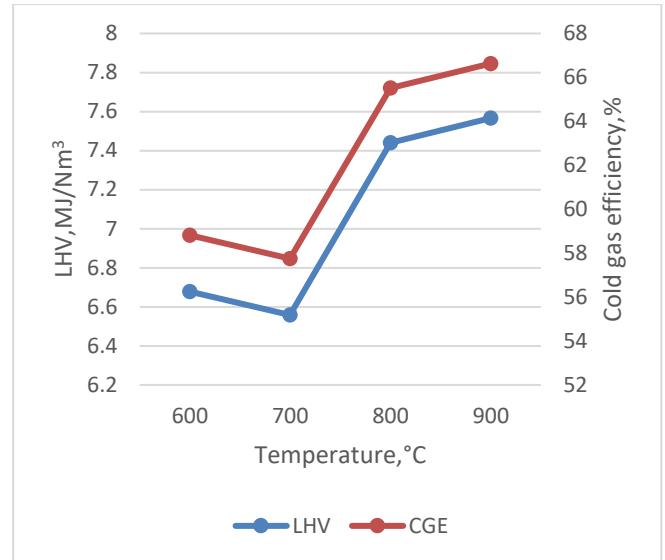

Figure 7. Lower heating value and cold gas efficiency of the product gas at different reactor temperatures.

4 Conclusion

The main objective of this work was to investigate the syngas production potential from gasification of agricultural wastes (grass pellets) using a commercial CPFD simulation software Barracuda VR. Experimental data were used to validate the CPFD model. Experiments were conducted on a 20 kW bubbling fluidized bed gasifier with air as a fluidizing gas and sand as the bed material. Grass pellets were fed to the reactor at 2.46 kg/hr. The samples were collected and measured in an offline GC. The product gas compositions obtained from the simulation results and the experimental data were compared for the model validation.

The influence of initial bed height, temperature and air to fuel ratio on the product gas compositions and gasifier performance were investigated. The result shows that with increase in initial bed height from 200 mm to 300mm there is a slight increment in the product gas yield and a significant increment in the reactor temperature. Different air to fuel ratios, 0.4, 0.6, 0.8, 1, 1.2, were simulated and the result shows that the quality of the product gas decreases with increase in the air to fuel ratio from 0.4 to 1.2. More carbon dioxide and nitrogen are released in the product gas at the higher value of air to fuel ratio. Decrease in the $CH_4, CO,$ and H_2 fractions in the product gas reduce the heating value of the gas. Increase in temperature from 600°C to 900°C enhances the product gas quality. The fraction of hydrogen and carbon monoxide in the product gas increased from 17% to 21% and 19% respectively. Similarly, the CGE of the product gas increased from 58% to 66.6% with increase in reactor temperature.

The CPFD model developed in this work can predict results that are good in agreement with the experimental

data. Therefore, the model can be utilized to optimize the gasification reactor.

References

C. E. Agu, L.-A. Tokheim, C. Pfeifer, and B. M. Moldestad. Behaviour of biomass particles in a bubbling fluidized bed: A comparison between wood pellets and wood chips, *Chemical Engineering Journal*, 363: 84-98, 2019. https://doi.org/10.1016/j.cej.2019.01.120

U. Arena, L. Zaccariello, and M. L. Mastellone. Fluidized bed gasification of waste-derived fuels, *Waste Management*, 30(7): 1212-1219, 2010/07/01/2010. https://doi.org/10.1016/j.wasman.2010.01.038

U. Arena and F. Di Gregorio. Gasification of a solid recovered fuel in a pilot scale fluidized bed reactor, *Fuel*, 117: 528-536, 2014. https://doi.org/10.1016/j.fuel.2013.09.044

J. Alvarez. Hydrogen production from biomass and plastic mixtures by pyrolysis-gasification, *International Journal of Hydrogen Energy*, 39(21): 10883-10891, 2014. https://doi.org/10.1016/j.ijhydene.2014.04.189

R. Beetstra, J. Nijenhuis, N. Ellis, and J. R. van Ommen. The influence of the particle size distribution on fluidized bed hydrodynamics using high-throughput experimentation, *AIChE journal*, 55(8): 2013-2023, 2009. https://doi.org/10.1002/aic.11790

J. C. Bandara, C. Jayarathna, R. Thapa, H. K. Nielsen, B. M. Moldestad, and M. S. Eikeland. Loop seals in circulating fluidized beds–Review and parametric studies using CPFD simulation, *Chemical Engineering Science*, 115917, 2020. https://doi.org/10.1016/j.ces.2020.115917

R. B. Bates et al., Steam-air blown bubbling fluidized bed biomass gasification (BFBBG): Multi-scale models and experimental validation, *AIChE Journal*, 63(5):1543-1565, 2017. https://doi.org/10.1002/aic.15666

J. Chen et al., Analysis of biomass gasification in bubbling fluidized bed with two-fluid model, *Journal of Renewable and Sustainable Energy*, 8(6): 063105, 2016. https://doi.org/10.1063/1.4967717

A. Erkiaga, G. Lopez, M. Amutio, J. Bilbao, and M. Olazar. Influence of operating conditions on the steam gasification of biomass in a conical spouted bed reactor, *Chemical engineering journal*, 237: 259-267, 2014. https://doi.org/10.1016/j.cej.2013.10.018

J. Grace and G. Sun. Influence of particle size distribution on the performance of fluidized bed reactors, *The Canadian Journal of Chemical Engineering*, 69(5): 1126-1134, 1991. https://doi.org/10.1002/cjce.5450690512

R. Jaiswal, C. E. Agu, R. K. Thapa, and B. M. E. Moldestad. Study of fluidized bed regimes using Computational Particle Fluid Dynamics, Proceedings of the 59th Conference on Simulation and Modelling, 2018. DOI:10.3384/ecp18153271

R. Jaiswal, N. C. I. Furuvik, R. K. Thapa, and B. M. E. Moldestad. Investigation of the segregation and mixing behavior of biomass in a bubbling fluidized bed reactor using a CPFD model, Proceedings of the 60th SIMS Conference on Simulation and Modelling, 2019. https://doi.org/10.3384/ecp20170164

R. Jaiswal, N. C. Furuvik, R. K. Thapa, and B. M. Moldestad. Method of identifying an operating regime in a bubbling fluidized bed gasification reactor, *International Journal of Energy Production and Management*, 5(1): 24-34, 2020. Doi: 10.2495/EQ-V5-N1-24-34

M. Niu, Y. Huang, B. Jin, and X. Wang. Simulation of Syngas Production from Municipal Solid Waste Gasification in a Bubbling Fluidized Bed Using Aspen Plus, *Industrial & Engineering Chemistry Research*, 52 (42): 14768-14775, 2013/10/23 2013. https://doi.org/10.1021/ie400026b

L. Shen, Y. Gao, and J. Xiao. Simulation of hydrogen production from biomass gasification in interconnected fluidized beds, *Biomass and bioenergy*, 32(2): 120-127, 2008. https://doi.org/10.1016/j.biombioe.2007.08.002

K.-A. Solli, R. K. Thapa, and B. M. E. Moldestad. Screening of Kinetic Rate Equations for Gasification Simulation Models, The 57th SIMS Conference on Simulation and Modelling SIMS 2016, Linköping University Electronic Press, 142: 105-112. DOI: 10.3384/ecp17142105

R. Xiao, B. Jin, H. Zhou, Z. Zhong, and M. Zhang. Air gasification of polypropylene plastic waste in fluidized bed gasifier, *Energy Conversion and Management*, 48 (3): 778-786, 2007. https://doi.org/10.1016/j.enconman.2006.09.004

J. Xie, W. Zhong, B. Jin, Y. Shao, and Y. Huang. Eulerian–Lagrangian method for three-dimensional simulation of fluidized bed coal gasification, *Advanced Powder Technology*, 24(1): 382-392, 2013. https://doi.org/10.1016/j.apt.2012.09.001

Paper 2

Air gasification of wood chips, wood pellets and grass pellets in a bubbling fluidized bed reactor
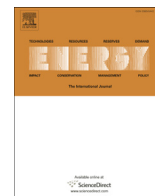
Air gasification of wood chips, wood pellets and grass pellets in a bubbling fluidized bed reactor

Janitha C. Bandara [a, *], Rajan Jaiswal [a], Henrik K. Nielsen [b], Britt M.E. Moldestad [a], Marianne S. Eikeland [a]

[a] University of South-Eastern Norway, Faculty of Technology, Kjølnes Ring 56, 3918, Porsgrunn, Norway
[b] University of Agder, Jon Lilletuns Vei 9, 4879, Grimstad, Norway

ABSTRACT

Gasification is an attractive method for biomass-to-energy conversion and fluidized bed design is one of the best options for large scale operation. A bubbling fluidized bed reactor was used to analyze the effects of biomass type, equivalence ratio (ER) and temperature for product gas compositions. Wood chips, wood pellets and grass pellets were gasified between 650 °C and 800 °C temperature. The ER was varied between 0.08 and 0.16. Gasification of grass pellets was difficult at 800 °C due to agglomeration and the gas composition was poor compared to wood. The reactor performances improved over the temperature and 650 °C was not sufficient to achieve a reasonable carbon conversion. Nitrogen dilution at higher ERs was counter weighted by improved carbon conversion at higher temperatures. The highest carbon conversion was achieved at 800 °C which were 75.8% and 70.6% for wood chips and wood pellets at 0.15 and 0.16 ERs respectively.

1. Introduction

Bioenergy owns an enduring place in future energy profile, especially due to its dispatchable characteristics and competency in delivering the full spectrum of fossil based fuels and chemicals [1,2]. The share of bioenergy was 12.5% in 2019, whereas 90% of the bioenergy feedstock emerged from lignocellulosic materials such as wood, grass and straws [3–6]. Liquid fuels from biomass is a high prospect for the future, where gasification is an efficient conversion method due to the high carbon conversion and versatility of the product gas [7–12].

Gasification converts the solid biomass into a gaseous mixture of carbon monoxide (CO), hydrogen (H_2), methane (CH_4), carbon dioxide (CO_2) and other light gases such as ethane, propane etc. High molecular cyclic or polycyclic hydrocarbons, which are also known as condensable tars, can be present. Air, oxygen, steam or a mixture of these is used as a gasifying agent [13–15]. Theoretically speaking, a pure gasification process is endothermic. The asking enthalpy can be generated inside by oxidizing a part of the biomass or possible to integrate from an external source, which are known as auto-

thermal and allo-thermal gasification respectively. The product gas is diluted with N_2 whenever the air is used, whereas the reactor temperature varies between 700 °C and 1100 °C. Except the dual reactor circulating fluidized bed configuration in Fig. 2 (left), the major processing steps of drying, pyrolysis, oxidation and reduction reactions take place in a single reactor. Fixed bed designs as in Fig. 1 are the oldest, whereas fluidized bed designs as illustrated in Fig. 2 and entrained gasifiers are efficient developments to operate in large scale. Major reactions take place inside a gasification reactor are given in Table 1 [12,16].

The gasifying agent, reactor designing, physical and chemical properties of biomass, reactor temperature and pressure, residence time, equivalence ratio (ER), steam-to-biomass ratio (SBR) and the catalysts are the succeeding parameters for the gas composition [17–23]. Heating value of the product gas is possible to upgrade from 5 MJ/Nm³ to 18 MJ/Nm³ if the gasifying agent is shifted from air to oxygen or steam. The H_2 and CO contents can be maximized up to 60% and 40%–45% with steam and oxygen respectively. The H_2 and CO contents from air gasification vary between 10% and 25% [12,24,25]. Tar is identified as one of the major barriers in commercialization of gasification due to process hindrance in clogging pipes and engines, turbine fouling and catalyst poisoning in Fischer–Tropsch (FT) synthesis and solid oxide fuel cells [7,9,26]. Bubbling fluidized bed (BFB) is the simplest designing of

* Corresponding author. 64A, Vallermyrvegen, 3917, Porsgrunn, Norway.
E-mail address: Janitha.bandara@usn.no (J.C. Bandara).
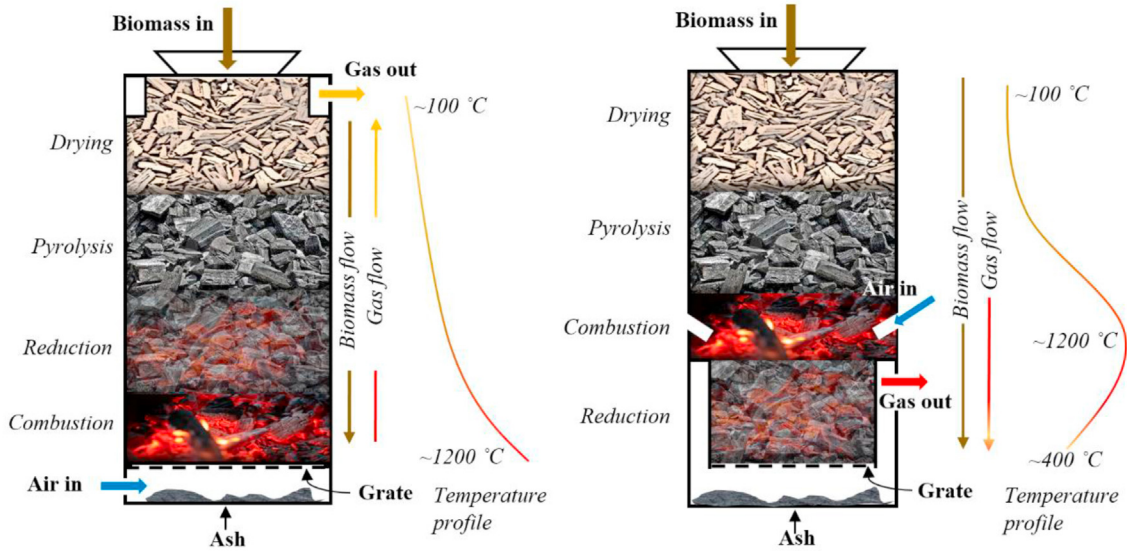
Fig. 1. Updraft (left) and downdraft (right) fixed-bed gasifiers.
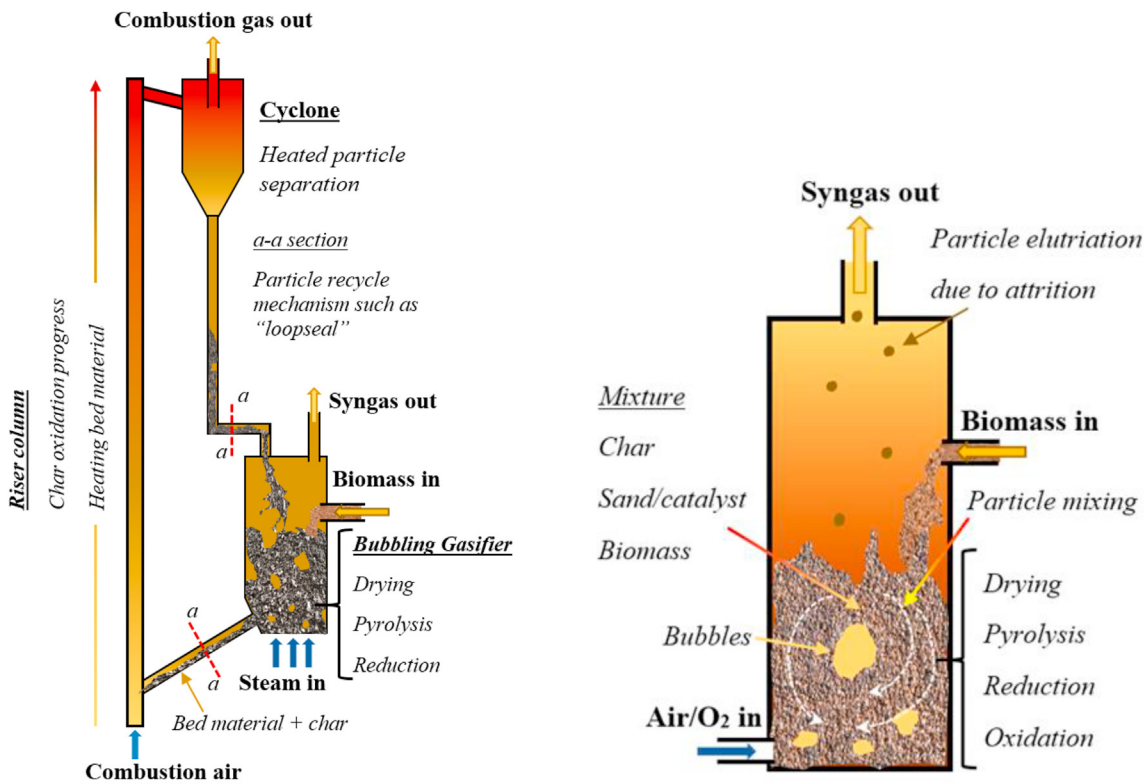
Fig. 2. Fluidized bed gasification, duel-reactor circulating fluidized bed (left) and bubbling fluidized bed (right).

fluidized bed gasification. Of biomass, which has been studied many researchers [19,25,27–42]. A solid carbon fraction is remained after the pyrolysis. The primary drive of using a gasifying agent is to bring all the carbon into the gaseous phase, as biomass carrying oxygen and hydrogen is not sufficient. Using of oxygen involves a high operational cost and therefore, air is used as the gasifying agent in general applications. Majority of these reactors are auto-thermal in which, additional amount of air (than the requirement for stoichiometric gasification) is supplied to trigger

the oxidation reactions and consequently to keep up the target reactor temperature. The typical equivalence ratios (ER) used in previous studies have been between 0.2 and 0.4, whereas using 0.2 or higher ERs has emerged as a thumb rule [38]. Using of higher ERs is disadvantageous, especially in air gasification, as the product gas is diluted with N_2 for a higher degree. Therefore, minimization of the excess air supply than what is required for pure gasification. This can only be achieved by upgrading the auto-thermal reactor into an allo-thermal or a hybrid reactor. Electrical heated walls is

Table 1
Basic homogeneous and heterogeneous reactions of gasification.

Stoichiometric Reaction			Reaction name	Enthalpy (kJ/mol)
$C + O_2$	→	CO_2	Char combustion	(-394)
$C + 0.5O_2$	→	CO	Char partial oxidation	(-111)
$CO + 0.5O_2$	→	CO_2	CO oxidation	(-283)
$H_2 + 0.5O_2$	→	H_2O	Hydrogen combustion	(-242)
$C + H_2O$	↔	$H_2 + CO$	Steam gasification	+131
$C + CO_2$	↔	$2CO$	Boudouard reaction	+172
$C + 2H_2$	↔	CH_4	Methanation	(-75)
$H_2O + CO$	↔	$H_2 + CO_2$	Water-gas shift reaction	(-41)
$CH_4 + H_2O$	↔	$3H_2 + CO$	Methane reforming	+206
Drying and pyrolysis - Endothermic				
Tar conversion, reforming and oxidation				

not viable in a commercial scale BFB gasifier and however, such a reactor operated at pilot scale is useful in setting up the operational limits.

An electrically heated hybrid reactor was used in this work to study the minimum ER in a BFB biomass gasifier. The minimum ER was defined as the airflow sufficient enough to convert all the char without accumulation in the reactor bed. Lower temperatures down to 650 °C was also tested as the equilibrium reactor temperature at auto-thermal conditions for reduced ERs is low. In order to strengthen the discussion, three different feedstock those of woodchips, wood pellets and grass pellets were gasified between 650 °C to 800 °C. The ER was gradually increased from approximately 0.1 for each feedstock at each temperature. The Change in the gas composition and other performance indicators such as gas yield, carbon conversion were recorded as a function of temperature and ER for each feedstock.

2. Materials and experimental methods

Wood pellets, wood chips and grass pellets were the feedstock and as illustrated in Fig. 3, the pellets were 6 mm in diameter. The 30−40 mm length pellets were broken during the feeding through screw conveyors. The chips were heterogeneous in size and sieved using 30 mm sieve. Compositions of the feedstock were tested at Eurofins testing facility and the results are given in Table 2.

2.1. Experimental system description

The bubbling fluidized bed reactor is a collaborative development of University of South-eastern Norway and BOKU, Austria. The reactor operates at atmospheric pressure where the diameter and height are 0.1 m and 1 m respectively. Electrical heaters are used to heat the rector and gasifying air supply. As illustrated in Fig. 4, fuel is stored in a silo and conveyed to the reactor using two screw feeders. The non-conductive flange connection between two screws avoids and N_2 supply in hopper avoid any heat flow the reactor to hopper. The feedstock inlet is 0.25 m above the bottom.

Temperature and pressure are measured along the reactor, silo, screw conveyor, air pre-heater, air inlet, gas outlet and reactor heating coil. Sensor data acquisition, temperature controlling and safely shutdowns are controlled by a central PLC unit. The hot conveyor operates continuously at a constant speed in order to avoid any formation of "*Biomass Bridge*" between two screws. The feed rate of biomass is pre-calibrated as a function of cold conveyor motor capacity. The cut-off temperatures for reactor heater and air-preheater are 1000 °C and 600 °C respectively. Nitrogen flushing of the reactor starts at emergency shutdowns.

SRI gas chromatography (GC) was used in gas analysis where CO2 was detected by a silica gel packed column and N_2, O_2, CH_4, and CO by molecular sieve 13X packed column. Helium was the carrier gas and the H_2 composition was calculated by the difference. The accuracy of calculating the H_2 composition by difference was validated with several samples using N_2 as the carrier gas.

The reactor was initially filled with two litters of 200−400 μm sand particles (density-2650 kg/m^3). The reactor heaters and the air preheater were switched on while the bed was at fluidization conditions. Once the bed material reached 650 °C, the fuel feeding was started which kept constant for all experiments. ER was manipulated with the airflow and reactor heaters were energized accordingly to maintain the desired temperature. The bed pressure was constantly monitored which was useful in identifying any clinker formation. The samples were extracted at 10 min intervals and kept for cooling down in order to let the tar condense. Precautionary measures were always taken to remove the gas volume collected inside the sampling pipe during the previous sampling.

Equation 01, 02, 03 and 04 is used to calculate the lower heating

Fig. 3. Size range of wood pellets, grass pellets and wood chips.

Table 2
Biomass properties.

Biomass	Ultimate analysis (%)				Proximate analysis (%)				LHV (dry) MJ/kg
	C	H	O	N	Fixed C	Volatile	Moisture	Ash	
Wood pellets	50.9	6.0	42.6		14.0	77.8	7.9	0.30	18.9
Grass pellets	46.9	5.7	33.7	3.19	12.6	69.5	8.4	9.49	16.7
Wood chips	51.0	6.1	42.2		13.5	74.8	11.1	0.58	18.8
Standards									

Ash-EN 14775, Heating value-EN 14918, Moisture-EN 14774, Ultimate-EN 15408, Volatile-EN 15402
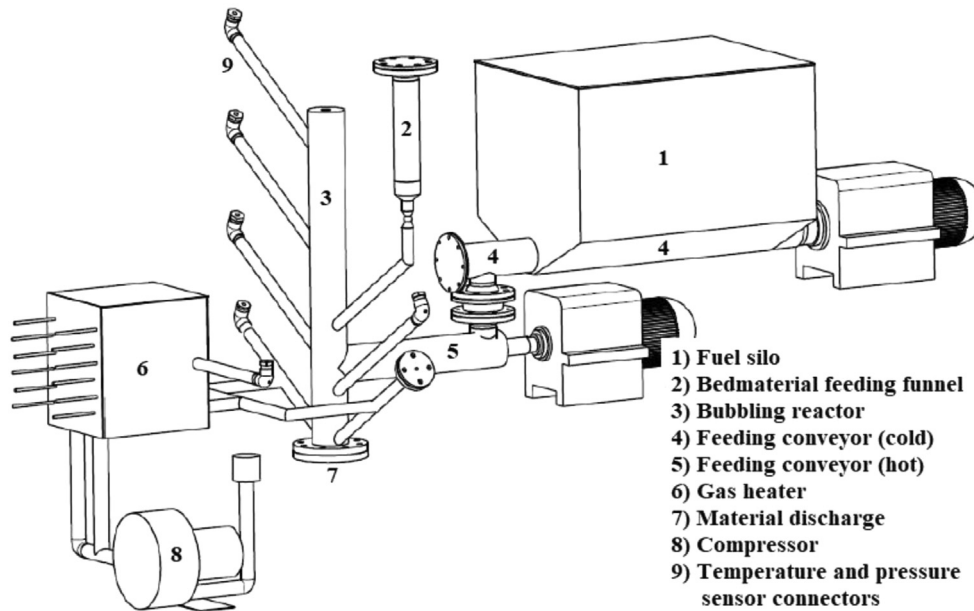
Fig. 4. Bubbling fluidized bed experimental rig with auxiliary attachments.

1) Fuel silo
2) Bedmaterial feeding funnel
3) Bubbling reactor
4) Feeding conveyor (cold)
5) Feeding conveyor (hot)
6) Gas heater
7) Material discharge
8) Compressor
9) Temperature and pressure sensor connectors

value of synthesis gas (LHV), the gas yield (GY), the carbon conversion efficiency (CCE %) and the cold gas efficiency (CGE %) respectively, which are the main parameters used in comparing the gasifier performance [27,41].

$$CGE = \frac{GY* LHV_{syngas}}{LHV_{biomass}}\, 100\% \qquad \text{Equation 4}$$

$$LHV\left(MJ\big/m^3\right) = \{[H_2]*107.98 + [CO]*126.36 + [CH_4]*358.18\}\big/1000 \qquad \text{Equation 1}$$

$$GY\left(\frac{Nm^3}{kg\ biomass}\right) = \frac{Volume\ rate\ of\ producer\ gas\left(\frac{Nm^3}{h}\right)}{Biomass\ feed\ rate\left(\frac{kg}{h}\right)} \qquad \text{Equation 2}$$

$$CCE\% = \frac{12(CO\% + CO_2\% + CH_4\% + 2*C_2H_4\%)*GY}{22.4*fuel\ C\%*100}\, 100\% \qquad \text{Equation 3}$$

3. Results and discussion

The screw conveyor was robust with pellets and however, frequent blockages were observed for woodchips. The narrow pipe section connecting two screw conveyors resulted in frequent hindrance for the flow of woodchip, whereas moist biomass powders caused stuck between the screw and the surrounding pipe of the conveyor. Interrupted flow was identified either by increasing reactor temperature or decreasing bed pressure drop.

The calibration of feed screw for grass pellet is depicted in Fig. 5 where wood pellets and woodchips showed a similar profile. The feed rate was fluctuating in positive and negative directions from the average. Due to the periodic operation of cold conveyor at lower feed rates, the reactor experienced zero biomass inflow frequently. As the product gas composition is a strong function of pyrolysis

Fig. 5. Variation of fuel feed rate for grass pellets measured in 2 min time periods.

Table 3
Actual airflow and ER for different experiments.

Biomass	Feed Rate (kg/h)	Stoichiometric Air (kg/h)	Actual air flowrate (kg/h)			
			1.5	2	2.5	3.0
			Equivalence Ratio (ER)			
Wood pellet	2.42	19.6	0.075	0.100	0.125	0.150
Grass pellet	2.72	21.3	0.070	0.090	0.120	0.140
Wood chips	2.30	18.9	0.080	0.100	0.130	0.160

products, varying feeding of biomass could exert a certain uncertainty to the measured gas composition. As illustrated in Fig. 6, a wider screw-pitch at the start of the hot conveyor could collect a certain amount of biomass even under the periodic operation of cold conveyor. A narrowing pitch towards the reactor inlet results in a steady biomass flow while converging pipe dia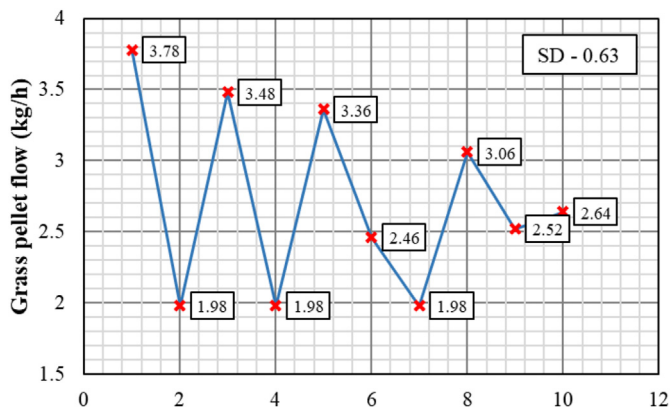meter guarantees a complete filling of biomass over the entire cross section. Further, an inclined cold conveyor with N_2 flushing could retard the migration of sand into the conveyor, because abrasion of sand between the screw and the pipe wall can erode the pipe.

3.1. Experimental results of gasification

Precise tuning of biomass flow was difficult and therefore, the cold conveyor was operated at 2% capacity, which resulted in 2.3 kg/h, 2.42 kg/h and 2.7 kg/h flowrates for woodchips, wood pellets and grass pellets respectively. The minimum air flowrate of 1.5 kg/h was selected based on the minimum fluidization velocity of the bed material. The calculated ER values based on flowrates and the biomass ultimate analysis are given Table 3. The changed air flowrate, to change the ER, could alter the fluidization conditions, whereas being a small diameter reactor, changing the biomass feed rate could have worse effects. Drying and pyrolysis processes extract energy from the bed, which reduce the bed temperature at biomass injection. The more the biomass inflow, the more the temperature reduction, which will change the pyrolysis conditions.

Further, segregation of biomass and bed material is also possible. Therefore, a proper selection of the bed material and the fluidization velocity is vital. Gas production rate was approximated using the N_2 balance between inlet and outlet. The final gas composition is triplet averaged and so does the subsequent calculated values such as LHV, carbon conversion etc. However, the aforementioned uncertainties are not completely eliminated.

For lower ER below 0.1, the reactor temperature could not maintain above 650 °C without the electrical heaters. At higher ERs, it was possible to take up the temperature to 750 °C range being the electrical heaters switched off and however, the heaters were continuously operated for higher temperatures than 800 °C range. The temperature varied by ±20 °C during certain experiments, especially during the efforts of operating the reactor in autothermal conditions.

The lower limit of ER for biomass gasification has been slightly above 0.2 in literature. Any remaining oxygen above the bed surface leads to oxidation of CO, H_2, and CH_4 that can decrease the gas quality. Whenever biomass is fed to the bed surface, the most efficient approach is to maximize the gas fraction during pyrolysis. The air flowrate should be carefully selected as it is adequate merely to oxidize the char inside the bed. Consequently, the oxygen is totally consumed before leaving the particle bed. The bed pressure drop remains constant if the char is completely converted, whereas the pressure drop should develop over time if not. The dynamic bed pressure drop for wood chips for different experimental cases are illustrated in Fig. 7. The first graph represents the gasification at 0.08 ER and 650 °C temperature. Initial jump in the pressure drop was due to the start of biomass feeding. The trend line illustrates a gradual increment of bed pressure over time, suggesting the accumulation of unconverted char. A similar trend, however with a less gradient, is observed for increased ER of 0.130 at the same temperature. The final graph in Fig. 7 represents
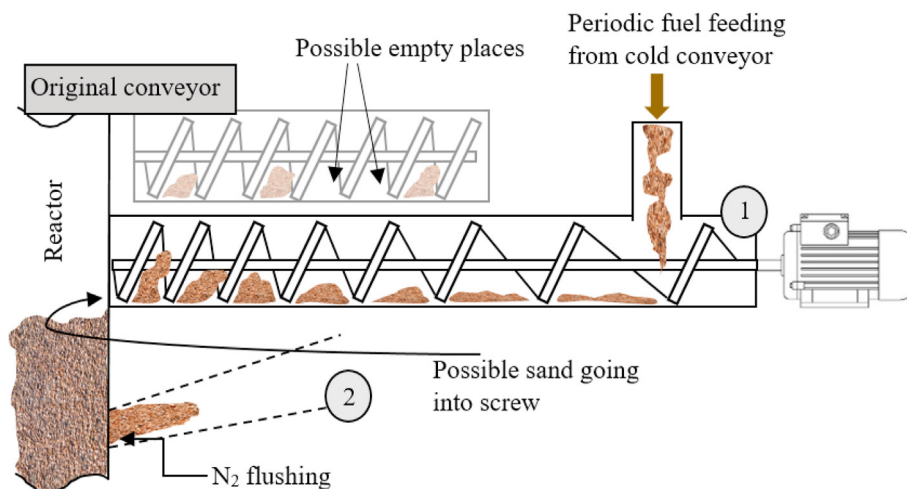
Fig. 6. Conveyor modification; 1- varying pitch, 2 - converging pipe.
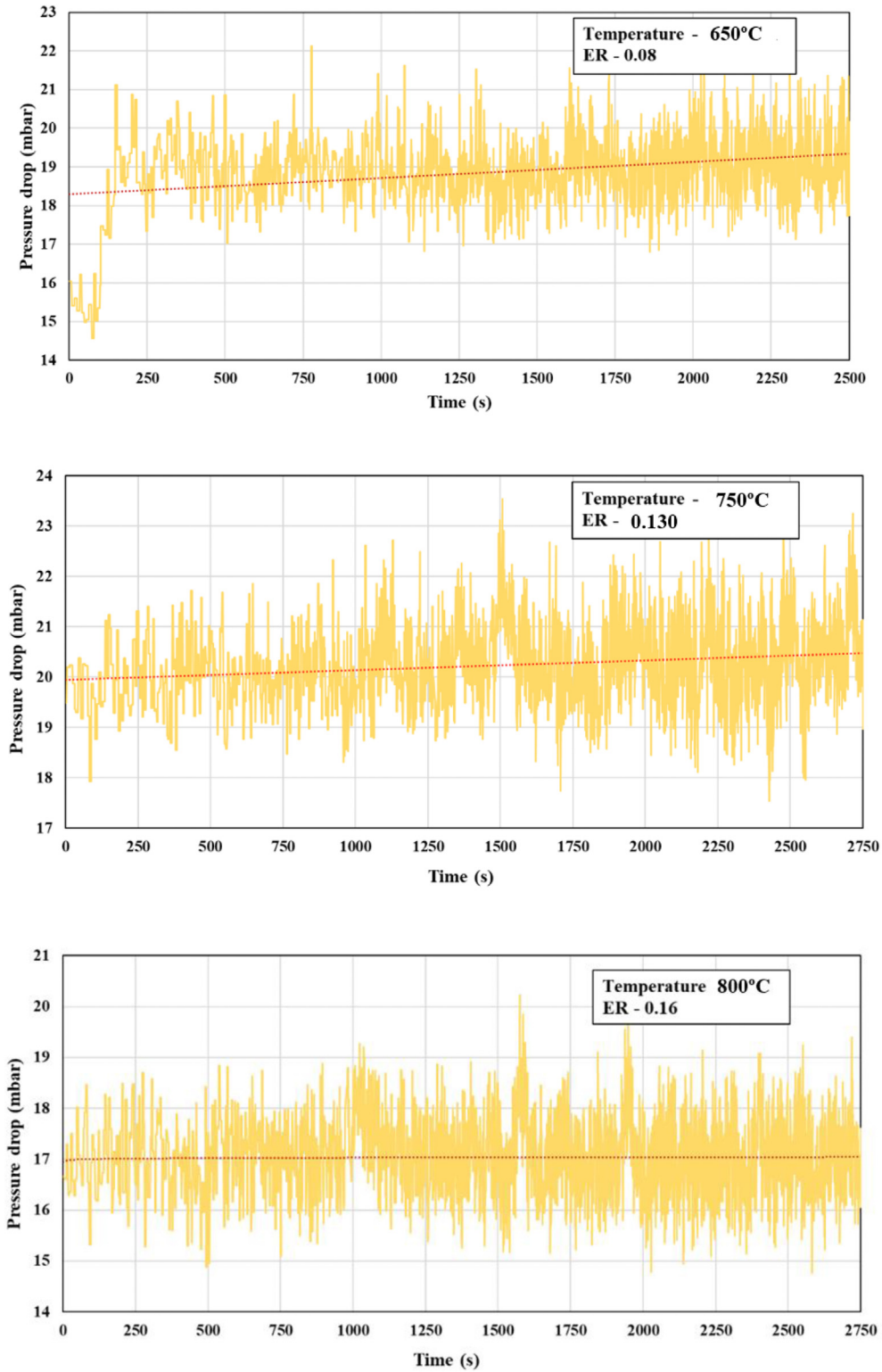
Fig. 7. The change of bed pressure with time for different ER and temperature.

the gasification at 800 °C and 0.16 ER, where the pressure drop remains approximately constant over time. Consequently, it can be concluded that the 0.16 ER is marginally sufficient to oxidize the total char fraction generated at 800 °C for wood chips.

3.2. Gasification of wood chips

Fig. 8 summarizes the product gas composition obtained with wood chips. The presence of oxygen is less than 1% for all the temperatures and ER ranges, which is hardly noticeable at the bottom of the bar chart. The gas sampling was carried out manually
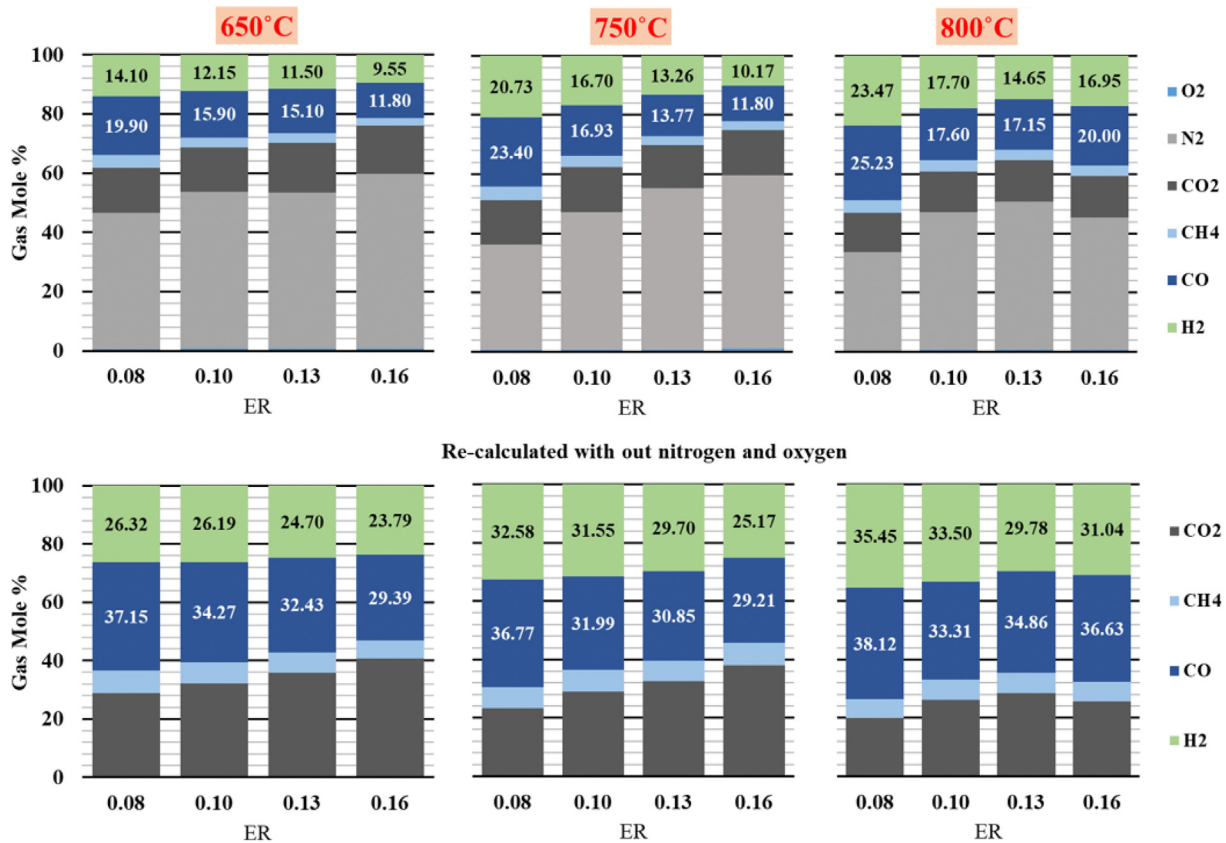
Fig. 8. Product gas composition of wood chips at different equivalence ratio and reactor temperatures.
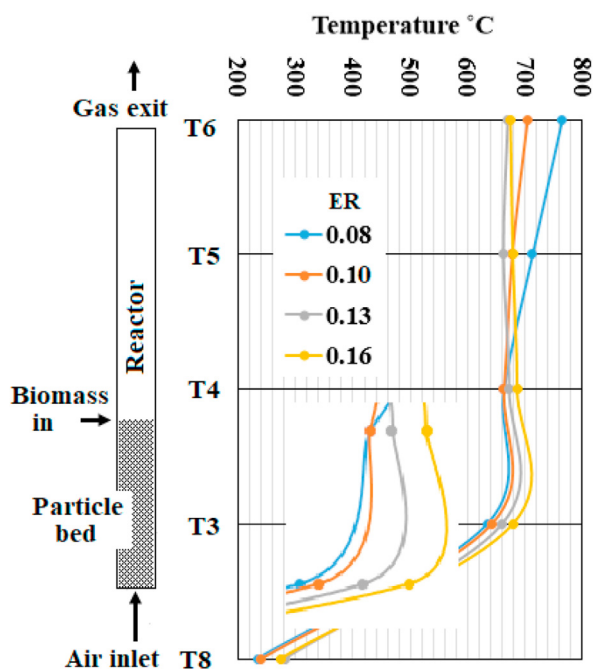
Fig. 9. Temperature profile along the reactor height at 650 °C operation for different ERs of woodchips.

with airtight syringes and therefore, some air contamination was expected. However with the observed low O_2 concentrations, it can be concluded that the air contamination was minimum during the sampling and further, the gas resident time was sufficient to oxidative reactions to complete.

The temperature profile along the reactor at 650 °C and for different ERs are illustrated in Fig. 9. The temperature sensors T8, T3 and T4 are located at air inlet, inside to the bed and just above the bed respectively. Electrical heaters were in operation for lower ERs of 0.08 and 0.1 where the average temperature of reactor wall was 750 °C. Therefore, the product gas was continuously heated from the bed surface to the exit. The temperature gain in 0.08 ER is higher than 0.1 because of the low gas flow. In contrast, the gas temperatures at ERs of 0.13 and 0.16 were approximately constant from above the bed to exit. The electrical heaters were not used and the reactor wall temperature was same as the reactor bed. The endothermic characteristics of progressing pyrolysis reaction is the main reason for observed temperature drop just above the bed (T4). Even though the bed temperature was nearly constant around 650 °C, the comparison for different ERs has slight uncertainty because of the temperature variation at the gas exit.

In general, for air gasification in auto-thermal conditions, the most suitable position for biomass feeding is above the bed surface. If the biomass is fed to the bottom of the bed, the O_2 can easily react with the evolved gases instead of char particles degrading the gas composition. Consequently, there is possible accumulation of char particles inside the reactor. However as the biomass is fed above the bed, the bed material and fluidization velocities should be selected carefully so that the generated char is well mixed with the bed material without segregating towards the bed surface.

According to Fig. 8, a significant effect from temperature and ER on the gas composition can be observed. In the temperature range of 650 °C and 750 °C, the H_2 and the CO molar compositions gradually decrease with increasing ER. The collective effect of

Fig. 10. Gas composition of CH_4, H_2, CO_2 and CO as a function of reactor temperature for woodchips.

Fig. 11. Product gas composition for wood pellets at different equivalence ratio and reactor temperatures.

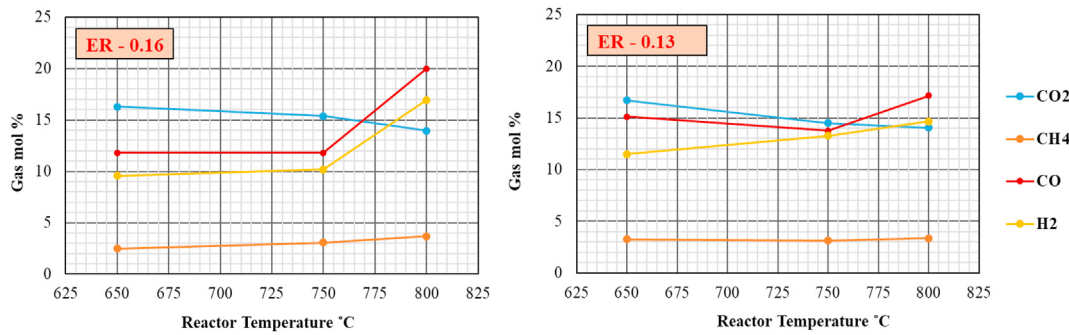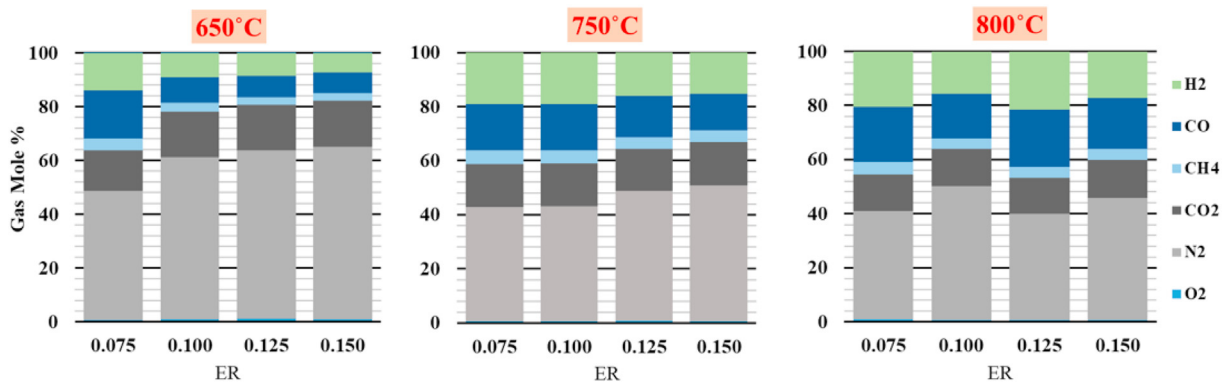amplified N_2 content in the product gas and possible gas phase oxidation reactions can be the reasons. In contrast at 800 °C temperature, H_2 and CO compositions drop initially and improve from 0.13 to 0.16. The increased O_2 supply and high reaction rates at increased temperature could accelerate the tar cracking reactions. Fig. 10 carries the same information in Fig. 8 and however, the gas compositions (included N_2 and O_2) are plotted as a function of temperature for different ERs. Variation of the gas compositions between 650 °C and 750 °C at 0.16 ER is very little. At 800 °C temperature and 0.16 ER, the H_2 and CO compositions improve by 66% and 69% respectively showing an exponential trend. The CH_4 composition increases slightly from 650 °C to 800 °C in linearly. The reforming and tar cracking reactions are accelerated at higher temperatures resulting higher H_2 and CO. At 0.13 ER, H_2 linearly increases from 650 °C to 800 °C without a sharp change at 450 °C as observed at 0.16 ER. The decreasing profile and the compositions of CO_2 are similar for both ERs. The CH_4 composition is nearly constant over the entire temperature range. The reduction of CO content from 650 °C to 750 °C is difficult to explain, which can be a result of measurement uncertainty. Furthermore, the reactor temperature exerts a significant impact on the pyrolysis product yield and gas phase compositions. The higher the temperature, the higher the gas yield and the lower the tar yield. Consequently, a less gas residence time is sufficient to complete the tar conversion reactions. With the absence of external heating, the freeboard temperature may not be higher in a regular auto-thermal reactor and consequently, the tar cracking reactions may retard.

The total energy yield, which is a function of the gas heating value and the gas yield, has an equal importance as the gas composition, especially when the product gas is used for thermal energy generation. The performance indicators of the product gas flow, gas yield, LHV, carbon conversion efficiency (CCE %), cold gas

efficiency (CGE %) and energy production rate for woodchips at different temperatures and ERs are given in Table 4. The product gas flow was calculated using N_2 balance where the accuracy mainly depends on precise measurement of the inlet air flowrate and the GC measurements. As the calculating steps of LHV, CCE% and CGE% are incorporated with the gas yield, any uncertainty involved with the product gas flowrate can appear in those parameters too.

The sharp change of the gasification temperature from 750 °C and 800 °C is clearly reflected by the data in Table 4 as well. Similar to the gas composition, a significant difference cannot be observed in the gas yield between 650 °C and 750 °C for the entire ER range. However, as the values compared for 0.16 ER, the gas yield has improved by 30% at 800 °C compared to 750 °C. The increasing

Table 4
Gasification performance indicators for wood chips.

ER	Product Gas	Gas Yield	LHV	CCE	CGE	Energy Rate
	(Nm^3/h)	(Nm^3/kg biomass	(MJ/Nm^3)	%	%	MJ/h
650 °C						
0.08	2.11	0.92	5.52	38.80	28.15	11.65
0.1	2.44	1.06	4.53	38.90	26.70	11.05
0.13	3.07	1.33	4.31	50.13	31.98	13.24
0.16	3.27	1.42	3.41	46.62	26.97	11.16
750 °C						
0.08	2.71	1.18	6.86	54.10	44.85	18.57
0.1	2.78	1.21	5.35	46.92	35.89	14.86
0.13	2.92	1.27	3.91	41.78	27.59	11.42
0.16	3.31	1.44	3.68	46.66	29.47	12.20
800 °C						
0.08	2.90	1.26	7.25	57.83	50.89	21.07
0.1	2.77	1.21	5.48	45.36	36.67	15.18
0.13	3.22	1.40	4.94	51.79	38.42	15.90
0.16	4.32	1.88	5.68	75.83	59.27	24.54

Fig. 12. Gas composition of CH_4, H_2, CO and CO_2 as a function of reactor temperature for wood pellets.
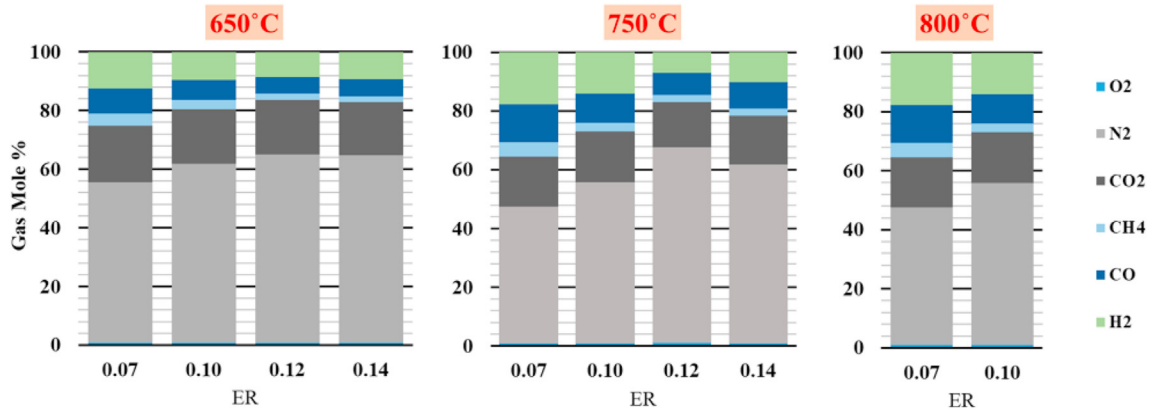
Fig. 13. Product gas composition for grass pellets at different equivalence ratio and reactor temperatures.

trend and numerical values of gas yield are similar to literature data. LHV is mainly a function of the relative compositions of H_2, CO and CH_4, which therefore decreases with the ER and increases with the temperature. In spite of some minor deviation, the CCE% and CGE% are improved with both ER and temperature. The energy flow was calculated as a multiplication of gas flowrate and the LHV, which is considerably low at 650 °C and gradually improves for higher temperatures. According to the authors, the better operating conditions are highlighted in Table 4. The combination of temperature 800 °C and 0.08 ER gives the highest LHV. Nevertheless the CCE% and CGE% are relatively low. Similarly, respective values are even lower at 750 °C and 0.08 ER. Despite the fact of slightly lower LHV of 5.68 MJ/Nm^3, the temperature of 800 °C with 0.16 ER gives the best values for other parameters where the CCE% and CGE% have reasonable values of 76% and 60% respectively. Therefore, any prospected experiments at higher ERs should be carried out above 800 °C reactor temperature. Char accumulation was not observed in the bed at 800 °C temperature and 0.16 ER. Therefore, remaining 24% of the carbon is included in the tar, elutriated fine char and soot carbon.

3.3. Gasification of wood pellets and grass pellets

The gas compositions for wood pellets are given in Figs. 11 and 12, whereas Fig. 13 presents the information related to grass pellet gasification. Equivalent information as in Table 4 for wood pellets and grass pellets are given in Table A1 and Table A2 respectively in appendix. The gas compositions related to all the experimental runs are given in Table A3. The ERs of wood pellets and grass pellets are slightly different from wood chips as it was difficult to fine tune the screw feeder. Grass pellets contain significantly higher ash content compared wood and moreover, the ash melting temperature is lower. This fact was reflected with the failed attempts of operating the reactor over 800 °C where large agglomerates formed covering the total reactor cross section. A picture of an agglomerate formed during the experiments is given in Fig. 14. Successful experiments could perform for 0.07 and 0.1 ER at 800 °C temperature. However, the oxygen loading is above 0.1 ER, which leads to local hotspots that initiate agglomerates.

Wood chips and wood pellets show approximately similar results. However, a clear difference can be observed in gas

Fig. 14. Formation of agglomerates during grass pellet gasification.

compositions of grass pellets gasification compared to the wood chips and wood pellets. The H_2 and CO fractions are lower for grass pellets in all the experiments, whereas the CO_2 fraction is higher. At 650 °C, the gas composition from wood chip is richer in H_2 and CO than for wood pellets. In contrast at 750 °C, the wood pellets gas composition is richer in H_2 and CO. At elevated temperature, a clear trend cannot be observed for wood chips and wood pellets. Wood chips are higher in moisture than wood pellets whereas wood pellets might lose a fraction of volatiles during pelletizing process.

The CCE% and the CGE% improve with temperature and ER. A significant difference of the gas yield (+34%), LHV (+15%), CCE (+46%) and CGE (+54%) can be observed between 0.13 and 0.16 ERs at the 800 °C temperature for wood chips. In contrast, the particular parameters are approximately similar for wood pellets between 0.125 and 0.15 ERs. In general, the gasification performance parameters for wood pellets are equally better in 750 °C and 800 °C temperatures whereas wood chips have the best gasifier performance at 800 °C. In the temperature ranges of 750 °C and 800 °C, the temperature variation was ±20 °C during the experiments, which could be a decisive factor for the comparison of gas compositions and other parameters.

As the wood chips and pellets are concerned, the reduced CCE% is mainly due to unaccounted tar and char particle migration with the exhaust gas stream. Further, a char accumulation was observed at reduced ERs and temperatures. If the char particle migration is assumed to be similar at specific ERs, the improved carbon conversion at elevated temperature is mainly due to triggered tar cracking reactions. Further, according to the literature, tar yield from pyrolysis is maximized between 500 °C and 600 °C, and is sharply reduced above 700 °C [43]. However, the CCE is not significantly improved with temperature for the grass pellets. Therefore, it can be concluded that the migration of char particles with the exhaust gas is the dominant factor for the reduced CCE related to grass pellets.

4. Conclusion

Three different biomass feedstock of wood chip, wood pellet and grass pellets, were gasified in an electrically heated bubbling fluidized bed reactor. Four different ERs approximately 0.075−0.16 and three different temperatures of 650 °C, 750 °C and 800 °C were tested. Uncertainties related to discontinuous feeding of biomass and ±20 °C temperature variation could affect the results comparison.

Gasification of grass pellets were not successful due to agglomerations and reduced carbon conversion. Further experimental efforts with different bed material sizes and catalytic particles are suggested for the grass pellets. At lower temperatures, increased ER decreased the gas quality as a result of N_2 dilution. In contrast at 800 °C temperature, minor reduction of H_2 and CO content at increased ER was outweighed by improved carbon conversion and gas yield. The respective H_2 and CO contents were 16.9% and 20% for wood chips and 17.2% and 18.8% for wood pellets at 800 °C temperature. The respective ERs were 0.16 and 0.15. Reactor temperature of 650 °C was not sufficient for an acceptable gas composition and carbon conversion. The best performance for wood chips was observed at 800 °C and 0.16 ER with 75% carbon conversion. For wood pellets, both 0.125 and 0.15 ER at 800 °C gave the best overall performance with a 70% of carbon conversion. The main motivation for using low ERs compared to literature values was to identify the minimum ER that was sufficient to maintain a steady char content without accumulation in the reactor. It can be concluded that the approximate minimum ER is 0.16 for wood chips, which is possible to deviate depending on the pellet size and the bed conditions such as fluidization conditions and height. Even if the minimum ER of 0.16 is not sufficient to maintain the reactor temperature, it is fairly sufficient to convert the char fraction completely, which is the main purpose of the gasifying agent. If the inlet air can be heated sufficiently with a waste or sustainable heating source, this approach has a practical significance as well.

Credit author statement

Janitha C. Bandara − Conceptualization, Methodology, Investigation, Writing original draft. Rajan Jaiswal − Methodology, Investigation. Henrik K. Nielsen − Supervision, Editing. Britt M.E. Moldestad − Supervision, Editing. Marianne S. Eikeland − Supervision, Editing.

Declaration of competing interest

The authors declare that they have no known competing financial interests or personal relationships that could have appeared to influence the work reported in this paper.

Appendix

Table A1
Gasification performance indicators for wood pellets

ER	Product Gas	Gas Yield	LHV	CCE	CGE	Energy Rate
	(Nm^3/h)	(Nm^3/kg biomass)	(MJ/Nm^3)	%	%	(MJ/h)
650 °C						
0.075	2.02	0.84	5.38	33.64	25.00	10.89
0.1	2.14	0.88	3.36	28.19	16.54	7.20
0.125	2.57	1.06	2.91	31.25	17.14	7.47
0.15	3.01	1.25	2.71	36.69	18.76	8.17
750°C						
0.075	2.29	0.94	6.05	38.28	31.72	13.82
0.1	3.03	1.25	6.00	50.60	41.77	18.19
0.125	3.37	1.39	5.19	52.36	40.12	17.48
0.15	3.86	1.60	4.89	58.28	43.42	18.91
800°C						
0.075	2.41	1.00	6.40	41.23	35.42	15.43
0.1	2.61	1.08	5.13	39.42	30.73	13.39
0.125	4.11	1.70	6.45	69.93	60.85	26.51
0.15	4.30	1.78	5.66	70.62	55.91	24.35

Table A2
Gasification performance indicators for grass pellets

ER	Product Gas	Gas Yield	LHV	CCE	CGE	Energy Rate
	(Nm^3/h)	(Nm^3/kg biomass)	(MJ/Nm^3)	%	%	(MJ/h)
650 °C						
0.07	1.77	0.65	3.96	22.43	14.33	7.01
0.1	2.11	0.78	3.02	23.71	13.03	6.38
0.12	2.51	0.92	2.41	26.06	12.36	6.05
0.14	3.03	1.11	2.43	30.95	15.04	7.36
750°C						
0.07	2.08	0.76	5.26	28.50	22.33	10.93
0.1	2.35	0.86	3.85	27.81	18.48	9.05
0.12	2.42	0.89	2.60	24.38	12.89	6.31
0.14	3.18	1.17	3.14	34.94	20.34	9.96
800°C						
0.07	2.08	0.76	5.26	28.50	22.33	10.93
0.1	2.35	0.86	3.85	27.81	18.48	9.05

Table A3
Gas molar composition for all experimental runs with different ERs, temperatures and feedstock

Wood Chips											
T (°C)	650.00				750.00				800.00			
ER	0.080	0.100	0.130	0.160	0.080	0.100	0.130	0.160	0.080	0.100	0.130	0.160
O2	0.60	0.70	0.90	0.70	0.63	0.67	0.93	1.20	0.50	0.63	0.70	0.65
N2	45.83	52.90	52.53	59.15	35.73	46.40	55.13	58.40	33.30	46.53	50.10	44.75
CO2	15.40	14.95	16.70	16.30	14.83	15.37	17.23	15.37	13.20	13.77	14.05	13.95
CH4	4.17	3.40	3.27	2.50	4.67	3.93	3.37	3.07	4.30	3.77	3.35	3.70
CO	19.90	15.90	15.10	11.80	23.40	16.93	10.07	11.80	25.23	17.60	17.15	20.00
H2	14.10	12.15	11.50	9.55	20.73	16.70	13.27	10.17	23.47	17.70	14.65	16.95
CH4 + H2 + CO	**38.17**	**31.45**	**29.87**	**23.85**	**48.80**	**37.57**	**26.70**	**25.03**	**53.00**	**39.07**	**35.15**	**40.65**

Wood Pellets											
T(°C)	650.00				750.00				800.00			
ER	**0.075**	**0.100**	**0.125**	**0.150**	**0.075**	**0.100**	**0.125**	**0.150**	**0.075**	**0.100**	**0.125**	**0.150**
O2	0.73	0.90	1.13	0.90	0.67	0.70	0.80	0.70	0.83	0.77	0.70	0.70
N2	47.83	60.23	62.73	64.20	42.33	42.55	47.90	50.07	40.10	49.40	39.25	45.00
CO2	15.07	17.00	16.93	17.20	15.67	15.60	15.63	16.20	13.67	13.83	13.30	14.25
CH4	4.53	3.33	2.77	2.65	5.10	5.00	4.27	4.33	4.50	3.77	4.10	4.00
CO	17.97	9.40	7.77	7.65	17.07	17.10	15.23	13.53	20.43	16.50	21.05	18.85
H2	13.87	9.13	8.67	7.40	19.17	19.05	16.17	15.17	20.47	15.73	21.60	17.20
CH4 + H2 + CO	**36.37**	**21.87**	**19.20**	**17.70**	**41.33**	**41.15**	**35.67**	**33.03**	**45.40**	**36.00**	**46.75**	**40.05**

Grass Pellets											
T (°C)	650.00				750.00				800.00			
ER	**0.070**	**0.100**	**0.120**	**0.140**	**0.070**	**0.100**	**0.120**	**0.140**	**0.070**	**0.100**	**0.120**	**0.140**
O2	0.80	0.93	0.87	0.90	0.93	0.93	1.03	0.87	0.93	0.93		
N2	54.63	61.07	64.27	63.93	46.53	54.87	66.50	60.93	46.53	54.87		
CO2	19.33	18.50	18.43	18.10	17.10	17.10	15.37	16.50	17.10	17.10		
CH4	4.33	3.17	2.13	1.93	4.80	2.97	2.47	2.53	4.80	2.97		
CO	8.50	6.83	5.80	5.93	12.90	9.97	7.70	8.90	12.90	9.97		
H2	12.40	9.50	8.50	9.20	17.73	14.17	6.93	10.27	17.73	14.17		
CH4 + H2 + CO	**25.23**	**19.50**	**16.43**	**17.07**	**35.43**	**27.10**	**17.10**	**21.70**	**35.43**	**27.10**		

References

[1] Ahrenfeldt J, Thomsen TP, Henriksen U, Clausen LR. Biomass gasification cogeneration — a review of state of the art technology and near future perspectives. Appl Therm Eng 2013;50(2):1407−17. 2013/02/01/.

[2] Ferreira SD, Lazzarotto IP, Junges J, Manera C, Godinho M, Osório E. Steam gasification of biochar derived from elephant grass pyrolysis in a screw reactor. Energy Convers Manag 2017;153:163−74. 2017/12/01/.

[3] Afgan NH, Gobaisi DA, Carvalho MG, Cumo M. Sustainable energy development. Renew Sustain Energy Rev 1998;2(3):235−86. 1998/09/01/.

[4] Szczodrak J, Fiedurek J. Technology for conversion of lignocellulosic biomass to ethanol. Biomass Bioenergy 1996;10(5):367−75. 1996/01/01/.

[5] Kirch T, Medwell PR, Birzer CH, van Eyk PJ. Small-scale autothermal thermochemical conversion of multiple solid biomass feedstock. Renew Energy 2020;149:1261−70.

[6] Kaur-Sidhu M, Ravindra K, Mor S, John S. Emission factors and global warming potential of various solid biomass fuel-cook stove combinations. Atmos Pollut Res 2020;11(2):252−60. 2020/02/01/.

[7] Asadullah M. Barriers of commercial power generation using biomass gasification gas: a review. Renew Sustain Energy Rev 2014;29:201−15. 2014/01/01/.

[8] Singh Siwal S, Zhang Q, Sun C, Thakur S, Kumar Gupta V, Kumar Thakur V. Energy production from steam gasification processes and parameters that contemplate in biomass gasifier − a review. Bioresour Technol 2020;297: 122481. 2020/02/01/.

[9] Sikarwar VS, et al. An overview of advances in biomass gasification. Energy Environ Sci 2016;9(10):2939−77. https://doi.org/10.1039/C6EE00935B.

[10] Heidenreich S, Foscolo PU. New concepts in biomass gasification. Prog Energy Combust Sci 2015;46:72−95. 2015/02/01/.

[11] Safarian S, Unnþórsson R, Richter C. A review of biomass gasification modelling. Renew Sustain Energy Rev 2019;110:378−91. 2019/08/01/.

[12] Sansaniwal SK, Pal K, Rosen MA, Tyagi SK. Recent advances in the development of biomass gasification technology: a comprehensive review. Renew Sustain Energy Rev 2017;72:363−84. 2017/05/01/.

[13] Ghassemi H, Shahsavan-Markadeh R. Effects of various operational parameters on biomass gasification process; a modified equilibrium model. Energy Convers Manag 2014;79:18−24. 2014/03/01/.

[14] Anis S, Zainal ZA. Tar reduction in biomass producer gas via mechanical, catalytic and thermal methods: a review. Renew Sustain Energy Rev 2011;15(5):2355−77. 2011/06/01/.

[15] Belgiorno V, De Feo G, Della Rocca C, Napoli RMA. Energy from gasification of solid wastes. Waste Manag 2003;23(1):1−15. 2003/01/01/.

[16] Ongen A, Ozcan HK, Ozbas EE. Gasification of biomass and treatment sludge in a fixed bed gasifier. Int J Hydrogen Energy 2016;41(19):8146−53. 2016/05/25/.

[17] Abdoulmoumine N, Kulkarni A, Adhikari S. Effects of temperature and equivalence ratio on pine syngas primary gases and contaminants in a bench-scale fluidized bed gasifier. Ind Eng Chem Res 2014;53(14):5767−77. 2014/04/09.

[18] Narváez I, Orío A, Aznar MP, Corella J. Biomass gasification with air in an atmospheric bubbling fluidized bed. Effect of six operational variables on the quality of the produced raw gas. Ind Eng Chem Res 1996;35(7):2110−20. 1996/01/01.

[19] González-Vázquez MP, García R, Gil MV, Pevida C, Rubiera F. Comparison of the gasification performance of multiple biomass types in a bubbling fluidized bed. Energy Convers Manag 2018;176:309−23. 2018/11/15/.

[20] Aydin ES, Yucel O, Sadikoglu H. Numerical and experimental investigation of hydrogen-rich syngas production via biomass gasification. Int J Hydrogen Energy 2018;43(2):1105−15. 2018/01/11/.

[21] Sheth PN, Babu BV. Experimental studies on producer gas generation from wood waste in a downdraft biomass gasifier. Bioresour Technol 2009;100(12): 3127−33. 2009/06/01/.

[22] Pereira EG, da Silva JN, de Oliveira JL, Machado CS. Sustainable energy: a review of gasification technologies. Renew Sustain Energy Rev 2012;16(7): 4753−62. 2012/09/01/.

[23] Lapuerta M, Hernández JJ, Pazo A, López J. Gasification and co-gasification of biomass wastes: effect of the biomass origin and the gasifier operating conditions. Fuel Process Technol 2008;89(9):828−37. 2008/09/01/.

[24] Gómez-Barea A, Leckner B. Modeling of biomass gasification in fluidized bed. Prog Energy Combust Sci 2010;36(4):444−509. 2010/08/01/.

[25] Pio DT, Tarelho LAC, Matos MAA. Characteristics of the gas produced during biomass direct gasification in an autothermal pilot-scale bubbling fluidized bed reactor. Energy 2017;120:915−28. 2017/02/01/.

[26] Asadullah M. Biomass gasification gas cleaning for downstream applications: a comparative critical review. Renew Sustain Energy Rev 2014;40:118−32. 2014/12/01/.

[27] Meng F, Ma Q, Wang H, Liu Y, Wang D. Effect of gasifying agents on sawdust gasification in a novel pilot scale bubbling fluidized bed system. Fuel 2019;249:112−8. 2019/08/01/.

[28] Campoy M, Gómez-Barea A, Villanueva AL, Ollero P. Air−Steam gasification of biomass in a fluidized bed under simulated autothermal and adiabatic conditions. Ind Eng Chem Res 2008;47(16):5957−65. 2008/08/01.

[29] Pio DT, Tarelho LAC, Tavares AMA, Matos MAA, Silva V. Co-gasification of refused derived fuel and biomass in a pilot-scale bubbling fluidized bed reactor. Energy Convers Manag 2020;206:112476. 2020/02/15/.

[30] Subramanian P, Sampathrajan A, Venkatachalam P. Fluidized bed gasification of select granular biomaterials. Bioresour Technol 2011;102(2):1914–20. 2011/01/01/.

[31] Sarker S, Bimbela F, Sánchez JL, Nielsen HK. Characterization and pilot scale fluidized bed gasification of herbaceous biomass: a case study on alfalfa pellets. Energy Convers Manag 2015;91:451–8. 2015/02/01/.

[32] Karatas H, Olgun H, Akgun F. Experimental results of gasification of cotton stalk and hazelnut shell in a bubbling fluidized bed gasifier under air and steam atmospheres. Fuel 2013;112:494–501. 2013/10/01/.

[33] Behainne JJR, Martinez JD. Performance analysis of an air-blown pilot fluidized bed gasifier for rice husk. Energy Sustain Dev 2014;18:75–82. 2014/02/01/.

[34] Kim YD, et al. Air-blown gasification of woody biomass in a bubbling fluidized bed gasifier. Appl Energy 2013;112:414–20. 2013/12/01/.

[35] Hervy M, Remy D, Dufour A, Mauviel G. Air-blown gasification of Solid Recovered Fuels (SRFs) in lab-scale bubbling fluidized-bed: influence of the operating conditions and of the SRF composition. Energy Convers Manag 2019;181:584–92. 2019/02/01/.

[36] Makwana JP, Pandey J, Mishra G. Improving the properties of producer gas using high temperature gasification of rice husk in a pilot scale fluidized bed gasifier (FBG). Renew Energy 2019;130:943–51. 2019/01/01/.

[37] Fremaux S, Beheshti S-M, Ghassemi H, Shahsavan-Markadeh R. An experimental study on hydrogen-rich gas production via steam gasification of biomass in a research-scale fluidized bed. Energy Convers Manag 2015;91: 427–32. 2015/02/01/.

[38] Nam H, Rodriguez-Alejandro DA, Adhikari S, Brodbeck C, Taylor S, Johnson J. Experimental investigation of hardwood air gasification in a pilot scale bubbling fluidized bed reactor and CFD simulation of jet/grid and pressure conditions. Energy Convers Manag 2018;168:599–610. 2018/07/15/.

[39] Arena U, Di Gregorio F. Gasification of a solid recovered fuel in a pilot scale fluidized bed reactor. Fuel 2014;117:528–36. 2014/01/30/.

[40] Yu MM, Masnadi MS, Grace JR, Bi XT, Lim CJ, Li Y. Co-gasification of biosolids with biomass: thermogravimetric analysis and pilot scale study in a bubbling fluidized bed reactor. Bioresour Technol 2015;175:51–8. 2015/01/01/.

[41] Serrano D, Kwapinska M, Horvat A, Sánchez-Delgado S, Leahy JJ. Cynara cardunculus L. gasification in a bubbling fluidized bed: the effect of magnesite and olivine on product gas, tar and gasification performance. Fuel 2016;173: 247–59. 2016/06/01/.

[42] Ismail TM, Ramos A, Monteiro E, El-Salam MA, Rouboa A. Parametric studies in the gasification agent and fluidization velocity during oxygen-enriched gasification of biomass in a pilot-scale fluidized bed: experimental and numerical assessment. Renew Energy 2020;147:2429–39. 2020/03/01/.

[43] Di Blasi C, Signorelli G, Di Russo C, Rea G. Product distribution from pyrolysis of wood and agricultural residues. Ind Eng Chem Res 1999;38(6):2216–24. 1999/06/01.

Paper 3

A CPFD model to investigate the influence of feeding positions in a gasification reactor

A CPFD MODEL TO INVESTIGATE THE INFLUENCE OF FEEDING POSITIONS IN A GASIFICATION REACTOR

RAJAN JAISWAL, NORA C. I. S. FURUVIK, RAJAN K. THAPA & BRITT M. E. MOLDESTAD
Department of Natural Science and Maritime Science, University of South-Eastern Norway, Porsgrunn, Norway.

ABSTRACT

The efficiency of a gasification process is directly related to the rate of biomass conversion into product gas. The rate of fuel conversion depends on the interaction of fuel with the bed material, the gasifying agent, and the residence time of fuel particles. The interactions and the residence time depend on the fuel feeding positions along the height of the reactor. Thus, the fuel feeding position in a gasification reactor is an important parameter that influences the efficiency of the gasification process; longer residence time of the fuel particles in the bed enables efficient carbon conversion and less tar formation. In this work, in-bed and on-bed feed positions of the fuel particles have been investigated using a computational particle fluid dynamics (CPFD) model. The model is developed and validated against experimental data obtained from a bubbling fluidized bed gasification reactor. Experiments were carried out in a 20 kW pilot scale bubbling fluidized bed gasification reactor. Wood pellets of 3–30 mm length and 5 mm diameter are fed into the reactor at a mass flow rate of 2.4 kg/h. The molar flow rate of the producer gas, which typically consists of CH_4, CO, CO_2, and H_2 for both the in-bed and on-bed cases, is calculated by the CPFD model. The results show that CO and CH_4 concentrations increase in the product gas when the biomass is fed at the location near to the bottom of the bed, while CO_2 and H_2 increase in the case of on-bed feed. The fuel particles segregate, followed by partial combustion of the smaller fuel particles on the bed surface in the case of on-bed feed. The total mass of the bed including unreacted char is higher for on-bed feed, indicating that the char is consumed slowly. The CPFD model can predict the product gas compositions, the fuel conversion, changes in the bed hydrodynamics, and the product gas yield at different feeding positions of the fuel particles. Thus, the model can be useful for design purposes.

Keywords: computational particle fluid dynamics, feed positions, fluidized bed, gasification, wood pellets.

1 INTRODUCTION

Gasification of biomass is a sustainable conversion technology to cope with an increasing environmentally friendly energy demand. The interest for gasification using fluidized bed is growing, since the process provides uniform heat transfer and fuel flexibility [1]. Ideal mixing of the fuel particles, the bed material, and the gas phase promotes excellent heat transfer in a fluidized bed. The efficiency of the gasification process is determined by the conversion rate of biomass (to the product gas) [2]. The conversion of solid biomass into producer gas is a complex thermochemical process that occurs in several steps. The first step is drying and devolatilization. The volatile components are released as soon as the biomass is fed into the reactor, and this step is known as pyrolysis. The char remaining after volatilization of biomass is gasified at temperatures in the range of 700°C–800°C using steam or air as the gasifying agent. For a given feedstock, the quality of the product gas is dependent on the air to fuel ratio [3, 4], the temperature of the reactor [3], the residence time of fuel in the reactor [5, 6], and the feed position [7]. The feed position of biomass to the reactor influences the distribution of biomass inside the bed, and thus the fuel conversion efficiency. The conversion rate of biomass is dependent on the contact time between the biomass and the gasifying agent and the amount of heat the biomass requires for chemical conversion. The density difference between the bed material and the biomass causes particles to segregate in a fluidized bed.

Furthermore, the lift force exerted by the gas bubbles that envelops the biomass during devolatilization transports the lower-density and larger-size biomass to the surface of the bed [8, 9]. The segregation of biomass is more intense in the case of on-bed feed as the biomass tends to remain on the surface of the bed, increasing the residence time. The residence time of the biomass can be estimated based on the transportation time of the biomass between two reference locations, the relative amount of the fuel participating in reactions, and the time elapsed before complete conversion of the biomass is achieved [6].

Several experimental works have been conducted on the on-bed and in-bed feed of fuel in the past. Ross *et al.* [10] used a lab-scale bubbling fluidized bed to study the influence of feed positons. They measured the gas compositions at different axial locations and found a higher concentration of C_1–C_3 hydrocarbons when the feed position was on the bed surface. In another work, Vriesman *et al.* [11] studied the influence of feed positions on the nitrogen conversion into NH_3 and HCN in a fluidized bed gasifier at different temperatures and equivalence ratios. They found that the feed positions do not influence the product gas. Di Celso *et al.* [12] investigated the influence of feed positions on fluidized bed gasification and concluded that the in-bed feed position has improved carbon conversion compared to on-bed feeding. There is very limited literature available to illustrate the effect of feed positions in the gasifier using a computational particle fluid dynamics (CPFD) model.

In this work, a CPFD model is developed using the commercial software Barracuda to study the influence of the feed position. Experimental data are obtained from gasification of wood pellets in a pilot-scale bubbling fluidized bed reactor. A computational setup is developed and the results from the simulations are compared with experimental data to validate the model. The CPFD model is used to study the influence of on-bed and in-bed feed positions on the product gas yields, char conversion, and bed behavior. The CPFD model developed in this work can be used to design and study a pilot-scale and industrial scale gasifier.

2 EXPERIMENTAL STUDY OF BIOMASS GASIFICATION

2.1 Experimental setup

The experimental setup consists of a cylindrical reactor with inner diameter of 0.1 m and height of 1.0 m. The reactor is made of stainless steel, and the thickness of the walls is 4 mm. The reactor is heated up with three electric heating elements mounted externally on the wall of the reactor. To prevent heat loss, the outer surface of the reactor is insulated with 200-mm-thick fiberglass and the inner surface is coated with a refractory material. Five pressure sensors and five thermocouples, which measure the change in pressure and temperature during the operation of the reactor, are attached at different heights. Figure 1 shows the experimental setup, the dimensions of the reactor, and the dimensions of the wood pellets used in this work. The biomass from the silo (A) is conveyed to the reactor (B) via a cold screw attached to the silo and a hot screw connected to the reactor. The feed rate of the wood pellets is calibrated by measuring the average flow rates at specified motor speeds. The mass flow rate of air supplied to the reactor is measured with a BROOK air flowmeter. An electric heater is used to heat the compressed air before it is passed into the reactor. The outlet of the reactor is open to the atmosphere and the product gas passes through the flaring system (D) where it is burned to avoid direct discharge of combustible gases to the atmosphere. A sampling line (C) is connected at the top of the reactor and the collected gas samples are measured in an offline SRI gas chromatograph (GC). The GC has a thermal conductivity detector (TCD) and
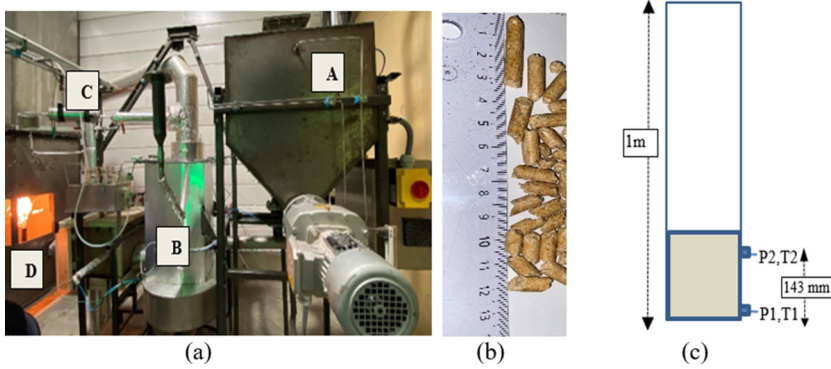
Figure 1: Experimental setup: (a) experimental rig, (b) wood pellets, (c) reactor dimensions.

Table 1: Properties of the particles.

Material	Density, ρ_p	Mean diameter	Sphericity, φ_p	Particle volume fraction, ε_p
Sand	2600 kg/m^3	$d_m = 0.292$ mm	0.86	0.52
Wood pellets	1300 kg/m^3	8.9 mm	-	0.44

uses helium as the carrier gas. The GC can measure the major components of the gas sample. Table 1 shows the density (, mean diameter , sphericity (), and volume fraction () of the particles.

The experiment is carried out as a continuous process where the air flow rate is 2 kg/h and the feed rate of wood pellets is 2.42 kg/h. The wood pellets are cylindrical in shape with 6 mm diameter and 3–30 mm length. Sand particles of mean diameter 292 μm are used as the bed material. The mean particle size of the sand is obtained using sieve analysis, and the volume equivalent spherical diameter of the wood pellets is calculated from eqn (1):

$$d_{m,s} = \left(\frac{6V_P}{\pi} \right)^{1/3}$$
(1)

where V_P is the mean particle volume and is the mean volume equivalent spherical particle diameter.

2.2 Experimental results

The air to fuel ratio is maintained at a constant value with a continuous air supply of 2 kg/h and a feed rate of wood pellets of 2.42 kg/h. A static bed height of 0.2 m is used for the experiment. Initially, the bed material is heated with both an electric heater and pre-heated air up to 750 °C. The temperature of the reactor is maintained at .

Figure 2a shows the temperature variation in the bed with time measured by the temperature sensor T2. As soon as the wood pellets are fed into the reactor at , volatile gases are released consuming heat from the system. The drop in temperature during volatilization is marked as ΔT. The corresponding pressure variations of the bed, measured by pressure
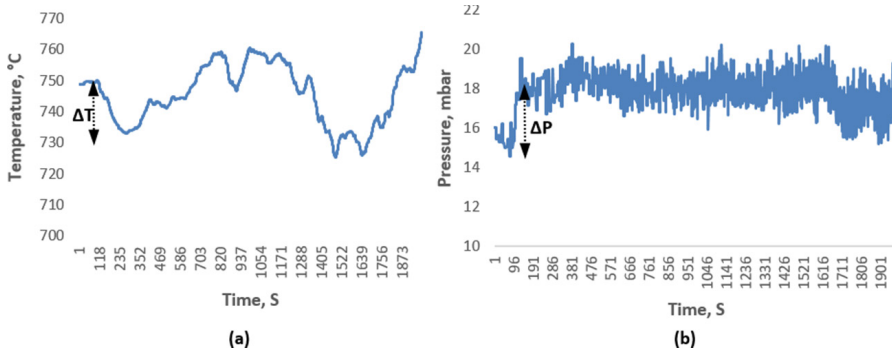
Figure 2: (a) Temperature and (b) pressure in the bed at air velocity 2 kg/h.

sensor P1, are shown in Fig. 2b. Since the P1 sensor is located at the bottom of the bed, it gives the total pressure of the bed. The increase in pressure drop from 15 to 18 mbar is due to the increasing wood pellets' load on the bed during the experiment. The pressure after 134 s is about constant, indicating that the amount of wood pellets added to the bed and the rate at which the wood pellets are converted into product gases and char are constant. Three samples of the product gases are taken at 15-minute intervals and analyzed in the GC. The average molar percentages of the product gases from the three samples are calculated and considered as the representative values of the product gases. The average molar percentages of CH_4, CO, CO_2, N_2, H_2 and O_2 in the samples are 4.97%, 17.09%, 15.58%, 42.5%, 19.08%, and 0.69%, respectively.

3 COMPUTATIONAL MODEL

A cylindrical geometry with the same dimensions as the reactor used in the experiment is drawn in AutoCAD and imported to Barracuda. A uniform grid of totally 5120 cells is generated using the default grid setting available in Barracuda. Pressure and flow boundary conditions are defined at the top and bottom of the reactor as shown in Fig. 3. Data points are located at different heights along the reactor to measure pressure, temperature, and gas compositions. Two positions, on-bed and in-bed, at heights of 24 and 4 cm from the bottom of the reactor, are used to feed biomass into the reactor. The close pack volume fraction is 0.63 and the maximum momentum redirection from collision is 40%. The normal-to-wall momentum retention and tangent-to-wall momentum retention are 0.3 and 0.99, respectively.

In the CPFD model, it is assumed that the volatilization of biomass is an instantaneous process. As soon as the biomass is fed into the reactor at 700–800°C, the volatile components are released and the char particles left after volatilization of biomass are gasified at a sufficient temperature and air flow rate. The degradation of biomass into volatile components and char follows various reaction routes. The major reactions and the corresponding kinetics for the gasification process used in this work are taken from literature and are listed in Table 2.

The biomass in the CPFD model is initialized as volatile components, char, and ash. The composition and quantity of the volatile components, char, and ash used in the CPFD model are obtained from proximate analysis of wood pellets as listed in Table 3.
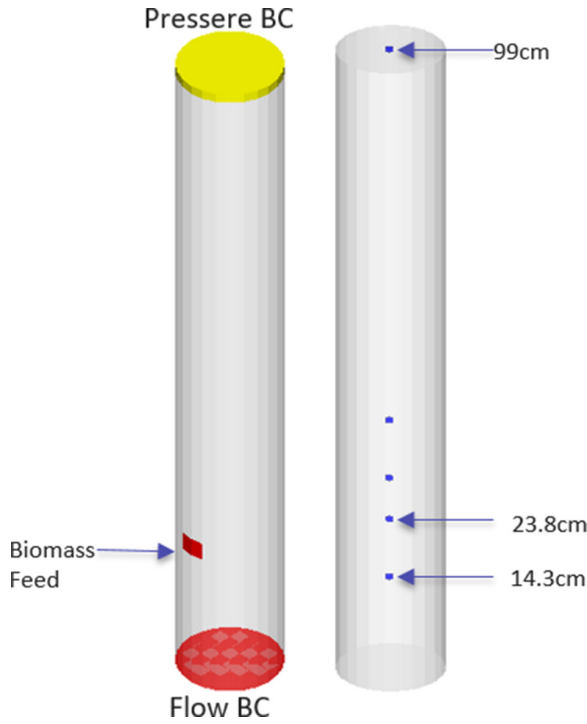
Figure 3: Boundary conditions and transient data points used in the CPFD model.

Table 2: Reactions and rate kinetics used in the CPFD model.

Chemical reactions	Kinetics
Char partial combustion [13] $2C + O_2 \leftrightarrow 2CO$	$r = 4.34 \times 10^{10} \, m_s \theta_f \exp\left(\dfrac{-13590}{T}\right)[O_2]$
CO oxidation [13] $CO + 0.5O_2 \leftrightarrow CO_2$	$r = 5.62 \times 10^{12} \exp\left(\dfrac{-16000}{T}\right)[CO][O_2]^{0.5}$
H_2 oxidation [14] $H_2 + 0.5O_2 \leftrightarrow H_2O$	$r = 5.69 \times 10^{11} \exp\left(\dfrac{-17610}{T}\right)[H_2][O_2]^{0.5}$
CH_4 oxidation [13] $CH_4 + 2O_2 \leftrightarrow CO_2 + 2H_2O$	$r = 5.0118 \times 10^{11} \, T^{-1} \exp\left(\dfrac{-24357}{T}\right)[CH_4][O_2]$
Water gas shift reaction [13] $CO + H_2O \leftrightarrow CO_2 + H_2$	$r = 7.68 \times 10^{10} \, T \exp\left(\dfrac{-36640}{T}\right)[CO]^{0.5}[H_2O]$
Methane reforming [15] $CH_4 + H_2O \leftrightarrow CO + 3H_2$	$r = 3.00 \times 10^5 \exp\left(\dfrac{-15042}{T}\right)[CH_4][H_2O]$

Table 3: Properties of wood pellets (proximate analysis).

Components	
Moisture content	7%
Volatile matter	78.75%
Fixed carbon	14.4%
Ash content	0.279%
LHV	18.94 MJ/kg

4 RESULTS AND DISCUSSION

In this section, CPFD model validation, influence of the feed positions on the composition of the product gas, and bed hydrodynamics are presented and discussed.

4.1 Model validation

CPFD models in Barracuda use the multiphase particle in cell approach, where gas–solid interaction is modelled using the combined Eulerian and Lagrangian approach. With the CPFD setup described in Section 3, simulations are carried out using the Wen and Yu drag model. The simulations are performed for 700 s with a time step of 0.001 s. The molar composition of the product gas is measured in the upper part of the gasifier. The product gas compositions obtained from the simulation and experiment are compared in Fig. 4. The results show that the CPFD model is predicting the gas compositions very well.

The product gas compositions in the gasification process is dependent on temperature, residence time, interaction of biomass with bed material, and the gasifying agent. The biomass breaks thermally into volatile components, char, and tar following different reaction routes. Figure 5 shows the variations in the product gas composition with time when the wood pellets are fed in-bed. The product gases are more stable in the case of in-bed feed of wood pellets compared to on-bed feed shown in Fig. 6. The wood pellets have a density approximately half of that of sand particles. When the bed is fluidized and the wood pellets are fed close to the bottom of the reactor (in-bed), the wood pellets have sufficient time and contact area to interact with the heated bed material and the fluidizing gas before they are
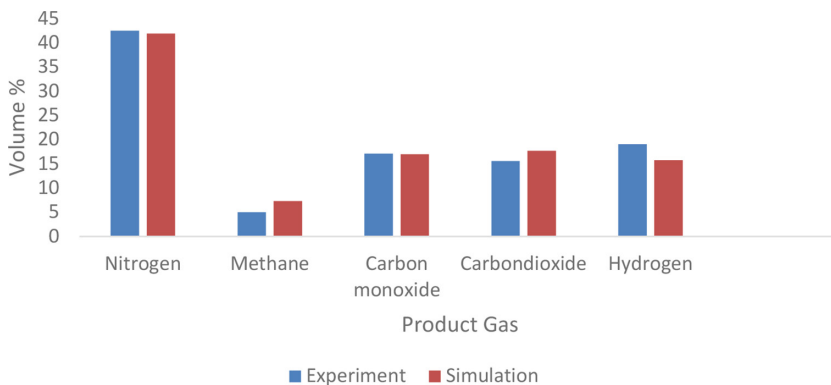

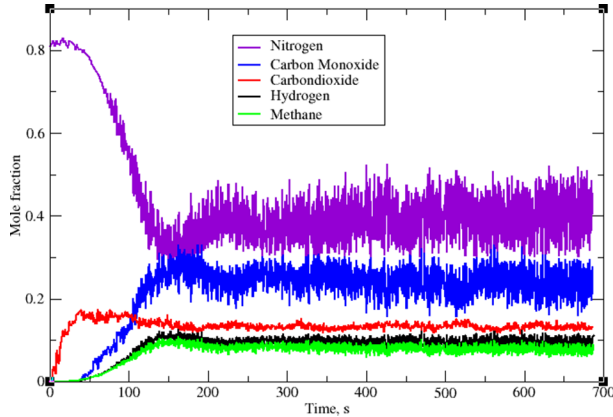Figure 4: Product gas compositions from the CPFD model and experiment.

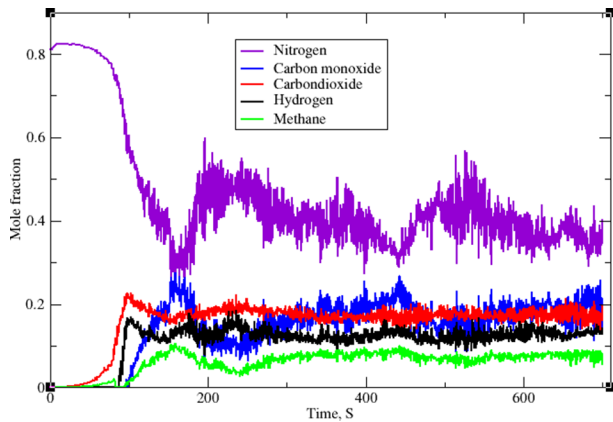Figure 5: Composition of product gases with in-bed feed of wood pellets.

Figure 6: Composition of product gases with on-bed feed of wood pellets.

transported to the upper region of the bed. This means that the wood pellets react in the bed and the solid fuel particles reaching the surface of the bed are mainly char. Mixing of the wood pellets with the bed material is limited in the case of on-bed feeding, and poor mixing results in larger variations in gas composition with time.

The composition of the product gas predicted by the CPFD simulations with on-bed and in-bed feed is compared in Fig. 7. The results show that with in-bed feed of biomass, the molar fraction of CH_4 and CO in the product gas increases from 7.3% and 17% to 7.8% and 23.4%, respectively. The presence of sufficient char inside the bed and longer interaction time of the char with the bed material and oxygen enhance the partial combustion reaction, resulting in a significant increase in CO. The fractions of H_2 and CO_2 are increased in the case of on-bed feeding compared to the case of in-bed feeding. The main part of oxygen from the gasifying agent (air) is consumed near to the surface of the bed. The oxidation reaction routes of CO, H_2, and CH_4 are dominant, which increases the H_2O and the CO_2 fractions. Due to the increase in H_2O in the free board, the water gas shift reaction increases producing more H_2 and CO_2.
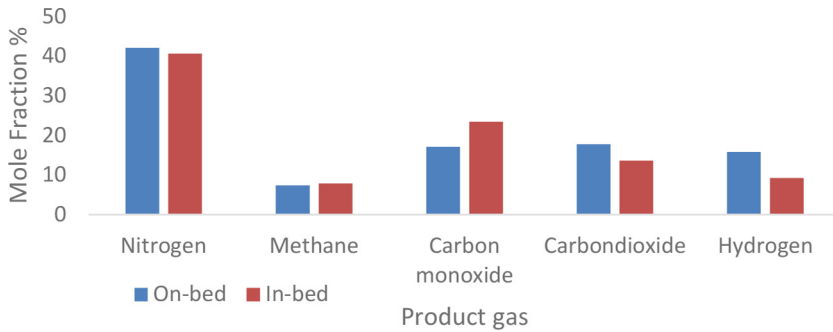
Figure 7: Average product gas compositions for on-bed and in-bed feed.

4.2 Char conversion

In the CPFD model, the mass of sand particles is assumed constant, whereas the biomass varies due to the convertion of biomass into a product gas, char, and tar. Thus, change in the total mass of the bed is only dependent on the biomass conversion rate in the bed. The total particle mass of the bed versus time for the on-bed and in-bed feed positions is presented in Fig. 8. For the same amount of biomass feed, the total mass of the particles is higher in the case of on-bed feed compared to in-bed feed. The total mass of the bed increases sharply initially and decreases after a certain period of time. The rapid increase in the total mass of the bed at the beginning is because the conversion rate of the char is slower. At this stage, maximum heat from the system is utilized for volatilization of biomass, followed by the dominant endothermic reactions. After a certain period of time, the exothermic reaction routes compensate the heat loss from the system, which increases the char conversion rate. The total mass of the bed thus increases gradually. It can be seen from Fig. 8 that during the first 100 s, the total mass of the bed increases at the same rate for both cases. After 100 s, increment in total mass of the bed is higher in the case of on-bed feed because the biomass dropped on the surface of the bed does not interact uniformly with the bed material. This results in more char particles to remain unreacted and to accumulate on the surface of the bed, increasing the total mass of the bed.
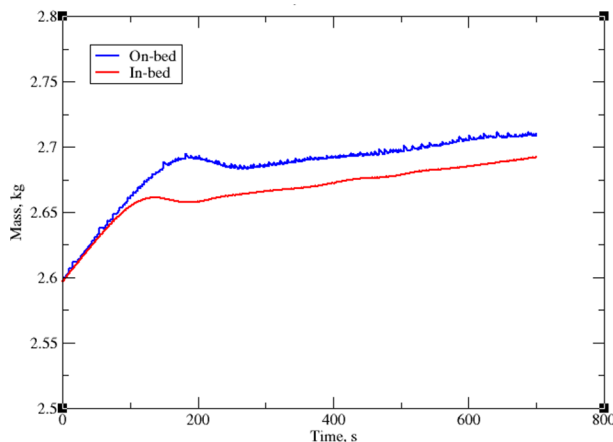

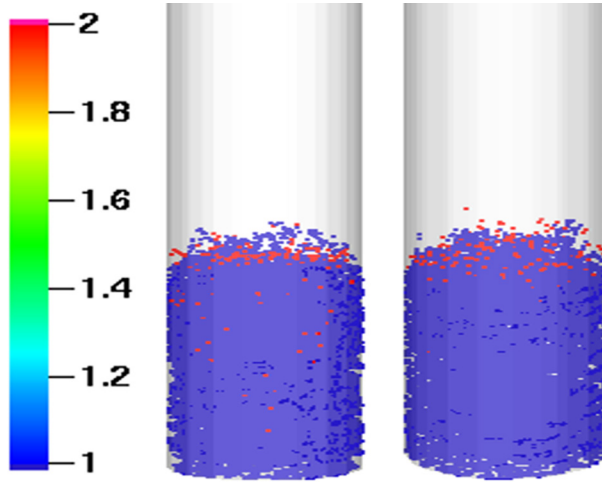Figure 8: Change in total mass of the bed with time.

Figure 9: Particle species of the bed at 221 s. In-bed feed to the left and on-bed feed to the right.

4.3 Bed hydrodynamics

The density of the wood pellets is approximately half of the density of sand particles. When the bed is fluidized and the wood pellets are fed near the bottom of the reactor, they are transported to the upper region of the bed with time. The movement of fuel particles from lower to upper region is dependent on the superficial gas velocity and the rate of consumption of fuel inside the bed. Figure 9 compares the distribution of fuel particles inside the bed for on-bed and in-bed feed after 221 s. It shows that the fuel particles are mixed with the bed material in the case of in-bed feed. Before the particles are transported to the surface, they have sufficient time to interact with the bed material and air, increasing the gasifier performance as discussed in sections 4.2 and 4.3. With on-bed feed, the fuel particles are segregated and remain accumulated on the surface of bed, affecting the char conversion rate. Mixing of the fuel particles can be enhanced by increasing the superficial gas velocity. However, for maximum gasifier efficiency and provided air to fuel ratio, the increment of superficial gas velocity is limited to operate the gasifier in a specified operating regime [16].

5 CONCLUSION

A CPFD model developed in Barracuda VR in this work is used to predict the effect of on-bed and in-bed feed positions on the gasification process. The CPFD model is developed and validated against experimental data from a pilot scale bubbling fluidized bed gasifier. Wood pellets are used as the feed and air as the fluidizing gas. The product gas compositions and char conversion are measured for the on-bed and in-bed feed positons of biomass. The influence of the feed position on the product gas composition, char conversion, and bed behavior is investigated.

The result shows that the volume percentages of CH_4, CO, H_2, CO_2, and N_2 in product gas for the on-bed case are 7.3%, 17%, 15.7%, 17.7%, and 42%, respectively, and for the in-bed case, the volume percentages are 7.8%, 23.4%, 9.1%, 13.6%, and 40%, respectively. The increase in the fraction of CO in the case with in-bed feed is due to the enhanced char partial combustion route. In the case of on-bed feed, the H_2O fraction increases in the free board,

which enhances the water gas shift reaction and increases H_2 and CO_2 fractions in the product gas. It is found that for the same amount of biomass feed, the mass of unreacted char is higher when the biomass is fed above the surface of the bed. In addition, the accumulation of char occurs on the surface of the bed. The residence time of the biomass increases when it is injected near the bottom of the bed, which provides sufficient time for the biomass to interact with the bed material and the gasifying fluid. In the case of in-bed feeding of biomass, the biomass is well mixed and distributed inside the bed, and thus the conversion of char occurs efficiently. The developed CPFD model is able to predict the product gas compositions, fuel conversion, bed hydrodynamics, and the product gas composition under different operational conditions, and will be important for further simulations and design purposes.

REFERENCES

[1] Jaiswal, R., Agu, C.E., Thapa, R. & Moldestad, B.M., Study of fluidized bed regimes using Computational Particle Fluid Dynamics. *Linköping Electronic Conference Proceedings*, **153**, pp. 271–276, 2018. https:// doi.org/10.3384/ecp18153271

[2] Timmer, K.J. & Brown, R.C., Transformation of char carbon during bubbling fluidized bed gasification of biomass. *Fuel*, **242**, pp. 837–845, 2019. https://doi.org/10.1016/j.fuel.2019.01.039

[3] Begum, S., Rasul, M., Akbar, D. & Naveed, R., Performance analysis of an integrated fixed bed gasifier model for different biomass feedstocks. *Energies*, **6**, pp. 6508–6524, 2013. https://doi.org/10.3390/en6126508

[4] Manyà, J.J., Sánchez, J.L., Ábrego, J., Gonzalo, A. & Arauzo, J., Influence of gas residence time and air ratio on the air gasification of dried sewage sludge in a bubbling fluidised bed. *Fuel*, **85(14)**, pp. 2027–2033, 2006. https://doi.org/10.1016/j.fuel.2006.04.008

[5] Ling, M., Esfahani, M.J., Akbari, H. & Foroughi, A., Effects of residence time and heating rate on gasification of petroleum residue. *Petroleum Science and Technology*, **34(22)**, pp. 1837–1840, 2016. https://doi.org/10.1080/10916466.2016.1230752

[6] Agu, C.E., Pfeifer, C., Eikeland, M., Tokheim, L.-A. & Moldestad, B.M.E., Measurement and characterization of biomass mean residence time in an air-blown bubbling fluidized bed gasification reactor. *Fuel*, **253**, pp. 1414–1423, 2019.

[7] Wilk, V., Schmid, J.C. & Hofbauer, H., Influence of fuel feeding positions on gasification in dual fluidized bed gasifiers. *Biomass and Bioenergy*, **54**, pp. 46–58, 2013. https://doi.org/10.1016/j.biombioe.2013.03.018

[8] Jaiswal, R., Furuvik, N.C.I., Thapa, R.K., & Moldestad, B.M.E., Investigation of the segregation and mixing behavior of biomass in a bubbling fluidized bed reactor using a CPFD model. *Linköping Electronic Conference Proceedings*, **170**, pp. 164–169, 2019.

[9] Fiorentino, M., Marzocchella, A. & Salatino, P., Segregation of fuel particles and volatile matter during devolatilization in a fluidized bed reactor—I. Model development. *Chemical Engineering Science*, **52(12)**, pp. 1893–1908, 1997. https://doi.org/10.1016/s0009-2509(97)00018-3

[10] Ross, D., Noda, R., Horio, M., Kosminski, A., Ashman, P. & Mullinger, P., Axial gas profiles in a bubbling fluidised bed biomass gasifier. *Fuel*, **86(10)**, pp. 1417–1429, 2007. https://doi.org/10.1016/j.fuel.2006.11.028

[11] Vriesman, P., Heginuz, E. & Sjöström, K., Biomass gasification in a laboratory-scale AFBG: influence of the location of the feeding point on the fuel-N conversion. *Fuel*, **79(11)**, pp. 1371–1378, 2000. https://doi.org/10.1016/s0016-2361(99)00278-1

[12] Di Celso, G.M., Rapagna, S., Marina, S. & Zanoelo, E.F., Effect of biomass feed position on the kinetics of devolatilization in a fluidized bed. *Chemical Engineering Transactions*, **37**, pp. 235–240, 2014.

[13] Xie, J., Zhong, W., Jin, B., Shao, Y. & Huang, Y., Eulerian–Lagrangian method for three-dimensional simulation of fluidized bed coal gasification. *Advanced Powder Technology*, **24(1)**, pp. 382–392, 2013. https://doi.org/10.1016/j.apt.2012.09.001

[14] Bates, R.B., Steam-air blown bubbling fluidized bed biomass gasification (BFBBG): Multi-scale models and experimental validation. *AIChE Journal*, **63(5)**, pp. 1543–1565, 2017. https://doi.org/10.1002/aic.15666

[15] Solli, K.-A., Thapa, R.K. & Moldestad, B.M.E., Screening of kinetic rate equations for gasification simulation models. *Proceedings of The 9th EUROSIM Congress on Modelling and Simulation, EUROSIM 2016*, **142**, pp. 105–112, 2016. https://doi.org/10.3384/ecp17142105

[16] Jaiswal, R., Furuvik, N.C.I., Thapa, R.K. & Moldestad, B.M.E., Method of identifying an operating regime in a bubbling fluidized bed gasification reactor. *International Journal of Energy Production and Management*, **5(1)**, pp. 24–34, 2020. https://doi.org/10.2495/eq-v5-n1-24-34

Paper 4

Influence on the fluidization pattern of a freely bubbling fluidized bed with different modes of air supply

Influence on the fluidization pattern of a freely bubbling fluidized bed with different modes of air supply

Rajan Jaiswal *, Marianne S. Eikeland, Britt M. E. Moldestad, Rajan K. Thapa

University of South-Eastern Norway, Faculty of Technology, Kjølnes rig 56, 3918, Porsgrunn, Norway

rajan.jaiswal@usn.no

Abstract

Bubbling fluidized bed (BFB) reactors are extensively used in several process applications like gasification, pyrolysis, drying, and combustions due to their excellent mixing properties and good temperature control. The bubble dynamic and particle movement in the reactor is primarily responsible for uniform heat and mass transfer and mixing. The properties of bubbles in BFB are governed by the gas distribution inside the reactor or supply of the fluidizing gas. This work investigates the influence on the fluid dynamic behaviour of the BFB reactor at different fluidizing gas injection systems using the Computational Particle Fluid dynamic model. Three different modes of fluidizing gas injection include uniform injection, air injection via twenty-five nozzles, and air supply via side nozzles along the reactor height in a gasification reactor of 10.04 cm diameter. Air is used as the fluidizing gas and silica sand as the bed material. The CPFD model is developed in Barracuda Virtual reactor 20.01. The CPFD model is validated against the experimental data obtained from the Electrical Capacitance Tomography (ECT) sensors. The result depicts the better fluidization quality of the bed with uniform air supply as flow boundary and air injection via twenty-five nozzles located at the bottom of the reactor. With air injection via two side nozzles along the reactor height, the bed is fluidized with large bubbles and particle entrainment in the freeboard zone of the reactor. A method is proposed to improve the fluidization quality of the bed while using side nozzles as inlet flow Boundary Conditions (BC) for air injection. The proposed method includes addition of four nozzles along the reactor wall instead of two which improves the fluidization quality of the bed in terms of smaller size bubbles without particle entrainment in the freeboard region.

Keywords: Gas distribution, flow boundary conditions, bubbling-fluidized bed, bubble properties, CPFD

1. Introduction

Fluidized bed reactors are widely used for several industrial applications like waste to energy conversion, chemical synthesis, granulation, drying of pharmaceutical products and raw agricultural products, chemical looping, catalyst regeneration, biomass gasification, pyrolysis etc. (Jaiswal et al., 2020; Bandara et al., 2021; Singh and Gbordzoe, 2017; Chang et al., 2013). The efficiency of the fluidized bed reactors largely depends on the gas distribution inside the reactor since the gas distribution influences the conversion process and the fluidization regime under which the reactor is operated. For instance, during the gasification of biomass or wastes using a bubbling fluidized bed reactor, the carbaneous feedstock is converted into higher calorific value gases in the presence of limited amount of oxidizing agent (Jaiswal et al., 2020). The amount of oxidizing medium present for the feedstock conversion depends on how well the fluidizing gas is distributed across the reactor cross-section. Similarly, the hot bed material which is in a continuous motion in such reactors acts as the thermal flywheel and provides the required heat for thermal degradation of the feedstocks. The particle

motion is governed by the bubbles rising in the bed and the properties of the bubbles for example bubble rise velocity, bubble diameter and bubble frequency is determined by the gas distribution inside the reactor. Additionally, the mixing phenomena of large biomass particles with bed material and the operating regime of the reactor is determined by the gas distribution (fluidizing gas) to the reactor. The fluidizing gas can be supplied to the particle bed through the distributor or nozzles (Basu et al., 2006). The most common method has been the use of a distributor plate that allows to distribute the fluidizing gas uniformly, supports the bed material, provides good gas-solid mixing, prevents channeling, and minimizes dead zones in the reactor (Depypere and Dewettinck, 2004). While using the air distributor or distributor plate, the supply gas velocity has to overcome the distributor plate resistance and lift entire mass of the particles against the gravity in order to fluidize. Alternatively, the fluidizing gas can be supplied to the reactor via orifice or nozzles which can be on the side of the reactor wall or at the bottom of the reactor. It is essential to characterize the fluidized bed behaviour for the specified fluidizing gas flow boundary

conditions for a smooth operation of the reactor (Sasic and Johnsson, 2005). Each of the fluidizing gas supply methods, with or without distributor, nozzles, orifice has its own limitation and advantages. For instance, the use of a distributor plate increases the auxiliary power consumption required to pump the gas through the reactor. Additionally, the distributor plate has to be selected depending on the reactor types and process as the distributor plays a critical role in the reactor performance (Raza et al., 2021). In addition, there are challenges in operating the reactor with the distributor plate, which requires cleaning and maintenance due to clogging of the pores of the distributor plate by the fine particles and sintering. The blockage of the pores in the distributor plate can lead to local de-fluidization and dead zones in the reactor. In this regard, operating the fluidized bed reactor without a distributor can be of great advantages as it can save the operational cost, and the construction and design cost of the distributor plate. At the same time, it helps to avoid the problem associated with the air distributor. Several studies have been conducted on design of the distributor plate and the influence of the distributor plate on the reactor performance (Geldart and Baeyens 1985; Saxena et al., 1979). However, the number studies on operation of a bubbling fluidized bed reactor without an air distributor and comparing the fluid dynamics behaviour of the bed operated with and without distributor are scarce (Agu et al., 2018).There are a few studies on operation of a fluidized bed reactor without an air distributor where large size particles are used at the lower region of the bed and the bed is fluidized by passing the gas through the bed of stationary large particles (Agu et al., 2018).

In a single study, reported on the operation of reactor without an air distributor Agu et al. has studied the bed behaviour with different types of particles and gas velocity based on the pressure and solid circulation using CPFD simulation. However, no information is provided about the grid size and number of computational cells in the article (Agu et al.,2018). The grid number or computational domain in such simulations have significant impact on the fluid dynamics behaviour of the bed and the pressure and flow boundary conditions. Additionally, there are no studies in the literature that mention the influence on the bubble properties in a fluidized bed reactor operated without a distributor plate. Therefore, more work is required to characterize the fluid dynamics behaviour of the bed without an air distributor and compare the fluid dynamics behaviour of the bed with a distributor and different modes of gas supply to the reactor.

The objective of this work is to investigate the fluid dynamics behaviour of the bed without air distributor and compare with uniform air supply methods. The uniform air supply methods include use of an air distributor and nozzles. A cold flow model of the fluidized bed reactor with different air injection methods are simulated using a CPFD model developed in Barracuda VR 20.01. For the case without air distributor the bed is fluidized with air supply from two nozzles (holes) located at the opposite side of the reactor wall. The fluid dynamics behaviour of the bed in terms of solid fraction fluctuation and bubble properties are reported briefly. The results from the CPFD simulations are compared with experimental data obtained from a cold fluidized bed equipped with ECT sensors and an air distributor. A method to improve the fluidization quality of the bed without an air distributor is proposed.

2. Material and methods

2.1. Experimental set up

A cold fluidized bed reactor equipped with ECT sensors, and a data acquisition system are used for the experiments. The reactor is 10.04 cm in internal diameter and 150 cm in height. The reactor column is fitted with an air distributor at the bottom and is open at the top. The air distributor is 3mm thick with a 10.04 cm internal diameter. It has a porosity of 40% with a flow area of 36.6 cm^2 which allows the fluidizing gas to pass through the bed uniformly. The reactor is equipped with twin-plane ECT sensors that are located at 15.7 cm and 28.7 cm from the air distributor. Each of the sensors consists of 12 electrodes mounted on the outer wall of the reactor that allows to capture raw data in the form of matrix or images. The online images are extracted from the capacitance measurements using the Linear Back Projection algorithm. The cross-section of each sensor is divided into 32*32 square pixels of which 812 are the effective pixels that lie within the bed. Each pixel holds a normalized relative permittivity value between 0 and 1, which represents the solid-gas fraction. The details of the reactor set up can be found elsewhere (Agu et al., 2019). The reactor is filled with sand material and fluidized by using compressed air. The fluctuation of solid volume fraction is measured from the transient data for each gas velocity. The raw data from the experiments were processed in MATLAB to obtain the solid fraction fluctuation, bubble properties, and bed flow dynamics behaviour.

2.2. Simulation set up

The CPFD simulations in this work have been carried out using a commercial software Barracuda VR which consists of numerical codes specially designed for applications in the multiphase flow systems like industrial fluidized bed reactors.

Initially, the reactor is filled with bed material with a static bed height of 30 cm. The properties of bed

material like density (2650 kg/m3), and particle size distribution, sphericity (0.86), close pack volume fraction (0.63), are defined similarly to that of the experiment. The particle size distribution was measured from the sieve analysis with mean diameter 423μm.
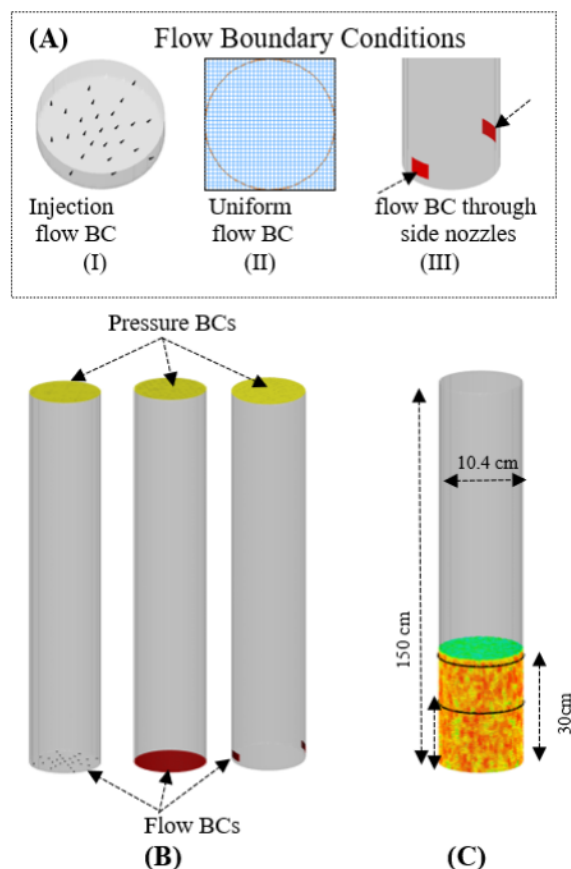

Figure 1: (A-B) flow and pressure boundary conditions, (C) flux planes, initial bed height and reactor dimension.

For the simulation of gas-particle flows, 3D multiphase particle-in-cell approach is used where solid particles are modeled as discrete Lagrangian methods and the fluid is modeled as Eulerian grid of cells. To create a virtual reactor, a CAD geometry equal to the experimental column is imported to Barracuda VR. A uniform grid of total 102400 cells were defined which provides the control volume for all fluid fields calculations. The reactor is operated at atmospheric pressure. Therefore, the pressure boundary condition is defined at the top of the reactor. Three different flow boundary conditions were set up for different modes of gas supply to the reactor as shown in Fig. 1(A). The fluidizing gas is supplied to the reactor using injections points, uniformly distributed along the reactor cross-section (grids or distributor) and through side nozzles (holes). 25 injection points were defined along the reactor cross-section shown in Fig. 1A(I). The mass flow rate through each nozzle (injection points) was equally distributed. Similarly, for the

second case, uniform flow boundary conditions are defined at the bottom of the reactor. The reactor cross-section is divided into 1024 cells. The 812 effective pixels or grids that cover the reactor cross-section as shown by the red circle in Fig. 1A(II)) is used as the flow BC. For the third case, two nozzles or holes located on the opposite side of the reactor wall are defined as the flow boundary conditions (as shown in Fig. A(III)). The size of the nozzles is 0.5 cm in diameter. Also, two planes are set up at heights 15.7 cm and 28.7 cm along the height of the reactor column to measure the transient raw data for each of the flow boundary conditions. The drag model used in fluidized bed simulations is an important factor that determines the force acting on a particle by the flow of fluid around it. In this work, the Wen-Yu and Ergun blended drag model is used where the Wen-Yu drag model is suitable for the dilute phase and the Ergun model is used for the dense phase. The details of the drag model, and the governing momentum and force equation can be found elsewhere (O'Rourke and Snider, 2012; Sinder, 2001; Andrews and O'Rourke, 1996; Weber et al., 2013).

3. Results and Discussion

For maximum conversion efficiency, it is important to operate a BFB reactor above minimum fluidization velocity and within a bubbling regime. In this work employs methods to identify the fluidization quality of the bed based on solid volume fraction fluctuation and bubble properties measurement. In addition, influence of different air supply modes on the fluid dyncmics behaviour of the bed are presented.

3.1. Model Validation

The CPFD model is validated by comparing the solid volume fraction fluctuation measured from the experimental data and CPFD simulations at different gas velocities as shown in Fig. 2. As the air was supplied through the static bed, initially the bed expanded as it reached the superficial gas velocity 0.065 m/s. The bed exhibited into the fluidization regime at superficial gas velocity 0.075 m/s. The results depict that the CPFD model followed a similar trend to that of minimum fluidization velocity and bed expansion. However, the solid fraction fluctuation during bed expansion was higher as predicted by the CPFD model compared to the experimental data. This may be due to the difference in the initialization (packing) of the bed material in the CPFD model compared to the experimental conditions.

Further, the bubbles rising in the bed at the superficial gas velocity of 0.1 m/s at different time steps are compared to check the model robustness. The bubbles rising in the bed at a pre-defined plane in the simulation setup and ECT sensors in the experimental set up were captured for both the

CPFD simulation data and the experimental measurement as shown in Fig. 3. The size of the bubbles and the path along which the bubbles move upward (along the center of the bed) in the bed were similar for both experimental tests and the CPFD simulations. However, the number of bubbles predicted by the CPFD model is higher at a lower superficial gas velocity (0.1 m/s). Due to increase in area of the flow boundary conditions in case of CPFD simulation, smaller size bubbles appeared in the CPFD simulation compared to experimental data.
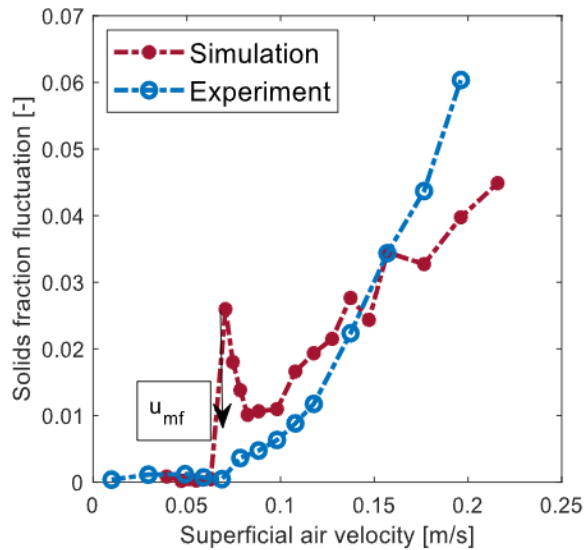

Figure 2: Solid fraction fluctuation at different superficial gas velocities obtained from CPFD simulation and experiment.
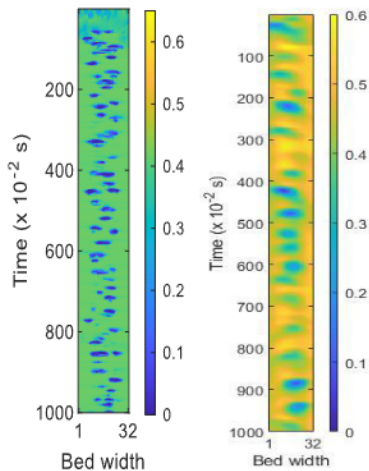

Figure 3: Comparing the rising bubbles in the bed obtained from the CPFD simulation (left side) and experiment (right side) as it reaches the plane at 15.7 cm at the superficial gas velocity 0.1 m/s.

3.2. Influence on solid fraction fluctuation

For a given superficial gas velocity, the variation of the gas-solid fraction in the bed can be used to characterize the fluidization pattern of the bed. The

solid fraction fluctuation across the cross section of the bed at height 27.5 cm and at the superficial gas velocity 0.15 m/s were captured over the measurement of 60s with time steps of 0.001. The average solid fraction fluctuation over the measurement period for different flow boundary conditions (injections BC, nozzle BC, uniform BC) from the CPFD simulation and experimental measurements with air distributor are compared in Fig. 4. The result illustrates that for the experimental measurements with an air distributor the solid fraction was lower towards the center of the bed, and it increases near to the wall of the reactor. A similar trend of solid fraction fluctuation was predicted by the CPFD model with the injection flow BC and the uniform flow BC. However, fluctuation in the solid fraction for both the cases were not smooth compared to the experimental measurements because of smaller bubbles in the bed with the uniform and injection flow BCs. Multiple smaller size bubbles were formed in case of the CPFD simulations due to an increase in flow boundary area as compared to that of the experiment. The decrease in the solid fraction at the lower region of the bed near to the center reveals a higher gas fraction in the region. The gas in a fluidized bed rises from the lower region of the bed to the upper region in the form of bubbles. Therefore, the depression of the solid fraction near to the center of the reactor and the increase near to the wall of the reactor illustrate that the bubbles rise upwards following the path near to center of the reactor. For the flow BCs with two nozzles near to the wall of the reactor, the solid fraction fluctuation was lower near to the wall of the reactor where the nozzles wre defined and near to the center of the bed. The fluidizing gas passes in the form of bubbles where some of the bubbles pass near to the wall while some follow the path near to the center of the bed.
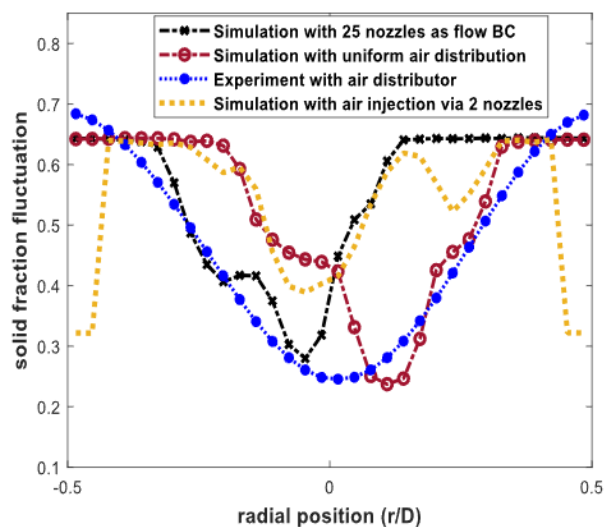

Figure 4: Radial distribution of the solid volume fraction for different flow boundary conditions at superficial gas velocity 0.15 m/s.

3.3. Influence on bubble properties and bed fluid dynamics behaviour

The bubble properties in a BFB reactor significantly influences the fluid dynamics behaviour of the reactor and its performance. The appearance and the movement of the bubbles in the bed is governed by the flow of fluidizing gas through the bed. For the same mass flow rate of the fluidizing gas with different flow boundary conditions, the bubble properties were measured. The influence on the bubble properties and fluidization quality of the bed with different flow boundary condition are compared. The bubbles in BFD can be distinguished from the dense phase by using a bubble solid threshold value. In this work the bubble solid threshold value of 0.2 is used to identify bubbles in the bed. For the CPFD simulations, the bubbles were identified as the zones (object) and the volume of the bubbles were measured by counting (with algorithm written in MATLAB) the number of the cells the bubbles occupied. The bubbles diameter were than calculated from equivalent spherical area.

Fig.5 compares the bubble frequency with respect to the bubble diameter for different flow boundary conditions over the measurement of 30 s. With the uniform flow boundary conditions, the result shows that different bubble sizes within the range of 2.5 cm< d_b <5 cm appeared in the bed with dominant frequency of the bubbles with 3 cm. Here, d_b is the bubble diameter in cm. While for the flow with two nozzles, the bubble diameters are comparatively large for the same mass flow rate (1.5 kg/ hr.) of the air as compared to that of uniform and injection flow BCs. With the injection flow (using 25 nozzles) the bubbles in the bed are smaller and uniform in size as shown in Fig.5(b). The smaller and uniform size bubbles in the bed means better fluidization quality of the bed which contributes to uniform heat transfer and better mixing. On contrary, the large size bubbles in case of flow BC via two nozzles (as shown in Fig.5(c)) can bypass the bed if such bubbles rise in the bed near to the wall of the reactor. Such large bubbles can grow into slugging bubbles as they rise in the bed and turn the bed into a slugging regime. Additionally, with large size bubbles in the bed, the bubble rise velocity in the bed increases significantly which may transform the bed into turbulent regime. When the bed is in the turbulent regime during gasification of biomass in BFB reactor, the fine particles can entraine in the freeboard region which may contaminate the product gases. The entrainment of fine particles in the freeboard region when the air is supplied to the reactor via two side nozzles is shown in Fig.7 F(a). Also, due to increase in gas velocity and bypassing of the fluidizing gas through the side of the bed (near to the wall of the reactor), less oxidizing medium is present for thermochemical conversion of feedstock in the bed where biomass is present. As a result,

more oxidizing medium is present in the free board region which can convert the carbon monoxide into carbon dioxide. Therefore, in order to supply the fluidizing gas to the reactor without a distributor (with side nozzles) it is essential to optimize the flow behaviour of the fluidizing gas to the reactor. This can be achieved by increasing the number of nozzles (or holes) along the reactor wall. In this work, the CPFD model was used to simulate a case with four different nozzles along the reactor wall. By increasing the number of side nozzles, entrainment of the bed particles were prevented as shown in the Fig.7(b). Similar, the bubble size is reduced (as shown in Fig.5(d)) and the bubble frequency is increased with large number of smaller size bubbles in the bed. With addition of two more side nozzles, better fluidization quality of the bed is achieved (as shown in Fig.6 and Fig.7.
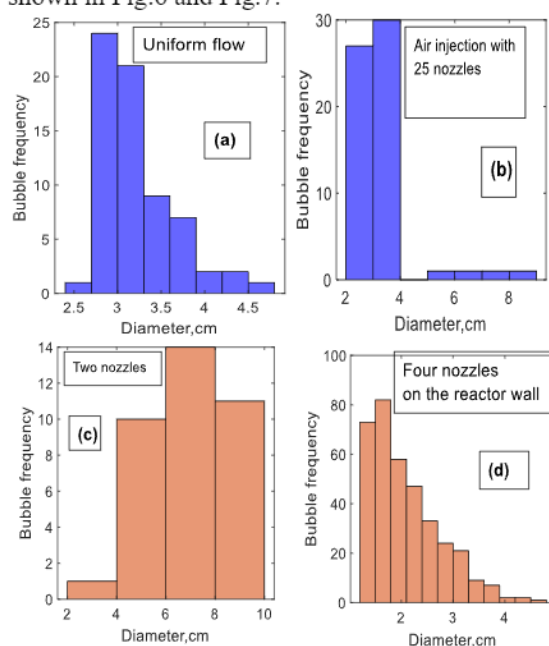

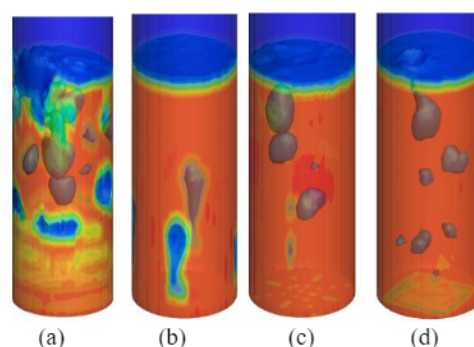Figure 5: Bubble frequency vs bubble diameter for different air supply systems.

Figure 6: (a-d), Iso-surface of the bubbles in the bed obtained during, air injection via four nozzles, two side nozzles, 25 nozzles at the bottom of the reactor, and uniform flow BC respectively.
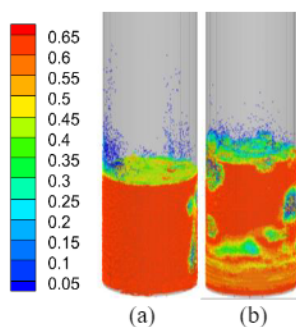
Figure 7: Particle volume fraction of the bed with (a) two side nozzles and (b) four side nozzles.

4. Conclusion

Bubbling fluidized bed reactors are extensively used for several industrial application due to uniform heat and mass transfer. The advantages of a such reactor can only be achieved with proper distribution of the fluidizing gas to the reactor. This work investigates three different methods to supply fluidizing gas to the reactor including uniform flow BC, air injection with twenty-five nozzles and air supply via side nozzles along the reactor wall. A CPFD model has been developed in Barracuda VR 20.01 and the model is used to investigate the fluidization quality of the bed in terms of solid fraction fluctuation and bubble properties. The CPFD model is validated against experimental data obtained from a cold fluidized bed equipped with ECT sensors and air distributor. The result depicts that a better fluidization quality of the bed is achieved with uniform air supply as flow boundary and air injection via twenty-five nozzles located at the bottom of the reactor. With air injection via two side nozzles along the reactor height, the bed fluidized with large bubbles and particle entrainment in the freeboard zone of the reactor. A method was proposed to improve the fluidization quality of the bed while using side nozzles as inlet flow BC for air injection. The proposed method includes addition of four nozzles along the reactor wall instead of two. With the addition of two nozzles, fluidization quality of the bed was improved in terms of smaller bubble sizes without particle entrainment in the freeboard region.

References

Agu, C.E., et al. (2019) 'Investigation of Bubbling Behavior in Deep Fluidized Beds at Different Gas Velocities using Electrical Capacitance Tomography', *Industrial & Engineering Chemistry Research*, 58(5): p. 2084-2098. https://doi.org/10.1021/acs.iecr.8b05013

Agu, C.E. and B.M.E. Moldestad. (2018) 'Distribution of Solids in a fluidized bed operated without a gas distributor', *Linköping Electronic Conference Proceedings*. (153), 248-254. http://dx.doi.org/10.3384/ecp18153248.

Andrews, M.J. and P.J. O'Rourke. (1996) 'The multiphase particle-in-cell (MP-PIC) method for dense particulate flows', *International Journal of Multiphase Flow*, 22(2): p. 379-402. https://doi.org/10.1016/0301-9322(95)00072-0.

Bandara, J.C., et al. (2021) 'Air gasification of wood chips, wood pellets and grass pellets in a bubbling fluidized bed reactor', *Energy*, 233: p. 121149. https://doi.org/10.1016/j.energy.2021.121149

Basu, P. et al. (2006) *Combustion and gasification in fluidized beds*, Taylor & Francis Group, LLC, chapter (11).

Chang, J., et al. (2013) 'Computational Investigation of a Turbulent Fluidized-bed FCC Regenerator', *Industrial & Engineering Chemistry Research*, 52(11): p. 4000-4010. https://doi.org/10.1021/ie3013659

Depypere, F., J.G. Pieters, and K. Dewettinck. (2004) 'CFD analysis of air distribution in fluidised bed equipment', *Powder Technology*, 145(3): p. 176-189. https://doi.org/10.1016/j.powtec.2004.06.005
Geldart, D. and J. Baeyens, 'The design of distributors for gas-fluidized beds',. Powder Technology, 1985. 42(1): p. 67-78. https://doi.org/10.1016/0032-5910(85)80039-5

Jaiswal, R., R.K. Thapa, and B.M.E. Moldestad. (2020) 'Study of agricultural waste gasification in an air-blown bubbling fluidized bed using a CPFD model', *In Proceedings of The 61st SIMS Conference on Simulation and Modelling SIMS 2020 - Linköping Electronic Conference Proceedings*, 176(56). https://doi.org/10.3384/ecp20176393

Jaiswal, R., et al. (2020) 'A CPFD model to investigate the influence of feeding positions in a gasification reactor',. *International Journal of Energy Production and Management*, 5(3): p. 223-233. https://doi.org/10.2495/EQ-V5-N3-223-233

O'Rourke, P.J. and D.M. Snider.(2012) 'Inclusion of collisional return-to-isotropy in the MP-PIC method',*Chemical Engineering Science*, 80: p. 39-54. https://doi.org/10.1016/j.ces.2012.05.047.

Raza, N., et al. (2021) 'Computational Analysis of the Hydrodynamic Behavior for Different Air Distributor Designs of Fluidized Bed Gasifier', *Front. Energy Res*, 9: p. 692066. https://doi.org/10.3389/fenrg.2021.692066

Sasic, S., B. Leckner, and F. Johnsson. (2005) 'Fluctuations and waves in fluidized bed systems: The influence of the air-supply system', *Powder Technology*, 153(3): p. 176-195. https://doi.org/10.1016/j.powtec.2005.03.012

Singh, R. and E. Gbordzoe. (2017), 'Modeling FCC spent catalyst regeneration with computational fluid dynamics', *Powder Technology*, 316: p. 560-568. https://doi.org/10.1016/j.powtec.2016.10.058

Saxena, S.C., A. Chatterjee, and R.C. Patel, 'Effect of distributors on Gas—Solid Fluidization',. Powder Technology, 1979. 22(2): p. 191-198. https://doi.org/10.1016/0032-5910(79)80026-1.

Snider, D.M.(2007) 'Three fundamental granular flow experiments and CPFD predictions', *Powder Technology*, 176(1): p. 36-46. https://doi.org/10.1016/j.powtec.2007.01.032.

Snider, D.M.(2001) 'An Incompressible Three-Dimensional Multiphase Particle-in-Cell Model for Dense Particle Flows', *Journal of Computational Physics*, 170(2): p. 523-549. https://doi.org/10.1006/jcph.2001.6747.

Weber, J.M., et al. (2013) 'Fluid bed characterization using Electrical Capacitance Volume Tomography (ECVT), compared to CPFD Software's Barracuda', *Powder Technology*, 250: p. 138-146. https://doi.org/10.1016/j.powtec.2013.10.005.

Paper 5

Image Processing and Measurement of the Bubble Properties in a Bubbling Fluidized Bed Reactor

Article

Image Processing and Measurement of the Bubble Properties in a Bubbling Fluidized Bed Reactor

Rajan Jaiswal [1],*, Britt. M. E. Moldestad [1], Marianne S. Eikeland [1], Henrik K. Nielsen [2] and Rajan Kumar Thapa [1]

[1] Department of Process, Energy and Environmental Technology, Faculty of Technology, Natural Sciences and Maritime Sciences, Campus Porsgrunn, University of South-Eastern Norway, Kjølnes 56, 3918 Porsgrunn, Norway

[2] Department of engineering sciences, Faculty of engineering and science, University of Agder, Jon Lilletuns vei 9, 4879 Grimstad, Norway

* Correspondence: rajan.jaiswal@usn.no; Tel.: +47-48666290

Abstract: The efficiency of a fluidized bed reactor depends on the bed fluid dynamic behavior, which is significantly influenced by the bubble properties. This work investigates the bubble properties of a bubbling fluidized bed reactor using computational particle fluid dynamic (CPFD) simulations and electrical capacitance tomography (ECT) measurements. The two-dimensional images (along the reactor horizontal and vertical planes) of the fluidized bed are obtained from the CPFD simulations at different operating conditions. The CPFD model was developed in a commercial CPFD software Barracuda Virtual Reactor 20.0.1. The bubble behavior and bed fluidization behavior are characterized form the bubble properties: average bubble diameter, bubble rise velocity, and bubble frequency. The bubble properties were determined by processing the extracted images with script developed in MATLAB. The CPFD simulation results are compared with experimental data (obtained from the ECT sensors) and correlations in the literature. The results from the CPFD model and experimental measurement depicted that the average bubble diameter increased with an increase in superficial gas velocities up to 4.2 U_{mf} and decreased with a further increase in gas velocities due to the onset of large bubbles (potential slugging regime). The bubble rise velocity increased as it moved from the lower region to the bed surface. The Fourier transform of the transient solid volume fraction illustrated that multiple bubbles pass the plane with varying amplitude and frequency in the range of 1–6 Hz. Further, the bubble frequency increased with an increase in superficial gas velocity up to $2.5U_{mf}$ and decreased with a further increase in gas velocity. The CPFD model and method employed in this work can be useful for studying the influence of bubble properties on conversion efficiency of a gasification reactor operating at high temperatures.

Keywords: fluidized bed; bubble diameter; bubble rise velocity; bubble frequency; computational particle fluid dynamic; image processing

1. Introduction

Fluidized beds are extensively used in applications such as chemical regeneration, catalytic conversion, gasification, chemical synthesis, and pneumatic transportation, and each of these process applications requires a unique fluidization regime. The fluidization bed regimes include minimum fluidization, bubbling, turbulent, fast fluidization, and pneumatic conveying [1–4]. The types of regimes are mainly dependent on the fluidizing gas velocity, density, and particles size of the bed material, aspect ratio, and reactor dimension [5,6]. The major advantages of fluidized bed include efficient heat transfer, better temperature control, good mixing, and better solid circulation. In order to achieve the benefits of a fluidized bed, firstly, the reactor must be operated strictly within the specific fluidization regime required for the process. Secondly, the problem associated with

fluidized beds must be avoided for a smooth reactor operation and to achieve the desired process efficiency. However, the two-phase flow of gas–solid coupled with heat and mass transfer and series reactions in the fluidized bed reactors are complex and not yet fully understood. Challenges in operating fluidized bed reactors such as lower chemical conversion, non-uniform products, agglomeration, entrainment of particles, and reactor failure are often reported. These difficulties encountered while operating fluidized bed reactors can be overcome with a thorough understanding of the fluid dynamic behavior of the reactor and bubble dynamics in the bed. The major objective of this paper is to investigate the fluid dynamics behavior of a bubbling fluidized bed (BFB) which is significantly influenced by the bubble properties.

An appropriate regime in a bubbling fluidized bed can be characterized by the better fluidization quality of the bed without any slug. Ideally, for better fluidizing quality of the bubbling bed, the bubbles should be large in number, uniformly distributed across the bed, and smaller in size. The bubbles formed in a fluidized bed are primarily responsible for good solid circulation, and gas–solid contact area, which determines the heat and mass transfer within the reactor. As the bubble rises from the bottom of the bed to the top, it carries particles with it, thus mixing binary particles in a gasification reactor. For a given gas velocity, the bubbling behavior of the fluidized bed can be characterized by the bubble properties such as bubble diameter, bubble rise velocity, and bubble frequency. The bubbles in dense fluidized beds are the regions where the particle concentration is low, whereas the region with higher solid concertation is referred to as the emulsion phase. As the fluidizing gas passes through the lower part of the bed (from the distributor), bubbles are formed. The bubbles grow in size, merge, split, and may disappear as they move within the bed. The bubble size in the fluidized bed is influenced by the air distribution, particle size distribution, bed geometry, superficial gas velocities, and bed height [7,8]. When the bubble size grows and equals the bed diameter, the bed tends to shift from bubbling to slugging, and the types of slugs can be axial slugs, wall slugs, and flat slugs [5]. There can be a slug in a bed with a smaller reactor diameter even if the bubble size is smaller than the bed diameter. Kunii et al. [5] showed that wall effect retards the rise velocity of the bubble when the ratio between bubble diameter and bed diameter is greater than 0.125 and also illustrated that when the ratio between bubble diameter to bed diameter is greater than 0.6, the bed transits from bubbling to slugging. The large size bubbles in the bed mean increased bubble rise velocity; thus, the bubbles may bypass the bed, reducing the residence time of gas phase and gas-to-solid contact time inside the reactor. Therefore, operating the bubbling bed with optimal bubbles size, velocity, and frequency is crucial for reactor safety and efficient fuel conversation.

Measurement Techniques in a Fluidized Bed

The fundamental understanding of bubble solid hydrodynamics in a fluidized bed can be achieved from the bubble properties that include bubble shape and size, bubble rise velocity, bubble frequency, etc. [8–10]. The bubble properties in a fluidized bed can be measured from experimental measurements and CFD simulations that produce reliable data. Several experimental measurement techniques have been proposed to measure the properties of fluidized bed and study its fluid dynamics behavior [11,12]. The measurement techniques broadly include intrusive techniques and non-intrusive techniques. The intrusive techniques consist of resistance, inductance, and thermal probes [13,14], while the non-intrusive techniques are based on imaging, laser, and tomography methods [15,16]. The major disadvantages of intrusive measurement techniques are that insertion of the probe inside the bed hinders the fluid dynamics behavior. The non-intrusive measurement techniques, on the other hand, can be used to measure bubble properties without interfering the flow hydrodynamics. Among the non-intrusive techniques (X-ray, γ-ray, and Ultrasonic tomography), electrical capacitance tomographic (ECT) is faster and can be used in real-time applications [15]. The ECT measurement techniques employ sensors that measure the relative permittivity between two non-conducting phases. The bubble

properties, for instance, bubble diameter and frequency, can be calculated based on the solid-to-void fraction extracted from the permittivity measurement. The velocity of bubbles can be obtained via a reconstruction method, for example, cross-correlation techniques, that gives a measurement of the bubble rising time from one sensor to another sensor position [17]. In such cases, the placement of the sensor is very important since the bubbles may split or coalesce as they rise from one position to another within the bed, making it difficult to track a single bubble. Reducing the spacing between the sensors can address such an issue; however, to avoid signal interference, the sensors cannot be too close. In this regard, another simple non-intrusive method to study the bubble properties in a fluidized bed, for instance, digital imaging technique, can be a reliable technique. With the digital imaging technique, images of the bed hydrodynamics are captured at different time frames, and the bubble properties are identified from the extracted images [18,19]. This work employs the digital imaging technique and ECT sensors for the measurement of bubble properties in a BFB reactor.

The non-intrusive experimental methods have been widely applied to identify the bubble properties; however, there are many challenges associated with experimental techniques. For instance, the experimental methods are expensive, and often such measurements are only carried out on a pilot-scale plant that produces specific results which may not represent the large-scale reactor conditions. Conducting experiments to observe the hydrodynamics properties of fluidized bed large-scale reactors in such a harsh environment and opaque nature of the reactor is extremely difficult. Moreover, to study the influence of different parameters that primarily influence the fluidized bed hydrodynamics, it is impossible to change the reactor dimensions, sensor positions, and other parameters during experimentation. Such experimental difficulties to identify the fluidized bed hydrodynamics can be overcome using Computational Fluid Dynamics (CFD) simulations. Several studies have been carried out to study fluidized bed hydrodynamics using a CFD model in the past. There are mainly two types of CFD approach used to study flow dynamics of the fluidized bed: the Eulerian-Eulerian method (continuum) and Eulerian–Lagrangian method (Continuum-Discrete) [20,21]. In the Eulerian-Eulerian approach, one particle phase is considered where only two interacting phases exist, one particle phase and the gas phase, which is called as Two-Fluid Model (TFM). TFM is widely used to study and simulate fluidized bed hydrodynamics [22,23]. However, the major drawback with the TFM method is that it accounts for the particles with the same density, diameter, and coefficient of restitution which often results in inaccurate prediction of the bed properties [24]. In the Eulerian–Lagrangian approach, discrete element models (DEM), on the other hand, are more reliable and predict better results than TME [25]. Individual particles are tracked with the DEM method, and particle–particle collision is considered, unlike the TFM model. Therefore, DEM requires enormous computing power to simulate real fluidized bed systems. Another Eulerian–Lagrangian approach, CPFD, that uses a multiphase particle-in-cell approach (MP-PIC), has gained popularity recently due to its capacity to simulate natural fluidized bed systems. In the MP-PIC approach, particles with the same properties, such as density, volume, etc., are grouped to form a parcel. Barracuda V.R. is a commercial CPFD software that uses the MPIC approach to simulate real fluidized bed systems [26,27]. Many studies have focused on using CPFD to study different fluidized bed systems [28,29]. Despite existing studies, there are some publications with the CPFD model on 3D bubbling fluidized beds that can predict the bubble properties [30]. Proper validation of the CPFD model to predict bubble properties of the bubbling fluidized bed with experimental work is still needed. In addition, digital imaging techniques applied for the measurement of the bubble properties from the three-dimensional CPFD simulation with experimental validation are scarce.

This work investigates the fluid dynamic behavior and bubble properties of a BFB reactor with Geldart B particles using CPFD simulations. The fluid dynamic behavior of a BFB was characterized from the bubble properties: bubble diameter, bubble rise velocity, and bubble frequency. The bubble properties were measured from the images

extracted from the plane at transient simulation time step. To illustrate the robustness of the CPFD model, the properties of the bed measured from the CPFD model at each superficial gas velocity are compared with the experimental data and different correlations. The experimental work has been carried out at an ambient condition on a bubbling fluidized bed with ECT sensors. The 2D raw data obtained from the ECT measurements are processed in MATLAB to measure the bubble properties.

2. Materials and Methods

2.1. Computational Particle Fluid Dynamic Model

The simulations in this work were carried out using the CPFD software Barracuda VR, which is commercial software specially designed for the application in multiphase flow systems such as fluidized bed reactors. Unlike other CFD software, the main advantages of using Barracuda VR are that it facilitates defining particle species with particle size distribution. It allows to define and simulate computational particles in order of 10^{15} and higher. Additionally, it uses 3D multiphase particle-in-cell approach for simulation of gas-particle flows and considers fluid-particle coupling with detailed consideration of thermal physics and reaction chemistry. For the fluid-particle simulations, Barracuda virtual reactor uses a combined Eulerian and Lagrangian approach where the solid particles are modeled as discrete Lagrangian methods and the fluid is modeled as Eulerian grid of cells. To create a virtual reactor in any CFD tool, the first step was to set up a grid that defined the control volume, cells, and boundary conditions for all fluid field calculations. A CAD geometry (equal to experimental reactor setup) was drawn in STL format in SolidWorks and imported to Barracuda VR to define grids. A total of 102,400 cells were specified with a uniform grid generation option available in Barracuda that divides the rector into cells uniformly. The number of cells (102,400) was defined so that the cross section of the reactor is divided into 32 × 32 pixels similar to the experimental set up. Three planes were set up at heights of 5 cm, 10 cm, and 15.7 cm along vertical direction of the reactor (Figure 1a). Flow and pressure boundary conditions are defined at the bottom and top of the reactor, respectively (Figure 1a). The solid volume fraction of the bed is set as 0.543 at the static condition, which is obtained experimentally by dividing the bulk density of the bed material with particle density. The parameters used for the development of the simulation model are summarized in Table 1. The details of the mathematical descriptions of the computational model in Barracuda can be found elsewhere [31–34].

Table 1. Simulation parameters used for the model development in a BFB reactor.

Parameters	Value
Particle density,	2650 kg/m^3
Particle diameter	302.46 μm
Gas density	1.225 kg/m^3
Bed diameter	10.4 cm
Initial bed height	30 cm
Superficial gas velocity	(0.137–0.4) m/s
Close pack volume fraction	0.64
Particle volume fraction	0.534
Total number of cells	102,400
Time step	0.001
Simulation time	60 s
Minimum fluidization velocity, U_{mf}	0.07 m/s

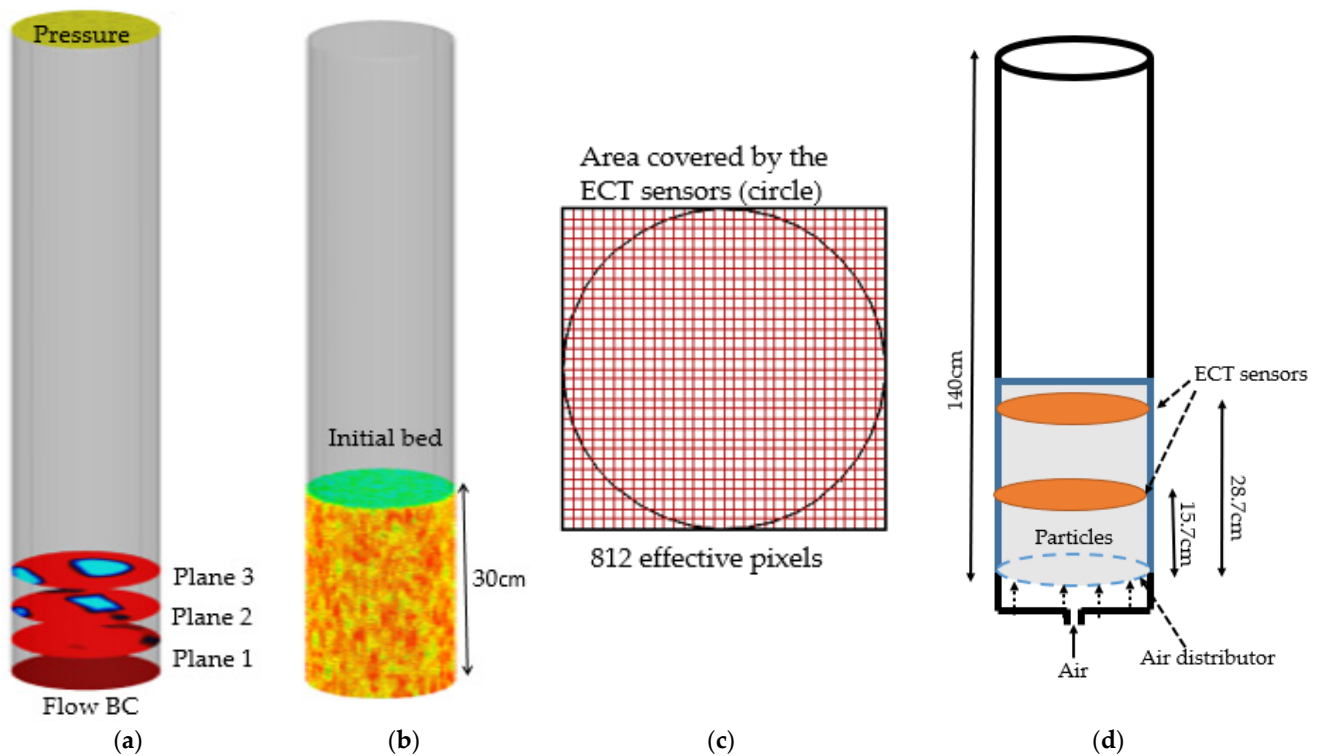**Figure 1.** (**a**) Flux planes along the vertical height and boundary conditions; (**b**) initial bed height in CPFD model; (**c**) area covered by the ECT sensors; (**d**) schematic diagram of the experimental setup.

The drag model in a fluidized bed is an important function which determines the force acting on the particles by the fluid flow around it. For the drag force calculation, the combined drag model, Wen-Yu and Ergun, is used with non-linear coefficient 2 and linear coefficient 180 [19]. Several studies showed a better prediction of the bubbling fluidized bed reactor using the blended Wen-Yu and Ergun drag model [1,35]. Similarly, the wall effect has a significant influence on the bubble properties and bed hydrodynamics and is significant in a fluidized bed reactor. In this study, the effect of the wall on the fluid particle motion is considered in terms of normal-to-wall momentum retention, and tangent-to-wall momentum retention. Normal-to-wall momentum retention is defined as the normal component of the particle momentum retained after the particle collision with the wall. When the particle collides with the wall, it tends to lose normal and tangential momentum. The tangential component of the particle momentum retained by the particle after collision with the wall is defined as the tangent-to-wall momentum retention.

Figure 2 illustrates the mathematical implementation of the parameters: tangent-to-wall momentum and normal-to-wall momentum retention, where u^{n+1} is the particle speed after collision and u^n is the particle speed before collision. The values 0.85 and 0.85 are selected for the tangent-to-wall momentum retention and normal-to-wall momentum retention, respectively. The value of 0.85 in normal-to-wall momentum means 85% of the momentum is retained. The sand particle is modeled as a hard sphere, and the values of these parameters are used as suggested in the literature [36]. These losses of the normal and tangential momentum with wall impact are described in Equation (1).

$$u^{n+1} = [(r_T - r_N)(1 - \cos\theta + r_N][u^n] \tag{1}$$

where r_T, and r_N are momentum retention factor for a tangential wall impact and momentum retention factor for a normal wall impact, respectively.
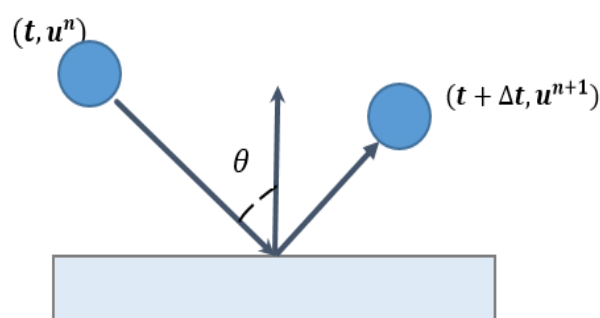
Figure 2. Illustration of momentum retention of the particle.

2.2. Experimental Setup

The experimental measurement technique in this work includes the use of electrical capacitance tomography sensors for the measurement of bubble properties in a bubbling fluidized bed reactor. The experimental setup consists of a 10.4 cm internal diameter reactor column equipped with the twin-plane ECT sensors and a data acquisition system. The twin-plane ECT sensors are located at 15.7 cm and 28.7 cm along the reactor height, as shown in Figure 1d. Each ECT sensor is composed of 12 equally spaced electrodes mounted on the outer wall of the reactor. The fluidizing gas is passed uniformly through the particle bed via an air distributor located at the bottom of the reactor. The raw data produced from the ECT sensors are either in the form of a numerical matrix or image that covers the entire sensor-measuring area. The cross-section of each sensor is divided into 32×32 square pixels, of which 812 are the effective pixels that lie within the bed (shown in Figure 1c). Each pixel holds a normalized relative permittivity value between 0 and 1, which represents the gas–solid fraction. The system was calibrated before experiments. The calibration was performed for both the extreme cases, i.e., when the sensor area is filled with higher permittivity material (air) and lower permittivity material (sand particles). Sand particles are used as the bed material and compressed air as the fluidizing gas. The properties of particles used are shown in Table 1. The data sampling frequency is sensitivity to local gas–solid fraction measurements in the fluidized bed. For instance, Yassir et al. [37] demonstrated the sensitivity of measurement span while using ECT sensors and suggested a 60 s measurement span for the extraction of reliable data in a bubbling fluidized bed. In this work, for each flow velocity, the data were logged for 60 s with a time step of 0.01 that produced a total of 6000 frames. Experiments were carried out at different airflow velocities, and the influence on bubble properties (bubble diameter and bubble frequency) was determined. Due to the large distance between the planes in the experimental set up (shown in Figure 1d), it was difficult to track the same bubble for the measurements of bubble rise velocity. As the bubbles rose from a plane at 15.7 cm to another plane at 28.7 cm, as shown in Figure 1d, the bubbles merged into a single large bubble or split into smaller bubbles (due to large distance between the measurement sensors). Therefore, bubble rise velocity was measured from the simulation data by tracking the centroid position in 3D bed, which is discussed in Section 2.3.

2.3. Methodology and Post-Processing the Simulation Data

Post-processing of the three-dimensional simulation data is significant for the analysis of the bed fluid dynamics behavior. In this work, MATLAB and Tecplot were used for data analysis and visualization. Barracuda VR 20.1 comes with a 3D data visualization and data extraction software Tecplot 360 EX (CPFD software Barracuda VR, Houston, TX, USA). The hydrodynamics of the bed was determined by measuring the bubble properties (bubble diameter, bubble rise velocity, and bubble frequency). In order to calculate the bubble properties, the first step was to identify the bubbles at different positions. The bubble position was defined by the region where the solid volume fraction reaches zero. Based on a threshold value of the solid–gas fraction of 0–0.2, the bubbles in the bed were

distinguished from the emulsion phase. In this work, a threshold value of ≤ 0.2 (solid volume fraction) was used to characterize the bubble region. The solid volume fraction of 0.2 is selected based on the suggestion made in previous studies [10]. To confirm the applicability of such a gas–solid threshold in this study, careful observation of the boundary region was carried out by checking the solid volume fraction of cells in the boundary region between the bubble and emulsion phase (as shown in Figure 3b). The bubble and its properties were determined from the images extracted from 2D horizontal and vertical planes.
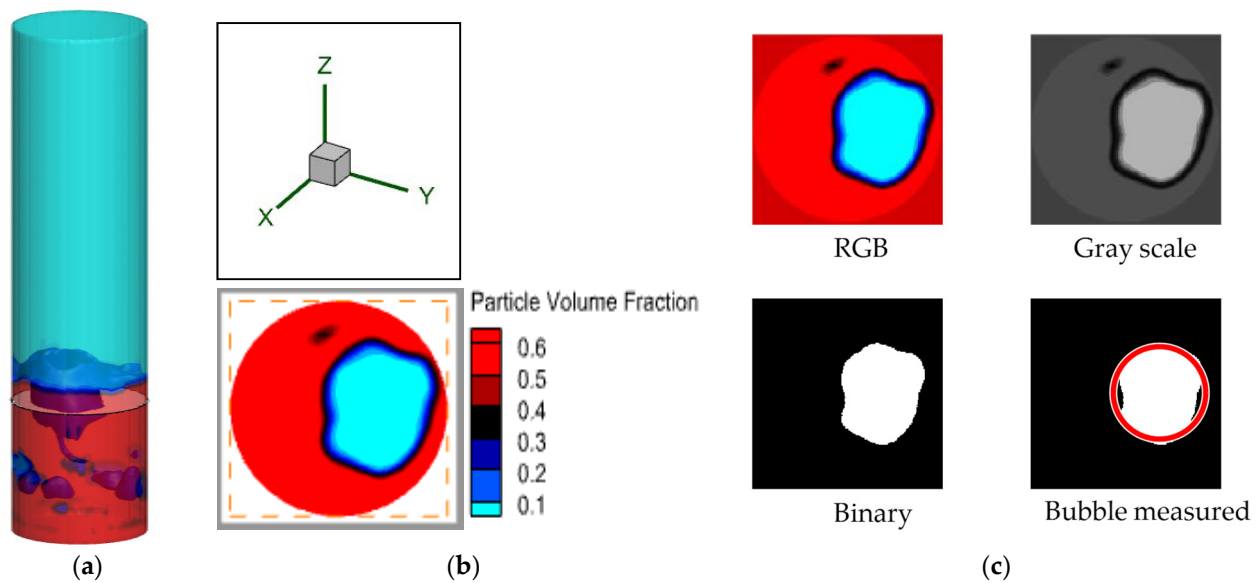
Figure 3. (**a**–**c**) Bubble measured from the extracted images from XY-plane (horizontal plane) at a height of 25.8 cm and superficial gas velocity of 0.25 m/s (The red circle represents equivalent bubble area).

The change in fluidization behavior of the bed with time at different gas velocities was captured in the form of images. For each superficial gas velocity, the simulation time was 60 s, and the images were extracted at 100 frames per second. Therefore, a total of 6000 frames (images) were produced for each selected superficial gas velocity. For the measurement of the bubble properties along the horizontal planes, the images were produced from the post-processing tool Techplot 360 available in Barracuda VR at the pre-defined planes along the vertical height. The extracted images were in RGB format. The images were converted into grayscale images and the grayscale images were further converted into binary images using a MATLAB code. Based on the bubble–solid threshold value (solid volume fraction ≤ 0.2), the bubble regions were identified from the binary images using the "image processing tool" available in MATLAB. The bubbles were identified as the objects and their properties such as centroid, area, and perimeter were calculated using the regionprops function available in MATLAB. Figure 3a–c shows the method adopted in this work to extract bubbles in the bed along the horizontal plane. The instantaneous three-dimensional iso-volume fraction of the bubbles rising in the bed is shown in Figure 3a. The two-dimensional view of a bubble as it reached plane 3 is illustrated in Figure 3b, and the stepwise method employed to measure the bubble from extracted 2D images is shown in Figure 3c.

Similarly, for the measurement of bubble properties along the vertical planes, the images were extracted at 100 frames per second for each gas velocity. In this case, the bubbles were identified from the RGB to binary images with a bubble ID assigned for each bubble. As the bubbles moved from one position to the upper part of the bed, the bubbles disappeared, split into two or more bubbles, or merged into a single bubble. Therefore, it was important to track the individual bubble to correctly calculate its properties as it

changed from one frame to another. For this reason, a unique bubble ID was assigned for each bubble, as shown in Figure 4. The ID contained information about the bubble name (with the number), bubble height, and diameter, which were used to track the individual bubbles as it moved from one position to another with time. The calculation of the bubble properties—bubble diameter, bubble rise velocity, and frequency—from both approaches are discussed in the results and discussion part.
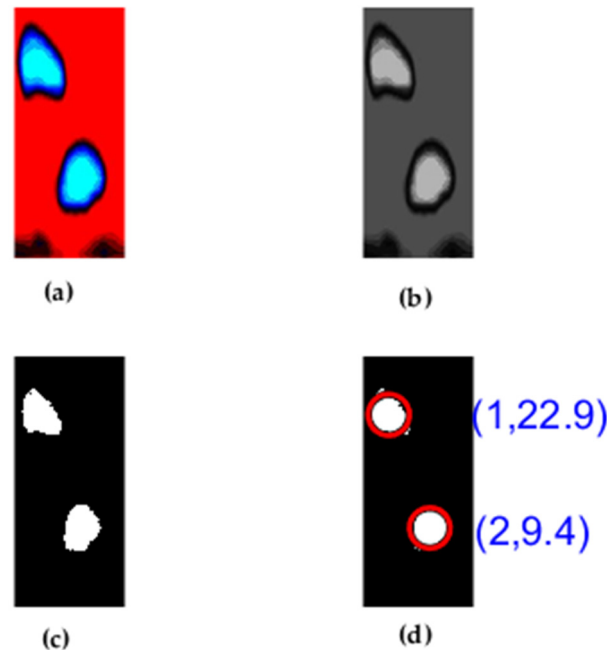
Figure 4. (**a**) RGB image extracted after post-processing; (**b**) grayscale image converted from RGB image; (**c**) binary image converted from grayscale image; (**d**) bubbles (with ID: diameter and position) distinguished from the emulsion phase (The red circle represents equivalent bubble area).

3. Results and Discussion

3.1. Bubble Diameter

The information about average bubble size for a given superficial gas velocity is an important parameter for designing a fluidized bed gasification reactor. In this work, the bubble diameter is determined from the measured bubble area. As a bubble moved vertically and reached the XY plane (plane 3), the area of the bubble was determined. The bubble area was measured by counting (with MATLAB algorithm) the number of pixels occupied by the bubble region. The effective bubble area corresponding to the bed diameter was calculated by multiplying the total effective area of the bed. The average bubble diameter was then calculated by the mean value over the measurement period (60 s).

Figure 5 compares the average bubble diameter obtained from the CPFD simulations, experimental measurement, and correlations for bubble diameter proposed by Mori et al. [38] and Werther et al. [39] (as shown in Equations (2) and (3)). The result depicts that the average bubble diameter increased with an increase in gas velocities. With the increased gas velocity, the bed was diluted with more air, which increased the void fraction. In addition, fluidizing gas in the fluidized bed tends to pass in the form of bubbles, which increased the average bubble size with an increase in superficial gas velocity. However, the increase in bubble diameter as measured from the CPFD simulation was not linear as compared to the correlations proposed by Mori et al. and Werther et al. The CPFD model predicted the average bubble diameter close to the experimental data for the selected superficial gas velocity, while it predicted the average bubble diameter close to Mori et al. correlations up to 0.3 m/s. With a further increase in gas velocity beyond 0.3 m/s, the average bubble diameter increased slightly. At this superficial gas velocity, the average bubble diameter increased up to 0.62 times the bed diameter. There were some bubbles in

the bed that approximately covered the bed diameter, which could convert into slug. With the increase in gas velocity, such bubbles tend to split as they rise in the bed.

$$d_b = 0.652 \left[A \left(U_0 - U_{mf} \right) \right]^{0.4} - \left(0.652 \left[A \left(U_0 - U_{mf} \right) \right]^{0.4} - d_{b0m} \right) \exp \left(-0.3 \frac{h}{D} \right) \quad (2)$$

$$d_{b0m} = 0.00376 \left(U_0 - U_{mf} \right)^2$$

where d_b, h, D are in [cm] and U_0, U_{mf} are in [cm/s]. A is cross sectional area of the bed, and d_{b0m} is the initial bubble size near the distributor.

$$d_b = d_0 \left[1 + 0.272 \left(U_0 - U_{mf} \right) \right]^{1/3} (1 + 0.0684h)^{1.21} \quad (3)$$

where $d_0 = 0.853$ for Geldart B particles.
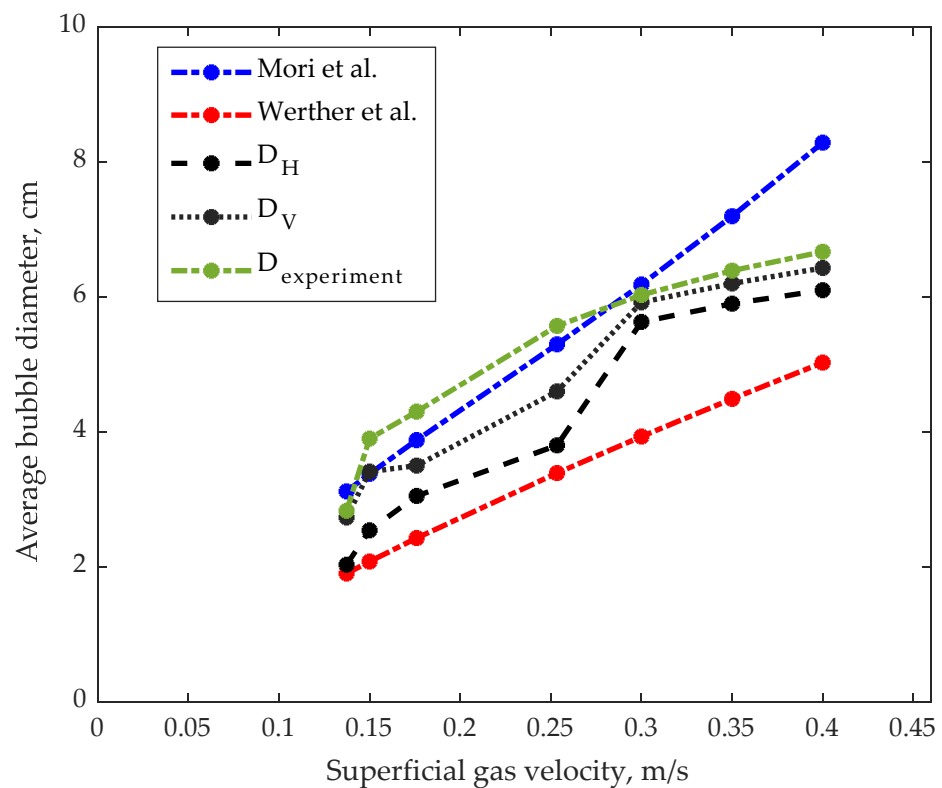
Figure 5. Comparing average bubble diameter for different superficial gas velocities obtained from CPFD simulations, experimental data, and different correlations (D_H and D_v are the average bubble diameter measured along the horizontal and vertical planes from the CPFD simulations, respectively) at 15.7 cm along the reactor height [38,39].

Similarly, Figure 6 compares the average bubble diameter from the CPFD model and the correlations at heights of 10 cm and 5 cm for different superficial gas velocities. The results show that the average bubble diameter at both bed heights increases with increasing superficial gas velocity, similar to that of plane 3. However, no slug appeared in the bed up to a height of 10 cm at the selected gas velocities. The average bubble diameter predicted by the CPFD model is in better agreement with the correlation proposed by Mori et al, while the Werther et al. correlation underpredicts the average bubble diameter at height 10 cm. For the bubbles reaching the lower plane at 5 cm, the average bubble diameter measured from the CPFD results agrees well with the Mori et al. correlation for all gas velocities; however, it is only in good agreement with the Werther et al. correlation up to gas velocity 0.25 m/s. The Werther correlation underpredicts the average bubble diameter at superficial

gas velocities higher than 0.25 m/s. The information about the average bubble diameter for the given bed conditions (fluidization velocity, aspect ratio, bed diameter, etc.) are useful for characterizing the bed fluidization quality. For instance, a bubble that is too large in the bed means either the bubble can convert into a slugging bed, or it may bypass the bed. On the other hand, if the bubble size is too small, it may not provide uniform mixing in case of a bed with a binary mixture of particles.
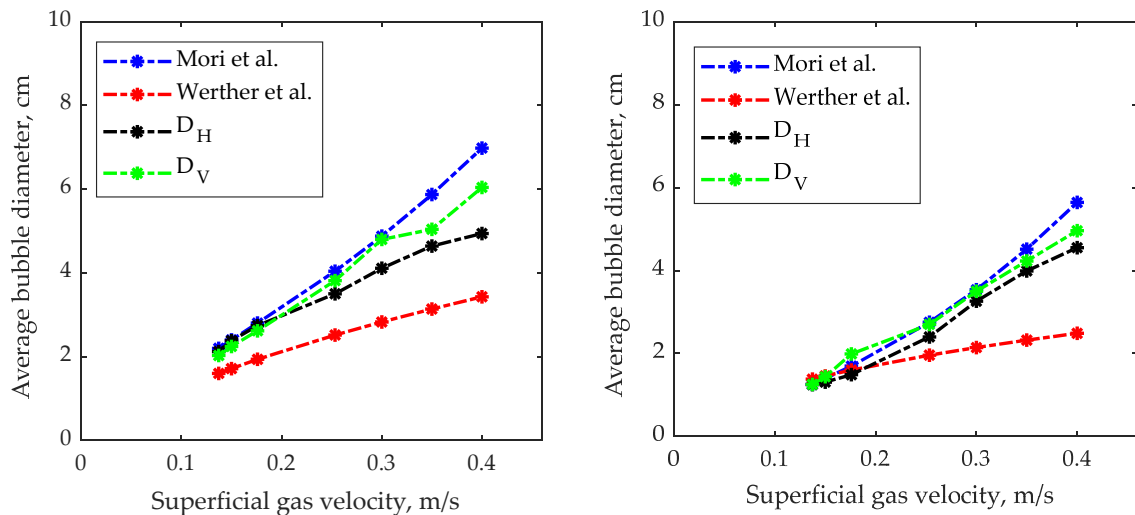
Figure 6. Average bubble diameter for different superficial gas velocities at height 10 cm (left side) and 5 cm (right side) [38,39].

3.2. Bubble Rise Velocity

The bubble rise velocity was estimated by using a detailed signal analysis method and a bubble displacement method. The bubble rise velocity from the detailed signal analysis method was obtained from the fluctuation of solid volume fraction from two planes at heights of 10 cm and 5 cm for each bubble passage. As the bubbles rise from plane 2 to plane 1, there is a time lag (Δt) between each bubble passage, as shown in Figure 7. The bubble rise velocity (U_{b1}) is obtained based on the distance between two planes (ΔH), as shown in Equation (4).

$$U_{b1} = \sum \frac{\Delta H}{\Delta t} , \ \Delta t = t2 - t1 \tag{4}$$
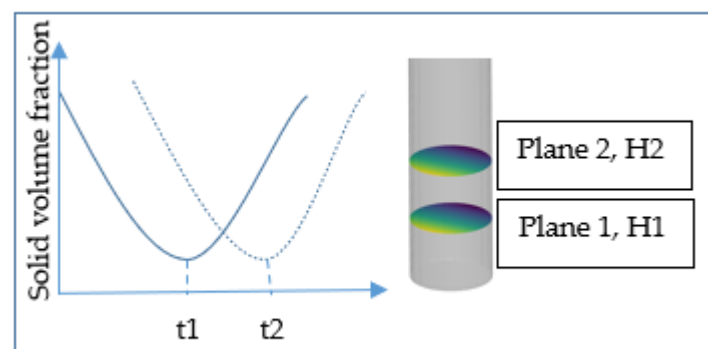
Figure 7. Schematic diagram showing the fluctuation of solid volume fraction as the bubble passes the planes.

When calculating the bubble rise velocity with the bubble displacement method, the bubble is tracked as it passes from one time step to another. As the bubbles move from one position to another, its centroid position changes, and the bubble displacement has

been calculated from the centroid positions in consecutive time steps. The bubble rise velocity, U_{b2}, is calculated from Equation (5).

$$U_{b2} = \sum \frac{\Delta d}{\Delta t} \tag{5}$$

$$\Delta d = \sqrt{(X_2 - X_1)^2 + (Y_2 - Y_1)^2}$$

where Δd is the displacement of the bubble centroid positions. (X_2, Y_1), (Y_1, Y_2) are the centroid positions in the consecutive time frames.

Figure 8a shows the fluctuation of the solid volume fraction from the simulation result at superficial gas velocity 0.25 m/s. As shown in Figure 8b, there is a time lag as the bubble moves from the lower plane to the upper plane. By measuring the time difference, the bubble rise velocity is calculated from the plane positions. The average bubble rise velocity as the bubble reaches 15.7 cm bed height at different superficial gas velocities is shown in Figure 9d. The experimental measurement of the bubble rise velocity was not possible, and therefore, the bubble rise velocity obtained from the CPFD model is compared with correlations for bubble rise velocity from the literature. The correlations proposed by Davidson et al. [40] and Agu et al. [41] have been used for the comparison. The result shows that the average bubble rise velocity increases with an increase in superficial gas velocity. With an increase in superficial gas velocity, the bubble diameter increased which increased the rise velocity of the bubbles in the bed. The bubble rise velocity predicted by the CPFD model does not increase linearly at different gas velocities, as predicted by the correlations. However, the bubble rise velocities predicted by the CPFD model are in agreement with the correlations. The CPFD model predicts the bubble rise velocity at different superficial gas velocities closer to the correlation proposed by Agu et al., while the correlation proposed by Davidson et al. overpredicts the bubble rise velocity. This is because the correlation proposed by Agu et al. is an improved version of the Davidson et al. correlation, where the author has proposed a correlation for bubble velocity based on the bubble-projected area.
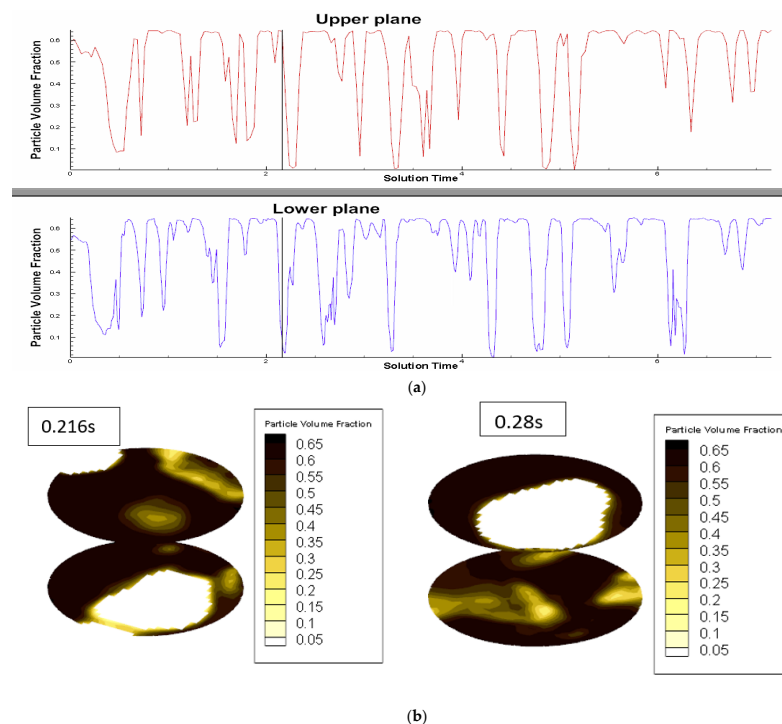
Figure 8. (**a**) Fluctuation of solid volume fraction as the bubble passes from lower plane to upper plane. (**b**) Mapping of the bubble on the lower plane and upper plane at different time steps.
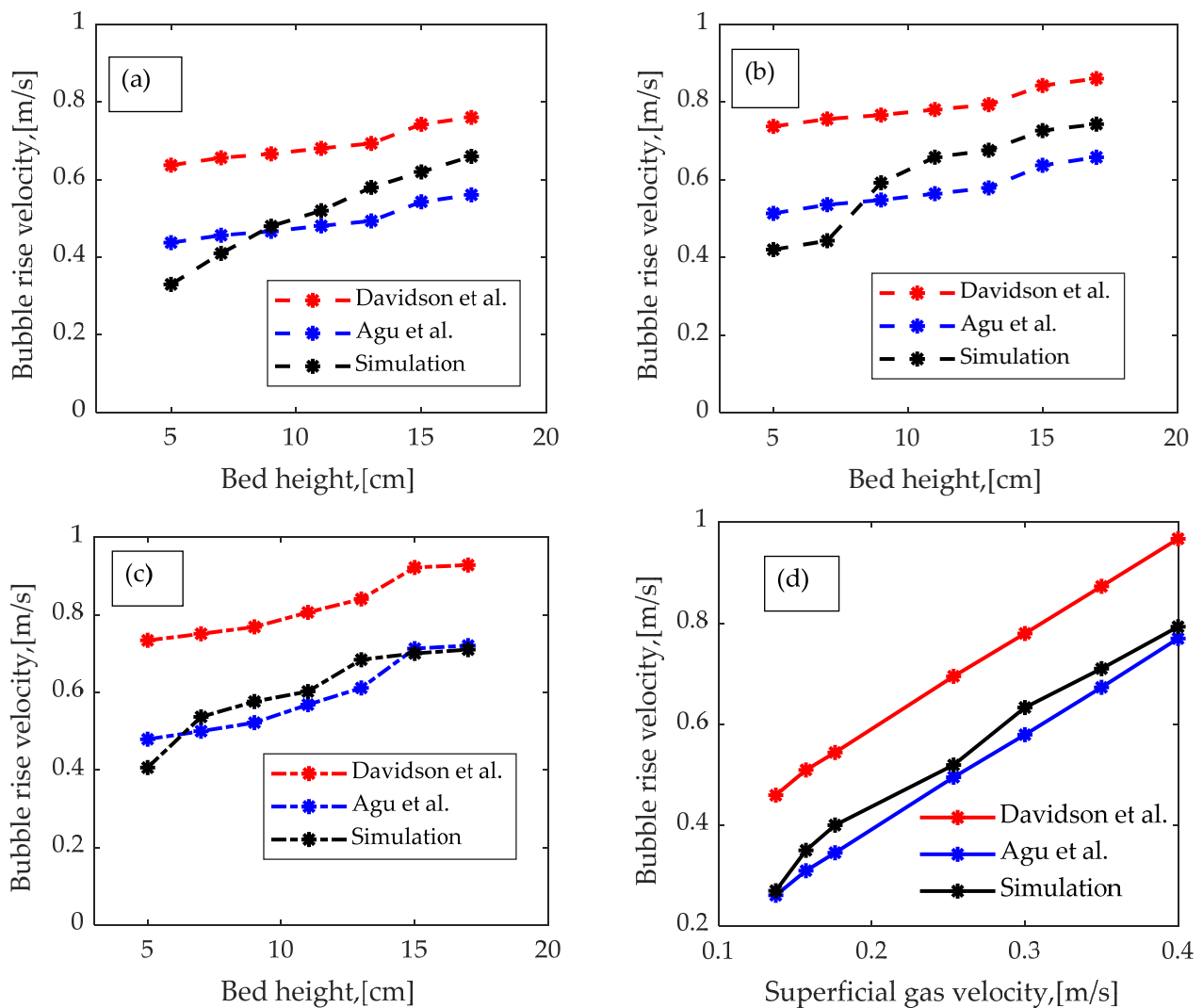
Figure 9. (**a**–**c**) Bubble rise velocity vs. bed height at different gas velocities of 0.13 m/s, 0.35 m/s, and 0.4 m/s, respectively; (**d**) average bubble rise velocity as the bubbles moved from the plane at 10 cm to the plane at 15.7 cm at different superficial fluidizing gas velocities [40,41].

    With the above method, tracking a bubble and measuring its rise velocity at the predefined plane, the chances are that the bubble may disappear, split, or coalesce, making it difficult to track its properties. Therefore, tracking the bubble rise velocity from one frame to another is more reliable as it does not lose any information. In order to calculate the rise velocity of the bubble as it moves, the easiest way is to measure the rise velocity by tracking the centroid position with time as discussed earlier. Figure 9a–c shows the mean bubble rise velocity at different superficial gas velocities and positions along the reactor height. The bubble rise velocity is obtained from the centroid positions (Equation (5)) as it moves from one frame to another. The result shows that the bubble rise velocity increases with an increase in superficial gas velocity 0.137 m/s to 0.4 m/s. Additionally, the bubble rise velocity increases as the bubble moves from the lower region to the upper part of the bed. Comparing the calculated bubble rise velocity from the CPFD model with the correlations of bubble rise velocity, the results illustrate that the CPFD model underpredicts the bubble rise velocity at the lower positions of the bed. At the upper part of the bed, the bubble rise velocity is higher than predicted by Agu et al. but lower than the Davidson et al. correlations. At the gas velocity of 0.137 m/s, the bubble rise velocity increases gradually with height, indicating that small bubbles are formed at the lower part of the bed. The bubble size and rise velocity increase gradually as the bubble moves from the lower

section to the upper section (as shown in Figure 9a). At superficial gas velocity of 0.35 m/s (Figure 9b), the bubble rise velocity increases slowly below 10 cm bed height, and there is a sudden increment in the bubble rise velocity afterward; this is due to coalescing of the smaller bubbles into large bubbles, which increases the rise velocity of the bubble.

3.3. Bubble Frequency

The bubble frequency is an important parameter influencing the gas and solid residence time inside the bubbling fluidized bed. There are many approaches to calculating the bubble frequency inside the bed. The simplest method is to count the number of bubbles over the measurement period [42]. Another approach is to plot the power spectrum density to obtain the bubble frequency [43]. In this work, the bubble frequency is obtained using both methods. The bubbles passing through a plane along the vertical height are measured, and the bubble frequency is calculated from Equation (6). Figure 10 shows the histogram plot of the number of bubbles of varying diameters counted at each superficial gas velocity over the measurement time. As can be seen from the figure, bubbles of different sizes pass the plane at height 15.7 cm. However, up to the superficial gas velocity of 0.25 m/s, there are many bubbles with smaller diameters. Therefore, operating the fluidized bed regimes below 0.25 m/s for this case can be effective, provided that the particles (in the case of bed with binary particles) do not segregate.

$$Bubble\ frequency,\ f_b = \frac{Total\ number\ of\ bubbles\ passing\ the\ plane}{sampling\ time} \qquad (6)$$
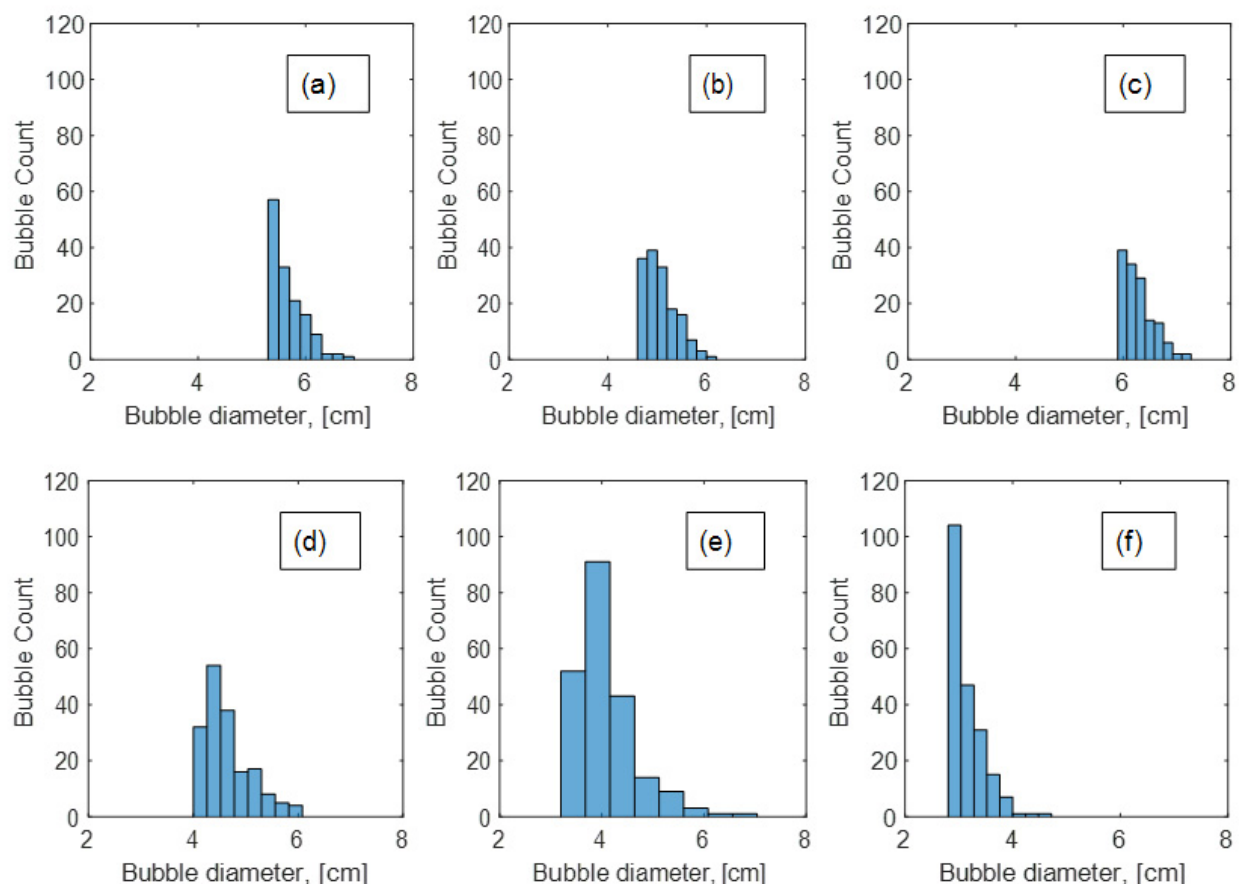

Figure 10. Bubble count vs. bubble diameter at superficial gas velocities of 0.4 m/s, 0.35 m/s, 0.3 m/s, 0.25 m/s, 0.176 m/s, and 0.15 m/s illustrated in the pictures from (**a**–**f**), respectively.

The plot of bubble frequency at different superficial gas velocities from the CPFD model, ECT measurement, and Agu et al. [41] correlation are compared in Figure 11. The result from the CPFD model shows that bubble frequency increases with an increase in superficial gas velocity up to 0.25 m/s and decreases further. The increase in bubble frequency up to 0.25 m/s is due to the formation of a large number of smaller size bubbles in the bed (as shown in Figure 10d–f). Due to the coalescence of the smaller bubbles to form larger diameter bubbles, the bubble frequency decreases for the higher gas velocities. At superficial gas velocity of 0.35 m/s, there is a slight increment in the bubble frequency due to split of the large diameter bubbles. The CPFD model predicts the bubble frequency close to the experimental data at higher gas velocities and overpredicts the bubble frequency at lower gas velocities. However, the simulations follow a similar trend of the bubble frequency as the experimental measurements. The Agu et al. correlation for the bubble frequency predicts the bubble frequency close to experimental data at lower gas velocities; however, it underpredicts the bubble frequency at higher gas velocities compared to the experimental and CPFD model. This is because the correlation proposed by Agu et al. is developed for deep beds.
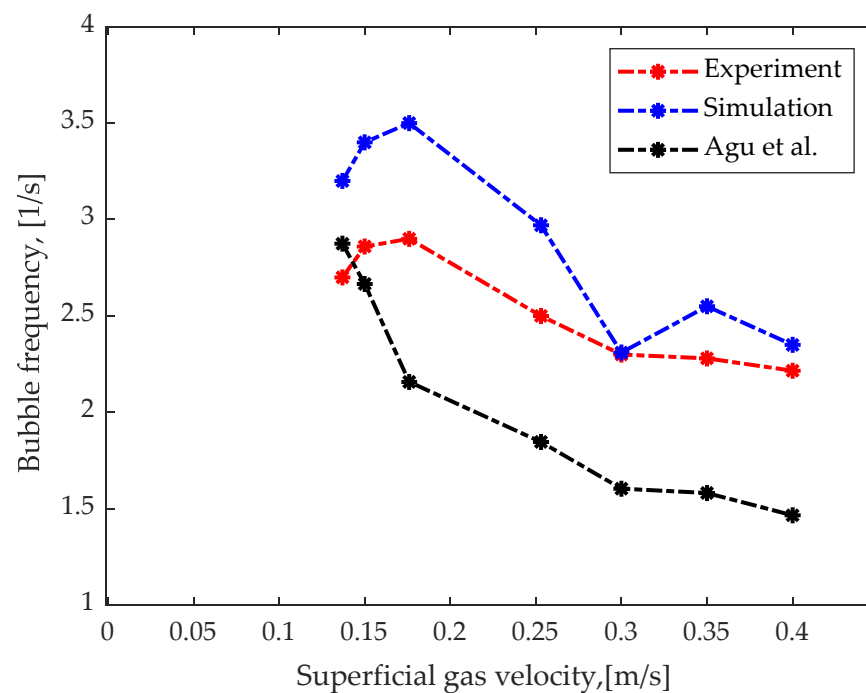
Figure 11. Bubble frequency vs. superficial gas velocities at 15.7 cm bed height [41].

The bubble frequency can be obtained from the fluctuation of the solid volume fraction signal. The solid volume fraction fluctuation for each time step is recorded at different gas velocities. An illustration of the fluctuation of the solid volume fraction at superficial gas velocity of 0.4 m/s is shown in Figure 12a. The bubble frequency is obtained from the Fourier transform of the time series plot of solid volume fraction. The Fourier transform of the solid volume fraction at superficial gas velocity of 0.137 m/s, 0.25 m/s, and 0.4 m/s at 15.7 cm bed height is shown in Figures 12b, 12c and 12d, respectively. The amplitude of the solid volume fluctuation is shown on the Y-axis and frequency on the X-axis. The amplitude gives information about the bubble size. For the bed with a single bubble, the frequency can be obtained, where the amplitude is at the maximum. However, for a bubbling fluidized bed, it is evident that there can be multiple peaks for multiple bubbles passing a plane, as shown in Figure 12c,d. The multiple peaks of the varying amplitude depict that there are multiple bubbles with different sizes passing the plane. With an increase in superficial gas velocity from 0.137 m/s to 0.4 m/s, the amplitude increases. This increase in the amplitude is due to an increase in the bubble size. There is no dominant frequency; however, for

each gas velocity, there are several peaks within the band of 1–6 Hz. For gas velocity of 0.137 m/s, the peak of the amplitude fluctuates within a narrow height, which indicates that there are multiple smaller bubbles. At 0.25 m/s, few large bubbles are observed (as indicated by the sudden increase in the amplitude). At superficial gas velocity of 0.4 m/s, the amplitude of the solid volume fraction fluctuation is approximately 60–100 within the band of 2–5 Hz. The higher amplitude with a wide range of bands indicates that the large number of bigger-sized bubbles pass the plane at 15.7 cm.

(a)

(b)

(c)

(d)
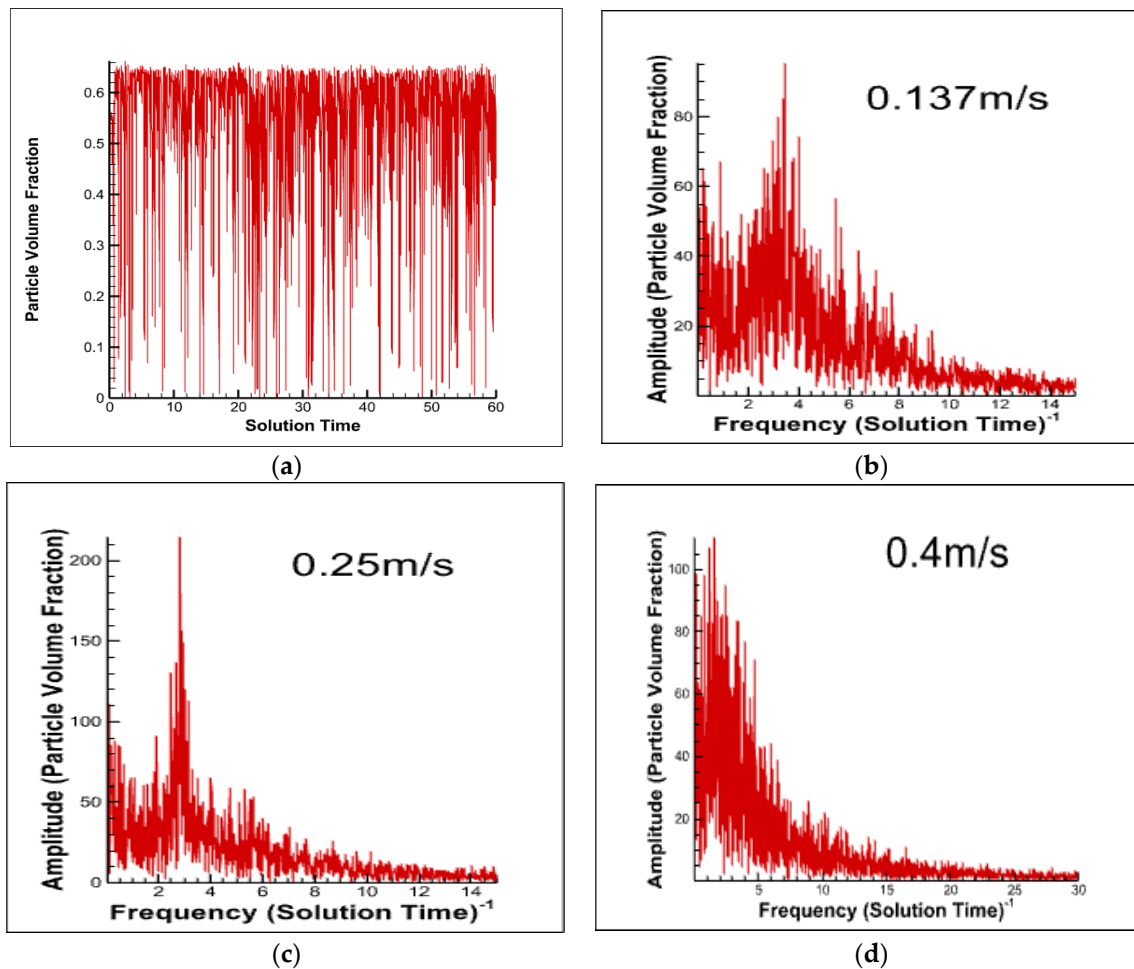
Figure 12. Figure showing: (**a**) fluctuation of particle volume fraction with time; (**b**–**d**) Fourier transform of the particle volume fraction for superficial gas velocities 0.137 m/s, 0.25 m/s, and 0.4 m/s, respectively.

4. Conclusions

The efficiency of a fluidized bed reactor depends on the bed fluid dynamic behavior, which is significantly influenced by the bubble properties. The bubble properties in a BFB are primarily responsible for heat and mass transfer, better mixing, and solid circulation. This work investigates the bubble properties of a bubbling fluidized bed reactor using computational particle fluid dynamic (CPFD) simulations and electrical capacitance tomography (ECT) measurements. The bubble properties measured in this work include average bubble diameter, bubble rise velocity, and bubble frequency at different superficial gas velocities and heights along the reactor. The two-dimensional images along the reactor horizontal and vertical planes of the BFB were extracted from the CPFD simulations at transient time steps and different operating conditions. The CPFD model was developed in a commercial CPFD software Barracuda Virtual Reactor 20.0.1. The bubble behavior and bed fluidization behavior are characterized from the bubble properties. The bubble

properties were determined by processing the extracted images with script developed in MATLAB. The CPFD simulation results are compared with experimental data from the ECT sensors and correlations in the literature.

The results from the CPFD model and experimental measurement depicted that the average bubble diameter increased with an increase in superficial gas velocities up to 4.2 U_{mf} and decreased with a further increase in gas velocities due to the onset of large bubbles (potential slugging regime). The result predicted by the CPFD model revealed that the bubble rise velocity was directly related to bubble diameter. The rise velocity of the bubbles increased with an increase in superficial gas velocity and bubble position in the bed. However, the increment in bubble rise velocity was not linear. The bubble moved slowly within the lower region of the bed. The bubble velocity increased significantly in the middle and upper region of the bed, followed by bubble coalescence at superficial gas velocity $5U_{mf}$. The Fourier transform of the transient solid volume fraction illustrated that multiple bubbles pass the plane with varying amplitude and frequency in the range of 1–6 Hz. Further, the bubble frequency increases with an increase in superficial gas velocity up to $2.5U_{mf}$ and decreased with a further increase in gas velocity.

The CPFD model and method employed in this work can be useful for the efficient design and operation of a bubbling fluidized bed gasification reactor. Further work will be focused on investigating the influence of bubble properties on gasifier conversion efficiency operated at high temperatures.

References

1. Jaiswal, R.; Agu, C.E.; Thapa, R.K.; Moldestad, B.M.E. Study of fluidized bed regimes using Computational Particle Fluid Dynamics. *Linköping Electron. Conf. Proc.* **2018**, *153*, 271–276. [CrossRef]
2. Jaiswal, R.; Furuvik, N.C.I.S.; Thapa, R.K.; Moldestad, B.M.E. Method of identifying an operating regime in a bubbling fluidized bed gasification reactor. *Int. J. Energy Prod. Manag.* **2020**, *5*, 24–34. [CrossRef]
3. Yang, W.-C. Other nonconventional fluidized beds. In *Handbook of Fluidizfition and Fluid-Particle Systems*; Siemens Westinghouse Power Corporation: Pittsburgh, PA, USA, 2003.
4. Geldart, D.; Baeyens, J. The design of distributors for gas-fluidized beds. *Powder Technol.* **1985**, *42*, 67–78. [CrossRef]
5. Kunii, D.; Levenspiel, O. *Fluidization Engineering*; Butterworth-Heinemann: Oxford, UK, 1991.
6. Johnsson, F.; Zijerveld, R.; Schouten, J.; Bleek, C.V.D.; Leckner, B. Characterization of fluidization regimes by time-series analysis of pressure fluctuations. *Int. J. Multiph. Flow* **2000**, *26*, 663–715. [CrossRef]
7. Issangya, A.S.; Cocco, R.A.; Karri, S.R.; Knowlton, T.M.; Chew, J.W. Bed density and bubble void fraction variation in a fluidized bed stripper. *Chem. Eng. Sci.* **2022**, *260*, 117837. [CrossRef]
8. Agu, C.E.; Tokheim, L.-A.; Eikeland, M.; Moldestad, B.M. Determination of onset of bubbling and slugging in a fluidized bed using a dual-plane electrical capacitance tomography system. *Chem. Eng. J.* **2017**, *328*, 997–1008. [CrossRef]
9. CHOI, J.H.; Son, J.E.; Kim, S.D. Bubble size and frequency in gas fluidized beds. *J. Chem. Eng. Jpn.* **1988**, *21*, 171–178. [CrossRef]
10. Karimipour, S.; Pugsley, T. A critical evaluation of literature correlations for predicting bubble size and velocity in gas–solid fluidized beds. *Powder Technol.* **2011**, *205*, 1–14. [CrossRef]
11. Yang, W.-C. Bubbling fluidized beds. In *Chemical Industries-New York-Marcel Dekker-*; Siemens Westinghouse Power Corporation: Pittsburgh, PA, USA, 2003; pp. 53–112.
12. Glicksman, L.; Lord, W.; Sakagami, M. Bubble properties in large-particle fluidized beds. *Chem. Eng. Sci.* **1987**, *42*, 479–491. [CrossRef]

13. Liu, J.; Grace, J.R.; Bi, X. Novel multifunctional optical-fiber probe: I. Development and validation. *AIChE J.* **2003**, *49*, 1405–1420. [CrossRef]

14. Du, B. *Hydrodynamics and Flow Structure, Gas and Solids Mixing Behavior, and Choking Phenomena in Gas-Solid Fluidization*; The Ohio State University: Columbus, OH, USA, 2005.

15. Du, B.; Warsito, W.; Fan, L.-S. ECT studies of gas− solid fluidized beds of different diameters. *Ind. Eng. Chem. Res.* **2005**, *44*, 5020–5030. Available online: https://pubs.acs.org/doi/10.1021/ie049025n (accessed on 31 August 2022). [CrossRef]

16. Sun, J.; Yan, Y. Non-intrusive measurement and hydrodynamics characterization of gas–solid fluidized beds: A review. *Meas. Sci. Technol.* **2016**, *27*, 112001. Available online: https://iopscience.iop.org/article/10.1088/0957-0233/27/11/112001 (accessed on 31 August 2022). [CrossRef]

17. Deen, N.G.; Godlieb, W.; Gorter, S.; Kuipers, J.A.M. An electrical capacitance tomography study of pressurized fluidized beds. In Proceedings of the 13th International Conference on Fluidization-New Paradigm in Fluidization Engineering, Gyeong-ju, Korea, 16–21 May 2010; Available online: https://dc.engconfintl.org/fluidization_xiii/26/ (accessed on 31 August 2022).

18. Caicedo, G.R.; Marqués, J.J.; Ruíz, M.G.; Soler, J.G. A study on the behaviour of bubbles of a 2D gas–solid fluidized bed using digital image analysis. *Chem. Eng. Process. Process Intensif.* **2003**, *42*, 9–14. [CrossRef]

19. Li, J.; Agarwal, R.K.; Zhou, L.; Yang, B. Investigation of a bubbling fluidized bed methanation reactor by using CFD-DEM and approximate image processing method. *Chem. Eng. Sci.* **2019**, *207*, 1107–1120. [CrossRef]

20. Lettieri, P.; Mazzei, L. Challenges and issues on the CFD modeling of fluidized beds: A review. *J. Comput. Multiph. Flows* **2009**, *1*, 83–131. [CrossRef]

21. Gidaspow, D. *Multiphase Flow and Fluidization: Continuum and Kinetic Theory Descriptions*; Academic Press: Cambridge, MA, USA, 1994.

22. Wang, W.; Lu, B.; Zhang, N.; Shi, Z.; Li, J. A review of multiscale CFD for gas–solid CFB modeling. *Int. J. Multiph. Flow* **2010**, *36*, 109–118. [CrossRef]

23. Singh, B.K.; Roy, S.; Buwa, V.V. Bubbling/slugging flow behavior in a cylindrical fluidized bed: ECT measurements and two-fluid simulations. *Chem. Eng. J.* **2020**, *383*, 123120. [CrossRef]

24. Acosta-Iborra, A.; Sobrino, C.; Hernández-Jiménez, F.; de Vega, M. Experimental and computational study on the bubble behavior in a 3-D fluidized bed. *Chem. Eng. Sci.* **2011**, *66*, 3499–3512. [CrossRef]

25. Wang, J.; van der Hoef, M.A.; Kuipers, J. Comparison of Two-Fluid and Discrete Particle Modeling of Dense Gas-Particle Flows in Gas-Fluidized Beds. *Chem. Ing. Tech.* **2013**, *85*, 290–298. [CrossRef]

26. Kraft, S.; Kirnbauer, F.; Hofbauer, H. CPFD simulations of an industrial-sized dual fluidized bed steam gasification system of biomass with 8 MW fuel input. *Appl. Energy* **2017**, *190*, 408–420. [CrossRef]

27. Cha, B.; Kim, J.; Son, S.R.; Park, D.S.; Il, M. CPFD simulation of fluidized bed flow in FCC regenerator. In *Computer Aided Chemical Engineering*; Elsevier: Amsterdam, The Netherlands, 2012; pp. 1153–1157. [CrossRef]

28. Thapa, R.K.; Frohner, A.; Tondl, G.; Pfeifer, C.; Halvorsen, B. Circulating fluidized bed combustion reactor: Computational Particle Fluid Dynamic model validation and gasfeed position optimization. *Comput. Chem. Eng.* **2016**, *92*, 180–188. [CrossRef]

29. Adkins, B.D.; Kapur, N.; Dudley, T.; Webb, S.; Blaser, P. Experimental validation of CFD hydrodynamic models for catalytic fast pyrolysis. *Powder Technol.* **2017**, *316*, 725–739. [CrossRef]

30. Córcoles, J.; Acosta-Iborra, A.; Almendros-Ibáñez, J.; Sobrino, C. Numerical simulation of a 3-D gas-solid fluidized bed: Comparison of TFM and CPFD numerical approaches and experimental validation. *Adv. Powder Technol.* **2021**, *32*, 3689–3705. [CrossRef]

31. O'Rourke, P.J.; Snider, D.M. Inclusion of collisional return-to-isotropy in the MP-PIC method. *Chem. Eng. Sci.* **2012**, *80*, 39–54. [CrossRef]

32. Snider, D.M. Three fundamental granular flow experiments and CPFD predictions. *Powder Technol.* **2007**, *176*, 36–46. [CrossRef]

33. Snider, D.M. An incompressible three-dimensional multiphase particle-in-cell model for dense particle flows. *J. Comput. Phys.* **2001**, *170*, 523–549. [CrossRef]

34. Andrews, M.J.; O'Rourke, P.J. The multiphase particle-in-cell (MP-PIC) method for dense particulate flows. *Int. J. Multiph. Flow* **1996**, *22*, 379–402. [CrossRef]

35. Weber, J.M.; Layfield, K.J.; Van Essendelft, D.T.; Mei, J.S. Fluid bed characterization using Electrical Capacitance Volume Tomography (ECVT), compared to CPFD Software's Barracuda. *Powder Technol.* **2013**, *250*, 138–146. [CrossRef]

36. Sommerfeld, M.; Huber, N. Experimental analysis and modelling of particle-wall collisions. *Int. J. Multiph. Flow* **1999**, *25*, 1457–1489. [CrossRef]

37. Makkawi, Y.T.; Wright, P.C. Electrical capacitance tomography for conventional fluidized bed measurements—Remarks on the measuring technique. *Powder Technol.* **2004**, *148*, 142–157. [CrossRef]

38. Mori, S.; Wen, C. Estimation of bubble diameter in gaseous fluidized beds. *AIChE J.* **1975**, *21*, 109–115. [CrossRef]

39. Werther, J. Effect of gas distributor on hydrodynamics of gas fluidized beds. *Ger. Chem. Eng.* **1978**, *1*, 166–174.

40. Davidson, J. Fluidized Particles. In *Mobile Particulate Systems*; Springer: Berlin/Heidelberg, Germany, 1995; pp. 173–196.

41. Agu, C.E.; Tokheim, L.-A.; Eikeland, M.; Moldestad, B.M. Improved models for predicting bubble velocity, bubble frequency and bed expansion in a bubbling fluidized bed. *Chem. Eng. Res. Des.* **2019**, *141*, 361–371. [CrossRef]

42. Weber, J.M.; Mei, J.S. Bubbling fluidized bed characterization using Electrical Capacitance Volume Tomography (ECVT). *Powder Technol.* **2013**, *242*, 40–50. [CrossRef]

43. Makkawi, Y.T.; Wright, P.C. Optimization of experiment span and data acquisition rate for reliable electrical capacitance tomography measurement in fluidization studies a case study. *Meas. Sci. Technol.* **2002**, *13*, 1831–1841. Available online: https://iopscience.iop.org/article/10.1088/0957-0233/13/12/305/meta (accessed on 31 August 2022). [CrossRef]

Paper 6

Investigation of Bubble Properties in a Bubbling Fluidized-Bed Gasification Reactor Using a Computational Particle Fluid Dynamic Model

Article

Investigation of Bubble Properties in a Bubbling Fluidized-Bed Gasification Reactor Using a Computational Particle Fluid Dynamic Model

Rajan Jaiswal,* C.E. Agu, Henrik Kofoed Nielsen, Marianne Sørflaten Eikeland, Britt Margrethe Emilie Moldestad, and Rajan Kumar Thapa

Read Online

ACCESS | Metrics & More | Article Recommendations | SI Supporting Information

ABSTRACT: The conversion efficiency, operation, and design of bubbling fluidized bed (BFB) reactors depend on the bed dynamics behavior, which is significantly influenced by the bubble properties. To establish the best operating condition for efficient conversion, this study investigates the dynamics behavior of a BFB reactor using experimental measurements and computational particle-fluid dynamics simulation. The simulations account for particle size distribution and variation of particle properties used in the experiments to eliminate the possible effects on the bed behavior. Compared with a cold bed of similar biomass load and gas velocity, the results show that bubbles propagate with a wider distribution, a smaller size, and a higher frequency in the hot gasifying bed. The bubble diameter and amount of unconverted char particles increase with increasing air flow rate at a constant air−fuel ratio. Although the solid particle distribution over the bed can be uniform with increasing air flow rate, the temperature and gas species distributions lack uniformity due to different degrees of reactions across the bed. An increase in the air flow rate also results in a decrease in the gas residence time, thereby lowering the biomass conversion efficiency in the bed. At the optimum gas residence time, the concentration of hydrogen is maximum, while the concentrations of carbon dioxide and water vapor are minimum in the product gas. For efficient biomass gasification in a bubbling bed, the superficial gas velocity, u_0, and average bubble diameter, D_b, over the bed are related by $gD_b/u_0 = 3.0$, where $g = 9.81$ m/s^2 is the gravity constant. This proposed model can therefore be used to size BFB reactors or set the operating gas velocity to achieve optimum gasification.

Optimum gas residence time for efficient gasification of biomass in bubbling fluidized bed

For efficient biomass conversion, $gD_b/u_0 = 3.0$
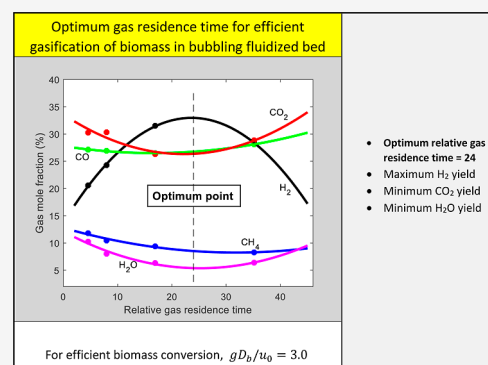
1. INTRODUCTION

Gasification of biomass using the fluidized bed technology has gained popularity in recent years for different applications such as syngas production and energy generation. Fluidized bed gasification is considered advantageous owing to the uniform distribution of heat and mass transfer, intense gas−solid mixing, and the possibility for continuous and large-scale operations.[1] Among different types of fluidized bed reactors for gasification processes, the bubbling fluidized bed (BFB) is extensively used as it is simple to operate and capable of handling a variety of feedstock.[2] Gasification, in general, is a thermochemical degradation process where the conversion of carbonaceous feedstocks into fuel gases is accomplished in two steps.[3] The first step is the devolatilization of the feedstock where volatile gases such as CO_2, CO, H_2, and CH_4 are released instantaneously. The second step is the conversion of char into producer gas. The char remaining after devolatilization undergoes gasification, and the conversion efficiency into product gases depends on how well the fuel particles are in contact with the fluidizing gas. With a BFB reactor, the contacts established between char particles and the bed material also determine the effectiveness of the reaction. The

bubbles formed in the bed are primarily responsible for gas−solid contact and mixing in the reactor. Therefore, bubble properties such as average bubble diameter, bubble rise velocity, and bubble frequency in the reactor are important parameters which determine thermochemical conversion and distribution of product gas species. In addition, entrainment of particles in the product gas, nonuniform temperature distribution, bed agglomeration, and so forth can be avoided with a proper understanding of the fluidized bed regime and bubble properties. An appropriate flow regime in a BFB can be characterized by a smooth fluidization quality where there is no flow of slugs. In such conditions, bubbles are smaller in size, larger in number, and uniformly distributed across the bed. However, the two-phase flow of gas and solids coupled with
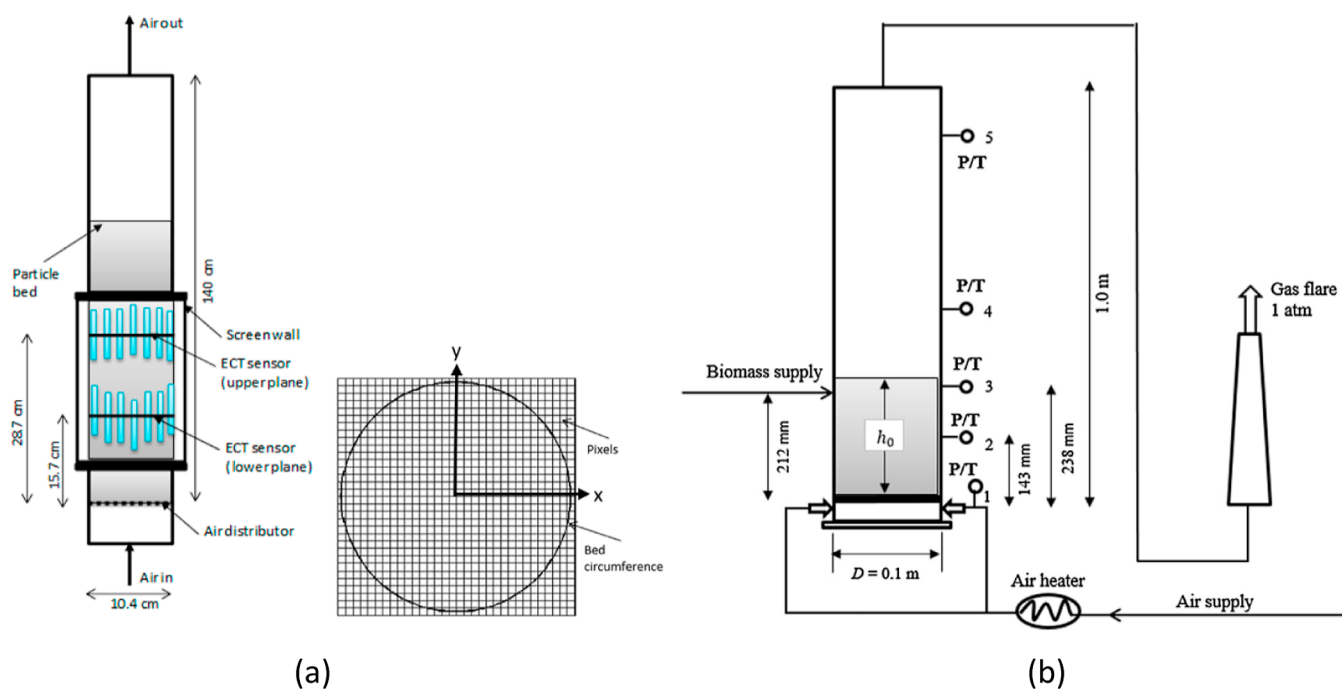
Figure 1. Overview of setups used in the test, showing a (a) cold fluidized bed column equipped with ECT sensors for measurement of solid fraction distribution and (b) biomass gasification reactor equipped with temperature and pressure sensors.

mass and heat transfer and a series of homogeneous and heterogeneous reactions in the fluidized bed is complex. Understanding such bubble dynamics and multiphase thermal phenomena occurring in gasification reactors is key for efficient operation and provision of useful information for the design and scale-up of such reactors.[4−6]

The major objective of this paper is to investigate the flow dynamics and thermal behavior of BFB reactors for an efficient gasification process. Several studies have been carried out on the measurement of bubble properties in fluidized beds using both experimental and numerical techniques. For instance, nonintrusive experimental techniques such as electrical capacitance tomography (ECT) and digital image sensing are widely used to measure the bubble properties in fluidized beds without interfering with the fluid flow dynamic behavior.[7−13] However, most of these works are devoted to measuring bubble dynamics in fluidized bed columns containing one type of particle. By contrast, gasification reactors usually come with a bed of solids containing mixtures of inert particles and active biomass particles of different size distributions. The mixture of binary particles in the reactor has a significant impact on fluidization patterns including mixing/segregation and bubble dynamics. Hence, the complexities arising in such gasification reactors cannot be predicted based on the information obtained from fluidized beds with one type of particle.[14] On the impact of the particle size distribution (PSD), Yang et al.[15] studied the dynamics and thermal properties of bubbles in a BFB, reporting that an increase in PSD leads to an increase in the bubble volume, aspect ratio, and mass fraction of combustible gases in the bed. In addition, the temperature and thermal conductivity of bubbles increase with the rising velocity, pressure, and density decrease. In this regard, measuring the bubble properties with binary mixtures of particles is crucial to characterize the fluid dynamic behavior in fluidized bed gasifiers.

Of the research studies so far on fluidized beds with a mixture of different particle types, the emphases are mainly on measuring the effect of gas velocity on the mixing, segregation, and distribution pattern of the lower-density feedstock and inert bed material. The effect of large irregular-shaped particles on the bubble dynamics has often been ignored. However, in the reports of Fotovat et al.[16] and Kiared et al.,[17] it is reported that notable changes can occur in the bed voidage and bubble properties when large particles are present. With such dynamic behavior, the heat and mass transfer interfacial area may vary in the bed during a gasification process. A few research studies have been conducted to measure bubble dynamic behavior in fluidized beds containing biomass and inert bed material, but mostly in cold-flow conditions.[7,16] Noting that biomass first degrades into gas and char components during gasification, it is essential when analyzing the bed behavior under ambient conditions to quantify the impact on bubble dynamics due to the presence of char particles instead of the raw biomass. Knowledge of the complex bubbling bed behavior will influence the decision on the selection of optimum operating parameters including superficial gas velocity and bed particle size in fluidized bed reactors.

This study therefore is aimed at determining criteria for selecting optimum operating parameters in a BFB biomass reactor. To achieve this, the dynamic behavior of fluidized beds with binary mixtures of solid particles is investigated using both experimental measurements and numerical computations. In a cold and nonreacting flow, ECT sensors are employed to measure bubble properties in the beds. The results are used to validate the numerical scheme setup for the simulation of biomass gasification in a reactor of similar geometry. For the numerical simulations, the computational particle-fluid dynamic (CPFD) model embedded in Barracuda virtual reactor (VR) is applied. The model uses a combination of Eulerian and Lagrangian methods similar to the conventional discrete element model (DEM) for fluid field and particle phase

calculations, respectively. Contrary to the two-fluid model (TFM) which is based on the Eulerian—Eulerian computational approach, DEM utilizes an approach where the individual particles are tracked while holding particle—particle collision into account and thus can be effectively applied for a system with different particle types and properties.[18] On the other hand, the TFM model only accounts for particles with the same density, diameter, and coefficient of restitution which often results in inaccurate prediction of the bed properties.[19,20]

Although the DEM approach requires enormous computing power to simulate fluidized bed reactors, making it less attractive for applications involving large numbers of particles (Deen et al., 2007), the CPFD model in Barracuda, however, uses the multiphase particle-in-cell (MP-PIC) approach where particles with similar attributes such as density, volume, and so forth are grouped together to form a parcel considered as a computational particle. By this configuration, it is therefore possible to simulate a large number of computational particles at lower computational cost and time. The efficiency and accuracy of numerical calculations using the MP-PIC model are better compared to other discrete element models and two-fluid models as demonstrated in various studies.[19,20] The MP-PIC approach has gained popularity in recent days due to its capacity to simulate industrial fluidized bed reactors.[21,22] Liu et al.[23] also illustrated the capability of this approach in their studies on the dynamics and thermal characteristics of mesoscale bubbles in a BFB coal gasifier.

Using the MP-PIC algorithm, CPFD simulation results are compared against the experimental data obtained from a 20 kW BFB gasification reactor in this study. At different air flow rates, the simulated results are analyzed to obtain bubble properties and investigate the effect of bubble flow on the distribution of gas and temperature in the bed as well as the gas composition in the product. Because gas—solid contact influences the efficiency of the biomass conversion process, the simulation is also used to derive the effect of bubble dynamic properties on the gas residence time. As particle segregation may distort the characteristic flow behavior, biomass particles are fed near the bottom of the bed, thus minimizing the segregation effect. The bed height-to-diameter ratio is kept below 2 to prevent the flow of slugs within the range of gas velocities applied in the test. In the subsequent sections, this methodology is given in detail. The results are presented and analyzed, and conclusions are clearly drawn.

2. METHODS AND MATERIALS

This section provides descriptions of the setup, material, and computational model implemented in this study for the purpose of evaluating the impact of bubble dynamic behavior on biomass gasification reactors.

2.1. Experimental Setup. The experimental setup consists of a cold BFB column equipped with ECT sensors and a data acquisition system as shown in Figure 1a. The reactor is a cylindrical transparent column 150 cm in height and 10.4 cm in internal diameter. The column is fitted with an air distributor at the bottom and is open to the atmosphere. The air distributor is 3 mm thick and 40% porous with a flow area of 34 cm^2 which allows the fluidizing gas to pass through the bed uniformly. The ECT32 software is used to measure solid volume fraction fluctuation and is capable of displaying the bed images in real time. The online images are extracted from the capacitance measurements using the Linear Back Projection algorithm.[24]

The twin-plane ECT sensors applied are located at 15.7 and 28.7 cm from the air distributor where each sensor comprises equally spaced 12 electrodes mounted on the outer wall of the column. The raw data produced from the ECT sensors are either in the form of a numerical matrix or an image that covers the entire sensor-measuring area. For proper measurement of solid distribution, the cross-section of each sensor is divided into 32×32 square pixels of which 812 effectively lie within the bed. Each pixel holds a normalized relative permittivity value between 0 and 1, which represents the solid volume fraction. The sensor calibration was performed before the experiment at both extreme cases, i.e., when the sensor area is filled with the lower-permittivity material (air) and then with the higher-permittivity material (bed particles). For each flow velocity, the data were logged for 60 s at a sampling frequency of 100 Hz, indicating a total of 6000 frames over the sampling period.

Figure 1b illustrates a 20 kW reactor applied in biomass gasification. The setup consists of a stainless-steel cylindrical column with a wall thickness of 4 mm, a height of 1.0 m, and an internal diameter of 10 cm. At startup and during the bed heat-up, three electric heating elements attached externally along the column wall are used. To minimize the heat loss, the inner side of the reactor is coated with a refractory material, while the outer part is insulated with a 200 mm-thick fiberglass. Five thermocouples and five pressure sensors distributed along the vertical axis are used to monitor the behavior in the reactor. The fuel supply is through a screw feeder, which is calibrated for each fuel applied. Air is supplied through two 10 mm steel pipes positioned 27.5 mm from the column base. The mass flow rate of air is measured with a BROOK air flowmeter (3809 series) operating in the range of 0.48—4.7 kg/h. Above the reactor column, a gas sampling point is installed. The product gas from the reactor is passed through a flare before being discharged into the atmosphere.

Samples of gas taken at 10 min intervals were analyzed offline using the SRI gas chromatograph. The gas chromatograph uses a TCD and helium as the carrier gas with an installed column comprising a packed molecular sieve 13x. The gas chromatograph operates at 10 psi in the temperature range of −15 to 200 °C and can provide the composition of the major fuel gases: carbon monoxide (CO), hydrogen (H_2), carbon dioxide (CO_2), and methane (CH_4) as well as nitrogen (N_2) and oxygen (O_2) in each gas sample by the gradient method. Each experiment was performed twice to confirm the repeatability, and the two data sets were averaged and recorded.

Sand particles were used as the bed material with a narrow PSD, 200—400 μm, and compressed air was applied as the fluidizing gas and gasification agent. The size of the sand particles was obtained from the sieve analysis. Two types of fuel particles, char and wood pellets, were used in the different parts of the experiments. The wood pellets were cylindrical in shape with a diameter of 6 mm and a length between 5 and 30 mm. The char particles used were collected (as unconverted char) from a series of gasification experiments based on wood pellets at 700—800 °C.[3] The char particles had a diameter in the range of 2—5 mm and a length within 1—15 mm. The properties of these particles are listed in Table 1. The particle (char, wood pellets, and sand) properties including sphericity, void fraction, and equivalent spherical diameter are calculated from the particle geometry using 1.

Table 1. Properties of the Bed Material, Wood Pellets, and Char Particles

material	density, ρ_p (kg/m³)	bulk density, ρ_{bp} (kg/m³)	equivalent diameter of the particle, $d_{p,s}$ (mm)	sphericity, φ_p	void fraction, ε
sand	2650	1537	0.302	0.86	0.42
wood pellets	1139	649	8.9	0.82	0.43
char	423	215	4.6	0.75	0.48

For a mixture of sand and char particles, cold-flow experiments were carried out at different bed compositions. Char particles were used instead of wood pellets since the mixture of char and inert bed material represents the real bed condition in the gasification process. It should be noted that during the gasification process, wood pellets do undergo rapid devolatilization, leaving the bed as a mixture of inert bed materials and char particles. In the experiment, a uniform mixture of char and sand particles was first obtained before being added in segments into the column to avoid segregation. To minimize the flow of slugs over a wide range of gas velocities, the initial bed height in each test was 20 cm, covering only the first ECT sensor at 15.7 cm above the air distributor.

$$\varepsilon = 1 - \rho_{bp}/\rho_p \tag{1}$$

$$d_{p,s} = \left(\frac{6V_P}{\pi}\right)^{1/3} \tag{2}$$

$$\varphi_p = \frac{6\pi^{1/3}V_P^{2/3}}{A_P} \tag{3}$$

Here, ε is the bed static void fraction, $d_{p,s}$ is the volume-equivalent spherical particle diameter, and φ_p is the sphericity of the particle, where ρ_{bp} is the particle bulk density, ρ_p is the true solid density, V_P is the particle mean volume, and A_P is the mean particle surface area.

The experiment and simulations were conducted at different gas flow rates and biomass loads. The gas flow rates were selected to ensure that entrainment of particles is prevented, and the bed is operated above the minimum fluidization velocity. The minimum fluidization and slugging velocities reported in Table 2 for the different beds were estimated by the methods described by Agu et al.[7]
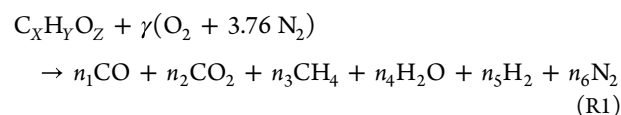
Table 2. Cold Bed Characteristic Velocities at Different Loads of Char Particles

char volume fraction (%)	0 (pure sand)	24.8	41.0	100 (pure char)
minimum fluidization velocity (cm/s)	7.64	7.76	8.96	98.7
minimum slugging velocity (cm/s)	22.7	30.0	36.1	113.7

2.2. Theory. An overview of the theory behind biomass conversion in a reactor is outlined. This section also presents a brief description of the computational model and its setup used for simulating the dynamic behavior of the BFB.

2.2.1. Chemistry of Biomass Conversion. The composition of product gas postgasification depends on the biomass constituent element and the gasifying agent. Biomass

molecules may contain traces of nitrogen and sulfur in addition to a large percentage of carbon, hydrogen, and oxygen. Neglecting the nitrogen and sulfur constituents, a unit of biomass can be represented as $C_XH_YO_Z$, where X, Y, and Z are the mole fractions of carbon, hydrogen, and oxygen, respectively, in the molecule. Assuming a one-step process, biomass conversion into the gaseous product under a limited supply of air ($O_2 + 3.76 \, N_2$) can be globally expressed as

$$C_XH_YO_Z + \gamma(O_2 + 3.76 \, N_2)$$
$$\rightarrow n_1CO + n_2CO_2 + n_3CH_4 + n_4H_2O + n_5H_2 + n_6N_2 \tag{R1}$$

where $\gamma = \left(\frac{M_{bio}}{M_{air}}\right)$ AFR and n_i, $i = \{1,2,..,6\}$, is the number of moles of each gas species contained in the product gas. M_{bio} and M_{air} are the molecular weights of biomass and air, respectively.

The expression above implies that for a constant value of air–fuel ratio (AFR) defined as the ratio of the mass flow rate of air to the mass flow rate of biomass, the composition and distribution of gases in the product are the same, suggesting maximum conversion and stable product. However, in practice, this might not be the case owing to the competitive side reactions among the reacting species. Other factors that may also influence the product composition include contact/residence time between the fuel particles and gasifying gas, temperature, as well as the mass distribution within the reactor. The degree to which these factors influence gasification varies with different reactor designs and operating configurations.

Biomass conversion is kinetically limited; therefore, to enhance gas diffusion, promote higher heat transfer, and increase the contact area, the size of biomass fed into the reactor should be considerably low (<50 mm). Below a certain temperature (<200 °C), only a drying process is possible where the moisture content evaporates, leaving behind dry solid fuel. At a higher temperature up to 500 °C, the dry particles undergo devolatilization or pyrolysis where it is decomposed into char, tar, and light gases as illustrated in Figure 2. The light gases consist of mainly CO, CO₂, CH₄, H₂,
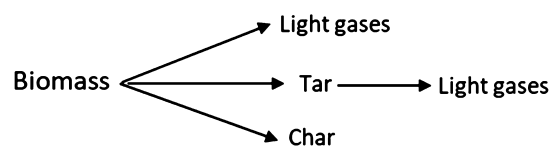
Figure 2. Illustration of parallel steps involved in biomass pyrolysis.

and H₂O. The composition of the pyrolysis product including the drying process also depends on the residence time and temperature where the rate constants, k [1/s], can be modeled in the Arrhenius form, eq 4.

$$k = A\exp(-E/RT) \tag{4}$$

Values of the frequency factor, A [1/s], and the activation energy, E [J/mol], for each step are obtained as described by Chan et al.[25] In the presence of the gasifying agent, e.g., a limited amount of air, the combustible gases (CO, CH₄, and H₂) and char (rich in carbon) undergo partial oxidation, releasing heat energy while reducing the chemical energy content of the pyrolyzed biomass. Moreover, with the limited supply of oxygen, some amount of tar will remain unconverted

in the product gas. Possible reactions during biomass gasification with air, which are also implemented in the computational model are listed in the Supporting Information.

2.2.2. Computational Particle Fluid Dynamics Model in the Barracuda Virtual Reactor. The CPFD model embedded in the Barracuda virtual reactor (VR) (version 21.0.1) was applied to simulate the bubbling bed behavior containing a mixture of sand and biomass particles. The Barracuda VR is a commercial software designed for the simulation of multiphase flow systems such as fluidized bed reactors and can be applied for a large number of computational particles in the order of 10^{15} or more. Barracuda uses a three-dimensional multiphase particle-in-cell approach for the simulation of gas-particle flow, capable of handling detailed thermal physics and reaction chemistry. For the fluid-particle simulations, the Barracuda VR uses a combined Eulerian−Lagrangian approach where solid particles are modeled using the discrete Lagrangian method, and fluid is modeled as an Eulerian grid of cells. While details of the computational model in Barracuda can be found elsewhere,[26−29] eqs 5 and 6 outline the mass and momentum equations of the gas phase and eqs 7 and 8 describe the particle velocity and probability density function $f(x, u_p, \rho_p, V_P, t)$ for tracking particle positions in the flow system. The energy eqs 9 and 10 are applied for gas and solid phases, respectively.

$$\frac{\partial(\varepsilon_g \rho_g)}{\partial t} + \nabla \cdot (\varepsilon_g \rho_g u_g) = \delta \dot{m}_p \tag{5}$$

$$\frac{\partial(\varepsilon_g \rho_g u_g)}{\partial t} + \nabla(\varepsilon_g \rho_g u_g u_g) = -\nabla p + F + \varepsilon_g \rho_g g + \nabla(\varepsilon_g \tau_g) \tag{6}$$

$$\frac{du_p}{dt} = D_P(u_g - u_p) + g - \frac{1}{\varepsilon_p \rho_p}\nabla \tau_p - \frac{1}{\rho_p}\nabla p \tag{7}$$

$$\frac{\partial f}{\partial t} + \nabla(f u_p) + \nabla u_p(f a_p) = 0 \tag{8}$$

$$\frac{\partial(\varepsilon_g \rho_g H_g)}{\partial t} + \nabla(\varepsilon_g \rho_g u_g H_g)$$
$$= \varepsilon_g\left(\frac{\partial p}{\partial t} + u_g \nabla p\right) - \nabla(\varepsilon_g k_g \nabla T_g) + f Q_{pg} + Q_w \tag{9}$$

$$C_v \frac{dT_p}{dt} = \frac{A_P}{m_P} h_{pg}(T_g - T_p) \tag{10}$$

Here, ρ_g, u_g, ε_g, and τ_g are gas-phase density, velocity, volume fraction, and stress tensor, respectively. u_p and a_p are the respective particle velocity and acceleration, while p is the fluid pressure and F is the total force exerted on the fluid by the particles, where D_P is the gas-particle momentum transfer coefficient. The gas temperature, T_g, is related to the specific enthalpy, H_g, and its magnitude is determined by the quantity of heat-exchanged with the particles, Q_{pg}, and with the environment, Q_w, through the reactor wall. The particle temperature, T_p, depends on the single particle surface area, A_P, mass, m_P, and the specific heat capacity, C_v. Since the reactor in this study is properly insulated to minimize interactions with the environment, $Q_w = 0$ can be applied.

The local particle solid volume fraction is expressed as $\varepsilon_p = 1 - \varepsilon_g$ to ensure continuity and is limited to the close-packed

solid volume fraction. The mass transfer rate, $\delta \dot{m}_p$, due to chemical reactions within the gas and solid species is related to the kinetic rate constants of the pyrolysis process and different possible reactions during gasification. The relevant constitutive equations including the various heat transfer coefficients, h_{pg}, implemented in the model are described in the Supporting Information.

The momentum transfer F between gas and particles depends on the drag model, which greatly influences the accuracy of the model simulation. Several drag models can be found in the literature,[30,31] and a number of these are included in the drag model library of the Barracuda software. With a linear coefficient of 2 and a nonlinear coefficient of 180, the Gidaspow drag model which is a combination of Ergun and Wen-Yu drag models was used. Several studies[32,33] have also shown good predictions of the fluid dynamic behavior of a BFB reactor using this blended drag model. It should be noted that either the Wen-Yu or the Ergun drag model can also be used. However, as confirmed in the previous studies, the Ergun model is best suited when the gas volume fraction is below 0.8, while above it, the Wen-Yu model gives a better prediction of the bed behavior. Since both the dense and dilute-phase regions exist continuously over and across a bubbling bed reactor, it is therefore important to apply such a blended drag model as Gidaspow for better simulation results.

For the simulation of virtual reactors using any CPFD tool, a grid defining the control volume, cells, and boundary conditions for all fluid field calculations is required. In this study, a CAD geometry of the reactor was produced in the STL format using SolidWorks and then imported to the Barracuda VR to define the grids. A total of 102,400 cells were specified with a uniform grid generation, dividing the reactor into uniform cells. This number of computational cells was defined such that the cross-section of the VR could also be divided into 32 × 32 pixels similar to the ECT experimental setup. Note that the number of grid sizes can be reduced to decrease the computational time but may introduce some level of bias when comparing the simulated results with the experimental data. Of the 1024 pixels, the effective number covering the bed's cross-sectional area is 812 as shown in Figure 3. In addition, three monitoring planes were defined at heights of 5, 10, and 15.7 cm along the vertical direction of the reactor. An inlet flow boundary condition was applied at the bottom, and a pressure boundary condition was defined at the top of the reactor.

The close-packed volume fraction of the bed is set to correspond to the lowest static void fraction as listed in Table 3 for each particle type. The same PSD obtained in the experiments was also implemented in the Barracuda simulation to eliminate possible effects and bias associated with single particle size. The particles were initialized with a static height of 2 times the reactor diameter. As particle collisions and wall effects have significant impacts on the bed fluid dynamics, the effect of the wall on the fluid particle motion was considered as 0.33 for normal-to-wall momentum retention and 0.85 for tangential-to-wall momentum retention. The maximum momentum redirection from the collision was set as 40%, and the coefficient of restitution for the simulation was used as 0.9. The simulation time was 300 s, selected after a preliminary steady-state evaluation as discussed in the subsequent section. The time step, 0.001 s, specified in Table 3 is the maximum allowable in the simulation. The actual time step is limited by
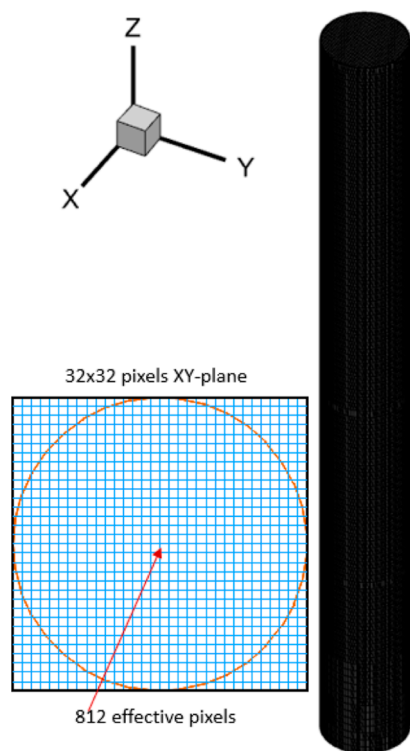
Figure 3. Grid and meshing of the computational domain.

the Courant−Friedrichs−Lewy (CFL) number or temperature changes. Depending on the set limits of these control parameters, the solver in Barracuda can reduce the time step by 3 orders of magnitude from the specified value. The maximum temperature change is 3000 K, which corresponds to the maximum permissible temperature of the reactor. The CFL number is a dimensionless parameter measuring how far the fluid travels in a single time step and can be calculated for a given flow direction from

$$CFL = \frac{u\Delta t}{\Delta x_{cell}} \tag{11}$$

where Δx_{cell} is the cell dimension, u is the fluid velocity, and Δt is the time step in the flow direction. In order to maintain stability, accuracy, and speed of the calculation, the VR automatically adjusts the time step to keep the CFL number between 0.8 and 1.5 as specified in this study.

3. RESULTS

As this study focuses on the simulation of fluidized bed behavior in a gasifier, the CPFD tool employed is first validated with the experimental data. The bubbling behavior of a fluidized bed is characterized by certain bubble dynamic properties including the bubble size, bubble frequency, and the rise velocity. With the setup equipped with ECT sensors, these dynamic properties can be visualized over time at a given superficial gas velocity. As suggested in Table 2, a bed of pure biomass particles cannot be easily fluidized due to its high minimum fluidization velocity, and even if it does, the

fluidization will not be smooth. However, the bed of pure sand particles with lower particle size, higher density, and less irregularity in shape can be fluidized easily.

To clearly evaluate the performance of the model simulation, the behavior of the bed with only sand particles is shown in Figure 4 for different gas velocities, 0.176 and 0.35 m/s. The color bar indicates that the blue region with nearly 0 permittivity is filled with a void or gas pocket, which can be regarded as a bubble. Regions with higher values of permittivity contain higher fractions of solid particles. As shown, smaller bubbles at the measurement plane cluster form a larger one as the velocity increases. The figure also shows that a single large bubble tends to flow along the central axis of the bed. However, between each time interval, the frequency of generation and rise of bubbles is higher with the lower velocity. At 0.35 m/s, there are apparently more idle periods in the bed where it is free of bubbles. This suggests that the larger bubble at the high velocity is mainly slug, generated at a frequency of about 3.5 Hz. It should be noted that the minimum slugging velocity of this bed is 0.227 m/s as reported in Table 2; hence, at the high velocity, it is clear that the bed is slugging.

Compared with the experimental data, the model simulation accurately predicts the flow behavior across the gas velocities. The bubble rise frequency and the spread over the cross-section are similar. There is also a good match in the rising of the large bubbles along the center line. Since the CPFD simulation can capture the dynamic behavior of the fluidized bed, the model can be used to simulate the systems containing binary mixtures of solid particles.

The model simulation is further extended to the bubbling behavior in a biomass gasification reactor. In the gasifier, wood pellets were used as the feedstock, while the bed temperature was maintained within 1023 K. The simulation test was carried out at four different air flow rates where the wood pellets were fed at corresponding rates to achieve a constant air−fuel ratio of 0.813, selected to avoid combustion of the fuel particles. The air also used as the fluidizing gas was fed into the reactor from the bottom of the bed. The bed material used was the same as that of experiments under ambient conditions as listed in Table 1. The bed height was initialized at an aspect ratio of 2, while the biomass feed position was near the bottom of the bed at a height of 5 cm. The devolatilization composition of the wood pellets used in the simulation was obtained from the proximate analysis as given in Table 4.

To validate the CPFD model in the hot reacting bed conditions, a quantitative comparison of the mole fraction of gas species in the product gas is performed against the experimental data at an air flow rate of 2 kg/h. Figure 5a shows the evolution of gas temperature and species composition simulated at the outlet of the reactor over time. As can be seen, a steady-state condition is attained in the reactor after 5 min. Henceforth, the simulated results presented and analyzed are based on the average data obtained over the last 30 s of the simulation run.

Compared with the experimental data, Figure 5b shows the simulated mole fractions of the various gas species. The prediction errors relative to the experimental data are also

Table 3. Simulation Parameters Employed for the CPFD Model Development

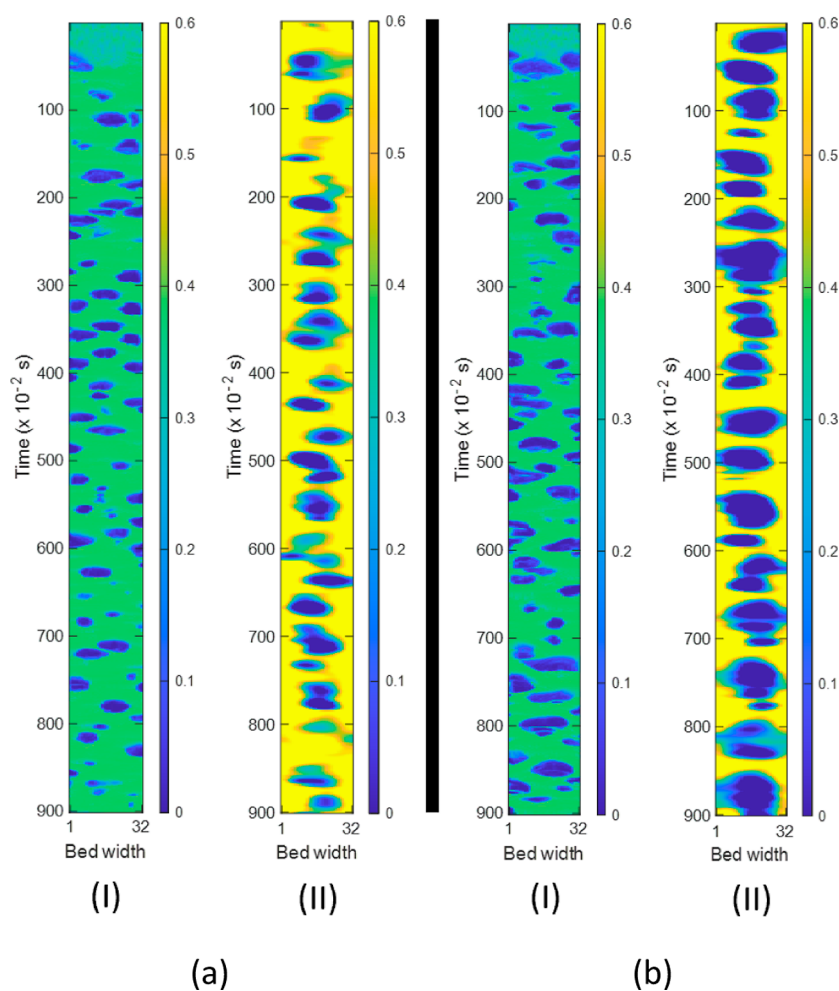| parameters	close pack fraction (−)	solid volume fraction (−)	total cell number (−)	time step (s)	simulation time (s)	initial bed height (cm)
set values	0.64	0.534	102,400	0.001	300	20

Figure 4. Stacks of the measurement plane over time, showing evolution of bubbles in the bed of sand particles at different superficial gas velocities of (a) 0.176 and (b) 0.35 m/s, comparing the (I) simulation data with (II) experimental data from the ECT setup.

Table 4. Proximate Analysis of Wood Pellets as Implemented in the CPFD Model

components	mass fraction (%)	volatile composition (% wt)				
		H_2	CH_4	CO	CO_2	H_2O
ash	0.3					
fixed carbon	15.2					
volatile	84.5	3.54	9.24	63.54	16.34	7.34

shown. Except for nitrogen and carbon dioxide, the model simulation tends to overpredict the gas composition. Though the relative errors in CH_4 and H_2O are high, their respective absolute errors are quite small and are within acceptable limits for analysis. The qualitative trends of the predicted mole fractions also follow closely those of the experiment. The fraction of N_2 in the product gas is the highest while that of H_2O is the least as given by both simulation and experiment. Table 5 provides the raw values of the simulated gas composition for the four different air flow rates. The amount of unconverted char particles in each case is also shown. Based on the unconverted char particles, the minimum fluidization velocity and slugging velocity as predicted according to Agu et al.[7,34] are given in the table. Compared with the inlet superficial air velocity at the operating temperature, the data clearly show

that the fluidized bed at different feed rates is operated within the bubbling regime.

Further analysis of the results is presented in the following subsections to properly evaluate the influence of bubbling bed behavior on gasification of biomass while aiming at finding the criteria for optimum operating conditions.

3.1. Bubble Diameter and CPFD Predictions. The bubble properties which quantify the behavior of a fluidized bed include bubble diameter, rise velocity, and bubble frequency. Within the bubble regime, the rise velocity and frequency are directly related to bubble diameter. While bubble diameter and rise velocity increase along the bed height due to coalescence, the bubble frequency decreases. At a given plane along the bed, the bubble frequency can be easily measured by counting the number of bubbles at a specified time interval. The bubble velocity is however difficult to measure at a given plane due to the continuous distortion and coalescence of the rising bubbles. For the purpose of this study, measuring only the average bubble diameter over the bed height can provide sufficient information for analysis.

Note that ECT sensors only provide information about the solid distribution across the bed cross-section at a measurement position. Therefore, the bubble dimension and size can only be quantified in a two-dimensional plane. As bubbles usually contain some amount of solid particles in their wake, a threshold of 0.2 can be used to define the bubble-emulsion
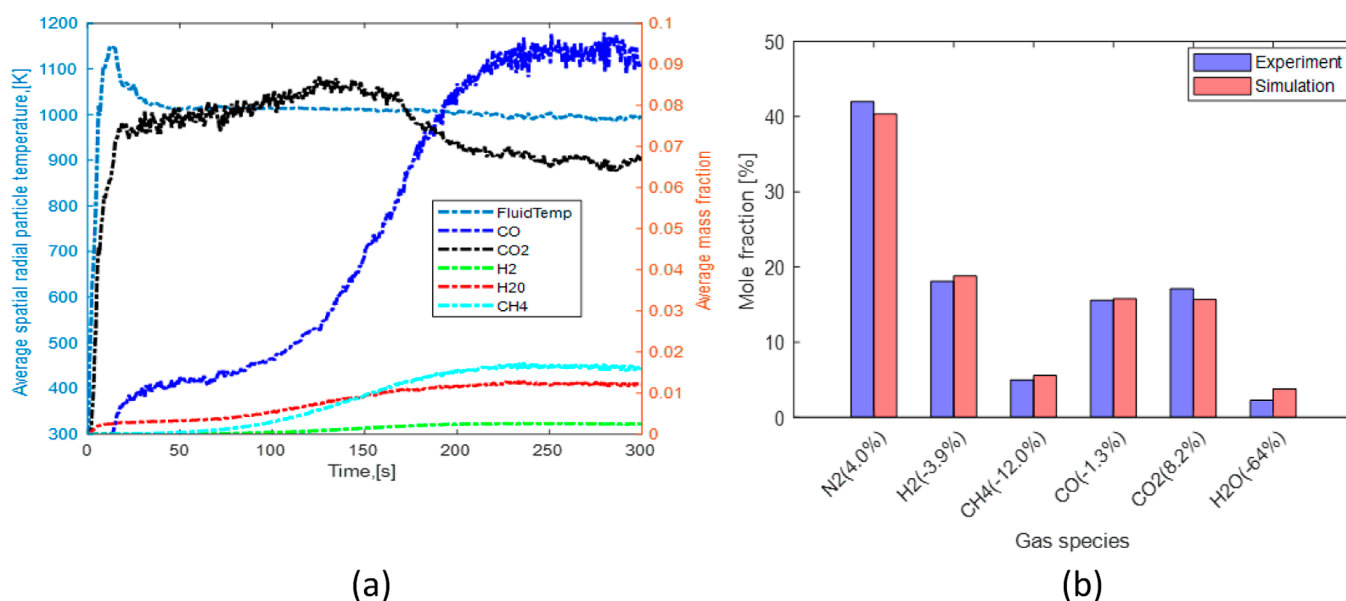
(a)   (b)

Figure 5. (a) Evolution of product gas composition simulated with the CPFD model over time, confirming a steady-state solution after 5 min of simulation time; (b) simulated average gas composition compared with the experimental data at a 2 kg/h air flow rate.

Table 5. Product Gas Compositions and Unreacted Biomass at Different Air Flow Rates with an Air−Fuel Ratio of 0.813

air flow rate (kg/h)	air velocity (cm/s)	mole fraction (%)	N_2	H_2	CH_4	CO	CO_2	H_2O	unconverted char volume fraction (%)	predicted bed characteristic properties	
										u_{mf} (cm/s)	u_{ms} (cm/s)
experiment	2	20.6	42.0	18.1	5.0	15.6	17.1	2.3	21.6	3.47	58.8
CPFD simulation	1	12.9	41.1	16.7	4.9	16.5	17.0	3.8	11.9	3.38	52.7
	2	20.6	40.3	18.8	5.6	15.8	15.7	3.8	21.6	3.47	58.8
	3	30.9	37.4	15.2	6.5	16.8	19.0	5.0	29.3	3.64	64.2
	4	41.2	37.5	12.9	7.4	17.0	18.9	6.4	35.5	3.87	68.8

(a)   (b)   (c)
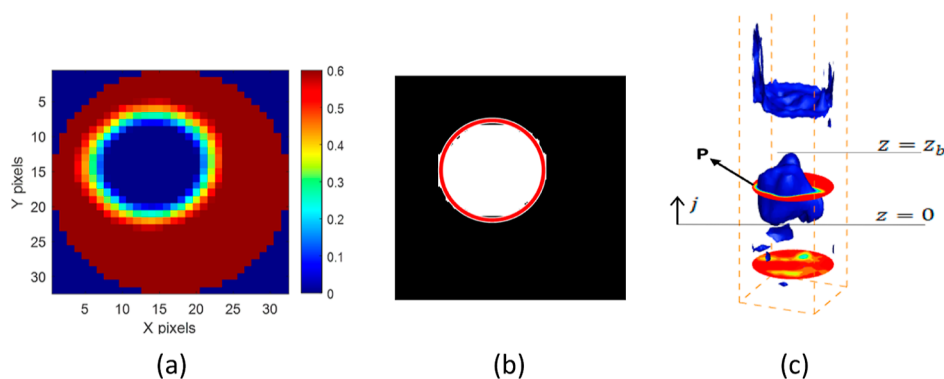
Figure 6. Illustration of (a) emulsion and bubble regions with a boundary, (b) equivalent bubble region in the binary display, (c) and three-dimensional view of bubbles in the CFPD simulation domain.

phase boundary.[8−10] Figure 6a displays a typical image from the bed of pure sand particles captured at the height of 15.7 cm when bubbles flow through at an air velocity of 0.25 m/s. As can be seen, the gas bubble occupies the bed region where the solid fraction is lower than 0.2. To acquire the bubble properties from the ECT data stored over the 812 pixels in each frame, an algorithm was developed in MATLAB, where the data are first converted into binary numbers (white and black regions) to distinguish the bubble region from the rest of the bed as shown in Figure 6b.

Because bubble generation and propagation are dynamic, the indicated bubble diameter at a given time corresponds to the projected cross-section of the bubble. If the bubble has a flat surface (i.e., if viewed as a cylindrical object), the projected area measured for a single bubble will remain constant during the bubble passage across the measurement position. However, for a spherical, oval, or elliptical bubble, the projected area will increase from 0 when the bubble enters the measurement plane to a maximum and then decrease to zero when the bubble leaves the plane; a detailed explanation of this behavior can be found in 9. As noted in the literature, the maximum

projected area is considered the same as the cross-sectional area of the bubble through the center. The bubble diameter based on the ECT data is therefore obtained as described below.

$$D_b = \frac{1}{n} \sum_k \left(\sqrt{\frac{4}{\pi} A_{\max,k}} \right) \tag{12}$$

Here, n is the number of frames over which flow of bubbles are identified and $A_{\max,k} = (N_{\max,k}/N_{\text{eff}})A_B)$ is the maximum projected area across the measurement plane at frame k, where $N_{\max,k}$ is the number of pixels occupied by the projected bubble, $N_{\text{eff}} = 812$ is the effective number of pixels across the bed, and A_B is the bed cross-sectional area.

Contrary to eq 12, the true bubble diameter can be obtained from the measurement of the bubble volume after being identified. In the CPFD model simulation, the bubble dimension can be described in three-dimensional space, thereby providing value for the bubble volume. Using the solid fraction of 0.2 for the bubble-emulsion phase boundary, Figure 6c presents a typical three-dimensional view of a bubble formed in the bed. If V_b is the volume of the bubble, the volume-equivalent spherical bubble diameter, D_b, can be obtained from

$$D_b = \sqrt[3]{\frac{6V_b}{\pi}} \tag{13}$$

Supposing S_b is the projected area at the plane P, the bubble volume is thus

$$V_b = \int_0^{z_b} S_b dz \tag{14}$$

where z_b is the height of the bubble. Since an analytical expression of S_b is cumbersome, the volume of the bubble can be approximated as

$$V_b \approx \frac{A}{2N_{\text{eff}}} \Delta z \sum_j^{n_z} (N_{b,j} + N_{b,j-1}); \quad n_z = z_b/\Delta z \tag{15}$$

Here, Δz is the size of the computational grid along the vertical axis and $N_{b,j}$ is the number of grids on the horizontal plane occupied by the bubble at position j. With the bubble volume estimated from eq 15, the true bubble diameter can then be established from eq 13.

Figure 7 compares the bubble diameters simulated with the CPFD model against the experimental data from the ECT setup. At different gas velocities and char loads, the bed behavior is well predicted, particularly in the beds of pure sand particles and 5% wt char load. Below 0.25 m/s, the different beds are in a bubbling regime. However, as can be seen from the experimental data, the sand bed transits into a slugging regime where the bubble diameter is relatively constant over a wide range of gas velocities. The simulation results also predict the bed behavior in the two regimes including the transition phase.

Observing the behavior at different char loads, the bubble diameter is lower in the bed of 5% wt char compared to the sand particle bed. This behavior can be attributed to an increase in solid packing density due to the ingress of a small fraction of char particles within the matrix of the fluidized sand particles. Moreover, the relatively small amount of char particles may also be dragged into the bubble wakes, resulting in the bubble break-up. With the continuous breakup of
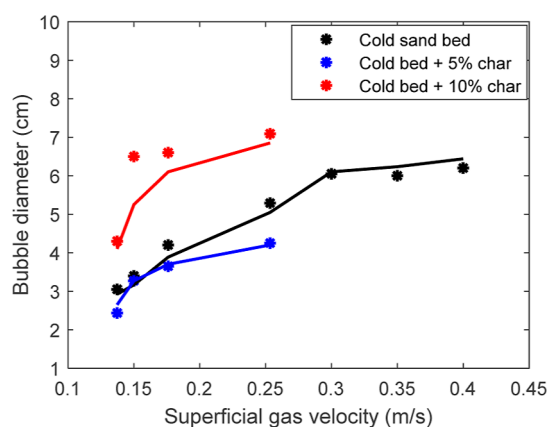

Figure 7. Variation of bubble diameter in cold beds, comparing the behavior at different biomass loads across a range of superficial gas velocities, where data points are experimental values and solid lines are the simulated values.

bubbles, the fluidization quality is enhanced, delaying the possibility of slug flow in the bed as can be observed in the figure. When the char fraction is increased, the bed voidage increases. This therefore results in rapid bubble growth as they form and rise since the bed resistance to the flow is reduced. Owing to this, the bubble diameters in the 10% wt char bed are larger than those of pure sand at given gas velocities. The rise of large bubbles coupled with continuous interaction with the irregularly shaped char particles may be chaotic and difficult to predict. Hence, the significant difference between the predicted bubble diameters and those of the experiment above 0.15 m/s can be attributed to the chaotic behavior of the bed with 10% wt char particles.

3.2. Dynamic of Bubbles in the Gasification Bed. Depending on the magnitude, the dynamic behavior during generation and propagation of bubbles through a fluidized bed reactor will influence the reactor performance and the product output. Among the various impacts are the effect on the bed load, the effect on the temperature and gas distribution, and the effect on the gas residence time.

3.2.1. Effect on Bed Load and Performance. As suggested in eq R1, the product gas composition at the same air–fuel ratio is the same independent of the air flow rate. However, the distribution of gas species shown in Table 5 for different air flow rates suggests that flow behavior in the fluidized bed influences biomass conversion. Noting that biomass gasification is kinetically limited, the bed size and extent of contacts between the reacting species can account for this behavior. With an increase in the air flow rate at a constant air–fuel ratio, the biomass feed rate increases. Higher biomass feed over a fixed mass of bed material may increase the sensible heat loss, thereby leading to a lower rate of conversion and a corresponding increase in the amount of unconverted char particles in the bed.

Figure 8a illustrates the evolution of bubbles comparing the bed behavior for gasification at a 2 kg/h air flow rate against the cold beds with 5 and 10% wt char particles. Though the superficial gas velocity, u_0, differs for the different beds, their respective excess velocity, $u_0 - u_{\text{mf}}$, is approximately the same, 0.17 m/s. The excess velocity provides the driving force for bubble generation and propagation in the fluidized beds. At the same value of $u_0 - u_{\text{mf}}$, different beds are expected to behave the same. However, the figure shows that the flow behavior
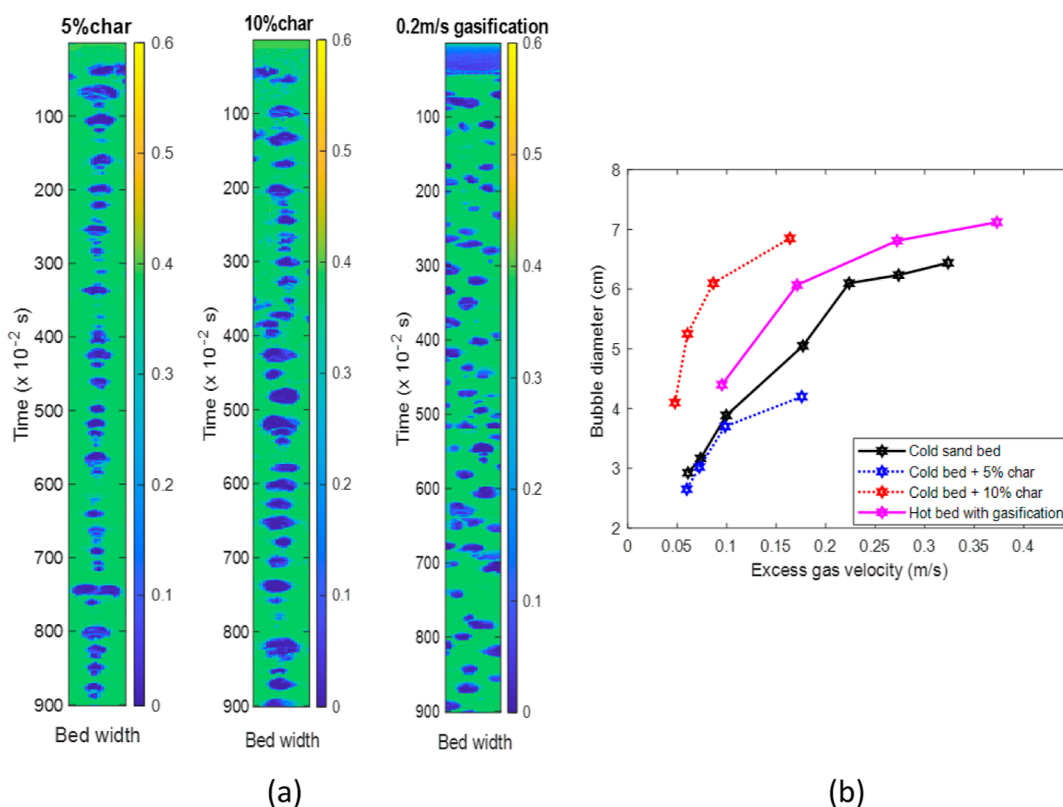
Figure 8. (a) Stacks of measurement plane over time, showing evolution of bubbles in cold beds with different char loads (5 and 10% wt) and a gas velocity of 0.25 m/s compared with behavior in the bed with wood pellets gasifying at 2 kg/h air flow (b) variation of bubble diameter with excess velocity and biomass load, comparing hot and cold beds.
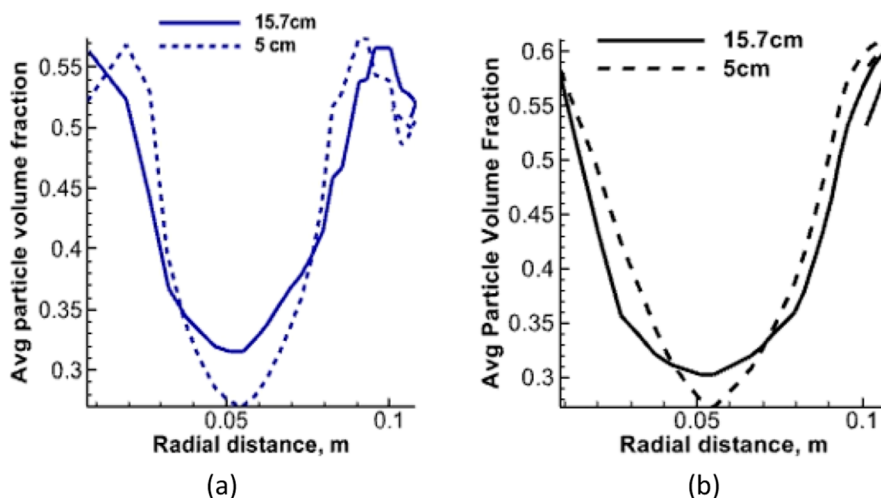
Figure 9. Radial distribution of bulk solid particles in the gasifier, comparing behavior over the bed height at different air flow rates: (a) 2 kg/h and (b) 3 kg/h.

differs across the different beds owing to variations in the amount of char particles. In the cold beds, virtually, only single bubbles rise through the central axis, whereas there are a multiple number of bubbles spread across the hot bed. The higher bubble frequency and distribution in the hot bed may be associated with an increase in the solid packing density due to a lower volume fraction of the accumulated char particles.

During the gasification process, a fraction of the fluidizing gas is consumed as it reacts with the biomass particles. The release of volatile gases in the bed will result in a higher gas fraction compared to the equivalent cold bed. Moreover, the

amount of char particles varies with time due to continuous conversion phenomena. Unlike cold bed conditions, these conversion steps, devolatilization and char conversion, can cause a significant change in the bed void fraction. The variation in gas−solid fractions therefore alters the bubble properties. Figure 8b compares the average bubble diameter over the hot bed at different air flow rates. As expected, the bubble size increases with the excess velocity and the amount of biomass load in the bed. The figure also depicts that smaller bubbles are formed at lower feed rates. Bubbles grow in size when the biomass feed rate is increased due to higher char

Figure 10. Radial distributions of temperature and gas species concentration within the gasifier bed, comparing behavior over the bed height at an air flow rate of 2 kg/h.

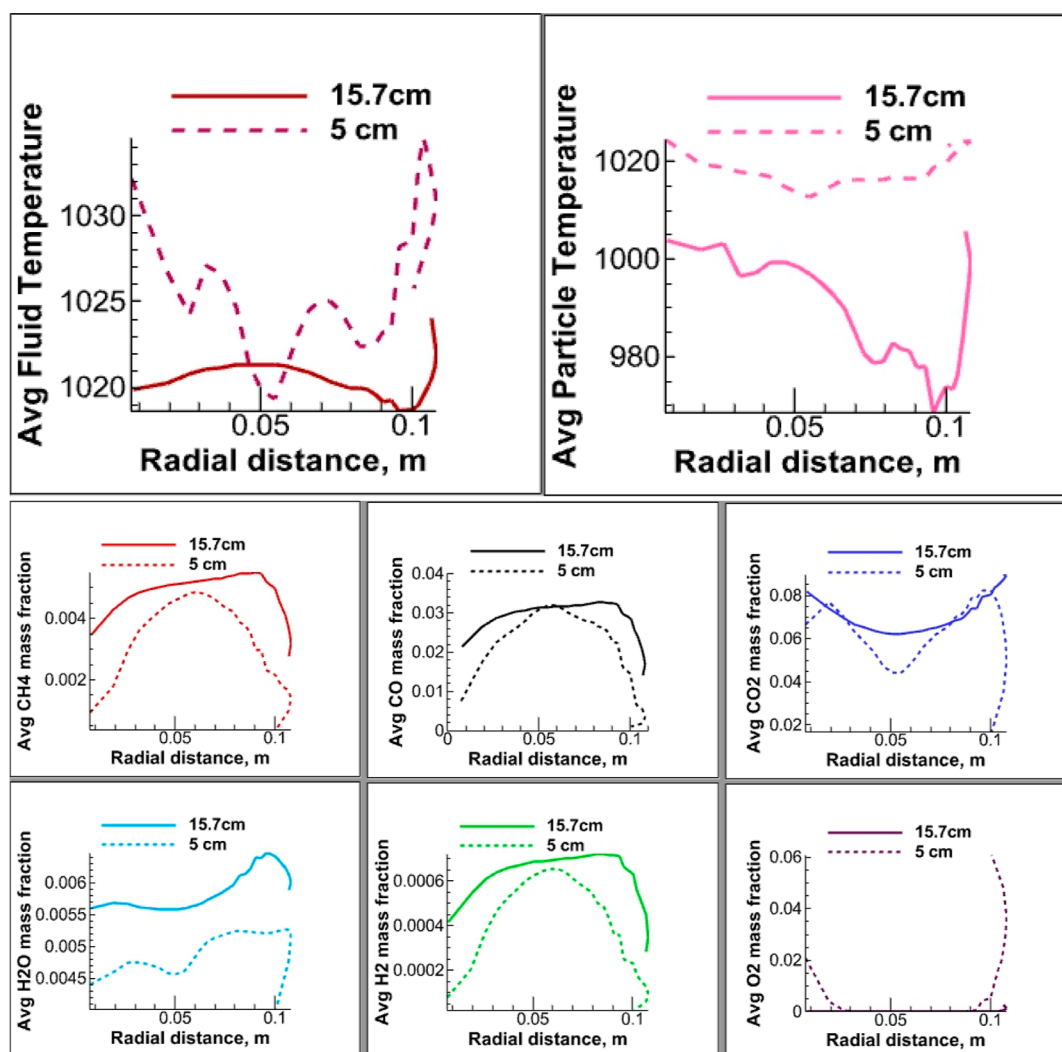accumulation, which is similar in trend to that of the cold bed containing sand and char particles as explained previously. Bubbles in the reacting hot bed are distributed throughout the cross-section contrary to the cold bed conditions; see Figure 8a. The bubble distribution in the hot bed emanates from the chaotic movement as they form and rise up in the bed. With the presence of biomass, bubbles are split and formed into irregular shapes and sizes. The gas released in the bed due to rapid devolatilization also influences the bubbles to move randomly, resulting in their distribution throughout the bed. Comparing with data in Table 5, the increase in bubble diameter and consequently the reduction in the bubble frequency as the air flow rate increases may have had an adverse effect on the conversion efficiency since the mole fractions of the gas species tend toward the values characterizing the devolatilization process. The associated rise in the bubble velocity might have also contributed to the impediment in the gasification process due to a drop in the gas residence time.

3.2.2. Effect on Temperature and Gas Species Distribution. The conversion efficiency of biomass in fluidized beds solely depends on the distribution of mass and heat across the bed. Rising bubbles create a temporal void over the bed,

whereas the region with higher solid concentration poses a greater resistance to the gas flow; therefore, a higher fraction of gas will tend to follow the bubble path. The larger the bubble size, the greater the bed voidage over the expanded volume. The distributions of total solid particles (bed material and biomass) across the bed at two different positions are shown in Figure 9. At both air flow rates, the solid fraction decreases from the walls toward the central axis due to the rise and position of bubbles. As the bubbles rise up in the bed, they tend to spread wider across the bed cross-section, decreasing the solid concentration. Since the total mass of the particles is approximately the same over the bed at a steady state, the fraction of solids within the region of the central axis is higher in the upper part. When considering a single bubble, this result indicates that the volume of the bubble is approximately the same, but the aspect ratio (height to width) decreases as the bubbles rise through the bed. At the biomass feeding position, 5 cm above the base, the lateral distribution of particles is similar for the different air flow rates, basically due to the rise of a large number of small bubbles that spread across the bed. However, with increasing air flow rate, both the lateral and axial distribution of the solids are enhanced.
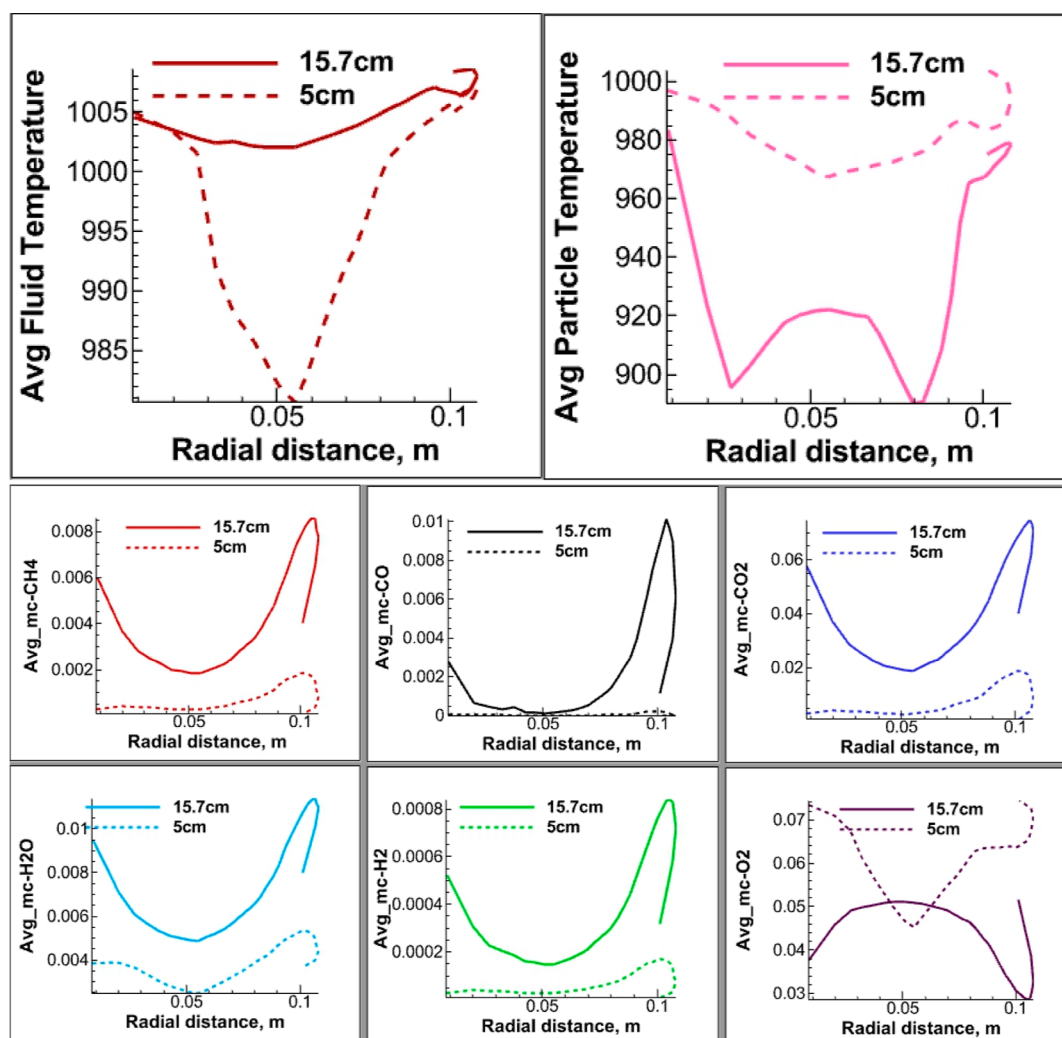
Figure 11. Radial distributions of temperature and gas species concentration within the gasifier bed, comparing behavior over the bed height at an air flow rate of 3 kg/h.

Since the solid particle concentration is higher near the walls than around the central axis, the distribution of gas–solid contacts may also be nonuniform across the bed. Consequently, the distributions of temperature and gas species will be affected. Figures 10 and 11 present the temperature and gas species distributions in the bed at 2 and 3 kg/h air flow rates. In the plane of biomass feeding position, the particle temperature is close to uniform. The drop in both gas and particle temperatures, especially within the central axis, suggests that there are some endothermic activities such as biomass devolatilization taking place in the bed. Since the bed temperature near the wall is closer to the target value of 1023 K, this also implies that a larger fraction of biomass particles is located along the central axis, particularly near the bottom of the bed, thus giving rise to the temperature distribution similar to that of the solid fraction. Toward the bed surface, the endothermic conversion of char particles with the gasifying agents including H_2O and CO_2 dominates the particle oxidation by O_2 and H_2 as represented in SR1−SR2 (described in the Supporting Information), causing a further decrease in the particle temperature. Moreover, several competitive gas-phase reactions (SR5−SR9) both exothermic and endothermic take place along the bed height, resulting in an equilibrium temperature slightly lower than the target temperature across

the bed. In the figure, it can also be seen that the bed temperature decreases with increasing air flow rate, which can be associated with an increase in the endothermic activities due to higher char accumulation.

However, the profile of gas species distribution across the different air flow rates differs from that of gas temperature. While the gas fraction increases toward the central axis at lower air flow rates, the species mass fraction decreases toward the center as the superficial gas velocity increases. Considering the concentration of oxygen at different air flow rates, the variation in gas fraction distribution can be explained. Near the walls, oxygen is present, indicating also that the concentrations of char particles and combustible gas species are significantly low in the region. At a 2 kg/h air flow rate, O_2 is completely consumed along the bubble path; hence, the convex nature of the distribution is solely due to participation of gas species in the gasification process (SR8 and SR9). The presence of oxygen along the central axis at 3 kg/h shows that oxidation activities are low at the higher gas flow rate, although there is some improvement toward the upper part of the bed. Compared with the bed at a 2 kg/h air flow rate where smaller bubbles are formed, the larger bubbles with higher rise velocity in the bed of 3 kg/h airflow may have resulted in lower contact time between the char particles and active gas species.
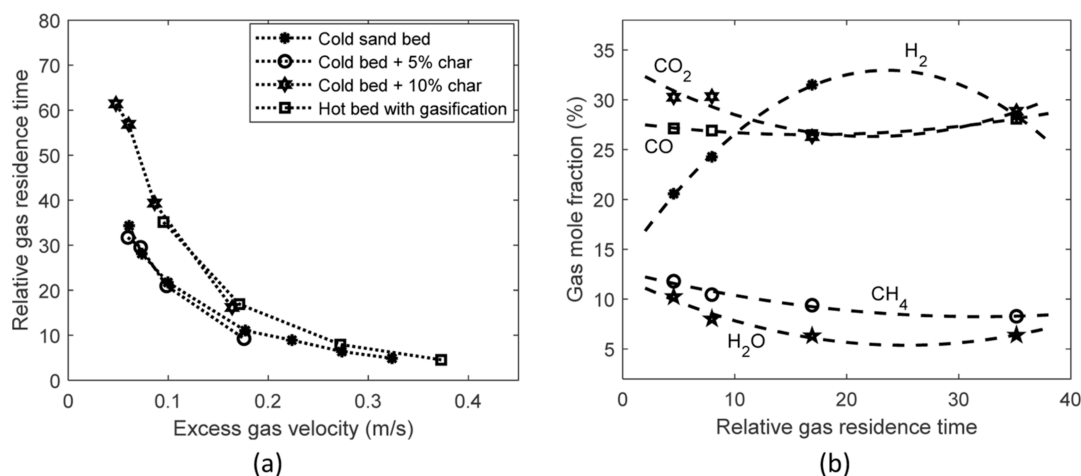
Figure 12. (a) Variation of relative gas residence time with excess gas velocity, showing the (b) effect on product gas composition in the bubbling bed gasifier.

As noted, the gasification process is kinetically limited; hence, with an increase in bubble size and rise velocity, the gas residence time for effective reactions will decrease. The drop in particle temperature along the bubble path also greatly impacts the rate of reactions between the char and oxygen within the bed. Since most of the possible gas-phase reactions are exothermic and can be activated with the indicated gas temperature, only sufficient time is therefore required for the reactions to complete, especially those involving oxygen. Hence, the homogeneous gas-phase reactions proceed in the freeboard of the reactor as there is no O_2 recorded among other species at the reactor outlet as listed in Table 5.

3.2.3. *Effect on Gas Residence Time and Product Distribution.* It has been widely reported that gas−solid mixing in a bubbling bed is enhanced with increasing gas velocity due to an increase in bubble diameter that leads to higher solid circulation as bubbles erupt from the bed surface. This may be true for beds where there is no chemical reaction between the bed component and to some extent true in the case of solid distribution where reactions occur as can be seen in Figure 9. However, the increase in bubble velocity with an increase in bubble diameter may give rise to higher gas escape, reducing the residence time of the various gas species which are supposed to participate in the gasification. Since the effective distribution of heat and mass as well as sufficient gas−solid contact time is essential for the efficient conversion of biomass in a fluidized bed, a compromise must be made in the size of bubbles generated in the bed.

Assuming constant flow velocities, the gas and bubble rise residence times, τ_g and τ_b, can be, respectively, expressed as

$$\tau_g = \frac{h_f}{u_0} \tag{16}$$

$$\tau_b = \frac{\delta_b h_f}{u_{br}} \tag{17}$$

where h_f is the bed height at the fluidized state, u_{br} is the bubble rise velocity, and δ_b is the volume fraction of the bubble over the bed defined as

$$\delta_b = \frac{G}{u_{br}} \tag{18}$$

The bubble volumetric flux, $G = u_0 - u_{mf}$, according to the two-phase theory can be applied.[35] Taking $u_{br} \sim \sqrt{gD_b}$, where $g = 9.81$ m/s^2 is the gravity constant, eqs 17 and 18 can be combined to give

$$\tau_b = \left(\frac{u_0 - u_{mf}}{gD_b} \right) h_f \tag{19}$$

Dividing eq 16 by eq 19, the relative gas residence time, $\tau_r = \tau_g/\tau_b$, becomes

$$\tau_r = \frac{gD_b}{u_0(u_0 - u_{mf})} \tag{20}$$

Equation 20 suggests that τ_r increases with increasing bubble diameter, and it is possible to achieve a higher gas residence time with a higher gas flow rate. The relative gas residence time in a bubbling bed is a characteristic value, decreasing with excess gas velocity due to increasing bubble diameter. As shown in Figure 12a, τ_r follows a certain path which depends mainly on the solid packing density. In cold beds with a relatively small fraction of biomass, the bed behavior is the same as that of the pure sand particles. When biomass is relatively high such that the bed voidage is larger than that of pure sand particles, the value of τ_r is the same as that of a hot bed at the same excess velocity. However, at higher velocities where bubbles are fully developed or slugs tend to flow in the bed, the residence time decreases toward values independent of the flow condition.

Against the gas residence time, the composition of gas species in the product gas is shown in Figure 12b. The result indicates that the length of time gas spends in the bed plays a significant role in the series of conversions expected in the reactor. The optimum relative residence time is about 24, and it is characterized by a maximum yield of hydrogen and minimum yields of carbon dioxide and water vapor. This indicates that gasification processes aimed at converting CO_2 and H_2O to CO and H_2 are at the best performance when $\tau_r \approx 24$. Below the optimum residence time, the concentration of H_2 decreases while that of CO_2 becomes higher than that of CO due to poor utilization of oxygen in the bed and active oxidation of the combustible gases in the freeboard. With $\tau_r > 24$, poor distribution of particles in the bed also results in the escape of O_2 into the freeboard through the wall region of the

bed, thereby oxidizing the combustible gases and reducing their concentrations in the product gas.

Comparing the results in Figure 12 and data in Table 5, the amount of unconverted biomass particles lies between 5 and 10% wt at the optimum residence time, which is typical for an industrial scale. Nevertheless, it is difficult to establish the biomass load before an operation because of its dependency on the gas velocity and residence time. Since $\tau_r \approx 24$ with $u_0 - u_{mf} \approx 0.13$ m/s (estimated from Figure 12a) as the corresponding excess gas velocity at the best gasification performance, eq 21 can be derived from eq 20.

$$\frac{gD_b}{u_0} = 3.0; \ [\text{m/s}] \tag{21}$$

Equation 21 therefore defines the condition under which a BFB biomass gasifier can be operated at the best efficiency. It can be used to size the reactor or set the operating gas velocity, u_0, to achieve the optimum gasification. The average bubble diameter, D_b, is related to u_0 and minimum fluidization velocity, u_{mf}, of the bed under the operating condition and can be predicted using the available correlations in the literature.[8]

4. CONCLUSIONS

The effect of bubble dynamic properties on the fluidized bed in a biomass gasifier was investigated using the CPFD model simulated in Barracuda VR software. The model was first validated with a set of experimental data acquired from an ECT setup operated in cold conditions with different mixtures of sand and char particles. Furthermore, the model results were compared with gas composition obtained from a biomass gasifier at the same operating conditions.

Compared with the cold bed at the same gas velocity and char load, the observed bubble size was smaller in the hot reacting bed and the number of bubbles spread across the bed was higher. At the same air−fuel ratio, the amount of unconverted char particles increased with increasing air flow rate through the reactor. Following the result analysis, the associated increase in bubble diameter enhances the distribution of solid particles but lowers the gas residence time. With a decrease in the gas residence time, the bed temperature decreases, and the rates of biomass and gas species conversions drop. The concentration of oxygen is high, and its distribution is all over the bed when operating at a high air flow rate in spite of a low air−fuel ratio of 0.813. The gas-phase reactions therefore proceed in the freeboard where all the available oxygen is consumed by the combustible gas species, reducing their concentration in the product gas.

To achieve an efficient biomass gasification in the BFB where the hydrogen yield is maximum and the yields of carbon dioxide and water vapor are minimum, the optimum gas residence time relative to bubble time of flight is about 24. The optimum gas residence time is related to bubble diameter and superficial inlet gas velocity as established in this study. The reported condition for effective gasification of biomass in bubbling beds can be used to determine the operating gas velocity or the reactor size.

Although the results presented here are based on a relatively shallow bed of 10 cm diameter, it is expected that the method established for determining the optimum operating point can be applied to a larger bed. The effect of particle segregation and slug flow are not considered in the analysis; hence, further studies are required to evaluate the generality of the proposed

model for calculating the optimum operating condition for efficient conversion of biomass in fluidized beds.

ASSOCIATED CONTENT

Ⓢ Supporting Information

The Supporting Information is available free of charge at https://pubs.acs.org/doi/10.1021/acs.iecr.3c00626.

Chemical reactions and chemical kinetics of biomass gasification, reactions and rate kinetics used in the CPFD model, and constitutive models for the governing equations (PDF)

AUTHOR INFORMATION

Corresponding Author

Rajan Jaiswal − *Faculty of Technology, Natural Sciences and Maritime Sciences, University of South-Eastern Norway, 3918 Porsgrunn, Norway;* ⓘ orcid.org/0000-0002-2985-1381; Email: rajan.jaiswal@usn.no

Authors

C.E. Agu − *Faculty of Technology, Natural Sciences and Maritime Sciences, University of South-Eastern Norway, 3918 Porsgrunn, Norway*

Henrik Kofoed Nielsen − *University of Agder, 4879 Grimstad, Norway*

Marianne Sørflaten Eikeland − *Faculty of Technology, Natural Sciences and Maritime Sciences, University of South-Eastern Norway, 3918 Porsgrunn, Norway*

Britt Margrethe Emilie Moldestad − *Faculty of Technology, Natural Sciences and Maritime Sciences, University of South-Eastern Norway, 3918 Porsgrunn, Norway*

Rajan Kumar Thapa − *Faculty of Technology, Natural Sciences and Maritime Sciences, University of South-Eastern Norway, 3918 Porsgrunn, Norway*

Complete contact information is available at: https://pubs.acs.org/10.1021/acs.iecr.3c00626

Notes

The authors declare no competing financial interest.

REFERENCES

(1) Yang, T. Y.; Leu, L. Study of Transition Velocities from Bubbling to Turbulent Fluidization by Statistic and Wavelet Multi-Resolution Analysis on Absolute Pressure Fluctuations. *Chem. Eng. Sci.* **2008**, *63*, 1950−1970.

(2) Gómez-Barea, A.; Leckner, B. Modeling of Biomass Gasification in Fluidized Bed. *Prog Energy Combust Sci* **2010**, *36*, 444−509.

(3) Bandara, J. C.; Jaiswal, R.; Nielsen, H. K.; Moldestad, B. M. E.; Eikeland, M. S. Air Gasification of Wood Chips, Wood Pellets and Grass Pellets in a Bubbling Fluidized Bed Reactor. *Energy* **2021**, *233*, 121149.

(4) Furuvik, N. C. I. S.; Jaiswal, R.; Thapa, R. K.; Moldestad, B. M. E. CPFD Model for Prediction of Flow Behavior in an Agglomerated Fluidized Bed Gasifier. *Int. J. Energy Prod. Manag.* **2019**, *4*, 105−114.

(5) Timmer, K. J.; Brown, R. C. Transformation of Char Carbon during Bubbling Fluidized Bed Gasification of Biomass. *Fuel* **2019**, *242*, 837−845.

(6) Wu, X.; Peng, J.; Zhang, Y.; Wang, Z. Elutriation Characteristics of Multi-Component Mixtures in a Fluidized Bed Pyrolysis Process. *Particuology* **2021**, *58*, 131−138.

(7) Agu, C. E.; Tokheim, L. A.; Pfeifer, C.; Moldestad, B. M. E. Behaviour of Biomass Particles in a Bubbling Fluidized Bed: A Comparison between Wood Pellets and Wood Chips. *Chem. Eng. J.* **2019**, *363*, 84−98.

(8) Agu, C. E.; Tokheim, L. A.; Eikeland, M.; Moldestad, B. M. E. Improved Models for Predicting Bubble Velocity, Bubble Frequency and Bed Expansion in a Bubbling Fluidized Bed. *Chem. Eng. Res. Des.* **2019**, *141*, 361−371.

(9) Agu, E.; Ugwu, A.; Pfeifer, C.; Eikeland, M.; Tokheim, L. A.; Moldestad, B. M. E.; Moldestad, M. E. Investigation of Bubbling Behavior in Deep Fluidized Beds at Different Gas Velocities Using Electrical Capacitance Tomography. *Ind. Eng. Chem.* **2019**, *58*, 2084−2098.

(10) Chandrasekera, T. C.; Li, Y.; Moody, D.; Schnellmann, M. A.; Dennis, J. S.; Holland, D. J. Measurement of Bubble Sizes in Fluidised Beds Using Electrical Capacitance Tomography. *Chem. Eng. Sci.* **2015**, *126*, 679−687.

(11) Dai, L.; Yuan, Z.; Guan, L.; Wu, K.; Gu, C. Bubble Behaviour Investigation in a Wet Fluidized Bed Using Digital Image Analysis. *Can. J. Chem. Eng.* **2022**, *100*, 1965−1976.

(12) Singh, B. K.; Roy, S.; Buwa, V. v. Bubbling/Slugging Flow Behavior in a Cylindrical Fluidized Bed: ECT Measurements and Two-Fluid Simulations. *Chem. Eng. J.* **2020**, *383*, 123120.

(13) Zhang, Y.; Zhang, J.; Zhao, Y.; Zhang, X.; Yang, X.; Zhou, E.; Duan, C.; Wang, G.; Dong, L. Investigations on Dynamics of Bubble in a 2D Vibrated Fluidized Bed Using Pressure Drop Signal and High-Speed Image Analysis. *Chem. Eng. J.* **2020**, *395*, 125129.

(14) Cui, H.; Grace, J. R. Fluidization of Biomass Particles: A Review of Experimental Multiphase Flow Aspects. *Chem. Eng. Sci.* **2007**, *62*, 45−55.

(15) Yang, S.; Zhou, T.; Wei, Y.; Hu, J.; Wang, H. Dynamical and Thermal Property of Rising Bubbles in the Bubbling Fluidized Biomass Gasifier with Wide Particle Size Distribution. *Appl Energy* **2020**, *259*, 114178.

(16) Fotovat, F.; Chaouki, J.; Bergthorson, J. The Effect of Biomass Particles on the Gas Distribution and Dilute Phase Characteristics of Sand−Biomass Mixtures Fluidized in the Bubbling Regime. *Chem. Eng. Sci.* **2013**, *102*, 129−138.

(17) Kiared, K.; Larachi, F.; Cassanello, M.; Chaouki, J. Flow Structure of the Solids in a Three-Dimensional Liquid Fluidized Bed. *Ind. Eng. Chem. Res.* **1997**, *36*, 4695−4704.

(18) Wang, J.; Van Der Hoef, M. A.; Kuipers, J. A. M. Comparison of Two-Fluid and Discrete Particle Modeling of Dense Gas-Particle Flows in Gas-Fluidized Beds. *Chem. Ing. Tech.* **2013**, *85*, 290−298.

(19) Acosta-Iborra, A.; Sobrino, C.; Hernández-Jiménez, F.; de Vega, M. Experimental and Computational Study on the Bubble Behavior in a 3-D Fluidized Bed. *Chem. Eng. Sci.* **2011**, *66*, 3499−3512.

(20) Deen, N. G.; van Sint Annaland, M.; van der Hoef, M. A.; Kuipers, J. A. M. Review of Discrete Particle Modeling of Fluidized Beds. *Chem. Eng. Sci.* **2007**, *62*, 28−44.

(21) Snider, D. M.; Clark, S. M.; O'Rourke, P. J. Eulerian-Lagrangian Method for Three-Dimensional Thermal Reacting Flow with Application to Coal Gasifiers. *Chem. Eng. Sci.* **2011**, *66*, 1285−1295.

(22) Kraft, S.; Kirnbauer, F.; Hofbauer, H. CPFD Simulations of an Industrial-Sized Dual Fluidized Bed Steam Gasification System of Biomass with 8 MW Fuel Input. *Appl Energy* **2017**, *190*, 408−420.

(23) Liu, X.; Wang, S.; Du, Y.; Zheng, M.; Yang, S.; Wang, H. CFD Study of the Thermochemical Characteristics of Mesoscale Bubbles in a BFB Gasifier. *Adv. Powder Technol.* **2021**, *32*(). DOI: 10.1016/j.apt.2021.05.039.

(24) Zheng, J.; Peng, L. A Deep Learning Compensated Back Projection for Image Reconstruction of Electrical Capacitance Tomography. *IEEE Sens J* **2020**, *20*, 4879−4890.

(25) Chan, W. C. R.; Kelbon, M.; Krieger, B. B. Modelling and Experimental Verification of Physical and Chemical Processes during Pyrolysis of a Large Biomass Particle. *Fuel* **1985**, *64*, 1505−1513.

(26) Andrews, M. J.; O'Rourke, P. J. The Multiphase Particle-in-Cell (MP-PIC) Method for Dense Particulate Flows. *Int. J. Multiph. Flow* **1996**, *22*, 379−402.

(27) O'Rourke, P. J.; Snider, D. M. Inclusion of Collisional Return-to-Isotropy in the MP-PIC Method. *Chem. Eng. Sci.* **2012**, *80*, 39−54.

(28) Snider, D. M. An Incompressible Three-Dimensional Multiphase Particle-in-Cell Model for Dense Particle Flows. *J. Comput. Phys.* **2001**, *170*, 523−549.

(29) Snider, D. M. Three Fundamental Granular Flow Experiments and CPFD Predictions. *Powder Technol.* **2007**, *176*, 36−46.

(30) Wen, C. Y.; Yu, Y. H. Mechanics of Fluidization. *Chemical Engineering Progress, Symposium Series* **1966**, *62*().

(31) GidaspowGidaspow, D. D. *Multiphase Flow and Fluidization: Continuum and Kinetics Theory Descriptions*; Academic Press Inc.: San Diego, California, USA, 1994.

(32) Jaiswal, R.; Agu, C. E.; Thapa, R. K.; Moldestad, B. M. E. Study of Fluidized Bed Regimes Using Computational Particle Fluid Dynamics. In *Proceedings of The 59th Conference on imulation and Modelling (SIMS 59)*, 26-28 September 2018, Oslo Metropolitan University, Norway; 2018; Vol. 153.

(33) Weber, J. M.; Layfield, K. J.; van Essendelft, D. T.; Mei, J. S. Fluid Bed Characterization Using Electrical Capacitance Volume Tomography (ECVT), Compared to CPFD Software's Barracuda. *Powder Technol.* **2013**, *250*, 138−146.

(34) Agu, C. E.; Pfeifer, C.; Moldestad, B. M. E. Prediction of Void Fraction and Minimum Fluidization Velocity of a Binary Mixture of Particles: Bed Material and Fuel Particles. *Powder Technol.* **2019**, *349*, 99−107.

(35) Kunii, D.; Levenspiel, O. Second, Ed., 1991.*Fluidization Engineering*.

Paper 7

Alternative Energy - Evaluation of Waste Feedstocks for Heat Generat on and Syngas Product on

Alternative Energy - Evaluation of Waste Feedstocks for Heat Generation and Syngas Production

*Rajan Jaiswal[1], Cornelius Emeka Agu[1], Britt Margrethe Emilie Moldestad[1], Henrik Kofoed Nielsen[2], Marianne Sørflaten Eikeland[1], Mladen Jecmenica[1], Rajan Kumar Thapa[1]

[1]University of South-Eastern Norway, Faculty of Technology, Natural Sciences and Maritime Sciences, Kjølnes ring 56, 3918, Porsgrunn, Norway

[2]University of Agder, Jon Lilletuns vei 9, 4879 Grimstad, Norway

*Corresponding Author

Email: rajan.jaiswal@usn.no

Abstract

The current global warming has shifted the world energy demand towards renewable energy resources. Utilization of solid waste materials enhances both the renewable energy demands and purification of the surrounding environment. This study therefore evaluates conversion of different solid waste particles in a bubbling fluidized bed for energy and syngas productions. To ensure a high energy content, the different feedstocks, wood, paper, garden, and fish wastes are densified and used in pellet form in an air gasifier over the equivalence ratio $0.15 - 0.35$. For a fair comparison, the tests are carried out at about the same starting bed temperature, 650 °C. Beside the nature of biomass, the results show that particle bulk density impact significantly on the bed mixing strength and thus on the conversion process. The higher the particle density, the better the carbon conversion efficiency. However, where the associated char particles are less reactive as in the case of fish pellets, a higher bed temperature is desired to achieve an efficient conversion. Of the four feedstocks, wood pellets have the best carbon conversion efficiency, about 70% over the tested equivalence ratios. While the paper pellets have the least carbon conversion of about 60% among the plant-based biomasses due to low particle density, the energy conversion efficiency is 85% and highest due to high gas yield strength compared to other feedstocks. Moreover, the moisture content of biomass plays little or no role in the conversion provided that the devolatilization process takes place within the bed where the necessary oxidations are effective. Hence, this study provides an insight into a method for analyzing performance of a fluidized bed reactor and can be used as a basis for further studies to ascertain the effect of temperature on gasification of different biomass types, particularly those of animal origin.

1. Introduction

The primary energy source until now is the fossil fuel that accounts for about 83% of the energy used globally[1]. However, worsening climate conditions at an alarming rate due to environmental component degradation by fossil fuel consumption has compelled society and researchers to explore alternative clean energy sources and technologies. In addition, rapid population growth, industrialization and urbanization have increased the energy demand at an unprecedented rate. At the same time, an enormous amount of waste is produced from various sectors. Failure to manage this waste effectively could severely affect the climate[2]. The major sources of waste include agricultural and forest residue, as well as industrial and community wastes. The collective generation of urban and industrial waste is estimated to be approximately $7 - 10$ billion tons per year, with residential waste contributing 2.01 billion tons of solid residue[3]. The amount of waste generation regionally depends on the region's income, climate factor and socio-cultural pattern. A 1% increase in a country's national income corresponds to a 0.69% rise in the quantity of waste generated [4]. The most common method of waste

disposal has been landfilling. However, landfilling of wastes possess serious environmental hazards like greenhouse gas emissions, leachate formation, unpleasant odors, fires, contamination of water sources, and urging alternative waste management methods [5].

In this regard, the utilization of wastes for energy extraction can be a wise alternative which address two major issues: the waste management problem and supply of clean energy demand. In addition, waste-to-energy processes can significantly reduce the issues of landfills, promote a circular economy, satisfy lower carbon footprint goals, and diversify energy dependence sources[6–8]. Waste can be converted to energy via waste-to-energy conversion technology following biochemical[9] or thermochemical conversion routes[10]. Thermochemical conversion technologies such as gasification, pyrolysis, and combustion are widely used for waste-to-energy extraction as these technologies provide flexibility in terms of feedstock selection[11,12]. Biomass pyrolysis is an endothermic process that decomposes biopolymers into char, a mixture of condensable and non-condensable gases in an inert environment. Conversely, combustion is thermal degradation of biomass in an oxidant-rich environment that produces heat energy and carbon dioxide as the byproduct. Another thermal conversion route is gasification which converts carbonaceous biomass into higher calorific value syngas and char in an oxidant deficit environment. Among the thermochemical technologies, gasification provides higher quality gaseous output as the product called syngas or producer gas, which can be utilized for power generation or production of valuable chemicals and fuels[13,14]. In addition, the gasification of biomass can be endothermic or exothermic depending on the types of gasification reactor, oxidizing medium and mass flow rate of the oxidant used. For instance, with air as the oxidant, the char partial oxidation reaction involved during the conversion process can sustain the required energy demand[15,16]. The potential for producing high-quality gaseous output and achieving auto-thermal operation makes waste-to-energy extraction through gasification more energy-efficient when compared to other thermal conversion methods such as pyrolysis and combustion. The product gas from the gasification process depends on the types of feedstocks, reactor design and process parameters[17]. The process parameter varies significantly depending on the type of gasifier[14]. The most used gasification reactors are fixed bed, fluidized bed, and entrained flow reactors. Depending on the direction of gas inlet, fixed bed reactors are divided into updraft-fixed bed reactors and downdraft-fixed bed reactors[14]. In an updraft gasifier, the fuel is added from the top while the gas is injected form the bottom of the reactor. The direction of gas and fuel supply in the downdraft fixed bed gasifier is in the same direction. Therefore, the conversion efficiency in the fixed bed gasifier is significantly influenced by the contact time between the feed and gasifying medium. An entrained flow reactor is another type of gasification reactor operated at high temperature and pressure[18]. In the entrained flow reactors, the oxidant and fuel particles flow concurrently, and higher reactor temperature enables product gas with lower tar. However, the economic sustainability of such reactors is constrained by the reduce lifetime of the components and the plant, as such reactors are operated under extreme operating conditions. In contrast, the operating temperature and pressure of the fluidized bed reactors can be maintained uniformly over the reaction area, resulting in a high reaction rate. In a fluidized bed gasifier, the hot particle bed material (sand, olivine, etc.) is fluidized by passing the fluidizing gas through the static bed. The feedstock is injected in or on the top of the bed which is then mixed with the fluidized hot particle, resulting in homogeneous heat and mass transfer. A fluidized bed reactor can be a circulating or a bubbling type[14,19]. In circulating fluidized beds, high air flow is required to circulate the hot bed particles heated in the combustion chamber to the bubbling zone. Comparatively, lower fluidizing gas velocity, but sufficiently enough to fluidize the bed in a bubbling regime is required in a bubbling fluidized bed. The bubbles formed in the bed are primarily responsible for gas-solid contact and mixing to provide homogenous heat transfer from the hot bed material to fuel particles[20], enabling gasification to occur at a relatively lower temperature than in fixed-bed gasifiers[21]. The

significant advantages of a bubbling fluidized bed in contrast to other gasification reactors, includes simple design, low investment and operational cost, superior quality of the product gas, elevated thermal conversion efficiency and good operational control. Furthermore, the bubbling fluidized bed has become increasingly popular in waste-to-energy plants because of its versatility in selecting feedstocks and its ease of scalability [22]. However, a consistent supply of waste feedstock is essential to ensure continuous operation of a large-scale commercial plants. This can only be achieved by utilizing waste materials from diverse sources and blending them together. The wastes generated from various sectors are heterogeneous with varying shape, size, density, and moisture content. Such wastes or their mixtures cannot be fed to the reactor directly as they can cause operational challenges such as blockage of the feeding system, discontinuous feed, and lowering conversion rate. In addition, the lower density wastes have lower calorific value which may not be suitable for energy-efficient output. Densification of such wastes in the pellet form (palletization) is an alternative method to enhance the feedstock's calorific value and avoid the conversion challenges[23]. The details of several waste palletization and co-palletization processes and their influence on the feedstock quality and waste to energy conversion processes can be found elsewhere[24,25] . This work evaluates syngas production and heat generation potential from gasification of wastes feedstock in a bubbling fluidized bed reactor. The waste feedstocks selected include municipal wastes (paper wastes), industrial wastes (fish feed processing industry wastes) and forest wastes (wood pellets and garden wastes). Several research have been conducted on the gasification of wastes from various sectors. However, the abundantly researched feedstock has been wood pellets due to higher carbon content and accessibility of the feedstock. Many research works have been published on the influence of operating parameters on the syngas quality, carbon conversion efficiency and cold gas efficiency. However, limited experimental work are available on the gasification feedstock selected in this work. Shruti et al.[26] investigated air gasification of garden waste in a pilot scale downdraft gasifier from experimental and numerical analysis. The author reported maximum gasification efficiency at an equivalence ratio of 0.32 and increase in calorific value of producer gas to 5.3 MJ/Nm3 when sugarcane bagasse was added to the garden waste[26]. Similarly, Hassen et al. studied gasification of garden waste at equivalence ratio 0.32 and reported lower heating value (3.59 MJ/Nm3) of the producer gas. The author also reported discontinuous flame due to clinker formation in the downdraft gasifier with high ash content (~10%) in the feed[27]. A. Fazil et al. performed gasification of high ash content (~ 17%) paper-rich commercial refuse-derived fuel (RDF) in downdraft gasifier and reported a lower heating value of 4.34 MJ/Nm3 and corresponding cold gas efficiency of 59.24% at an equivalence ratio of 0.34. The authors mixed sawdust with 75% RDF to reduce the ash fraction of the feed and then reported an enhancement in the product gas heating value with lower tar content during co-gasification of the blended feedstock[28].

Among the reported limited experimental works on the garden waste and paper waste gasification, the focus has been mainly on using downdraft and updraft gasifiers. Moreover, no literature is available on gasification of fish wastes, paper wastes and garden residue in a bubbling fluidized bed reactor. This work therefore explores the syngas production and energy generation potential from fish wastes, agricultural garden wastes, and paper wastes in a bubbling fluidized bed reactor. The waste feedstocks in pellet form are fed to a bubbling fluidized bed gasifier in air deficit environment. The syngas and energy production potential of the waste feedstocks are evaluated and compared with the commercial wood pellets gasification under the same gasifying environment. The study will hence provide insights into the wastes-to-energy production potential from various sources, thus attracting researchers and stakeholders interested in waste management and energy extraction via renewable energy sources.

2. Materials and methods

This section describes the materials, experimental set up and process parameters employed in this study to evaluate heat generation and syngas production potential from waste feedstocks.

2.1 Feedstock characterization

The selected feedstocks are from municipal, industrial, and forest wastes. The municipal wastes include paper and carboard generated from households while the industrial wastes are residues from fish food processing industry. The garden waste comprises different organic residues such as small branches, leaves, grass clippings, wood debris, etc. The fish wastes were obtained in a pellet form from the SINTEF Tel-Tek Norway lab facilities. Similarly, commercial wood pellets were used as the standard fuel to compare the syngas production potential from other waste feedstocks. To increase the heating value of the rest of feedstocks (garden wastes and paper wastes) during the conversion process, thereby avoiding any challenges, their densification was carried out in the pellet form using an industrial pelleting machine designated as KHAL pelleting press from Scanship, Norway. Prior to palletization, each of the feedstocks was cut into smaller sizes and dried up to the required moisture content (10 - 25%). No additives were introduced in the process, although it is possible to make pellets of different diameters with a certain additive that improves binding of the raw material constituents. During the process, the compression ratio, i.e., the ratio of pellets diameter to length, was adjusted to obtain pellets of uniform shape and high strength. Finally, the mean properties of the different feedstocks were obtained as given in Table 1.

The particle density of each feedstock was measured from the ratio of mass of a particle to its volume over six different samples. Similarly, the bulk density was calculated from the mass of the pellets in a one-liter volume of a container. The density and bulk density of the feedstock are important in quantifying the fluidization properties of particle mixtures as later discussed. Inert sand particles with size range, 500 – 800 μm was used as the bed material. Although the sand particles do not participate in the reaction, they act as the thermal flywheel, providing required thermal energy to sustain the conversion process. The size of the particles is a critical parameter in a fluidized bed gasifier as it significantly influences the fluid dynamic behavior and mixing phenomena. Selecting smaller size particles can transform the bed from the bubbling to turbulent at the operating gas flow rate. In addition, there can be fine particles in the product gas due to high fluidizing gas velocity. Conversely, too large size particles may be difficult to fluidize and may result in a bed transition from bubbling to slugging behavior. Therefore, within the air flow rate range, 3 - 6 kg/h applied in this study, a bed material with appropriate particle size was selected so that the bed remains in a bubbling fluidized state during the conversion of the feedstocks, targeted at 600 - 850 °C.

Table 1. Properties of bed material and waste feedstocks used in this study.

Particles	Size range [mm]	Particle diameter [mm]	Volume equivalent diameter [mm]	Particle density [kg/m3]	Solid fraction [-]	Char density [kg/m3]	U_{mf} [m/s] @ 750 ºC
Sand Particles	0.4 – 0.85	0.685	0.685	2650	0.53	-	0.18
Paper pellets	20 – 28	12	17.25	986	0.35	156	2.22
Fish pellets	10	8	9.87	1289	0.45	260	2.02
Garden waste pellets	20 – 33	8	12.73	1226	0.34	423	3.12
Wood pellets	15 – 21	6	9.87	1177	0.52	323	2.29

Using a standard sampling procedure, approximately 3 - 5 kg of each feedstock was prepared and sent to a certified laboratory, Eurofins AS Norway for analysis. The analysis of the feedstock was carried out using standardized methods and different ISO standards. The analysis also revealed the ultimate and proximate data as well as the heating values of the samples as listed in Table2.

Table 2. Results from ultimate and proximate analyses of different solid wastes used as feedstocks.

Components	Paper pellets	Fish pellets	Garden waste pellets	Wood pellets
Ultimate analysis (dry basis., wt. %)				
H	5.3	8.2	5.3	6.1
C	42.8	57.4	47.7	51.3
O	37.8	21.2	36.8	42
N	0.25	7.34	0.63	0.11
S	0.113	0.463	0.056	0.01
Proximate analysis (dry basis., wt. %)				
Moisture	26	2.6	13.7	7.9
Ash	13.65	4.91	9.47	0.55
Volatiles	54.8	83.4	65.1	77.3
Fixed carbon	5.55	9.09	11.73	14.25
Heating value, (MJ/kg)	10.503	26.479	18.567	20.382
Standards				
Ash-EN 14775, Heating value-EN 14918, Moisture-EN 14774, Ultimate-EN 15408, Volatile-EN 15402				

2.2 Experimental set up and operational procedure

The experimental set up consists of a 20-kWh bubbling fluidized bed reactor developed in collaboration with University of South-Eastern Norway and BOKU Austria. The reactor is cylindrical column made of stainless-steel of 1.5 m in height, 10 cm in diameter and thickness of 4mm. The reactor is operated at an atmospheric pressure and equipped with a few thermocouples and pressure sensors mounted along the reactor heights as shown in Figure 1. Pressure and temperature are measured along the reactor column, air pre-heater, air inlet, product gas outlet, silo, screw conveyer and the heating coil. Three heating coils surround the reactor wall externally which were used to supply heat to the reactor during the start-up. To prevent heat loss, the outer side of the reactor is insulated with fiberglass of thickness 200 mm. For a supply of fluidizing gas, the reactor consists of two inlets of diameter, 2 cm at the lower section as shown in Figure 1(b). The fluidizing gas is heated 300 - 400℃ before passing into the reactor with an air-preheater. The cut off temperature of the air-preheater and reactor were set to 600 ℃ and 1000 ℃ , respectively. The inlet mass flow rate of fluidizing air was controlled by a BROOK air flowmeter (3809 series). For the feedstock storage, the reactor is integrated with a silo where the pellets were conveyed via two screw conveyers: one mounted to the silo (a cold screw conveyer) and another (hot screw conveyer) attached to the reactor; see Figure 1 (a). As also shown, the two screws are connected with a non-conductive flange to avoid heat flow to the silo. In addition, nitrogen is continuously flushed through the silo at 0.6 liter/minute to prevent ignition of the fuel particles in the silo.

(a)   (b)
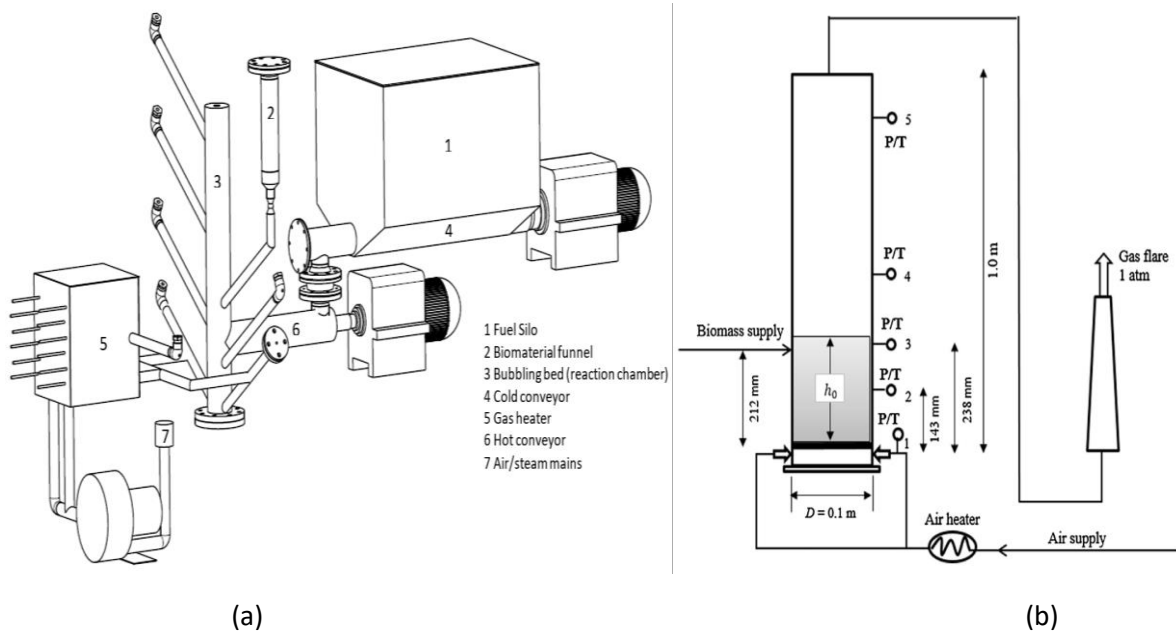
Figure 1. (a) Detailed description of a gasification rig used in this study (b) Schematic representation of the biomass gasification reactor showing different sensor positions.

Feeding system is a crucial part of a gasification process which requires uninterrupted flow of the feedstock into the reactor for continuous syngas production. Screw feeders were used as transport means to supply the feedstock to the reactor. To avoid peculiar operational challenges thereby mitigating flow of hot bed material to the screw, wear of the screw threads and erudition of pipe wall, the hot screw was located 5 - 10 cm above the static bed height. The hot screw is designed to run continuously at a constant speed during operation while the cold screw runs at specified rate which determines the flow rate of feedstock from the silo to the reactor. Between the two screw feeders in every batch of biomass supply, there is a time gap (idle time). Earlier study has shown that an increase in idle time could lead to sudden increase in bed temperature due to excess availability of oxygen for a continuous gasification process [14]. Also, continuous supply of biomass at the same feed rate when the temperature is decreasing can lead to bed instability, which may result in the bed losing its fluidized state due to accumulation of a significant amount of unconverted fuel particles. By increasing the screw rotation, the idle time can be reduced, although this could result in a relatively higher biomass flow rate and cause biomass bridge between the two screws[14]. Alternatively, by varying the screw pitch length and screw diameter, a flow continuity with lower idle time at a desired flow rate can be achieved as shown in Eq. (1). As feedstocks used in this work vary in density, size, and diameter; see Table 1, different screws with varying pitch and diameter were used for the cold conveyor to maintain the feed continuity within the idle time of 1 - 3 second. Three screws with different configurations were constructed and used as shown in Figure 2. Type A screw was used in the hot screw conveyer and Types B and C screws were used in the cold screw conveyor. Based on Eq. (1), the feed rate, Q depends on the diameter of the screw, d_S, pitch length, P, shaft diameter d_A, density of the pellets, ρ_p and number of rotations, ω. Therefore, for the fish and wood pellets which have smaller particle diameter, the Type C screw was used. The Type B screw was used for the paper and garden waste pellets due to their larger particle size. For each of the feedstock, the feed rate was calibrated as shown in Figure 2(b) prior to the experiments to acquire desired average flow rate of about 3kg/h.

$$Q = \frac{\pi}{4}(d_S^2 - d_A^2)P\rho_p\omega \qquad\qquad\qquad\qquad (1)$$
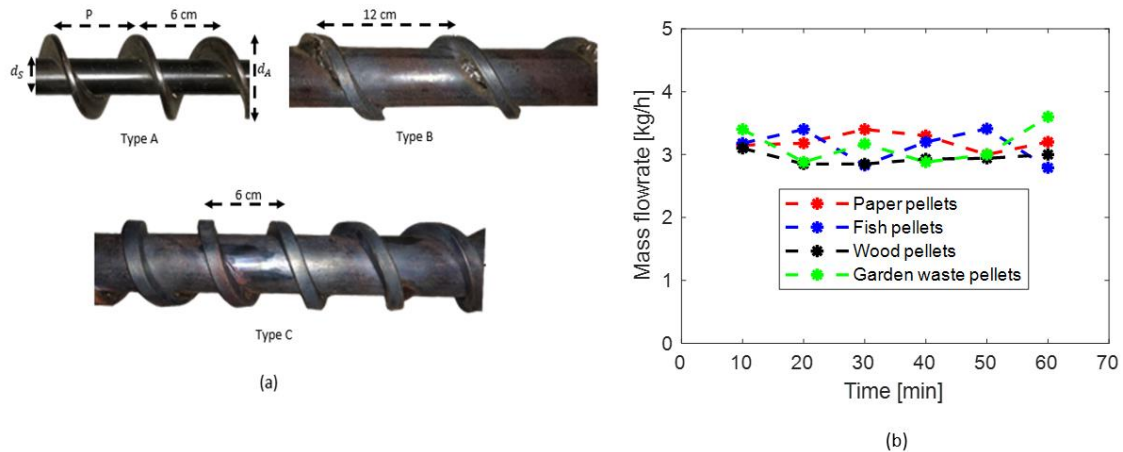
Figure 2. (a) Different designs of the pellet screw feeder used in this study (b) Screw feeder calibration for different feedstocks, showing the mean mass flow rate.

During the experiment, the reactor was initially filled with 2.2 kg bed material (sand particles) via bed material funnel, resulting in an initial bed height of about 21 cm. The density and size of the sand particles were 2650 kg/m³ and 500 - 800 μm, respectively as reported in Table 1. The particle bed was fluidized with air to enhance the bed heat-up to a temperature of about 400 ℃. At 400 ℃ , a small amount of biomass (about 3 kg/h) was fed to the reactor to initiate the combustion process in the excess air environment until the bed temperature reached 650 ℃. At this temperature, biomass flow rate was kept constant and the air supply to the bed was adjusted to start the gasification of the selected feedstock. The four different feedstocks were gasified at four air-to-fuel ratios in the range 0.95 – 2.1. When aiming for auto-thermal gasification, the choice of the air flow rate relative to the biomass feed rate is a crucial factor. Inadequate air flow rates could result in a higher tar content in the product gas and unconverted carbon in the bed, making it challenging to maintain the desired reactor temperature. Conversely, excessive air flow rates could lead to attrition and entrainment of particles as well as a high nitrogen fraction in the product gas. To address this, air flow rates ranging 3 – 6 kg/h were selected, considering the size distribution of the bed material and the biomass feed rate. With this configuration, it is worthy to emphasize that the goal was to assess the feasibility of achieving auto-thermal gasification for the different feedstocks. Due to the high ash content in the feedstocks, the starting bed temperature of 650 ℃ was chosen, particularly in the paper and garden waste pellets. A higher initial bed temperature could potentially cause the bed temperature to reach ash melting temperatures, resulting in the formation of ash clinkers in the bed[29].Moreover, the energy supplied to heat up the bed to this temperature can be considered as the major external energy input, which by evaluation of the output energy of the product gas, the feasibility of the overall process can be established.

Gasification of each feedstock at a specific air flow rate was conducted for one hour. Note that fresh bed material was employed for each experiment with different feedstock types. This approach was adopted to mitigate any potential impact on the reactor's hydrodynamic behavior due to generation of ash during the one-hour operation. The bed pressure and temperature were constantly logged in at 1.0 s interval for all indicators along the reactor axis. The pressure and temperature data are essential in identifying changes in hydrodynamic behavior of the bed resulting from accumulation of char and clinker formation. For each air-to-fuel ratio, the gas samples were extracted at 10 min intervals and cooled naturally to about 200 ºC to condense out tar component, leaving behind the free gas and water vapor. Precautions were taken to remove the gas volume collected inside the sampling pipe during the

previous sampling by flushing out the gas in a 200 ml syringe 3 to 4 times before taking a new sample. In the process, each sample was analyzed in an offline SRI gas chromatography (GC) where CO_2 was detected by a silica gel packed column and N2, O2, CH4, and CO by molecular sieve 13X packed column. Helium was used as the carrier gas, making it impossible to detect H2 due to existence of polarity between the two gases. Moreover, detection of H2O and C+ compounds were not possible with the set up.

3. Theory

A fluidized bed is in a bubbling state when the gas velocity is higher than the minimum fluidization velocity, U_{mf} of the bed but below a certain critical velocity to prevent slug or entrainment of particles. The various particle types characterized by density, shapes and size differences influence the bed behavior including segregation at a given operating flowrate. Temperature and pressure which influence the thermodynamic properties of the fluidizing gas, also play a significant part in the bed behavior. Table 1 lists the estimated minimum fluidization velocity of each of the particles involved in the test at 750 °C based on the Wen & Yu[30] correlations for the sand and biomass particles, respectively.

Due to several factors limiting the kinetics of the conversion in a bed, the unconverted amount of char can be estimated as proposed in Agu et al.[31]. Measurement of unconverted char provides a good indication of quality of the product gas and conversion efficiency. As noted above, knowledge of the bed hydrodynamic characteristics also provides information about the extent of mixing of particles, which also affects the efficiency of the conversion process. For a quick estimation of the bed average U_{mf} under a characterized binary mixture of sand and char particles, the correlation proposed in Agu et al. [32]can be applied.

Further, calculation of energy value of the product gas requires complete composition of the gas stream. Hydrogen and water vapor are among the vital species for this evaluation. Since the gas chromatography used in the analysis provides no information for these two species, an elemental and a mole balance can be used in their estimations. Assuming a molecule of biomass is represented by $C_X H_Y O_Z N_W$ where the constituent elements are carbon (C), hydrogen (H), oxygen (O) and nitrogen (N), neglecting the Sulphur content. Disregarding the entrainment of char and assuming a complete conversion of the biomass particles supplied during the measurement period, Eq. (2) expresses the stoichiometry of the reactions.

$$C_X H_Y O_Z N_W + r(O_2 + 3.76N_2) = n_1 CO + n_2 CO_2 + n_3 CH_4 + n_4 H_2 + n_5 H_2 O + n_6 N_2 + n_7 O_2 \qquad (2)$$
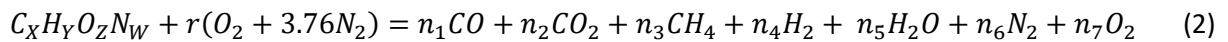
$$\begin{cases} \beta = \left(\frac{AFR}{\emptyset \varphi}\right)\left(\frac{\widehat{M}_{bio}}{\widehat{M}_{air}}\right) \\ \quad \emptyset = 1 - w_{ash} \\ \quad \varphi = 1 - w_{mois} \end{cases} \qquad (3)$$

where AFR is the mass flow rate of air to biomass supplied, w_{ash} and w_{mois} are the mass fractions of ash and moisture, respectively in the biomass and $\widehat{M}$ is the molecular mass of the indicated substance. With n denoting the total number of moles of the gaseous species in the product and y_j the mole fraction of the different species $j = \{CO, CO_2, CH_4, H_2, H_2O, N_2, O_2\}$, the elemental balance of equation (2) yields:

$$n_4 = \left(3y_{CO} + 4y_{CO_2} + y_{O_2}\right) - \frac{1}{n}\left(2X + Z + 2\beta - \frac{Y}{2}\right) \qquad (4)$$

$$n = \frac{W + 7.52\beta}{2y_{N_2}} \qquad (5)$$

$$y_{H_2} = \frac{n_4}{n} \tag{6}$$

By mole balance, the water vapor y_{H_2O} can be estimated from,

$$y_{H_2O} = 1 - (y_{CO} + y_{CO_2} + y_{CH_4} + y_{H_2} + y_{N_2} + y_{O_2}) \tag{7}$$

Considering that some amount of hydrogen and carbon are left in tar and char, the mass fraction of unconverted hydrogen, $X_{hydrogen}$ and carbon, X_{carbon} relative to a unit of biomass are obtained from Eq. (8) and (9), respectively, which are also derived from the elemental balance of the reaction stoichiometry.

$$X_{hydrogen} = \frac{\beta}{n}\left(\frac{Y}{n} - y_{H_2}\right) \tag{8}$$

$$X_{carbon} = \frac{\beta}{n}\left\{X - \left(y_{CO} + y_{CO_2} + y_{CH_4}\right)\right\} \tag{9}$$

The number of atoms, X, Y, Z and W of the biomass constituents in an ash-free condition as well as the biomass molecular weight are given by Eq. (10), where $\%w_i$ is the weight fraction of each constituent element.

$$\begin{cases} \widehat{M}_{bio} = \frac{1}{1-w_{ash}}\Sigma\left\{\frac{1}{100}\widehat{M}_i(\%w_i)\right\} \\ k = \frac{1}{1-w_{ash}}\left(\frac{\widehat{M}_{bio}}{\widehat{M}_i}\right)\left(\frac{1}{100}(\%w_i)\right) \\ k : \{X,Y,Z,W\}; \quad i = \{C,H,O,N\} \end{cases} \tag{10}$$

4. Results and Discussions

The performance of the reactor used in this test may be influenced by the mixing strength of the bed particles. For the different gas flow rates, $\dot{m}_{air}$, the amount of unconverted char particles may differ, leading to different degrees of fluidization. To ascertain the impact of the bed behavior on the conversion process, the analysis of the bed temperature, pressure, and accumulated char over the duration of the test at a given air-fuel ratio is presented in Table 3. The bed and exit temperatures were directly measured with the respective transmitters, **T2** and **T5** positioned along the bed axis. The amounts of unconverted hydrogen and carbon were calculated from Eq. (8) and (9), respectively as described above. Using the model listed in Agu et al. [31] an estimate of the accumulated unconverted char over the 60 minutes test duration were obtained.

Table 3. Parameters derived from gasification of the different feedstocks at different air flow rates.

Feedstock	$\dot{m}_{air}$ [kg/h]	$\dot{m}_{bio}$ [kg/h]	T_{bed} [°C]	T_{out} [°C]	$X_{hydrogen}$ [%], Eq. (8)	X_{carbon} [%], Eq. (9)	Unconverted char Agu et al.[31]	FI (-)
Wood pellet	3	2.95	710	636	0.04	1.50	9.23	1.16
	4	2.95	742	694	0.03	1.98	8.03	1.55
	5	2.95	752	712	0.01	2.13	7.25	1.91
	6	2.95	743	725	0.40	3.41	6.75	2.21
Fish Pellet	3	3.14	705	671	3.90	5.19	9.30	1.03
	4	3.14	621	638	2.98	5.37	9.27	1.06
	5	3.14	743	711	2.03	5.15	7.34	1.67
	6	3.14	744	736	1.90	5.54	6.75	1.98
Paper pellet	3	3.21	768	636	0.32	2.54	8.67	0.88
	4	3.21	790	624	0.25	2.10	7.63	1.14
	5	3.21	762	728	0.49	3.71	7.17	1.31
	6	3.21	763	703	0.32	3.53	6.60	1.55
Garden Waste pellets	3	3.15	744	697	0.60	3.07	9.09	1.38
	4	3.15	737	598	0.36	3.26	8.23	1.69
	5	3.15	815	653	0.31	3.41	6.90	2.40
	6	3.15	791	710	0.32	3.76	6.50	2.71

In the estimation of char accumulation, the total gas, $\dot{m}_{gasP}$ flowing through the bed after pyrolysis was considered and obtained as described in Eq. (11). The density of char particles, ρ_{char} also listed in Table 1 for each feedstock was calculated from Eq. (12), where ρ_{bio} is the biomass particle density, ε_s the solid volume fraction, and w_{Fcar} and w_{vol} are the weight fractions of fixed carbon and moisture in the biomass, respectively.

$$\dot{m}_{gasP} = \dot{m}_{air} + (w_{mois} + w_{vol})\dot{m}_{bio} \tag{11}$$

$$\rho_{char} = \left(\frac{w_{Fcar}}{\varepsilon_s}\right)\rho_{bio} \tag{12}$$

Using the amount of accumulated char over the operating period, the minimum fluidization velocity, U_{mfb} of the binary mixture of bed material and char particles is determined following the steps provided in the literature, Agu et al.[32] The fluidization index, $FI = \dot{m}_{air}/(\rho_{gasP}AU_{mfb})$ at each air flow rate measures the degree of bed mixture fluidization. Where $FI > 1$, the bed is fully fluidized. For $FI < 1$, the bed may be partially or un-fluidized. As shown in the table, the amount of accumulated char decreases with increasing air flow rate due to higher char oxidation. With a reduction in the char content, the fluidization of the bed gets smoother. Since $FI < 3.0$, the bed can be considered in a bubbling regime, although a better performance is expected in the FI range $1.5 - 2.5$. A higher value of the fluidization index can lead to a flow of large bubbles that reduces the effective gas residence time. When a bed is subjected to multiple number of bubbles of relatively smaller size, the mixing is effective.

For each of the feedstocks, Figure 3 presents the total pressure drop, **P1 – P5** across the bed over time at two different air flow rates, 3 and 6 kg/h. When the bed is fully fluidized, the pressure drop remains relatively stable across different gas rates. The magnitude of the pressure drop depends on

the bed voidage. At a lower air flow rate, the fuel particle accumulation is higher due to lower conversion rate. The increase in the biomass load increases the bed voidage, hence reducing the pressure drop. This behavior is seen across the different feedstocks. The pressure drop also tends to increase with time at different air flow rates, indicating a reduction in the bed voidage due to increasing fluidizing gas emanating from pyrolysis and char gasification. For paper pellets, there is a significant higher fluctuation in the bed across the different air flow rates. This shows that the bed is not properly fluidized compared to other feedstocks as can be ascertained from the fluidization index. Of the four biomasses, the wood pellets have the most stable bed behavior followed by the garden waste pellets due to their relatively high fluidization indices. For the fish pellets, though with comparable particle equivalent diameter as the wood pellets, the lower char density influences the relatively high instability of the bed.
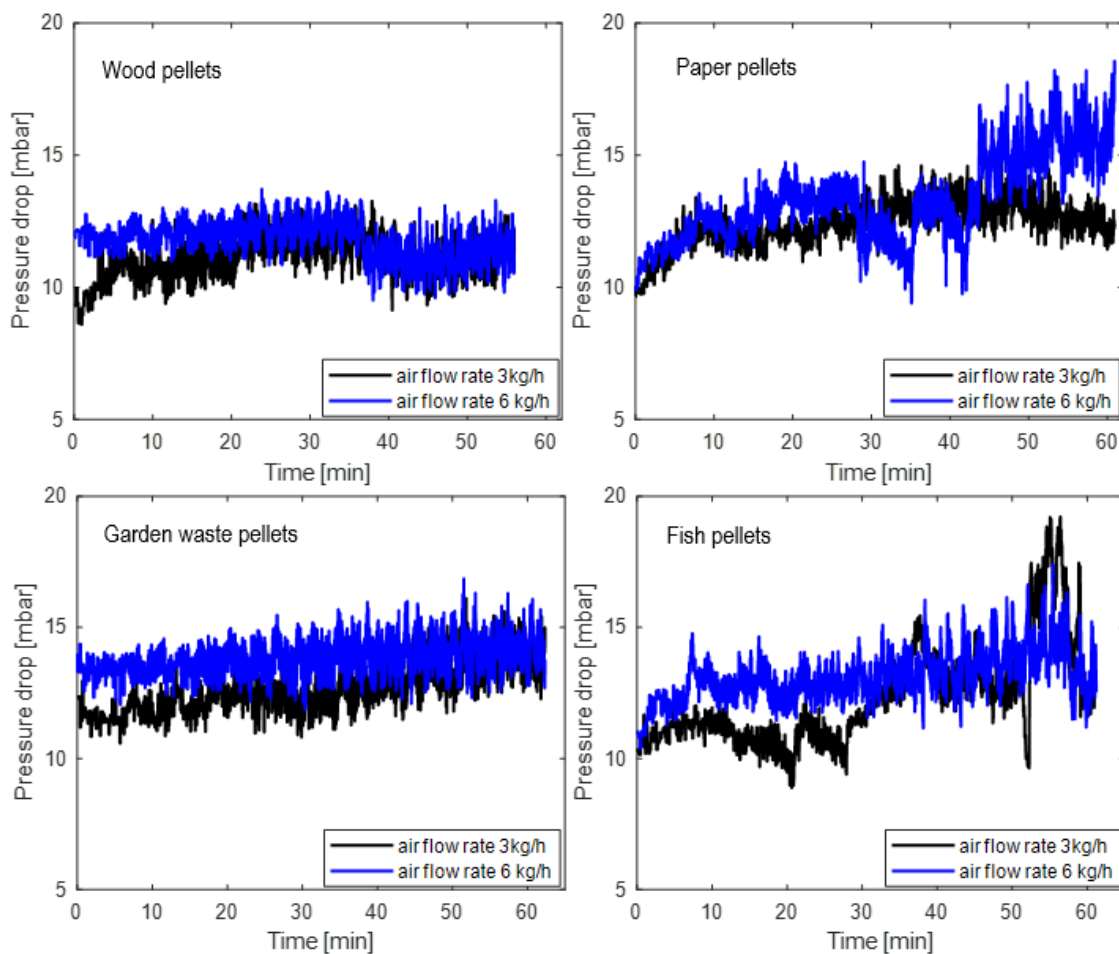

Figure 3. Variation of pressure drop over the bed during gasification of different feedstocks at air flow rates of 3 and 6 kg/h.

Compared with the pressure drop, Figure 4 shows that the bed temperature follows a similar behavior for the different feed stocks. It should be noted that temperature control of the bed during each experimental run is internally managed, and there is no additional heat source applied during the actual conversion process. External heaters were employed initially to raise the bed temperature, but on attaining the desired temperature, these heaters were deactivated. When biomass and air were introduced into the reactor, the bed temperature was automatically regulated through the oxidation of the fuel particles, resulting in a self-sustaining and autothermal process. The increase in temperature with time is an indication of a progressive oxidations which dominate the endothermic

pyrolysis of the feed biomass. At a 3 kg/h air flow rate, the higher accumulation of char particles increases the sensible heat loss. The bed temperature behavior also suggests that the bed is partially fluidized at lower air flow rates, where $FI < 1.6$. Since biomass is fed from top of the bed and gas from the bottom, the increase in the bed temperature shows that char particles sink down into the bed as the gas flow rate increases, possibly due to an increase in the solid circulation rate. As noted in Agu et al.[33], the paper pellets, due to high particle size and low particle density, must have shown an initial downward segregation at the lower gas rate and then an upward segregation at the higher air flow rate. Thus, a relatively higher amount of char particles is in the paper bed, resulting in a higher bed temperature at lower air flow rate than at a higher rate.
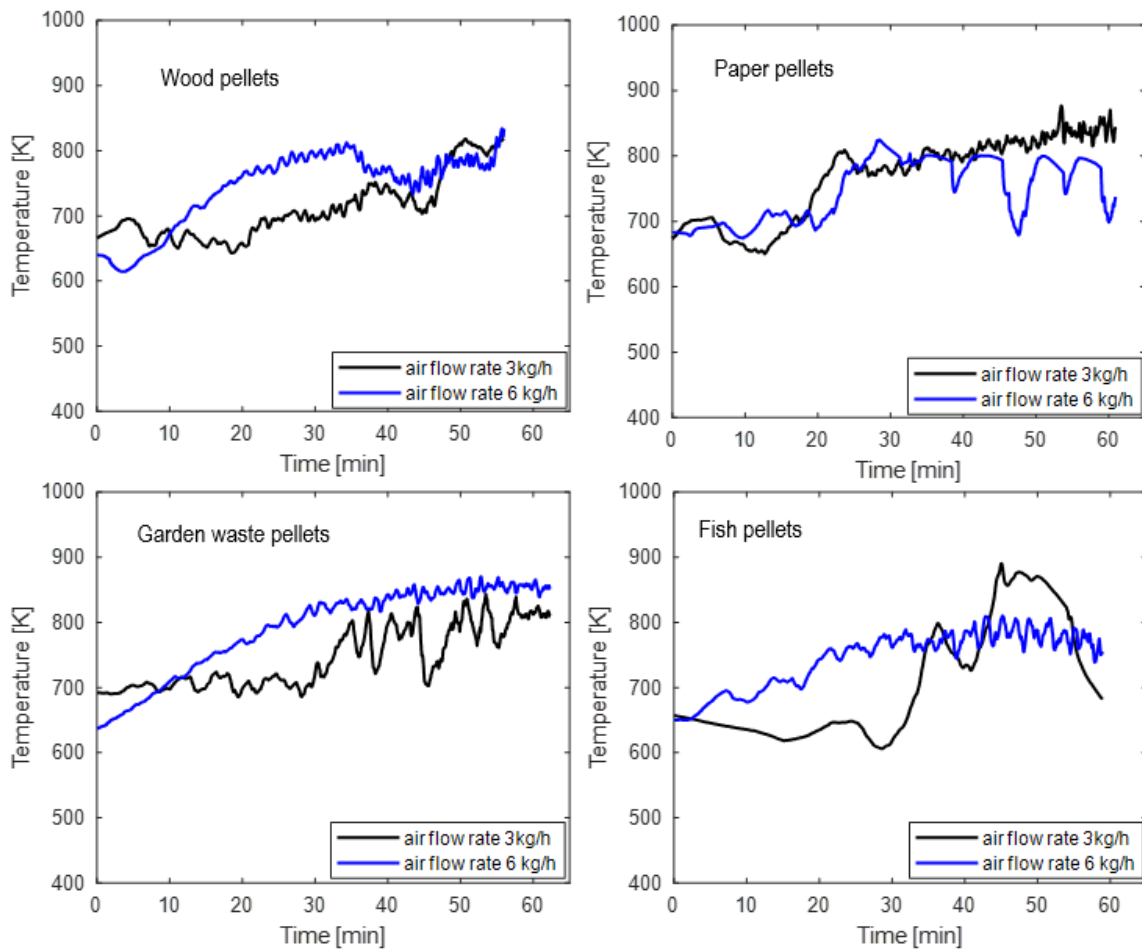

Figure 4. Variation of temperature over the bed during gasification of different feedstocks at air flow rates of 3 and 6 kg/h.

On average, the bed temperature is higher than the exit temperature across the different air flow rates. Since the raw biomass is fed on top, this suggests that devolatilization of the fuel particles is rapid and may have completed before the particles moves into the bed. Neglecting heat loss, the lower exit temperature also indicates that a significant amount of heat is absorbed from the gas during drying and pyrolysis processes. In the freeboard, it is expected that some exothermic activities occur, which should include water-gas-shift reaction between H_2O and CO, and others involving oxidation of the fuel gases: CO, H_2 and CH_4 by the residual oxygen. However, the relative difference between the exit and bed temperatures confirms that the possible exothermic reactions rarely occurred, therefore there is little or no O_2 in the freeboard. Figure 5 compares the product gas species for the different feedstocks at different air flow rates. While N2 mole fraction increases with

increasing air rate, the indicated O2 concentrations are stably low across the different flow rates. Although the equivalence ratios corresponding to the different air-fuel ratios are less than a unity, the presence of oxygen in the sample gas may be associated to residual air in the sampling syringe since the oxygen concentration is relatively constant over the test independent of the feedstock. Note that the amount of H2 and H2O reported in the figure are estimated from the measurement of other gas species and elemental balance as described by Eq. (6) and (7).
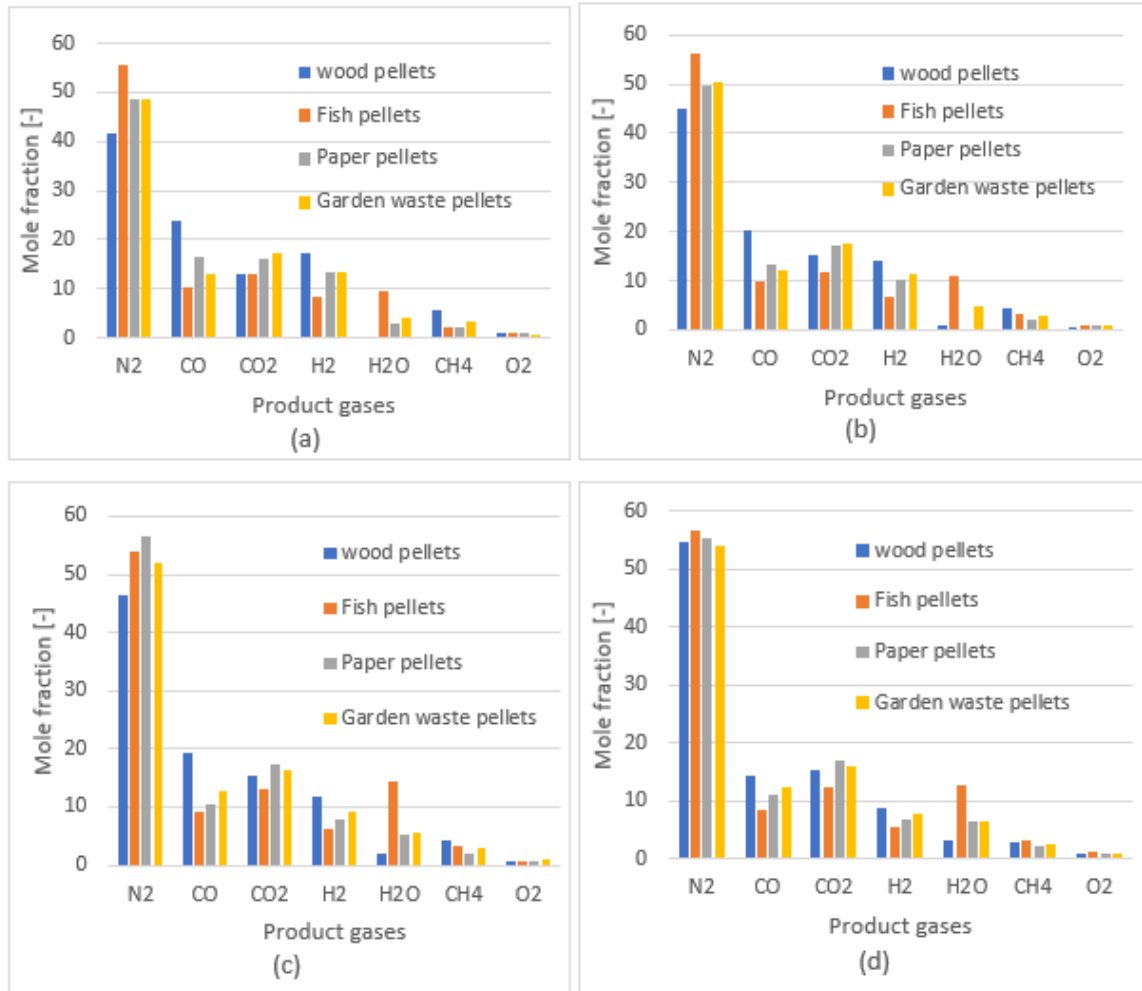

Figure 5. Product gas compositions obtained from gasification of the feedstocks at different air flow rates (a) 3 kg/h (b) 4 kg/h (c) 5 kg/h (d) 6 kg/h.

3.1 Effective carbon conversion and gasification yield strength

Several factors influence the degree of carbon conversion in a fluidized bed reactor, which include gas residence time, bed mixing strength, char particle size, shape and density, concentration of char and the various reacting gases, etc. while char is being consumed, the amount of gas production is increased. The gas yield can also be influenced by the moisture content of the biomass as well as the pyrolysis process. Both the effective carbon conversion efficiency and gas yield strength can be used to characterize the quality of a gasification process for a given feedstock. The carbon conversion efficiency, η_{carb} is expressed by Eq. (13) while the gas yield strength, G_γ can be obtained from Eq. (14), where $X_{uncmol} = X_{carbon} + X_{hydrogen}$ is the total amount of unconverted element in the biomass.

$$\eta_{carb} = 1 - \frac{nX_{carbon}}{\beta X} \qquad\qquad (13)$$

$$G_\gamma = \frac{(1-X_{uncmol})(1-w_{mois})}{w_{vol}} \qquad\qquad (14)$$

The results of the above equations are presented in Figure 6. The accumulated unconverted char is also presented for comparison. Note that the effective carbon conversion efficiency is a measure of how much carbon in the parent biomass is converted to a gaseous product at a given operating condition. Conversely, the unconverted char accumulation expresses the amount of char in the bed over a given period of operation. As shown, the carbon conversion efficiency tends to decrease with increasing fluidization index over the range of tested air flow rate, implying that the produced gas quality (i.e., the CO, CH4 and H2 contents) degrades as the air flow rate increases. While the η_{carb} value is highest in the wood pellets, the fish pellets show the least conversion efficiency for the same value of fluidization index. Like the conversion efficiency, paper and garden waste pellets show a continuous decreasing trend in the gas yield strength. Overall, the fish pellets generate a low-quality gas as both the carbon conversion and gas yield are relatively low over a wide range of air flow rate. This behavior can be attributed to the animal nature of the fuel particles with resultant char particles less reactive than those of plant origin.
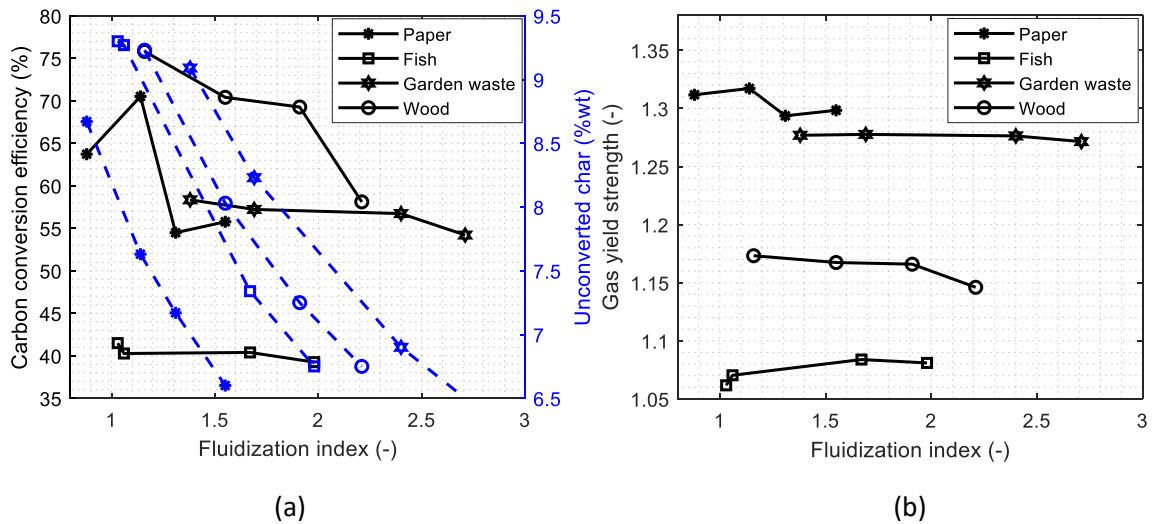

Figure 6. (a) Carbon conversion efficiency (b) Gas yield strength, comparing the bed behavior and quality of conversion of the different feedstocks over a range of fluidization index.

3.1 Product gas distribution

Due to different degrees of active reactions with the different feedstocks, the product gas distribution differs considerably over the range of tested equivalence ration (ER). As shown in Figure 7, the trend of H2 mole fraction is similar for the four feedstocks and decreases with increasing ER. However, CO and CO2 show varying trends across the different biomasses. For a top-feed configuration as used in this study, the major contribution of gas distribution is the water-gas shift reaction and the pyrolysis process, which are mainly influenced by the reactor temperature. Over the beds of garden waste and fish pellets where ER > 0.25, the CO fraction is relatively constant while the corresponding CO2 increases slightly, a behavior supported by a balance of high bed temperature and enhanced water-gas shift in the freeboard. The wood pellets follow the conventional behavior, where the concentrations of different fuel gases decrease with increasing ER. The higher bulk density of wood pellets influences mixing of the biomass with the bed before completion of devolatilization. This therefore enhances oxidation of CO, H2 and CH4 species in the bed with available O2. The higher

CO and CH4 fractions from the wood pellets compared to other feedstocks is also an indication that carbon conversion is better due to the mixing effect. The paper pellets, on the other hand, show an opposite trend in the CH4 distribution. Unlike the wood pellets with good bed mixing, the lower particle bulk density results in top segregation of the paper particles, preventing the fuel gases in participating in the bed oxidation, thus lowering the carbon conversion. As the carbon conversion is poor for the fish pellets, the concentrations of CO and H2 are lowest among the four feedstocks following their oxidations by the available O2.
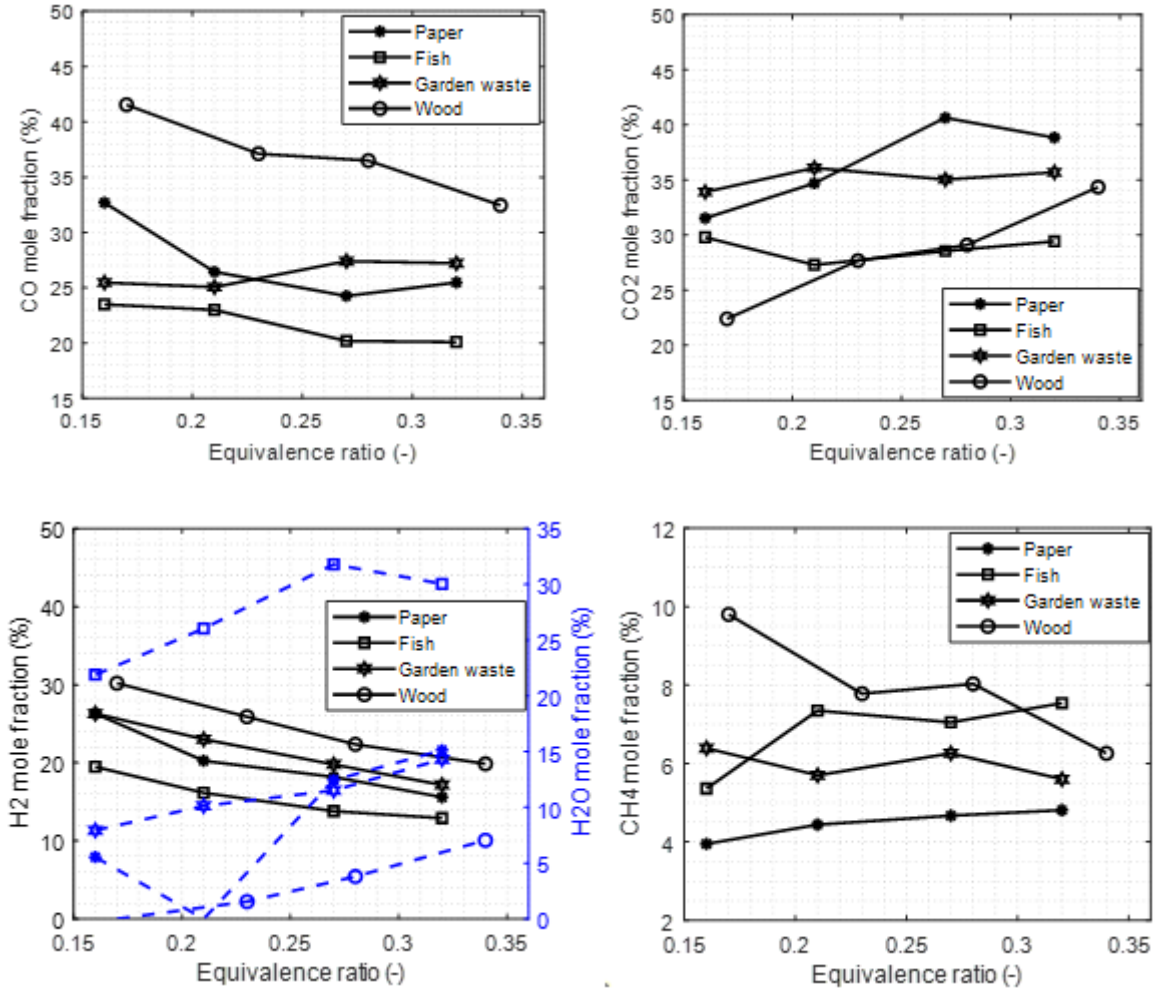

Figure 7. Nitrogen-free product gas distribution, comparing the performance of the different feedstock gasification at different equivalence ratios.

3.2 Energy conversion and efficiency

In addition to the gas yield, the quality of the produced gas can also be measured by its chemical energy value. It should be noted that gasification is a therchemical process, converting a less value feedstock into a high energy-valued gas. For an efficient gasification, the chemical energy stored in the gas, if possible, should be close to that contained in the feed biomass. Also, some useful heat can be recovered for a downstream process. For a given feed stock, the associated chemical and thermal energies from the product gas can be obtained from Eq. (15) and (16), respectively.

$$Erg_{chem} = \dot{m}_{gas} LHV_{gas} \tag{15}$$

$$Erg_{therm} = \dot{m}_{gas} \tilde{c}_{pgas}(T_{out} - T_{amb}) \tag{16}$$

Here, the gas mass flow rate, $\dot{m}_{gas}$, the lower heating value, LHV_{gas} and the specific heat capacity, $\tilde{c}_{pgas}$ are calculated from the following expressions. LHV_j is the heating value of each gaseous species, "j", and $\tilde{c}_{p,j}$ and $\widehat{M}_j$ are the corresponding specific heat capacity and molecular weight, respectively.

$$\dot{m}_{gas} = \dot{m}_{air}\left[1 + \frac{(1-X_{uncmol})(1-w_{ash})}{AFR}\right] \tag{17}$$

$$LHV_{gas} = \sum_i\left(x_j LHV_j\right); \qquad \tilde{c}_{pgas} = \sum_j\left(x_j \tilde{c}_{p,j}\right); \qquad x_j = \frac{y_j\widehat{M}_j}{\sum_j(y_j\widehat{M}_j)} \tag{18}$$

From the total energy value, $Erg_{tot} = Erg_{chem} + Erg_{therm}$ of the gas, the overall energy conversion efficiency, η_{tot} are expressed thus:

$$\eta_{tot} = \frac{Erg_{tot}}{(1-w_{ash})\dot{m}_{bio}LHV_{bio}} \tag{19}$$

Figure 8 shows that the chemical energy decreases with increasing equivalence ratio due to oxidation of the fuel gas species. As the oxidation process is accompanied with heat evolution, the thermal energy increases with the amount of oxygen supplied. While the relative amount of chemical energy is close for the different feedstocks, the overall energy efficiency differs significantly. The paper pellets have the highest efficiency, above 80%, while the fish pellets are below 40% across the range of equivalence ratio tested. As wood pellets have the highest relative chemical energy value, which differ from other feedstocks, the overall efficiency tends to decrease with increasing equivalence ratio. Although the gas yield is lowest in wood pellets among the plant-based biomasses, the higher energy efficiency compared to the garden waste, can be attributed to its higher carbon conversion efficiency, producing a gas with high CO content.
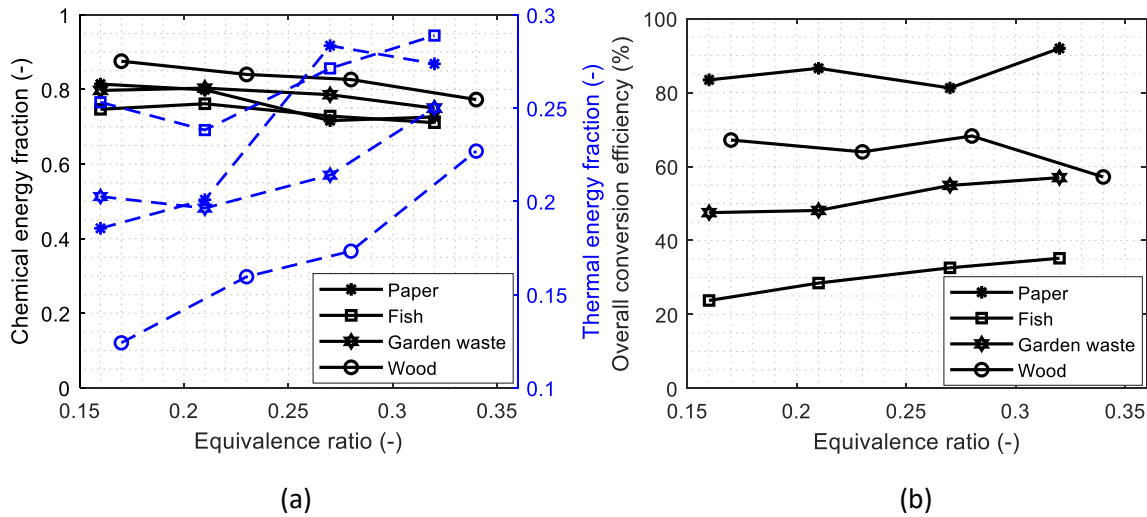

Figure 8. Energy value of the product gas, comparing performance of the different feedstocks at different equivalence ratios (a) contribution of chemical and thermal energies (b) overall conversion efficiency.

In summary, conversion of waste solid materials for energy and syngas productions in a bubbling fluidized bed is influenced by the bulk density and nature of biomass particles as well as the degree of mixing achievable in the bed. With a higher bulk density, a top-feeding configuration is still appropriate to achieve a good conversion, thereby avoiding the use of expensive and difficult to maintain screw feeder.

The nature of biomass, either plant-based or animal-based contributes immensely to the output of the reactor. From this study, it appears that the resultant char from the fish pellets is less reactive than those of the plant-based including wood, paper, and garden waste pellets. Hence, a very high reactor temperature is essential for fish pellet conversion, making an allothermal gasification inevitable.

In addition, the performance of paper pellets shows that moisture content has little or no influence in the conversion process. However, a high carbon content in a biomass impacts the particle density, thus enhancing the mixing in the bed for effective conversion. Though an efficient carbon conversion is desirable, the results further show that the strength of a biomass to yield gas in the conversion process is significantly needed to quantify the energy value and quality of the product gas.

5. Conclusion

This study demonstrates experimental results and analysis to evaluate conversion of different types of solid waste materials in a bubbling fluidized bed for energy generation and syngas production. The feedstocks tested include wood, paper, garden and fish wastes, and were used in pellets form for significant particle density and energy value. The degree of conversion of the different feedstocks in a 20-kWh air-biomass reactor was evaluated using three different key indicators such as effective carbon conversion efficiency, effective gas yield strength and energy conversion efficiency.

The results show that the biomass conversion depends on the particle bulk density, bed mixing strength and nature of the fuel particles. For a plant-based biomass, an autothermal gasification is achievable with carbon and energy conversion efficiencies lying in the range 55 – 75% and 50 – 90%, respectively over an equivalence ration 0.15 – 0.35. Due to poor reactivity of the fish pellets considered as animal-based, the corresponding conversion efficiencies are very low for an autothermal process to be applicable. Hence, a very high temperature achievable from an external heat source is required for efficient conversion of animal-based solid wastes. The higher the biomass bulk density, the greater the mixing strength of the bed. Therefore, feeding a dense biomass from top of the bed is adequate to achieve an efficient and effective conversion at the right reactor temperature.

Although, the results presented in this study is from a relatively shallow bed of 10 cm diameter, it is expected that the method established here to evaluate the solid waste conversion is applicable to any fluidized bed reactor. Further investigation is however desirable to evaluate the impact of reactor temperature on the produced gas quality and energy value. In addition, other types of animal-based solid wastes also need to be investigated to enhance a conclusion into the best method required for efficient conversion. To gain a better insight into the energy penalty in the syngas production from the solid waste materials, thorough analysis of energy flow across the fluidized bed reactor is paramount.

6. Reference

(1) Wang, X.; Lu, Y.; Chen, C.; Yi, X.; Cui, H. Total-Factor Energy Efficiency of Ten Major Global Energy-Consuming Countries. *J Environ Sci (China)* **2024**, *137*. https://doi.org/10.1016/j.jes.2023.02.031.

(2) Mousavi, S.; Hosseinzadeh, A.; Golzary, A. Challenges, Recent Development, and Opportunities of Smart Waste Collection: A Review. *Science of the Total Environment*. 2023. https://doi.org/10.1016/j.scitotenv.2023.163925.

(3)   Kumar, A.; Samadder, S. R. A Review on Technological Options of Waste to Energy for Effective Management of Municipal Solid Waste. *Waste Management*. 2017. https://doi.org/10.1016/j.wasman.2017.08.046.

(4)   Białowiec, A.; Micuda, M.; Koziel, J. A. Waste to Carbon: Densification of Torrefied Refuse-Derived Fuel. *Energies (Basel)* **2018**, *11* (11). https://doi.org/10.3390/en11113233.

(5)   Mor, S.; Ravindra, K. Municipal Solid Waste Landfills in Lower- and Middle-Income Countries: Environmental Impacts, Challenges and Sustainable Management Practices. *Process Safety and Environmental Protection*. 2023. https://doi.org/10.1016/j.psep.2023.04.014.

(6)   Hoang, A. T.; Varbanov, P. S.; Nižetić, S.; Sirohi, R.; Pandey, A.; Luque, R.; Ng, K. H.; Pham, V. V. Perspective Review on Municipal Solid Waste-to-Energy Route: Characteristics, Management Strategy, and Role in Circular Economy. *Journal of Cleaner Production*. 2022. https://doi.org/10.1016/j.jclepro.2022.131897.

(7)   Sonu; Rani, G. M.; Pathania, D.; Abhimanyu; Umapathi, R.; Rustagi, S.; Huh, Y. S.; Gupta, V. K.; Kaushik, A.; Chaudhary, V. Agro-Waste to Sustainable Energy: A Green Strategy of Converting Agricultural Waste to Nano-Enabled Energy Applications. *Science of the Total Environment* **2023**, *875*. https://doi.org/10.1016/j.scitotenv.2023.162667.

(8)   Caferra, R.; D'Adamo, I.; Morone, P. Wasting Energy or Energizing Waste? The Public Acceptance of Waste-to-Energy Technology. *Energy* **2023**, *263*. https://doi.org/10.1016/j.energy.2022.126123.

(9)   Negi, S.; Pan, S.-Y.; Shiau, Y.-J. Decarbonizing Food Waste Treatment through Anaerobic Codigestion with Yard Waste: Energy, Engineering, Economic, and Environmental Aspects. *ACS ES&T Engineering* **2023**, *0* (0). https://doi.org/10.1021/acsestengg.3c00120.

(10)   Liu, Q.; C. Chmely, S.; Abdoulmoumine, N. Biomass Treatment Strategies for Thermochemical Conversion. *Energy & Fuels* **2017**, *31* (4), 3525–3536. https://doi.org/10.1021/acs.energyfuels.7b00258.

(11)   Emeka Agu, C.; M. E. Moldestad, B.; Pfeifer, C. Assessment of Combustion and Gasification Behavior in a Bubbling Fluidized Bed Reactor: A Comparison between Biomass with and without Chemical Additives. *Energy & Fuels* **2020**, *34* (8), 9654–9663. https://doi.org/10.1021/acs.energyfuels.0c01408.

(12)   Kumar Soni, V.; Singh, G.; K. Vijayan, B.; Chopra, A.; S. Kapur, G.; S. V. Ramakumar, S. Thermochemical Recycling of Waste Plastics by Pyrolysis: A Review. *Energy & Fuels* **2021**, *35* (16), 12763–12808. https://doi.org/10.1021/acs.energyfuels.1c01292.

(13)   Corella, J.; M. Toledo, J.; Molina, G. A Review on Dual Fluidized-Bed Biomass Gasifiers. *Industrial & Engineering Chemistry Research* **2007**, *46* (21), 6831–6839. https://doi.org/10.1021/ie0705507.

(14)   Bandara, J. C.; Jaiswal, R.; Nielsen, H. K.; Moldestad, B. M. E.; Eikeland, M. S. Air Gasification of Wood Chips, Wood Pellets and Grass Pellets in a Bubbling Fluidized Bed Reactor. *Energy* **2021**, *233*, 121149. https://doi.org/10.1016/J.ENERGY.2021.121149.

(15)   Campoy, M.; Gómez-Barea, A.; L. Villanueva, A.; Ollero, P. Air–Steam Gasification of Biomass in a Fluidized Bed under Simulated Autothermal and Adiabatic Conditions. *Industrial &*

Engineering Chemistry Research **2008**, *47* (16), 5957–5965. https://doi.org/10.1021/ie800220t.

(16)   Zhang, Y.; Li, B.; Li, H.; Liu, H. Thermodynamic Evaluation of Biomass Gasification with Air in Autothermal Gasifiers. *Thermochim Acta* **2011**, *519* (1–2). https://doi.org/10.1016/j.tca.2011.03.005.

(17)   Suryawanshi, S. J.; Shewale, V. C.; Thakare, R. S.; Yarasu, R. B. Parametric Study of Different Biomass Feedstocks Used for Gasification Process of Gasifier—a Literature Review. *Biomass Conversion and Biorefinery*. 2023. https://doi.org/10.1007/s13399-021-01805-2.

(18)   Yang, Z.; Wang, Z.; Wu, Y.; Wang, J.; Lu, J.; Li, Z.; Ni, W. Dynamic Model for an Oxygen-Staged Slagging Entrained Flow Gasifier. *Energy & Fuels* **2011**, *25* (8), 3646–3656. https://doi.org/10.1021/ef200742s.

(19)   Thapa, R. K.; Frohner, A.; Tondl, G.; Pfeifer, C.; Halvorsen, B. M. Circulating Fluidized Bed Combustion Reactor: Computational Particle Fluid Dynamic Model Validation and Gas Feed Position Optimization. *Comput Chem Eng* **2016**, *92*. https://doi.org/10.1016/j.compchemeng.2016.05.008.

(20)   Jaiswal, R.; Agu, C. E.; Kofoed Nielsen, H.; Sørflaten Eikeland, M.; Margrethe Emilie Moldestad, B.; Kumar Thapa, R. Investigation of Bubble Properties in a Bubbling Fluidized-Bed Gasification Reactor Using a Computational Particle Fluid Dynamic Model. *Industrial & Engineering Chemistry Research* **2023**, *0* (0). https://doi.org/10.1021/acs.iecr.3c00626.

(21)   Ren, J.; Cao, J. P.; Zhao, X. Y.; Yang, F. L.; Wei, X. Y. Recent Advances in Syngas Production from Biomass Catalytic Gasification: A Critical Review on Reactors, Catalysts, Catalytic Mechanisms and Mathematical Models. *Renewable and Sustainable Energy Reviews*. 2019. https://doi.org/10.1016/j.rser.2019.109426.

(22)   Basu, P. *Combustion and Gasification in Fluidized Beds*; 2006. https://doi.org/10.1201/9781420005158.

(23)   Nobre, C.; Longo, A.; Vilarinho, C.; Gonçalves, M. Gasification of Pellets Produced from Blends of Biomass Wastes and Refuse Derived Fuel Chars. *Renew Energy* **2020**, *154*. https://doi.org/10.1016/j.renene.2020.03.077.

(24)   Li, W.; Yuan, Z.; Chen, X.; Wang, H.; Wang, L.; Lou, Z. Green Refuse Derived Fuel Preparation and Combustion Performance from the Solid Residues to Build the Zero-Waste City. *Energy* **2021**, *225*. https://doi.org/10.1016/j.energy.2021.120252.

(25)   García, R.; González-Vázquez, M. P.; Rubiera, F.; Pevida, C.; Gil, M. V. Co-Pelletization of Pine Sawdust and Refused Derived Fuel (RDF) to High-Quality Waste-Derived Pellets. *J Clean Prod* **2021**, *328*. https://doi.org/10.1016/j.jclepro.2021.129635.

(26)   Vikram, S.; Deore, S. P.; De Blasio, C.; Mahajani, S. M.; Kumar, S. Air Gasification of High-Ash Solid Waste in a Pilot-Scale Downdraft Gasifier: Experimental and Numerical Analysis. *Energy* **2023**, *270*. https://doi.org/10.1016/j.energy.2023.126912.

(27)   Siddiqui, H.; Thengane, S. K.; Sharma, S.; Mahajani, S. M. Revamping Downdraft Gasifier to Minimize Clinker Formation for High-Ash Garden Waste as Feedstock. *Bioresour Technol* **2018**, *266*. https://doi.org/10.1016/j.biortech.2018.06.086.

(28)   Fazil, A.; Kumar, S.; Mahajani, S. M. Gasification and Co-Gasification of Paper-Rich, High-Ash Refuse-Derived Fuel in Downdraft Gasifier. *Energy* **2023**, *263*. https://doi.org/10.1016/j.energy.2022.125659.

(29)   Furuvik, N. C. I. S.; Wang, L.; Jaiswal, R.; Thapa, R.; Eikeland, M. S.; Moldestad, B. M. E. Experimental Study and SEM-EDS Analysis of Agglomerates from Gasification of Biomass in Fluidized Beds. *Energy* **2022**, *252*, 124034. https://doi.org/10.1016/J.ENERGY.2022.124034.

(30)   Wen, C. Y.; Yu, Y. H. Mechanics of Fluidization. *Chemical Engineering Progress, Symposium Series* **1966**, *62* (1).

(31)   Agu, C. E.; Pfeifer, C.; Eikeland, M.; Tokheim, L. A.; Moldestad, B. M. E. Measurement and Characterization of Biomass Mean Residence Time in an Air-Blown Bubbling Fluidized Bed Gasification Reactor. *Fuel* **2019**, *253*. https://doi.org/10.1016/j.fuel.2019.05.103.

(32)   Agu, C. E.; Pfeifer, C.; Moldestad, B. M. E. Prediction of Void Fraction and Minimum Fluidization Velocity of a Binary Mixture of Particles: Bed Material and Fuel Particles. *Powder Technol* **2019**, *349*. https://doi.org/10.1016/j.powtec.2019.03.027.

(33)   Agu, C. E.; Tokheim, L. A.; Pfeifer, C.; Moldestad, B. M. E. Behaviour of Biomass Particles in a Bubbling Fluidized Bed: A Comparison between Wood Pellets and Wood Chips. *Chemical Engineering Journal* **2019**, *363*, 84–98. https://doi.org/10.1016/J.CEJ.2019.01.120.

Paper 8

Enhanced hydrogen production from gasification of wood pellets in a fluidized bed reactor with air-steam as oxidizing medium," Accepted for publication in the Journal

Enhanced Hydrogen production from gasification of waste feedstock in a fluidized bed reactor

Rajan Jaiswal[1], Britt M. E. Moldestad[1], Marianne Sørflaten Eikeland[1], Henrik Kofoed Nielsen[2], Rajan. K. Thapa[1]

[1]University of South-Eastern Norway, Campus Porsgrunn,[2]University of Agder, Grimstad Campus

[1]{rajan.jaiswal,britt.moldestad,Marianne.Eikeland,rajan.k
.thapa}@usn.no,[2]henrik.kofoed,nielsen@uia.no

Abstract. Syngas from the gasification of wastes and biomass can be utilized for a wide range of applications like power generation, producing biofuels, biomethane, and chemicals depending on the quality of the mixture gases. The product gas quality and yield significantly depend on the oxidizing medium.

This work aims to obtain the optimal parameters at which hydrogen-rich syngas can be produced from an auto-thermal gasification of wood pellets using air steam as the gasifying medium in a bubbling fluidized bed gasifier. A three-dimensional Computational Particle Fluid Dynamics model of the gasifier was developed in Barracuda VR by considering the heat transfer model, chemical kinetics rate, and particle size distribution. To check the CPFD model robustness, the CPFD results were validated with the experimental data obtained from a 20kW gasifier. The reactor was simulated in two steps: (I) thermal flow simulations at different equivalence ratios and (II) thermal flow simulations at different steam-to-air ratios. The results depicted that at an equivalence ratio of 0.25 (with air as the gasifying medium), better-quality syngas with higher bed temperature and lower unconverted carbon in the bed was observed. The hydrogen fraction in product gas was enhanced from 11 (vol.%) to 21-26 (vol.%) with the addition of (1-5) wt.% steam to the inlet fluidizing gas. Above the steam-to-air ratio of 0.05, unreacted steam in the product gas increased. The unconverted carbon in the bed increased significantly with a decrease in reactor temperature by 300°C at the steam-to-air ratio of 0.2. The optimal equivalence ratio at which the reactor sustained auto-thermal operation with enhanced gas quality and lower unconverted carbon in the bed was 0.25, with an optimal steam-to-air ratio of 0.05.

Keywords: Gasification, Fluidized bed, Hydrogen, steam-to-air ratio, CPFD

1   Introduction

With the worsening climate conditions and increased energy demand at an unprecedent rate, it is now urgent to shift to clean energy sources and clean energy technologies. Utilizing thermochemical conversion techniques for energy production from biomass and waste provides an alternative clean energy source to mitigate carbon-neutral goal

by substituting fossil fuel. The thermo-chemical conversion techniques include normally gasification, pyrolysis and combustion[1]–[3].

Among these, gasification is a prominent thermal degradation method to convert the carbaneous solid (biomass or wastes) into syngas in deficit oxidizing environment. The syngas from gasification mainly consists of CO, H_2, CH_4, and other gases which can be utilized for various applications like power generation, producing biofuels, biomethane and chemicals. The quality of the syngas mainly depends on types of feedstocks, the types and design of the gasifier, the oxidizing medium, and other operational parameters such as equivalence ratio, reactor temperature, catalyst, and bed material. The type of reactor has significant influence on the temperature uniformity, heat and mass transfer, and fuel conversion efficiency during the gasification process. The gasification reactor is mainly classified as fixed bed gasifier, fluidized bed gasifier, plasma gasifier and entrained flow gasifier [3], [4]. Among several gasification reactors, bubbling fluidized bed reactors have gained popularity due to uniform heat and mass transfer, good temperature control and proper mixing of the binary particle mixtures. This type of gasifier is also easy to scale up and can be operated at atmospheric pressure. In addition, the bubbling fluidized bed reactors are simple in design and can be operated at a relatively lower cost with a wide variety of feedstocks. In a bubbling fluidized bed, the hot bed material is set into motion by forcing the fluidizing gas against the particle bed which acts as primary source of thermal energy required during biomass gasification. The biomass (feedstock) undergoes rapid volatilization, pyrolysis, followed by tar cracking and char conversion into light gases, as shown in Fig 1.
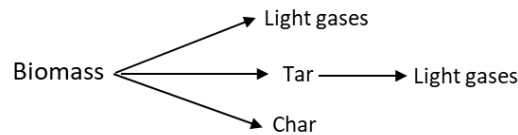

Fig 1. Schematic representation of biomass gasification steps [34].

The output raw gases from the gasification process largely depends on the oxidizing medium, typically air, steam, oxygen, CO_2, or a combination of these gases. Air is the cheapest and most used gasifying medium. The syngas with air gasification contains H_2 (10-18%), CO (12-30%), CH_4 (2-6%) and N_2 (35-60)% [5]. The lower heating value (LHV) of the producer gas is typically below 6 MJ/Nm^3, which is mainly suitable for power generation and as heat source in the boiler [6]. The reduced calorific value of syngas due to dilution with nitrogen makes air gasification less attractive. In contrast, the higher heating value of the producer gas with an enhanced hydrogen fraction can be achieved with steam as gasifying agent due to the reforming and cracking of tar and higher hydrocarbons [7]. The calorific value of the syngas can be increased to about 15-17MJ/Nm^3 [6], [8]. However, steam gasification is an endothermic process, the thermal input required to sustain the gasification process has to be supplied externally. Usually, the part of the feedstock is combusted in another chamber and the hot bed material is circulated to the gasification reactor[9]. Thus, the cost of steam generation and maintaining the reactor operating temperature during steam gasification is much higher. Another method is addition of pure oxygen with steam which promotes the

oxidation reaction providing the heat required for the gasification process. However, pure oxygen to operate a such reactor is expensive which is economically discouraging to implement at an industrial scale. Alternatively, steam and air gasification can be used to produce hydrogen-rich syngas with lower operational costs. Extensive research work has been published on biomass gasification with steam, air, steam-oxygen, oxygen enriched air and air-steam as gasifying medium [10]–[20]. Among the cited literature on air-steam gasification, the focus has been mostly on improving hydrogen yield in the product gas or investigating the influence of different operating parameters on the produced gas output. Little attention is given to operate the gasifier in an auto-thermal mode with air-steam as the gasifying medium.

Experimental methods to identify operational parameters for an auto thermal operation in a lab-scale reactor can be challenging. In addition, the parameters obtained from pilot scale operation may not be suitable for an auto thermal operation of industrial-scale reactors. In this regard, using a computational fluid dynamic tool can be of great advantage as it can be easily scaled up at lower costs provided that the CFD model is validated correctly. With the recent advancement in computational ability and parallel computation, the CFD simulations have emerged as a promising tool to study thermochemical conversion of biomass in fluidized bed reactors. There are mainly three CFD approaches to study dense reactive flow in a fluidized bed reactor: two-fluid model (TFM), computational fluid dynamic coupled with discrete element method (CFD-DEM) and multiphase-in-cell (MP-PIC). The major drawback of the TFM method is that it accounts for the particles with the same density, diameter, and coefficient of restitution, which often results in inaccurate prediction of the bed properties[21], [22]. Eulerian-Lagrangian approach, also known as DEM, is more reliable and predicts hydrodynamics better than TFM [23]. Individual particles are tracked with the DEM method, and particle-particle collision are considered, unlike the TFM model. Therefore, DEM requires enormous computing power to simulate fluidized bed reactors. Another Eulerian-Lagrangian approach that is known as Computational Particle Fluid Dynamics (CPFD) uses Multiphase-particle in cell (MP-PIC) [24]. This approach has gained popularity in recent days due to its capacity to simulate industrial fluidized bed reactors [25], [26]. In the MP-PIC approach, particles with similar attributes are grouped to form a parcel which is counted as a computational particle. In this way, the number of computational particles is reduced in the simulation, reducing the computational time.

This work employs a three-dimensional CPFD model to investigate an auto-thermal operation of a biomass reactor using air steam as a gasifying medium. A three-dimensional Computational Particle Fluid Dynamics model was developed by considering the Eulerian-Lagrangian approach for the fluid field and particle phase calculations. Also, the CPFD model was developed by considering the heat transfer model, chemical kinetics rate, and particle size distribution. The CPFD model was validated against the experimental data obtained from a 20kW bubbling fluidized bed gasifier. Further simulations were carried to find the optimal reactor temperature, equivalence ratio and steam-to-air ratio for an auto thermal operation of the gasifier using air-steam as fluidizing gas.

2 Computational particle fluid dynamic model and Methodology

A CPFD model was used to simulate unsteady and reactive gas-solid flow of wood pellets gasification in a bubbling fluidized bed reactor. The computational model was simulated using Barracuda VR (Version 21.1.1). It is a commercial numerical tool design for application in multiphase flow systems like fluidized bed reactors, which allows to simulate computational particles in order of 10^{15} and higher. Barracuda uses a three-dimensional multiphase Particle-in-cell approach to simulate gas-particle flow and considers fluid-particle coupling with detailed consideration of thermal physics and reaction chemistry. For the fluid-particles simulations, Barracuda virtual reactor uses a combined Eulerian and Lagrangian approach where the solid particles are modeled based on the discrete Lagrangian methods, and the fluid is modeled as Eulerian grid of cells.

2.1 Governing equations for gas phase and particle motion

The governing equations used for the MP-PIC approach where the gas phase is solved as the continuum and particle phase as discrete[27]–[30] are:

$$\frac{\partial(\varepsilon_g \rho_g)}{\partial t} + \nabla \cdot (\varepsilon_g \rho_g u_g) = \delta \dot{m}_p \tag{1}$$

$$\frac{\partial(\varepsilon_g \rho_g u_g)}{\partial t} + \nabla(\varepsilon_g \rho_g u_g u_g) = -\nabla p + f + \varepsilon_g \rho_g g + \nabla(\varepsilon_g \tau_g) \tag{2}$$

where, $\rho_g, u_g, \varepsilon_g$ and τ_g are the density, velocity, voidage and stress tensor of the gas phase respectively. The function f are conserved by using the Liouville equation as:

$$\frac{\partial f}{\partial t} + \nabla(f u_p) + \nabla u_p(f A_p) = 0. \tag{3}$$

The probability density function, $f(x, u_p, \rho_p, V_P, t)$, describes the particle phase, where x is the location in space, u_p is the particle velocity, ρ_p is the particle density, V_P is the particle volume and t is the time. The mass source term in Equation 1 can be written as:

$$\delta \dot{m}_p = -\iiint f \frac{dm_p}{dt} dm_p du_p dT_P. \tag{4}$$

where, m_p is the mass of the particles. The particle acceleration A_p is described as:

$$A_p = D_P(u_g - u_p) - \frac{1}{\varepsilon_p \rho_p} \nabla \tau_p + \frac{\bar{u}_p - u_p}{\tau D}. \tag{5}$$

The drag function D_P is related to the drag coefficient C_d as:

$$D_P = \frac{3}{4} C_d \frac{\rho_g}{\rho_p} \frac{|u_g - u_p|}{d_p}. \tag{6}$$

The inter-particle stress τ_p is given by:

$$\tau_p(\varepsilon_p) = \frac{P_s \varepsilon_p^\beta}{\max[\varepsilon_{cp} - \varepsilon_p, \alpha(1 - \varepsilon_p)]}. \tag{7}$$

where, ε_p is the close pack volume fraction. The particle volume fraction ε_p and the momentum transfer rate between the gas and the solid phase F is related to f as:

$$\varepsilon_p = \iiint f \frac{m_p}{\rho_p} dm_p du_p dT_P. \tag{8}$$

$$F = -\iiint f\left\{m_p\left[D_P(u_g - u_p) - \frac{1}{\rho_p}\nabla p\right] + u_p\frac{dm_p}{dt}\right\}dm_p du_p dT_P. \tag{9}$$

2.2   Drag Model

Wen-Yu drag model was used for the drag force calculation. The Wen-Yu drag model is based on single particle drag models and depend on the gas volume fraction ε_g to account for particle packing. The drag force and drag function can be calculated from 9 and 6. The drag coefficient $C_{d,W}$ is a function of Reynolds number Re_p as:

$$C_{d,W} = \begin{cases} \frac{24}{Re_p}\varepsilon_g^{-2.65}, Re_p < 0.5 \\ \frac{24}{Re_p}\varepsilon_g^{-2.65}(1 + 0.15Re_p^{0.687}), 0.5 \le Re_p \le 1000. \\ 0.44\varepsilon_g^{-2.65}, Re_p > 1000 \end{cases} \tag{10-13}$$

2.3   Reaction, reaction Kinetics and heat transfer

The thermochemical conversion in a fluidized bed typically occurs in the form of homogeneous, deposition, consumption, and catalytic reactions. The continuous reactions in the fluidized bed reactors are accompanied by rapid consumption or release of the gaseous or solid components, thereby altering the gas-solid fraction and the fluidization pattern. Conversely, the reaction rates and the reactant availability will be a strong function of the gas and solid mixing. Therefore, it is vital to model the reactions alongside the particle fluid dynamic and heat transfer in the fluidized bed gasifier. Different sets of homogeneous and heterogenous reactions and their kinetic rate employed for the CPFD model development are listed in Table 1. The rate of release of volatiles, the fluid-to-particle heat transfer [31], [32] as implemented in the model development are mentioned in the equations (14-16).

Rate of release of volatile components

$$dm/dt = -k\,m\,[kg/s] \tag{14}$$

rate coefficient: k=0.05Te$^{(-5500/T)}$ [1/s]

Fluid-to-particle heat transfer coefficient

$$h = \frac{(c_0 Re^{n1}Pr^{0.33}+c_1)k_f}{D_p} + c_2\ [J/m^2 sK] \tag{15}$$

$Re = |U_f - U_p|D_p/v_f$, $Pr = c_p\mu_f/k_f$, where, $c_0 = 0.37, c_1 = 0.1, c_2 = 0, n1 = 0.6$

Dense phase heat transfer coefficient

$$h_d = \frac{c_0 Re_p^{n1}k_f}{D_p}\left[\frac{J}{m^2 sK}\right] \tag{16}$$

$Re_p = \rho_f U_f d_p/\mu_f$, where, $c_0 = 0.525, , n1 = 0.75$

Table1. Reactions and rate kinetics used in the CPFD model [25], [33].

Heterogenous reactions	Corresponding kinetics
Char partial combustion $2C + O_2 \leftrightarrow 2CO$	$r = 4.34 \times 10^{10}\ m_s\theta_f \exp\left(\frac{-13590}{T}\right)[O_2]$
CO2 gasification $C + CO2 \leftrightarrow 2CO$	$r = 1.12 \times 10^6\ ms\theta f \exp\left(\frac{-13590}{T}\right)[O2]$
Char partial combustion $C + H_2O \leftrightarrow H_2 + CO$	$r = 1.272T^1\ m_s \exp\left(\frac{-22645}{T}\right)[H_2O]$
Homogeneous reactions	**Corresponding kinetics**
CO oxidation $CO + 0.5O_2 \leftrightarrow CO_2$	$r = 5.62 \times 10^{12} \exp\left(\frac{-16000}{T}\right)[CO][\ O_2]^{0.5}$
H$_2$ oxidation $H_2 + 0.5O_2 \leftrightarrow H_2O$	$r = 5.69 \times 10^{11} \exp\left(\frac{-17610}{T}\right)[H2][\ O_2]^{0.5}$
CH$_4$ oxidation $CH_4 + 2O_2 \leftrightarrow CO_2 + 2H_2O$	$r = 5.0118 \times 10^{11}\ T^{-1} \exp\left(\frac{-24357}{T}\right)[CH4][\ O_2]$
Water gas shift reaction $CO + H_2O \leftrightarrow CO_2 + H_2$	$r = 7.68 \times 10^{10}\ T^1 \exp\left(\frac{-36640}{T}\right)[CO]^{0.5}[H_2O]$
Methane reforming $CH_4 + H_2O \leftrightarrow CO + 3H_2$	$r = 3.00 \times 10^5 \exp\left(\frac{-15042}{T}\right)[CH4][H_2O]$

2.4   Computational set up and parameters

In this work, a pilot scale bubbling fluidized bed gasifier of internal diameter 10 cm and height 1 m was simulated. To create a virtual reactor for numerical calculations, a CAD geometry of the reactor column was produced in STL format using SolidWorks and imported in Barracuda (Version 21.1.1). The reactor was divided into a total of number 15984 of cells with uniform grid generation setting available in Barracuda. The size of each cell was 0.6*0.6 cm. The grid allowed to define boundary conditions and control volumes for all fluid field calculations. The reactor was operated at atmospheric pressure with pressure boundary conditions at the reactor outlet.

Different data points were defined along the reactor height to capture the transient properties (fluid and particle temperature, pressure, gas fraction, gas and particle velocity, particle volume fraction etc.) of the reactor. Similarly, air/steam inlet flow boundary condition was defined at the bottom of the column and biomass inlet flow boundary condition was defined at height 22 cm from the bottom. Fig. 2 shows the boundary conditions, transient data points, and grids as implemented in the CPFD model. Likewise, different parameter employed in the CPFD model development are listed in the Table 1. The properties of the wood pellets as implemented in the CPFD model can be found elsewhere [34]. The rector was initialized with bed material up to height 20 cm with initial bed temperature and fluid temperature of 800 ℃. The biomass was fed at flow rate of 3.1 kg/h at different air, air/steam flowrate and the bed properties were captured and analyzed as explained in the section 2.5.
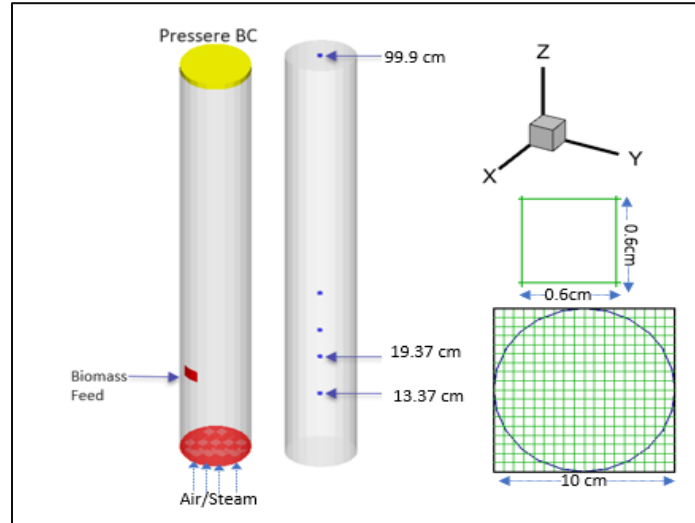
Fig. 2. CPFD model set up showing Boundary Conditions, data points and computational grids.

Table 2. Simulation parameters employed for the CPFD model.

Parameters	Value
Close pack fraction	0.64
Solid Volume fraction	0.534
Total computational cells	60000
Time step	0.001 s
Simulation time	300 s- 500 s
Reactor temperature	(800-900)℃
Equivalence ratio	0.15-0.3
Steam-to-air ratio (SA)	0.01-0.2
Bed material (Sand)	2650 kg/m3

2.5   Methodology

The methods and steps employed in this work to identify the optimal steam-to-air ratio for an auto-thermal gasification of wood pellets in a bubbling fluidized bed reactor is illustrated in Fig. 3. As shown in the block diagram, the first step was developing a computational model in Barracuda VR and validating the CPFD model with the experimental data. The model was then used to simulate gasification of wood pellets at different equivalence ratios (0.15-0.35) to find an optimal equivalence ratio ($ER_{Optimum}$) ratio for higher quality gas yield and bed temperature. The next step was to simulate thermal flow simulations at different steam-to-air mixture as gasifying medium and find optimal steam-to-air ratio ($SA_{Optimum}$ at higher quality gas yield with minimum carbon

in the bed. Further, at $ER_{Optimum}$ and $SA_{Optimum}$, thermal walls were defined to add heat during the gasification. The influence of heat addition on the product gas yield were measured. The results from each step are analyzed and reported in the following chapter.
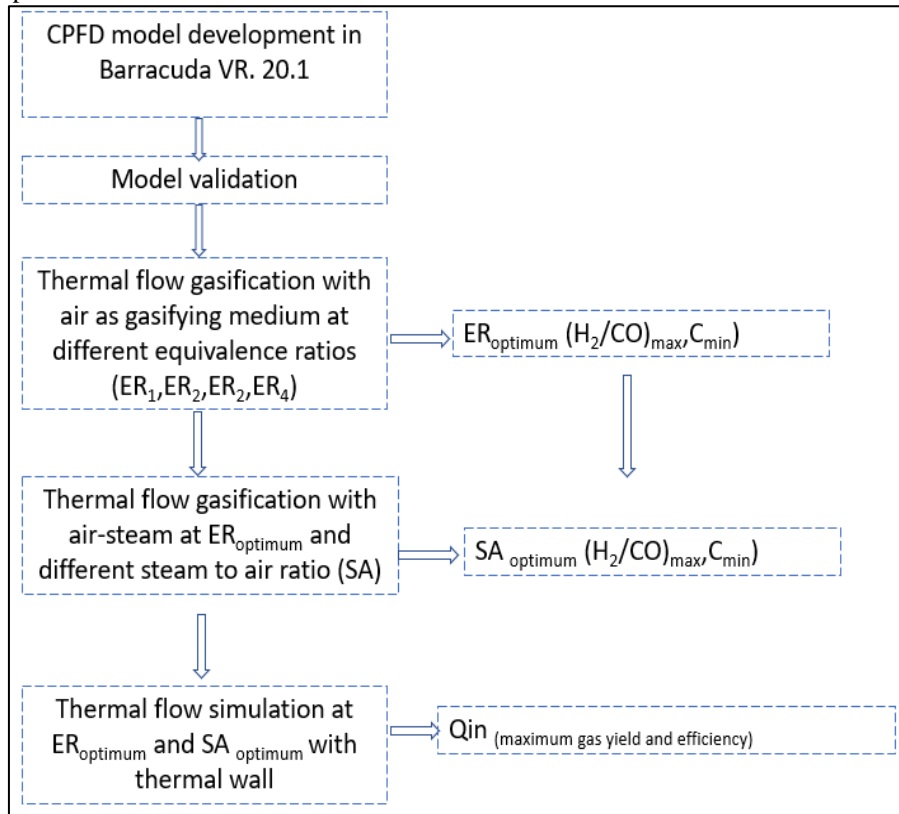

Fig. 3. Block diagram showing steps employed in this work to achieve air/steam gasification of wood pellets in auto-thermal conditions.

3   Result and Discussion

3.1   Model validation

Gasification of wood pellets was carried out on a 20kW bubbling fluidized bed gasifier at an equivalence ratio of 0.2 with air as the fluidizing gas. The reactor is a cylindrical column made of stainless steel with 10 cm internal diameter and 1.5 m height. The reactor is equipped with thermocouples, pressure sensors, an electric heating system, silo, screw feeder and gas chromatography. The experimental setup and method details can be found elsewhere [3], [34]. Initially, the reactor was filled with bed material and heated up to 400 ℃ with air pre-heater and electric heating elements mounted on the reactor column. With excess air supply pellets were combusted initially to heat up the

bed material from 500 ℃ to 800 ℃ rapidly. After the stable temperature was reached, the wood pellets mass flow ratio was increased to adjust the equivalence ratio required to initiate continuous gasification process. The flow rate of wood pellets was kept constant at 3.1 kg/h with the reactor temperature of 800℃ ± 30 ℃. The product gas samples were taken in every 10 minutes and the mole fraction of the gas components were averaged to get the representative value of gas fractions in the product gas.
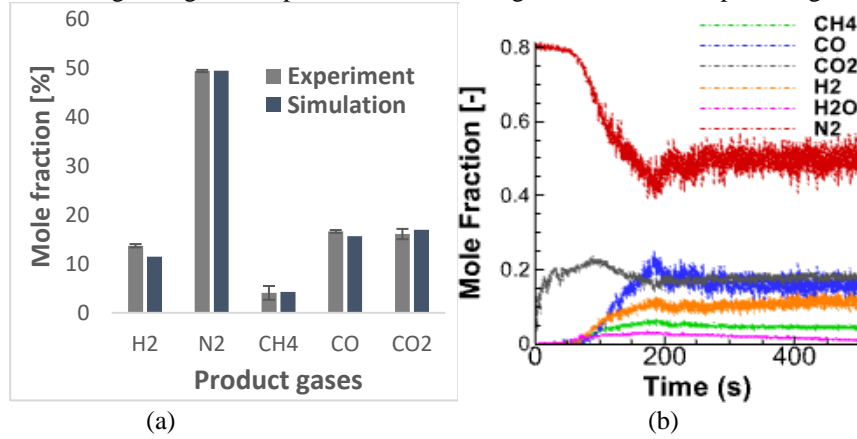

Fig. 4. (a) Comparison of product gas composition measured from experiments and CPFD simulation, the error bars show STD of measured gas compositions(b) Product gas fractions predicted by the CPFD model

With the same operating conditions as used in the experiment, the reactor was simulated using the CPFD model for 500 s, and the product gas was monitored. Fig. 4(b) shows the product gas volume fraction predicted by the CPFD simulation. As depicted in Fig. 4(b), CO2 fraction in the product gas was higher initially and after 200 s, the product gases were stable. Due to excess oxygen in the reactor initially, as the biomass was fed, the oxidation reactions were dominant, resulting in more CO_2 in the outlet gas. With the release of volatiles, simultaneously, all the reactions (heterogenous and homogenous) proceeded, resulting in the mixture of CH_4, N_2, H_2O, CO, CO_2 and H_2 yields in the product gas. The gas fractions after 200 s were averaged and compared with the experimental measurements, as shown in Fig. 4 (a). Comparing the average product gas compositions depicts that the CPFD model over-predicts the CO_2 and CH_4 fractions and under predict H_2 and CO fractions in the product gases. However, the error bar (standard deviation of the samples) for each gas fraction measured from the experiment (as shown in Fig. 4a) suggests that the average gas compositions predicted from the CPFD model are in good agreement. The CPFD model was then used to simulate the gasification reactor with air and air-steam mixture at different reactor operating conditions and the results are discussed in the following sections.

3.2 Thermal flow air gasification

The gasification process can be auto-thermal or allothermal, depending on the extent of exothermic or endothermic reactions during feedstock conversion. When air is used as the fluidizing gas, the char oxidation reaction (shown in Table 1) releases heat to the system, thus providing the required thermal energy to sustain the reactions depending on the feedstock moisture content, equivalence ratio, and initial bed temperature. An equivalence ratio of 0.15-0.3 is typically suitable for maximum gas yield with air as oxidizing gas for the gasification process [3], [35]. However, the mentioned equivalence ratio may not be suitable for efficient conversion when using steam-air as the fluidizing gas due to reducing reaction rates occurred by a decrease in bed temperature and gas residence time. In this regard, it was essential first to find a suitable equivalence ratio that sustained gasification without secondary heat addition and find the optimal steam-to-air ratio required for an auto-thermal operation of the reactor.

This work employs thermal flow gasification with air as the gasifying medium and quantifies an optimal equivalence ratio required to produce higher heating value gases, a lower amount of unreacted carbon in the bed, and higher bed temperatures. For this, thermal flow in the reactor was selected. Selecting thermal flow in the CPFD model allowed to calculate temperature gradients within the reactor due to initial fluid and particle temperatures, temperature boundary conditions, thermal walls, and chemical reactions. The initial bed temperature is a critical parameter when the objective is to run the reactor in auto-thermal mode. The reactor has to self-sustain the required pyrolysis thermal input. At the same time, the bed temperature has to be below the bed particle sintering temperature limit during the exothermic oxidation reactions. In this work, the initial bed temperature of 1073K was selected by considering the bed sintering temperature and pyrolysis temperature (Furuvik et al., 2022; Hosoya et al., 2007). With the constant flow rate of wood pellets (3.1 kg/h), the air supply was altered to change the equivalence ratio in the range of 0.15-0.3. For the same biomass feed and initial bed temperature, the influence of equivalence ratio on char accumulation, change in bed temperatures and product gas yield was measured from the CPFD simulations. Fig.5 compares the bed temperature fluctuation at height 13.4 cm, and total particle mass fluctuation predicted by the CPFD model at different equivalence ratios. As depicted in Fig.5(a), the average bed temperature varied significantly with an increase in equivalence ratio for the same initial bed temperature. At 0.13 equivalence ratio, the bed temperature decreased initially due to dominant endothermic reactions followed by the pyrolysis reactions. However, the average bed temperature stabilized later and fluctuated around 1050 K, indicating that the partial char oxidation reaction counterbalanced the thermal energy consumed by the endothermic reactions.
Conversely, elevated average bed temperature was observed at equivalence ratios 0.2, 0.25, and 0.3. The rise in bed temperature was due to the availability of sufficient oxidizing medium in the reactor that promoted the oxidation reactions releasing heat to the system. Similarly, the fluctuation in the total mass of the particle for different equivalence ratios are shown in Fig.5 (b). The bed material mass was constant at 2.5 kg. Therefore, the change in particle mass is due to variation in conversion rate of supplied biomass at different equivalence ratio. As illustrated in the Fig. 5 (a), the total

particle mass initially increased during the first 200s and then decreased. The initial increment in the particle mass was due to char accumulation in the bed with lower conversion rate of the biomass compared to total inlet flow rate of supplied biomass. The maximum accumulation rate of the char particles in the bed was higher at an equivalence ratio of 0.15 and lower at an equivalence ratio of 0.3. Due to higher oxygen availability in bed, the char conversion rate occurred faster at an equivalence ratio of 0.3, resulting in higher bed temperature (as shown in Fig. 5(a)) and vice-versa.
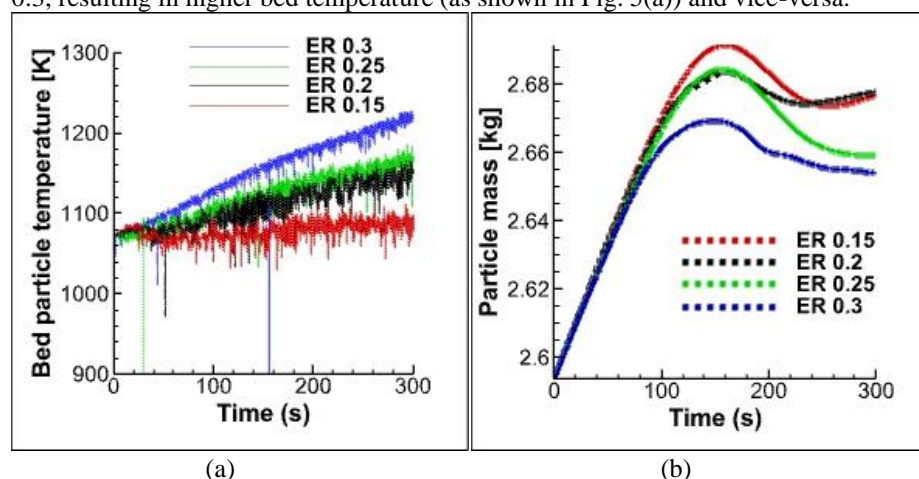

| (a) | (b) |

Fig.5. (a) Fluctuation of the bed temperature at height 13.37 cm at different equivalence ratios, (b) Change in total particle mass in the bed with time at different equivalence ratios.

Similarly, for equivalence ratios 0.15-0.3, the product gas compositions were compared, as shown in Fig. 6. The result depicts that at the equivalence ratio 0.15, the product gas compositions were enriched with CH_4, CO and H_2 fraction. As the air supply was increased, the product gas was diluted with nitrogen with lower CH_4, CO and H_2 fractions and higher CO_2 fraction in the product gas. Therefore, a lower equivalence ratio is preferred for higher-quality gas output with air as oxidizing medium. However, with steam-air as fluidizing gas, at lower equivalence ratio of 0.15 (as shown in Fig. 5a), the reactor may not self-sustain the required thermal energy for biomass conversion. Therefore, when selecting an equivalence ratio for using air-steam as fluidizing gas, other parameters like quality of the product gas, reactor temperature, and unconverted carbon in the bed have to be considered collectively. For instance, at an equivalence ratio of 0.3, the product gas was diluted with nitrogen. At an equivalence ratio of 0.2, the product gas quality was comparatively higher than the product gas quality at an equivalence ratio of 0.3. Similarly, the average bed temperature at an equivalence ratio of 0.2 was higher compared to the bed temperature at an equivalence ratio of 0.15 (Fig.5b). However, due to increase in char particle accumulation at the equivalence ratio of 0.2 (as shown in Fig. 5(a), steam could not be used since the addition of steam could accelerate the accumulation of unconverted carbon in the bed resulting in bed de-fluidization. Therefore, an equivalence ratio of 0.25 was selected for steam addition as, under this condition, the reactor temperature was higher with less char in the bed and better gas quality.
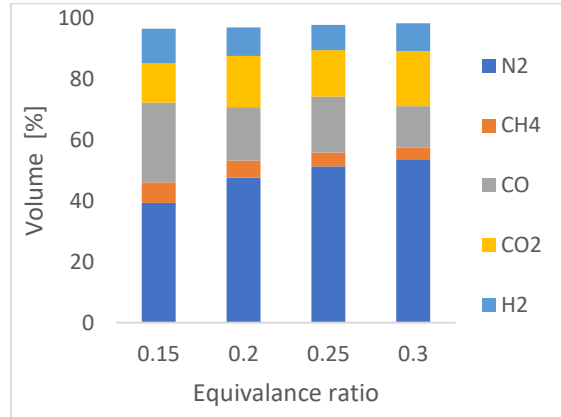
Fig.6. Product gas composition of wood pellets at different equivalence ratios.

3.3 Autothermal air-steam gasification

At an equivalence ratio of 0.25 and an initial bed temperature of 1073K, steam was added with air as gasifying and fluidizing medium. The air-to-steam ratio of 0.01-0.2 was selected and the influence of steam addition to the outlet product gas, bed temperature and char conversion are discussed.

Figure 7 shows the optimal steam-to-air ratio (SA) at which maximum hydrogen yield and the fraction of CO and H_2 in the product gas were obtained. The hydrogen concentration in the product gas was 11 (vol.%) with air as the gasifying medium at an equivalence ratio of 0.25 (Shown in Fig. 6). With the addition of 1 (wt.%) steam with air inlet, the H_2 fraction in the product gas approximately doubled 21.5 (vol.%) as depicted in Fig. 7 (a). With an increase in the steam-to-air ratio, the Hydrogen fraction in the product gas increased to 0.05*SA and decreased with a further increase in the steam fraction in the inlet gas supply. The increment in the Hydrogen fraction upto 0.05*SA was due to enhance water gas shift reaction, steam gasification reaction and methane reforming reaction (Shown in Table 1.), where CO, CH_4, and carbon reacted with added steam to produce Hydrogen-rich syngas. However, the Hydrogen concentration in the product gas decreased later due to the presence of excess unreacted steam in the product gas, as shown in Fig. 9. The excess of steam in the reactor reduced the reactor temperature and more of the CO couldn't convert to H_2 via water gas shift reaction thereby no increasing trend in Hydrogen fraction was observed above SA ratio 0.05.

Similarly, the ratio (γ') of fuel gases(CO and H_2) and CO_2 and H_2O are plotted as shown in Fig. 7(b). The result depicts that by using up to 5 wt.% steam in the inlet gas, the CO fraction in the product gas increased together with the H_2 yield due to enhance steam and CO_2 gasification reaction with char, resulting in a maximum value of $\gamma' \cong$ 4. However, γ' decreased with a further increase in steam concentration in the inlet flow due to increase in the unreacted H_2O concentration in the product gas. Therefore, for an equivalence ratio, the amount of steam that can promote efficient conversion depends on bed temperature and the amount of unreacted carbon particles in the bed.
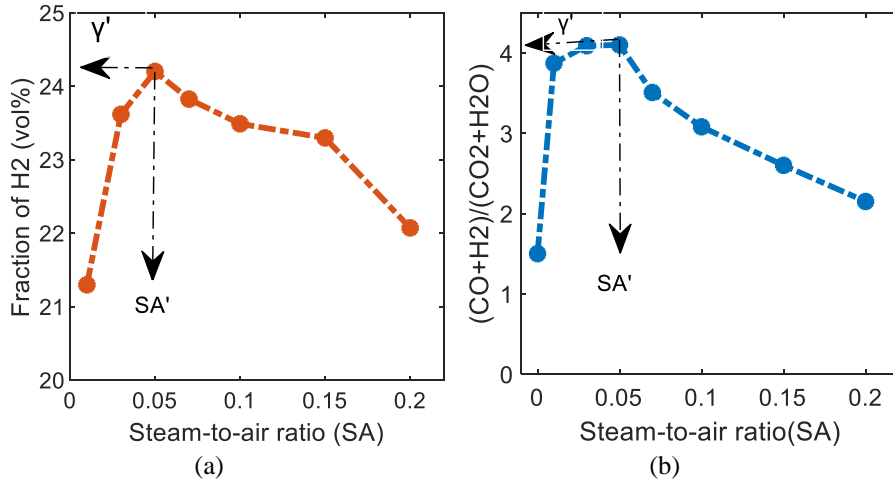
Fig. 7. (a) Change in Hydrogen fraction in the product gas outlet at different steam-to-air ratio, (b) optimal steam-to-air ratio for higher quality gas yield.
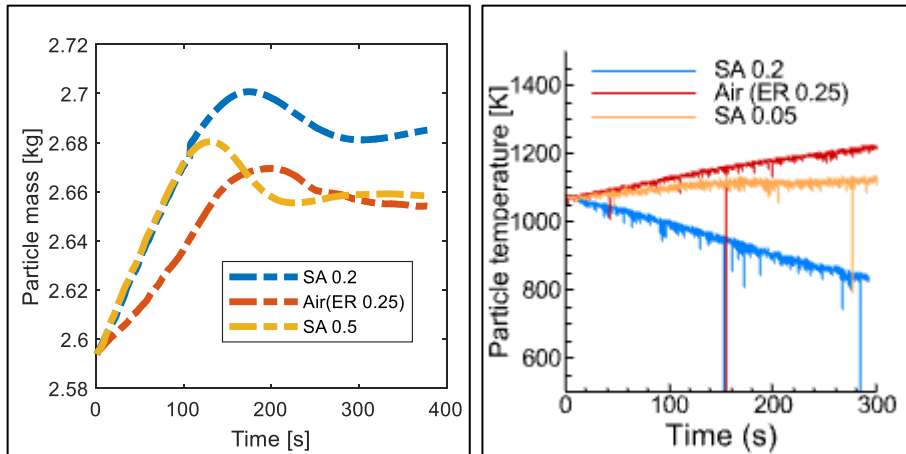

Fig. 8. Change in particle mass (left) and bed temperature (right) during conversion of wood pellets at different steam to air ratios.

The temperature of the bed should be high enough to proceed the homogenous and heterogenous reactions. At the same time, the amount of unconverted carbon in the bed should be proportional so that the fluid dynamics behavior is not hindered. A high char load on the bed can shift the bubbling regime bed into slugging or defluidization thus, obstructing the conversion phenomena. As shown in Fig. 8, the bed temperature started to decrease significantly at SA 0.2 with a rise in the mass of unconverted carbon in the bed. The CO_2 fraction decreased slightly at SA 0.2 and the H_2O fraction increased by ten times as SA was increased from 0.05 to 0.2. The reduced bed temperature and CO2 fraction and increased carbon in the bed the indicate slower oxidation reactions at SA 0.2. While, at a steam air ratio of 0.05, the bed temperature self-sustained the required

thermal input (depicted in Fig. 8b) and resulted in enhanced gas yield, as shown in Fig.9, with lower char accumulation in the bed (see Fig.8a).
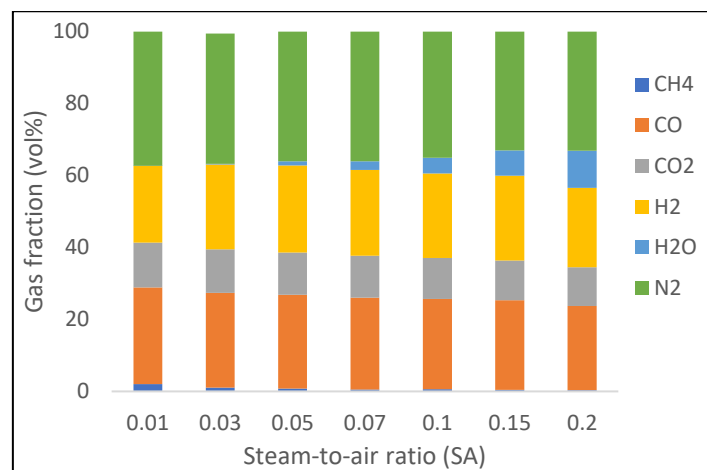

Fig.9. Change in product gas compositions at different steam-to-air ratios.

4   Conclusion

The thermochemical gasification in a fluidized bed is a promising method to convert wastes and biomass into syngas that can be utilized for power generation, producing biofuels, biomethane and chemicals. The quality of syngas significantly depends on the oxidizing medium.

This work aims to obtain the optimal parameters at which Hydrogen-rich syngas can be produced from auto-thermal gasification of wood pellets using air steam as the gasifying medium. For this, a three-dimensional Computational Particle Fluid Dynamics model was developed by considering the heat transfer model, chemical kinetics rate, and particle size distribution. The CPFD model was validated against the experimental data obtained from a 20kW bubbling fluidized bed gasifier. Further simulations were carried to find the optimal reactor temperature, equivalence ratio and steam-to-air ratio for an auto-thermal operation of the gasifier using air-steam as fluidizing gas.

The reactor was simulated in two steps: (I) thermal flow simulations at different equivalence ratios and (II) thermal flow simulations at different steam-to-air ratios at optimal equivalence ratio. The results depicted that at an equivalence ratio of 0.25 (with air as the gasifying medium), a better-quality syngas with higher bed temperature and lower unconverted carbon in the bed was observed. The Hydrogen fraction in product gas increased from 11 (vol.%) to > 21 (vol.%) with the addition of (1-5) wt.% steam to the inlet fluidizing gas. Above the steam-to-air ratio of 0.05, unreacted steam in the product gas increased. The unconverted carbon in the bed increased significantly with a decrease in the reactor temperature by 300°C at an equivalence ratio of 0.2. The optimal equivalence ratio at which the reactor sustained auto-thermal operation with

enhanced gas quality and lower unconverted carbon in the bed was 0.25, with an optimal steam-to-air ratio of 0.05.

5   References

[1]   Y. Wang, L. Huang, T. Zhang, and Q. Wang, "Hydrogen-rich syngas production from biomass pyrolysis and catalytic reforming using biochar-based catalysts," *Fuel*, vol. 313, p. 123006, Apr. 2022, doi: 10.1016/J.FUEL.2021.123006.

[2]   S. Heidenreich and P. U. Foscolo, "New concepts in biomass gasification," *Prog Energy Combust Sci*, vol. 46, pp. 72–95, Feb. 2015, doi: 10.1016/J.PECS.2014.06.002.

[3]   J. C. Bandara, R. Jaiswal, H. K. Nielsen, B. M. E. Moldestad, and M. S. Eikeland, "Air gasification of wood chips, wood pellets and grass pellets in a bubbling fluidized bed reactor," *Energy*, vol. 233, p. 121149, Oct. 2021, doi: 10.1016/J.ENERGY.2021.121149.

[4]   A. Sanlisoy and M. O. Carpinlioglu, "A review on plasma gasification for solid waste disposal," *Int J Hydrogen Energy*, vol. 42, no. 2, pp. 1361–1365, Jan. 2017, doi: 10.1016/J.IJHYDENE.2016.06.008.

[5]   D. T. Pio, L. A. C. Tarelho, and M. A. A. Matos, "Characteristics of the gas produced during biomass direct gasification in an autothermal pilot-scale bubbling fluidized bed reactor," *Energy*, vol. 120, pp. 915–928, Feb. 2017, doi: 10.1016/J.ENERGY.2016.11.145.

[6]   M. Campoy, A. Gómez-Barea, F. B. Vidal, and P. Ollero, "Air–steam gasification of biomass in a fluidised bed: Process optimisation by enriched air," *Fuel Processing Technology*, vol. 90, no. 5, pp. 677–685, May 2009, doi: 10.1016/J.FUPROC.2008.12.007.

[7]   C. Dupont, G. Boissonnet, J. M. Seiler, P. Gauthier, and D. Schweich, "Study about the kinetic processes of biomass steam gasification," *Fuel*, vol. 86, no. 1–2, pp. 32–40, Jan. 2007, doi: 10.1016/J.FUEL.2006.06.011.

[8]   J. Corella, J. M. Toledo, and G. Molina, "A Review on Dual Fluidized-Bed Biomass Gasifiers," *Industrial & Engineering Chemistry Research*, vol. 46, no. 21, pp. 6831–6839, Sep. 2007, doi: 10.1021/ie0705507.

[9]   J. Corella, J. M. Toledo, and G. Molina, "A Review on Dual Fluidized-Bed Biomass Gasifiers," *Industrial & Engineering Chemistry Research*, vol. 46, no. 21, pp. 6831–6839, Sep. 2007, doi: 10.1021/ie0705507.

[10]   L. Stanger *et al.*, "Dynamic modeling of dual fluidized bed steam gasification for control design," *Energy*, vol. 265, p. 126378, Feb. 2023, doi: 10.1016/J.ENERGY.2022.126378.

[11]   J. Y. Nam *et al.*, "Hydrogen-rich gas production from disposable COVID-19 mask by steam gasification," *Fuel*, vol. 331, p. 125720, Jan. 2023, doi: 10.1016/J.FUEL.2022.125720.

[12]   A. M. Ali *et al.*, "Polygeneration syngas and power from date palm waste steam gasification through an Aspen Plus process modeling," *Fuel*, vol. 332, p. 126120, Jan. 2023, doi: 10.1016/J.FUEL.2022.126120.

[13] S. S. Timofeeva, J. V. Karaeva, A. A. Kovalev, D. A. Kovalev, and Y. V. Litti, "Steam gasification of digestate after anaerobic digestion and dark fermentation of lignocellulosic biomass to produce syngas with high hydrogen content," *Int J Hydrogen Energy*, vol. 48, no. 21, pp. 7559–7568, Mar. 2023, doi: 10.1016/J.IJHYDENE.2022.11.260.

[14] P. Lv, Z. Yuan, L. Ma, C. Wu, Y. Chen, and J. Zhu, "Hydrogen-rich gas production from biomass air and oxygen/steam gasification in a downdraft gasifier," *Renew Energy*, vol. 32, no. 13, 2007, doi: 10.1016/j.renene.2006.11.010.

[15] E. Shayan, V. Zare, and I. Mirzaee, "Hydrogen production from biomass gasification; a theoretical comparison of using different gasification agents," *Energy Convers Manag*, vol. 159, 2018, doi: 10.1016/j.enconman.2017.12.096.

[16] M. Schmid, C. Schmidberger, and G. Scheffknecht, "Modelling and simulation of fluidized bed steam-oxygen gasification of sewage sludge using thermochemical equilibrium and experimental data," *Fuel*, vol. 341, 2023, doi: 10.1016/j.fuel.2023.127595.

[17] J. F. González, S. Román, D. Bragado, and M. Calderón, "Investigation on the reactions influencing biomass air and air/steam gasification for hydrogen production," *Fuel Processing Technology*, vol. 89, no. 8, pp. 764–772, Aug. 2008, doi: 10.1016/J.FUPROC.2008.01.011.

[18] P. M. Lv, Z. H. Xiong, J. Chang, C. Z. Wu, Y. Chen, and J. X. Zhu, "An experimental study on biomass air-steam gasification in a fluidized bed," *Bioresour Technol*, vol. 95, no. 1, 2004, doi: 10.1016/j.biortech.2004.02.003.

[19] Z. Afailal, N. Gil-Lalaguna, I. Fonts, A. Gonzalo, J. Arauzo, and J. Luis Sánchez, "Thermochemical valorization of argan nutshells: Torrefaction and air–steam gasification," *Fuel*, vol. 332, 2023, doi: 10.1016/j.fuel.2022.125970.

[20] R. Jaiswal, R. K. Thapa, and B. M. E. Moldestad, "Study of agricultural waste gasification in an air-blown bubbling fluidized bed using a CPFD model," in *Proceedings of The 61st SIMS Conference on Simulation and Modelling SIMS 2020, September 22-24, Virtual Conference, Finland*, 2021. doi: 10.3384/ecp20176393.

[21] J. Wang, M. A. Van Der Hoef, and J. A. M. Kuipers, "Comparison of two-fluid and discrete particle modeling of dense gas-particle flows in gas-fluidized beds," *Chem Ing Tech*, vol. 85, no. 3, 2013, doi: 10.1002/cite.201200101.

[22] D. M. Snider, S. M. Clark, and P. J. O'Rourke, "Eulerian-Lagrangian method for three-dimensional thermal reacting flow with application to coal gasifiers," *Chem Eng Sci*, vol. 66, no. 6, 2011, doi: 10.1016/j.ces.2010.12.042.

[23] X. Ku, T. Li, and T. Løvås, "CFD–DEM simulation of biomass gasification with steam in a fluidized bed reactor," *Chem Eng Sci*, vol. 122, pp. 270–283, Jan. 2015, doi: 10.1016/J.CES.2014.08.045.

[24] R. Jaiswal, B. M. E. Moldestad, M. S. Eikeland, H. K. Nielsen, and R. K. Thapa, "Image Processing and Measurement of the Bubble Properties in a Bubbling Fluidized Bed Reactor," *Energies (Basel)*, vol. 15, no. 21, 2022, doi: 10.3390/en15217828.

[25] R. K. Thapa, A. Frohner, G. Tondl, C. Pfeifer, and B. M. Halvorsen, "Circulating fluidized bed combustion reactor: Computational Particle Fluid Dynamic model validation and gas feed position optimization," *Comput Chem Eng*, vol. 92, 2016, doi: 10.1016/j.compchemeng.2016.05.008.

[26] S. Kraft, F. Kirnbauer, and H. Hofbauer, "CPFD simulations of an industrial-sized dual fluidized bed steam gasification system of biomass with 8 MW fuel input," *Appl Energy*, vol. 190, 2017, doi: 10.1016/j.apenergy.2016.12.113.

[27] P. J. O'Rourke and D. M. Snider, "Inclusion of collisional return-to-isotropy in the MP-PIC method," *Chem Eng Sci*, vol. 80, 2012, doi: 10.1016/j.ces.2012.05.047.

[28] D. M. Snider, "Three fundamental granular flow experiments and CPFD predictions," *Powder Technol*, vol. 176, no. 1, 2007, doi: 10.1016/j.powtec.2007.01.032.

[29] D. M. Snider, "An Incompressible Three-Dimensional Multiphase Particle-in-Cell Model for Dense Particle Flows," *J Comput Phys*, vol. 170, no. 2, 2001, doi: 10.1006/jcph.2001.6747.

[30] M. J. Andrews and P. J. O'Rourke, "The multiphase particle-in-cell (MP-PIC) method for dense particulate flows," *International Journal of Multiphase Flow*, vol. 22, no. 2, pp. 379–402, Apr. 1996, doi: 10.1016/0301-9322(95)00072-0.

[31] L.-S. Fan and C. Zhu, *Principles of Gas-Solid Flows*. 1998. doi: 10.1017/cbo9780511530142.

[32] W.-C. Yang, "Handbook of fluidization and fluid-particle systems," *China Particuology*, vol. 1, no. 3, 2003, doi: 10.1016/s1672-2515(07)60126-2.

[33] R. Jaiswal, N. C. I. S. Furuvik, R. K. Thapa, and B. M. E. Moldestad, "A CPFD model to investigate the influence of feeding positions in a gasification reactor," *International Journal of Energy Production and Management*, vol. 5, no. 3, 2020, doi: 10.2495/EQ-V5-N3-223-233.

[34] R. Jaiswal, C. E. Agu, H. Kofoed Nielsen, M. Sørflaten Eikeland, B. Margrethe Emilie Moldestad, and R. Kumar Thapa, "Investigation of Bubble Properties in a Bubbling Fluidized-Bed Gasification Reactor Using a Computational Particle Fluid Dynamic Model," *Industrial & Engineering Chemistry Research*, vol. 0, no. 0, May 2023, doi: 10.1021/acs.iecr.3c00626.

[35] D. T. Pio, L. A. C. Tarelho, and M. A. A. Matos, "Characteristics of the gas produced during biomass direct gasification in an autothermal pilot-scale bubbling fluidized bed reactor," *Energy*, vol. 120, pp. 915–928, Feb. 2017, doi: 10.1016/J.ENERGY.2016.11.145.

[36] N. C. I. S. Furuvik, L. Wang, R. Jaiswal, R. Thapa, M. S. Eikeland, and B. M. E. Moldestad, "Experimental study and SEM-EDS analysis of agglomerates from gasification of biomass in fluidized beds," *Energy*, vol. 252, p. 124034, Aug. 2022, doi: 10.1016/J.ENERGY.2022.124034.

[37] T. Hosoya, H. Kawamoto, and S. Saka, "Cellulose-hemicellulose and cellulose-lignin interactions in wood pyrolysis at gasification temperature," *J Anal Appl Pyrolysis*, vol. 80, no. 1, 2007, doi: 10.1016/j.jaap.2007.01.006.

usn.no